Proteo-Lipobeads: A novel platform to investigate strictly oriented membrane proteins in their functionally active form

Bio-UV-SPR: Exploring the ultraviolet spectral range for water-bound analytes in surface plasmon resonance spectroscopy

Dissertation

Zur Erlangung des Grades

Doktor der Naturwissenschaften

Am Fachbereich Biologie

Der Johannes Gutenberg-Universität in Mainz

Frank Andreas Geiss

geb. am 13. September 1986 in Frankfurt am Main

Mainz, 2018

Dekan: <content not available in online version>

1. Berichterstatter: <content not available in online version>

2. Berichterstatter: <content not available in online version>

Tag der mündlichen Prüfung: 18.12.2018

Frank Andreas Geiss

Proteo-Lipobeads: A novel platform to investigate strictly oriented membrane proteins in their functionally active form

Bio-UV-SPR: Exploring the ultraviolet spectral range for water-bound analytes in surface plasmon resonance spectroscopy

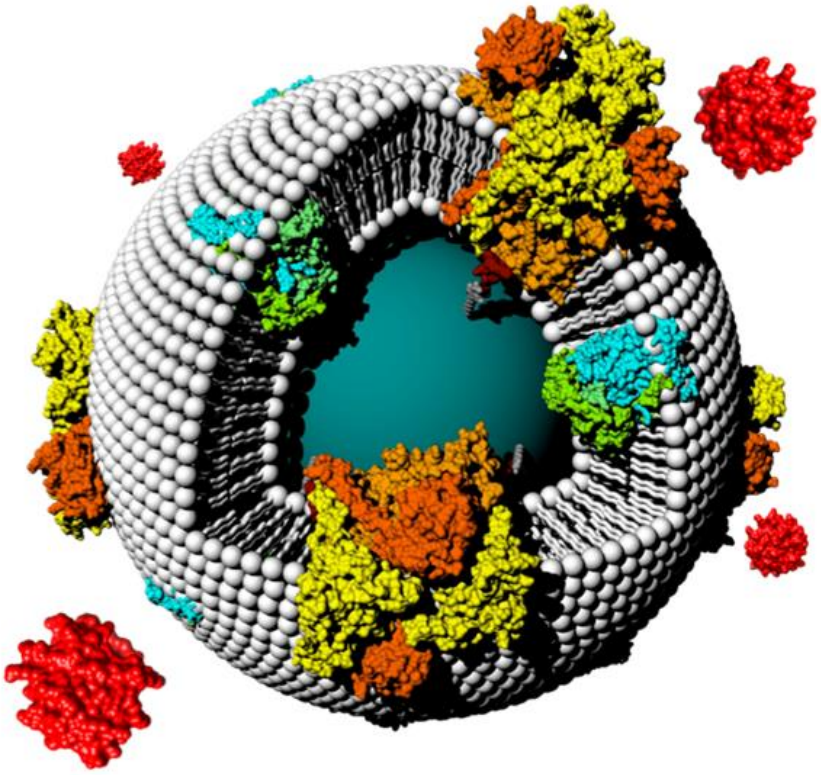

GOTT SCHUF DAS VOLUMEN,
DER TEUFEL DIE OBERFLÄCHE

Wolfgang Pauli

GOD MADE THE BULK;
SURFACES WERE INVENTED BY THE DEVIL

Wolfgang Pauli

0 Abstract

(Kurzzusammenfassung)

Abstract

The present thesis comprises two independent parts, the first one (*Proteo-Lipobeads*) representing approximately 80 % of the work, whereas the remaining 20 % are covered by the second topic (*Bio-UV-SPR*).

Membrane proteins, which need to be embedded in cell membranes or biomimetic membrane systems to provide function, are the target of many diseases. In the present work, proteo-lipobeads, which overcome the disadvantages of cells, liposomes, and solid-supported bilayer lipid membranes are introduced as a complementary system that enlarges the spectrum of possible investigation methods.

Proteo-lipobeads consist of spherical core particles determining their final size, the proteins of interest, which are oriented by attachment via his-tag technology, and a protein-tethered membrane, which is assembled by detergent removal via dialysis in the presence of the desired lipids. In this work, model proteins of the respiratory chain, cytochrome *c* oxidase and the cytochrome bc_1 complex, are investigated.

The results clearly indicate that the established membrane is dense, the proteins retain their functionality, and that the proteo-lipobead components constitute a modular system. The applicability in high-throughput assays, a certain storage stability, and the possibility to integrate systems that are more complex is evidenced. Besides the micrometer-sized agarose-based proteo-lipobeads, investigated by fluorescence microscopy, a nanometer-sized version is introduced using silica particles to enable UV/Vis spectroscopy. The results are documented by four publications.

In the second part, the commonly used surface plasmon resonance spectroscopy setup was improved to overcome limitations that preclude analyses of water-bound samples at absorption maxima below 350 nm. The answer to this problem is an aluminum grating excited by a white light source as demonstrated on a model protein. The results are documented in a research article.

Kurzzusammenfassung

Diese Arbeit umfasst zwei voneinander unabhängige Teile. Der erste repräsentiert ca. 80 %, der zweite ca. 20 % der Arbeit.

Viele Krankheiten sind assoziiert mit Membranproteinen. Um diese zu erforschen, müssen sie in eine Membran eingebettet werden, was durch Zellen oder biomimetische Membransysteme umgesetzt werden kann. Durch Proteo-Lipobeads (PLBs) sollen die Nachteile von Zellen, Liposomen und festkörperunterstützten Lipiddoppelschichten überwunden werden. Das Ziel ist nicht der vollständige Ersatz der letzteren, sondern ein ergänzendes System, welches das Spektrum der möglichen Untersuchungsmethoden ergänzt.

PLBs basieren auf kugelförmigen Kernpartikeln, welche die finale Größe bestimmen, den Membranproteinen, die durch His-Tag-Technologie gerichtet angebunden werden und einer proteingebundenen Membran, welche durch die Entfernung des Detergenz mittels Dialyse in Anwesenheit von Lipiden präpariert wird. In dieser Arbeit werden die Cytochrom-*c*-Oxidase und der Cytochrom-bc_1-Komplex aus der Atmungskette als Modellproteine verwendet.

Die Resultate zeigen, dass die Membran dicht ist, die Proteine ihre Funktionalität bewahren und die PLB-Komponenten ein Baukastensystem darstellen. Die Anwendbarkeit in Hochdurchsatz-Analysen, eine gewisse Haltbarkeit und die Integration eines komplexeren Enzymsystems werden demonstriert. Neben den mikrometergroßen Agarose-PLBs für die Fluoreszenz-Mikroskopie wird eine nanometergroße Version basierend auf Silica-Partikeln vorgestellt, die UV/Vis-Spektroskopie ermöglicht. Die Resultate sind in vier Publikationen dokumentiert.

Der zweite Teil befasst sich mit Oberflächenplasmonresonanzspektroskopie. Der herkömmliche Messaufbau ermöglicht keine Analyse von wassergebundenen Proben mit Absorptionsmaxima unter 350 nm. Wie anhand eines Modellproteins gezeigt wird, kann das Problem durch ein Aluminiumgitter, angeregt durch eine Weißlichtquelle, überwunden werden. Die Ergebnisse sind in einer Publikation dokumentiert.

Contents

I Theory

Chapter 1 *Biological Basics*

1.1 Biological membranes

The basic framework of biological membranes consists of lipids. A large variability of biological membranes is then achieved by the lipid composition, by further lipid modifications (e.g., glycosylation) and by the comprised membrane proteins and the modifications thereof.

A lipid is just defined as a molecule, which is soluble in nonpolar solvents and is of biological origin [1]. Further, lipids are assigned to certain subclasses, which are defined more in detail. The membrane-forming lipids are the phospholipids. The basic molecule is glycerol in the majority of cases, to which two lipophilic hydrocarbon chains (fatty acids) are covalently linked via an ester bond. Those can be specified by their length and by their number and positions of unsaturated (C-C double) bonds. With each unsaturated bond, the phase transition temperature decreases, hence unsaturated lipids are more fluent than saturated ones. Usually, only one of these fatty acids contains unsaturated bonds. At the third hydroxyl group of the central glycerol, a phosphate is covalently attached, which itself exhibits a variable moiety at the opposite end [2]. Lipid membranes are not exclusively build (referring to the lipid share) of phospholipids. A ubiquitous exemption, which even holds the largest share and is completely different in terms of structure, is cholesterol, which increases the rigidity of a membrane (Fig. 1.4 and related text) [3]. Hence, phospholipids are not exclusively present in biological membranes, but still they are the membrane-forming ones. In contrast, the lipids used for energy storage belong to a different class of lipids, the triglycerides (with a third fatty acid esterified to the central glycerol, instead of the polar phosphate moiety) [4].

A phospholipid hence contains a hydrophilic head and a lipophilic (hydrophobic) tail (Fig. 1.1). Due to solubility reasons, a bilayer is automatically formed in aqueous – thus polar – environment. The alternative of a micelle is not favored due to the cylindrical shape of phospholipids. The process of this spontaneous formation is called self-assembly. Biological membranes are therefore also referred to as lipid bilayers, where the hydrophilic tails are facing each other, defining the inner membrane space, while the hydrophilic heads at the outsides are facing the aqueous environment. Further, since a finite lipid bilayer still exhibits ends, the lipid bilayer assumes a spherical or ellipsoid shape. A compartment with defined inside and outside

is created [2]. Even though it is logically appropriate, the abbreviation BLM for bilayer lipid membrane (although historically introduced as black lipid membrane), is rather used in terms of biomimetic and thus artificial membrane systems, which are introduced in subchapter 1.4. An exemplary depiction of a phospholipid is given in Figure 1.1.

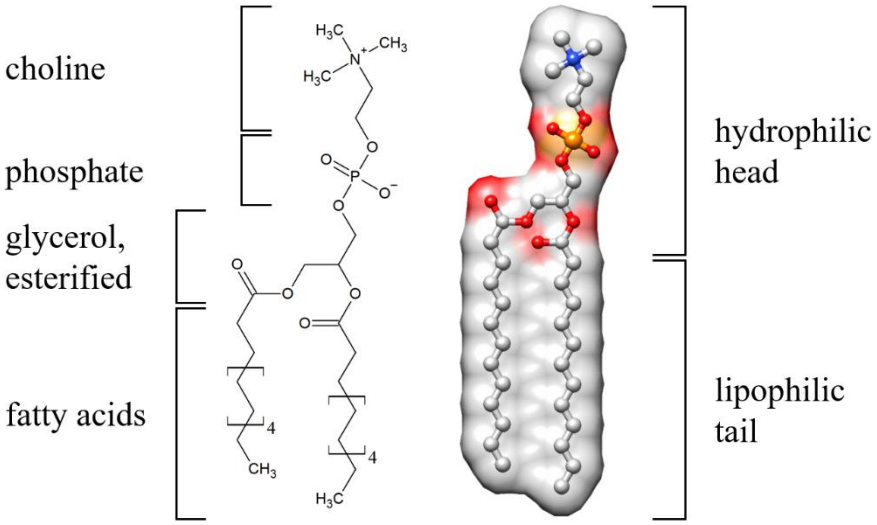

Figure 1.1: Exemplary phospholipid. A potentially membrane-forming phospholipid is depicted as structural formula (left) and as ball-&-stick projection with assigned molecular surface (right). The different parts of the phospholipid are specified with regards to their chemical components on the left, while the solubility is indicated on the right.

A common classification of phospholipids is referring to the head group, so the exemplary lipid in Figure 1.1 is a phosphatidylcholine, exhibiting a choline group attached to the phosphate. The most abundant phospholipid classes in human membranes, according to Andreoli *et al.*, 1987 [5], are summarized in Figure 1.2.

Structure	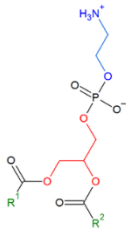	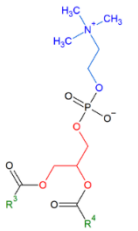	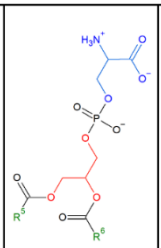	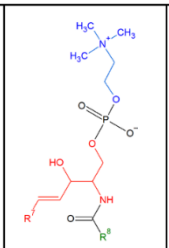	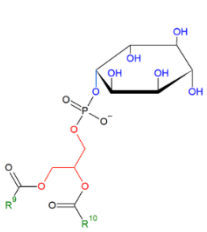
Name	Phosphatidyl-ethanolamine	Phosphatidyl-choline	Phosphatidyl-serine	Sphingo-myelin	Phosphatidyl-inositol
Backbone	Glycerol	Glycerol	Glycerol	Amino alcohol (sphingosine)	Glycerol
Charge	Neutral	Neutral	Neutral	Neutral	Negative

Figure 1.2: Most abundant phospholipids in humans. The variable moiety attached to the phosphate is depicted in blue, the backbone in red, and the variable fatty acids as $R^{1\text{-}6,\ 8\text{-}10}$ in green. R^7 is an exemption, since it belongs to the backbone sphingosine (therefore drawn in red). It consists of a hydrocarbon chain as well, hence it also acts like a fatty acid.

Among those, there is an exemption of the mostly valid statement that glycerol is the central component of a phospholipid. For sphingomyelin, it is the amino alcohol sphingosine.

Fatty acids usually have trivial names, and for further specifications at the first glance, the number of carbons and of C-C double bonds (also called the degree of saturation) are mentioned in brackets, separated by a colon. So, the phytanic acid, which contains 16 carbon atoms and is fully saturated, would be addressed as “phytanic acid (16:0)” [6]. The further nomenclature, of which several possibilities exist, is not of worth for understanding this work, so it is not discussed here.

The specifications about a membrane’s thickness differ within the literature, not least because of the different types and compositions, and ranges from 4 to 10 nm [7–9]. Within a membrane, membrane proteins are situated. Some are anchored within the membrane, themselves being situated intra- or extracellular (peripheral membrane proteins), others penetrate or completely cross the membrane, possibly protruding into the inner or outer compartment (integral membrane proteins) [10]. For a schematic depiction of the membrane, see Figure 1.3.

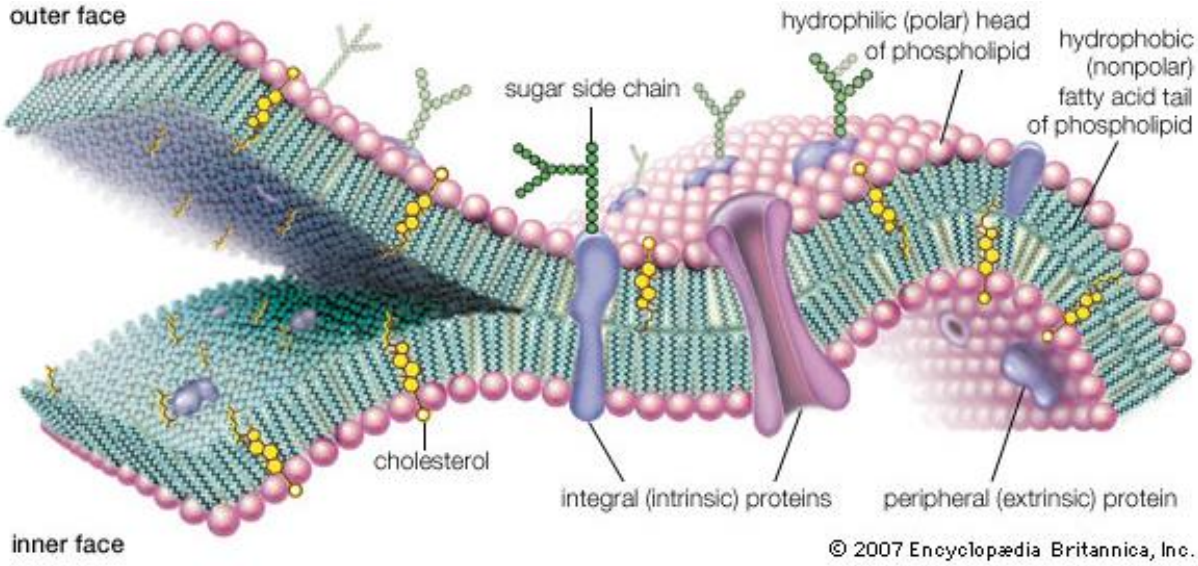

Figure 1.3: Schematic depiction of a biological membrane. Description is given within the text. Figure adapted from Encyclopaedia Britannica, 2007 [11].

Usually, if not, e.g., associated to filaments, membrane proteins (and lipids as well) can diffuse freely inside the membrane according to the fluid mosaic model, established by Singer & Nicolson in 1972 [12]. The fluidity of a membrane can be measured by a technique called fluorescence recovery after photobleaching (FRAP), where membrane lipids or membrane proteins are fluorescently labeled and subsequently the label is locally bleached. Having a fluid membrane, the unbleached molecules redistribute by means of diffusion, and the recovery of

fluorescence intensity can be followed over time. Finally, the fluorescence is uniform again, even though a bit lower than the initial one [13, 14].

The fluidity of a membrane is decreased by the insertion of cholesterol, and conversely, the stability is increased.
Cholesterol, exhibiting a completely different structure (Fig. 1.4), is the most abundant lipid at least in animal cell membranes, holding about 30 % in average [3, 15].

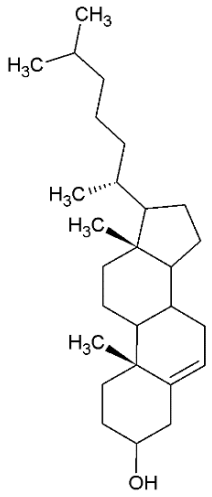

Figure 1.4: Structure of cholesterol.

Although relatively fluent, the membrane's primary purpose is its barrier function, separating the inside from the outside of the cell or a compartment thereof. Due to these sealing properties, only few chemical species can pass the membrane, while the remaining molecules require a specially tailored membrane protein, or a vesicle to perform exocytosis or endocytosis. The property of a membrane to be permeable for some chemical species and restrictive towards others is called semi-permeability.

The membrane is – although hydrophobic – permeable for water, which follows osmotic gradients. This basic permeability can be increased by the incorporation of aquaporins, which facilitate the transport of water across the membrane by orders of magnitude. The membrane is also permeable for small uncharged, rather nonpolar molecules like, e.g., oxygen, carbon dioxide and ammonia. Conversely, charged small molecules and ions, like Na^+ and Cl^-, are not able to pass [16]. This general approximation is not free of exceptions, such as the later discussed valinomycin, being a rather big molecule that contains both polar and nonpolar parts, which can enter the membrane nevertheless [17]. Moreover, and this is of great importance within the presented work, protons, present in the aqueous phase as H_3O^+, $H_5O_2^+$ etc., cannot pass an intact membrane.

The sealing properties of a dense membrane towards certain molecules enable the maintenance of concentration differences, leading to a chemical potential ($\Delta\mu$) between both sides, while regarding charged molecules, these sealing properties enable the maintenance of an electric potential ($\Delta\Phi$) across the membrane. Eventually, having a concentration gradient of charged molecules across the membrane, these merge into an electrochemical potential ($\Delta\tilde{\mu}$). Further, if different charged chemical species are present in different concentrations on both sides of a membrane, an equilibrium potential might set in that is different from zero, since electrical and

chemical potential might point in opposite directions. For one species of charged molecules, $\Delta\tilde{\mu}$ at equilibrium can be calculated by means of the Nernst equation

$$\Delta\tilde{\mu} = \frac{RT}{zF}\ln\frac{[\text{ion outside}]}{[\text{ion inside}]} = 2.3026\frac{RT}{zF}\lg\frac{[\text{ion outside}]}{[\text{ion inside}]}\ , \qquad (1.1)$$

where E is the electric potential, R is the ideal gas constant (R = 8.314 J mol^{-1} K^{-1}), T is the temperature in Kelvin, z is the charge, and F is Faraday's constant (F = 96,485.3 C mol^{-1}). For anions, z is a negative value, for cations, it is a positive one.

Mathematically considering the presence of several chemical species, each causing its own electrochemical potential, the overall electrochemical potential can be calculated using the Goldman equation (also called Goldman-Hodgkin-Katz voltage equation, different from the Goldman-Hodgkin-Katz flux equation), being a generalization of the Nernst equation, and assuming that the ions are acting completely independent from each other. Different from the Nernst equation, the Goldman equation includes a term for the permeability, and in doing so, ion channels and leak voltages can be considered. The Goldman equation for monovalent ions is described by

$$\Delta\tilde{\mu} = \frac{RT}{F}\ln\left(\frac{\sum_i^n P_{M_i^+}[M_i^+]_{out} + \sum_j^m P_{A_j^-}[A_j^-]_{in}}{\sum_i^n P_{M_i^+}[M_i^+]_{in} + \sum_j^m P_{A_j^-}[A_j^-]_{out}}\right)\ , \qquad (1.2)$$

with P for the permeability, M^+ for the monovalent cations, and A^- for the monovalent anions. For divalent cations, the equation becomes more complex.

The equilibrium electrochemical potential across a membrane is also referred to as membrane potential $\Delta\Psi$. The membrane potential acts as driving force within plenty of biochemical processes, e.g., any passive molecular flux through ion channels. Moreover, in terms of protons as charged chemical species, the membrane potential acts as first intermediate energy storage in adenosine triphosphate (ATP) synthesis, as well in respiration as in photosynthesis. The proteins mainly employed within this work are part of either the respiratory chain or the (bacterial) photosynthetic light reaction, and the formation of a proton gradient across an artificial membrane is the related target of detection in most cases [3, 18].

1.2 *Cytochrome* c *oxidase and the respiratory chain*

The cytochrome *c* oxidase (C*c*O), being part of the respiratory chain, is situated within the inner mitochondrial membrane in eukaryotes and in the plasma membrane in bacteria, respectively. The C*c*O applied in this thesis originated from *Paracoccus denitrificans*, so it is a bacterial one. Nevertheless, *P. denitrificans* is known to exhibit a respirational apparatus that is very similar to the mitochondrial one, even to such an extent that this bacterial species is considered as resembling the ancestor organism which was taken up by endocytosis, eventually forming mitochondria as described by the theory of endosymbiosis [19]. Although more recent phylogenetic studies places other bacteria close to the mitochondrial ancestor [20], a degree of similarity can be assumed that is sufficient to discuss the respirational processes by means of the mitochondrial ones on this level.

The respiratory chain serves to form ATP using the energy of $NADH + H^+$ and $FADH_2$ oxidation, both being products of the upstream glycolysis and citric acid cycle [21]. A schematic drawing is shown in Figure 1.5.

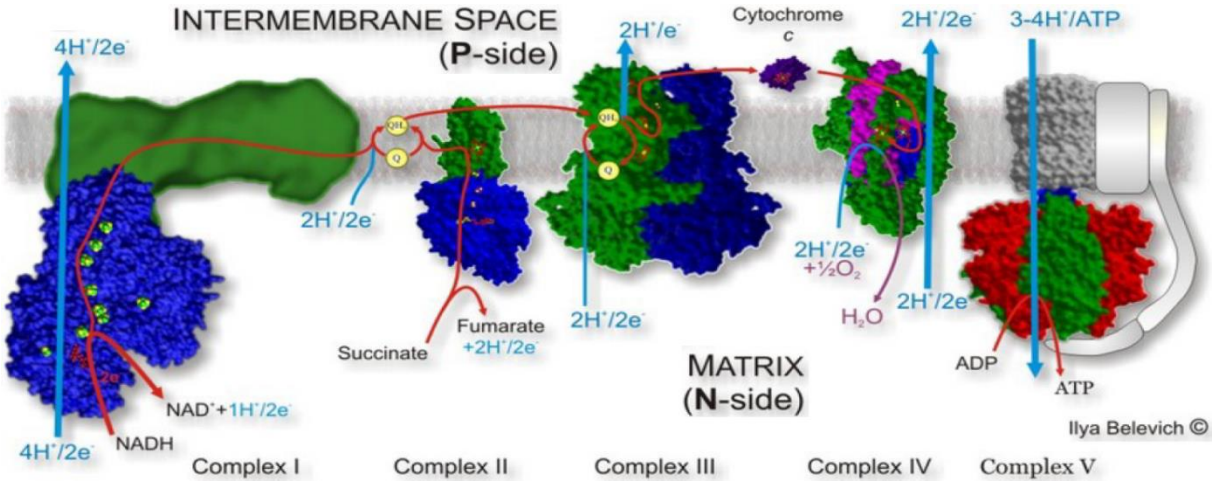

Figure 1.5. Respiratory chain. Complexes of the respiratory chain are numbered with roman digits, or named more specifically as explained in the text. The picture displays the proton and electron flux due to $NADH + H^+$ and $FADH_2$ oxidation, finally resulting in an electrochemical gradient by proton translocation across the membrane. By dissipation of the latter via the ATP synthase, ATP is produced. The electrons are finally forwarded to oxygen, forming water with additional, so-called chemical protons (in distinction to the pumped protons). Figure adapted from Belevich, 2007 [22].

The first enzyme complex of the respiratory chain is the NADH dehydrogenase or Complex I, where $NADH + H^+$ is oxidized to NAD^+, the latter returning into glycolysis and citric acid cycle for anew reduction. The two electrons are forwarded to the lipophilic electron carrier ubiquinone (Q, coenzyme Q), which diffuses freely within the hydrophobic inner part of the

membrane. During this chain of redox reactions, four protons are pumped through Complex I across the membrane. This is a first step contributing to the intermediate energy storage as electrochemical gradient by means of proton translocation, thus $\Delta\tilde{\mu}H^+$ [23, 24]. The translocation against the arising $\Delta\tilde{\mu}H$ is hence an active process, driven by the released oxidation energy. Referring to $\Delta\tilde{\mu}H$, the side belonging to the intermembrane space in case of mitochondria and to the periplasmic space in case of bacteria, respectively, is called P-side, meaning *positive*, while the matrix side is called N-side, meaning *negative*. Concerning the ΔpH component, the removal of protons from the N-side is contributing way more than the additional ones brought to the P-side, since the latter is usually way larger in volume and moreover well-buffered [25]. A further argumentation, indicating $\Delta\Phi$ as the main driving force of ATP synthesis rather than ΔpH, is discussed below. The scheme displayed in Fig. 2.6 emphasizes that the pumped protons are not the same as the ones that are released from $NADH + H^+$, but are taken from the proton pool of the matrix. This concept of release into a molecular pool and vice versa consumption thereof applies rather than having a single molecules that is handed over in a fixed succession. Moreover, the enzyme complexes are not arranged in clearly separated respiratory chains within the membrane; ratios of 1 Complex I accompanied with 3 Complexes III and 7 Complexes IV have been found [26]. Complex I is not covered by this thesis; for further literature, see Verkhovsky & Bogachev, 2010 (review) [27], or the more recent study Belevich *et al.*, 2016 [28].

The two electrons are forwarded one by one to Q, forming in a first step the radical ubisemiquinone ($QH^{\bullet-}$), and in a second step ubihydroquinone or ubiquinol (QH_2) by simultaneously taking up two protons. In parallel, the succinate dehydrogenase (Complex II) converts succinate to fumarate with the prosthetic group FAD, which is thereby reduced to $FADH_2$. $FADH_2$ is subsequently re-reduced by forming QH_2. (The first step is mostly discussed in terms of the citric acid cycle, taking place in the mitochondrial matrix and the bacterial cytoplasm, respectively, while the second step is usually assigned to the respiratory chain. Indeed, both occur at the same membrane-bound enzyme complex). The $FADH_2$ consumption is not related to any proton pumping activity, but the protons are taken up by Q on the N-side, while they are later released to the P-side (which also applies for Complex I), so $\Delta\tilde{\mu}H$ is further increased [3, 21].

QH_2 is oxidized by the bc_1 complex (bc_1, Complex III, coenzyme Q : cytochrome *c* oxidoreductase, cytochrome *c* reductase), which forwards the electrons to the water-soluble electron carrier cytochrome (cyt) *c*. The protons of QH_2 are released to the P-side. Additionally,

protons are translocated from the N-side to the P-side by means of the Q cycle. The latter was proposed by Peter Mitchell in 1975 [29] as possibility to overcome the mechanistic problem of switching from a two-electron to a one-electron carrier (Q to cyt *c*), thereby using the released energy more efficiently. Since the bc_1 complex of the respiratory chain is evolutionarily related to the one belonging to the anoxygenic photosynthesis [30], which is described in the next subchapter with focus on the bc_1 complex, the discussion of the bc_1 complex including its components and mechanisms like the Q-cycle is postponed.

Cyt *c* is a water-soluble protein of the intermembrane/periplasmatic space, which carries an iron ion in the center of its prosthetic heme *c* group (see below), Fe^{3+} in its oxidized form. By electron uptake, the iron is reduced to Fe^{2+}. Cyt *c* is re-oxidized by the C*c*O. As water-soluble electron carrier, which is not only involved in respiration, but also in the anoxygenic photosynthesis [31], it was employed for different experiments within the presented work. Its structure is depicted in Figure 1.6. It is almost ubiquitous in living beings and relatively conserved, by which it is an important candidate for molecular taxonomy [32].

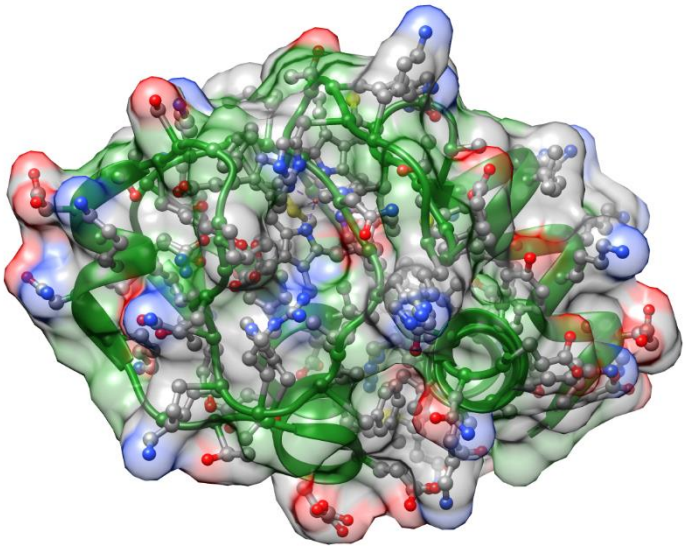

Figure 1.6: Cytochrome *c* (cyt *c*). Bovine heart cyt *c* is depicted with assigned surface, the backbone in green, other atoms colored by element (PDB file: 2B4Z, resolved by Mirkin *et al.*, 2008 [33]).

Briefly summarized, the C*c*O (Fig. 1.7), also referred to as Complex IV, forwards the electrons of reduced cyt *c* to molecular oxygen. The different kinds of final electron acceptors are usually name-giving for a respirational system, so what we have here is the oxygen respiration, common in all animals, plants, and fungi. Moreover, plenty of bacteria use the oxygen respiration, while the latter are not confined to it [34, 35]. Being the most employed protein within this thesis, the structure and the catalytic cycle are discussed a bit more extensively.

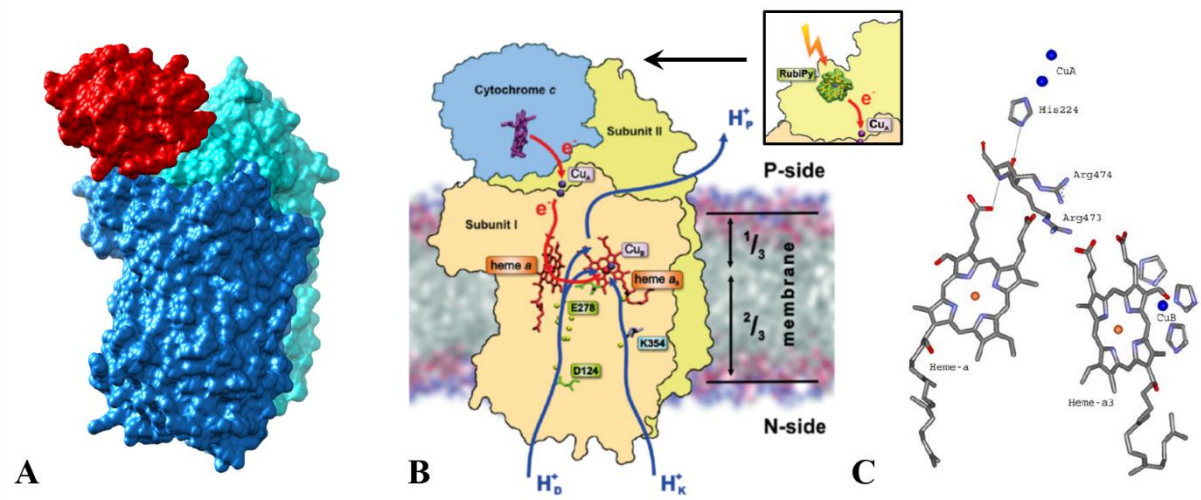

Figure 1.7: Cytochrome *c* oxidase (C*c*O). (A) C*c*O of *P. denitrificans* with subunit (SU) I (blue), SU II (turquoise), and cyt *c* (red), illustrated with assigned surface (PDB files: C*c*O: 1QLE, resolved by Harrenga & Michel, 1999 [36]; cyt *c*: 2B4Z, resolved by Mirkin *et al*., 2008 [33]). (B) Schematic depiction of C*c*O and cyt *c*, emphasizing the relevant components of the active center, which are the redox centers copper A (Cu_A), heme *a*, heme a_3, and copper B (Cu_B). Together, Cu_B and heme a_3 form the binuclear center (BNC). The electron and proton pathways are indicated as red and blue arrows, respectively. As an inset, the alternative light activation *in vitro* via specific Ru complexes is shown. (C) Molecular depiction of the catalytic redox center with hemes, copper ions, and associated amino acids of the protein. (B) is adapted from Belevich, 2017 (main illustration) [37] and Belevich *et al*., 2007 (inset) [38], (C) from Farver *et al*., 2006 [39].

After decades of difficulties, today there are several high-resolution X-ray structure data available, for example, of C*c*O of *Rhodobacter sphaeroides*, revealed in 1995 [40], bovine C*c*O, revealed in 1996 [41], and C*c*O of *Paracoccus denitrificans*, revealed in 2002 [42]. The utilized C*c*O was the latter one, and thus, the shown structures are the one of *P. denitrificans* (unless explicitly mentioned). The evolutionary classification of terminal oxidases in A-, B-, and C-type oxidases [25] is left out here, since the *P. denitrificans* C*c*O and all eukaryotic C*c*Os belong to the A-type terminal oxidases.

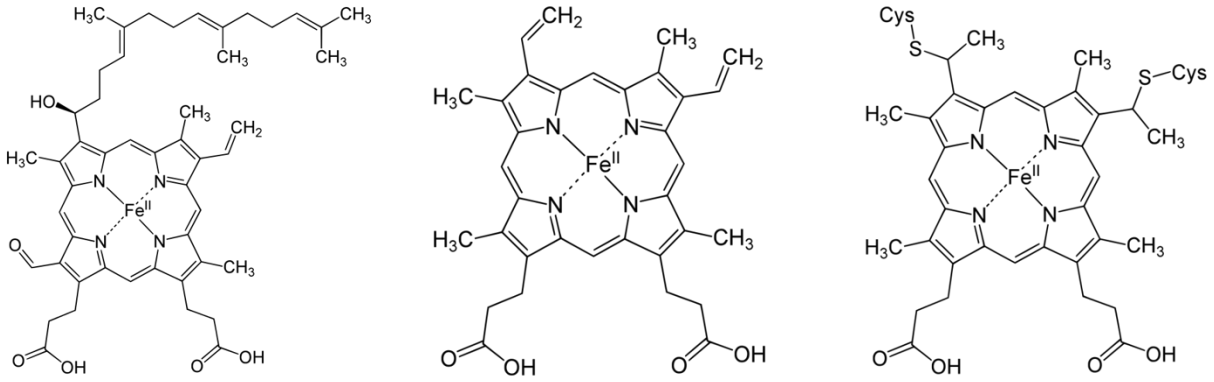

Figure 1.8: Different types of heme molecules. The central porphyrin ring system (also called tetrapyrrole due to its chemical composition) is the same in all hemes, while the side chains differ. Heme *c* is covalently bound to the protein, therefore the Cys residues are depicted as well. All structures are displayed according to Belevich, 2007 [22].

To clarify the notions: A cytochrome is a protein containing a heme as prosthetic group. There are different kinds of hemes. All of them comprise a porphyrin ring system, also referred to as tetrapyrrole, carrying a central iron ion. The residual molecule differs, and the different overall structures define the different types of hemes. The ones crucial for this work are depicted in Fig. 1.8. Cytochromes are involved in redox reactions by the uptake and delivery of one electron, thereby changing the charge of the central iron from Fe^{2+} to Fe^{3+} and back [43].

While the hemes *a* and *b* are non-covalently bound to protein via complex bonds, heme *c* is covalently attached via a cysteine residue of the protein, illustrated in Figure 1.8 [22]. The central Fe-containing porphyrin ring acts as chromophore, so the respective proteins were called cytochromes ("cell color").

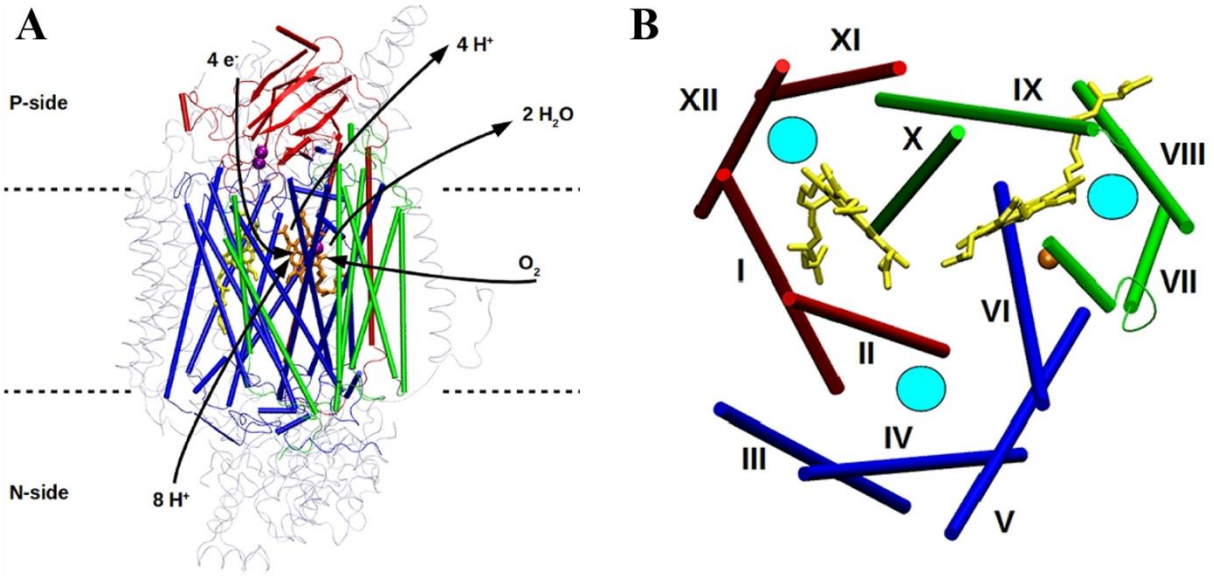

Figure 1.9: Core subunits of mitochondrial C*c*O. (A) The SUs I, II, and III are depicted in blue, red, and green, respectively, while the residual ten SUs are shown as gray, transparent ribbons. Copper atoms are colored in purple, heme *a* in yellow, and heme a_3 in orange. The membrane boundaries are schematically indicated by dashed lines. (B) Clusters of SU I (blue, red, and green; numbers indicate the respective transmembrane helices), two of them holding the redox-active cofactors. Pore regions, which are correlated with both chemical and pumped proton transport (see below), are additionally indicated (cyan-filled circles). Figure adapted from Wikström, 2018 [25].

All A-type terminal oxidases consist of a core of three subunits, SU I, II, and III (Fig. 1.9A), encoded within the mitochondrial DNA in case of eukaryotic organisms (while B- and C-type oxidases lack SU III). SU I and II contain the four redox centers that are crucial to perform the overall reaction, given by equation 1.3.

$$4\ \text{cyt}\ c^{2+} + O_2 + 8\ H^+_{\text{N-side}} \rightarrow 4\ \text{cyt}\ c^{3+} + 2\ H_2O + 4\ H^+_{\text{P-side}} \qquad (1.3)$$

In SU I, pore regions were found that are correlated with chemical and pumped proton transport (Fig. 1.9B) [25]. SU III, which contains no redox-active cofactors and is not directly involved

in proton translocation, is presumed to prevent suicide inactivation, where Cu_B leaves the enzyme as copper hydroxide under conditions of low H^+ activity in the vicinity of the BNC [44–46]. The SUs I-III are relatively conserved with a sequence homology between mammalian and bacterial C*c*O of 52 [47], 39 [48], and 50 % [49] for SU I, II, and III, respectively, which is considerably high regarding these evolutionary distances. There is one additional subunit in *P. denitrificans* and ten in mitochodrial C*c*O, the latter genetically encoded in the nucleus. The presumed regulatory function of these additional SUs is reviewed, for instance, by Kadenbach & Hüttemann, 2015 [50]. For a current research publication, see, for example, Sedlak & Robinson, 2015 [51]. For understanding the rather complex catalytic mechanism, focusing on the core structure is sufficient. The proton channels, shown in Fig. 1.7B, will be discussed after the catalytic cycle. After cyt *c* has bound to the respective binding site, its electron is forwarded via the Cu_A center (actually containing 2 copper ions) and heme *a* to the binuclear center (BNC), consisting of heme a_3 and Cu_B. Alternatively, the electrons can be donated by a Ru complex when excited by light (inset in Fig. 1.7B). This is no natural process, but widely used in research to reveal the catalytic cycle processes. The redox-active components of the catalytic center are shown in detail in Fig. 1.7C. The electrons are donated to oxygen simultaneously after binding, avoiding radical formation, then the electron gaps are refilled one by one, all the four taking the described path via the aforementioned redox centers.

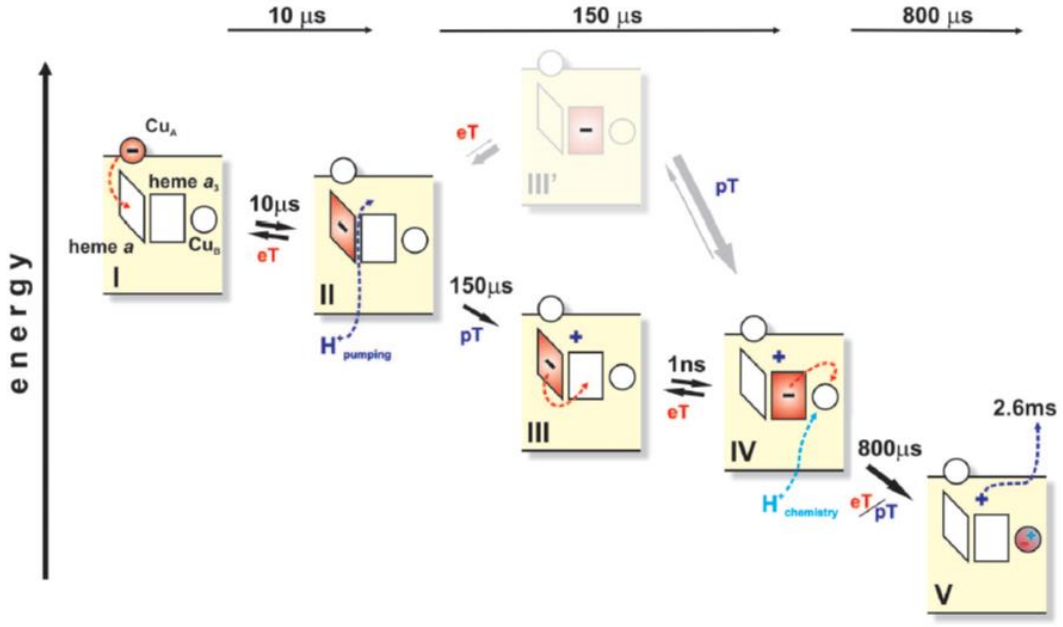

Figure 1.10: Electron transitions in the catalytic center of the C*c*O, correlated with proton translocation. Every electron taken up from cyt *c* is forwarded via Cu_A and heme *a* to the binuclear center (BNC), comprising heme a_3 and Cu_B. The symbols are defined in the box on the very left, while the yellow box itself represents the catalytic center of the C*c*O. eT means electron transfer, pT proton transfer, whereby protons are divided in so-called chemical protons, participating in the reaction with molecular oxygen, and pumped protons, which are dislocated from the N- to the P-side of the membrane. The periods indicated on top are not explained here. Figure adapted from Belevich *et al*., 2007 [38].

With each electron, one proton intended for the chemical reaction (referred to as chemical protons) is taken in, and one proton is pumped across the membrane (pumped protons). The consumption of electrons from the P-side and protons from the N-side in terms of water formation was found to be thermodynamically equivalent to a pumped proton per electron concerning $\Delta\tilde{\mu}H^+$, what allows for simply calculating with two pumped protons per electron [25]. Upon arrival of the last electron (and proton), the release of water occurs [38]. The electron transitions, proton translocations and assigned transition times are depicted in Fig. 1.10 as revealed by Belevich *et al.*, 2007 [38].

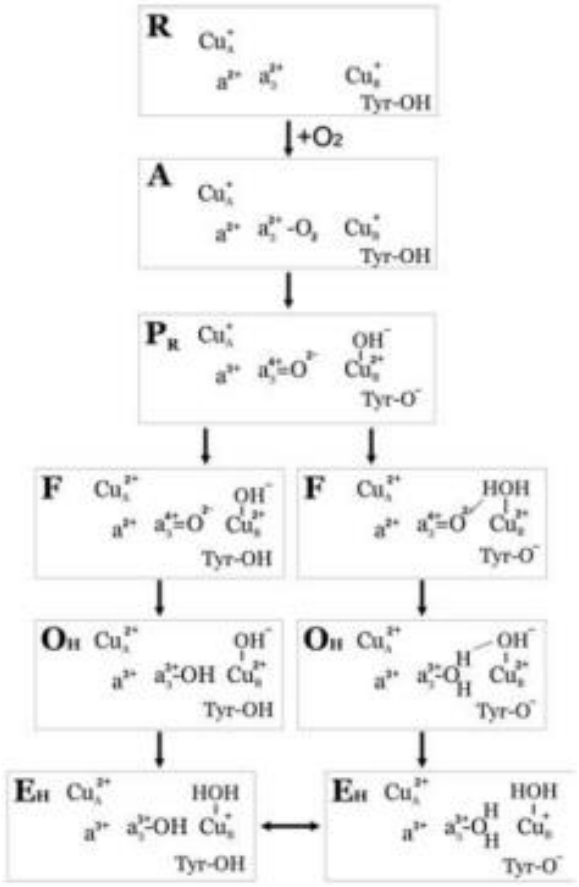

Figure 1.11: Intermediate states of C*c*O catalysis. Description is given within the text. Figure adapted from Belevich & Verkhovsky, 2008 [53].

With every arriving electron and proton, the catalytic center is structurally altered, resulting in different molecular states. Most of them were elucidated, others are still subject of discussion [25]. The states are comprised by the catalytic cycle. Fig. 1.11 introduces the common nomenclature and assigns the respective molecular structures. The names of the intermediate states refer to the BNC. R stands for reduced state, A for ferrous-oxy A intermediate ("compound A" was detected firstly and named by Chance *et al.* in 1975 [52]; ferrous refers to the iron situated in the center of each heme), P for peroxy intermediate, F for ferryl-oxo intermediate, O for fully oxidized, and E for one-electron reduced state. To avoid extensive digression, the assumed molecular structures are not further described. In case of further interest, a covering review that goes into detail is Belevich & Verkhovsky, 2008 [53], or, more recent, Wikström, 2018 [25].

A more comprehensive scheme displaying the catalytic cycle is given in Fig. 1.12A (whereas the proton pumping steps are emphasized in Fig. 1.12B) with the respective revealed transition times [53]. Another nomenclature was reported by Wikström in 2012 (Fig. 2.12C) [54]. It assigns the specifications C_0, C_{0A}, C_1, C_2, C_3, $C_{3'}$, and C_4 to the former R, A, E, O, F, P_R and

P_M, respectively. However, in a more recent review of Wikström, published in 2018 [25], the old nomenclature was picked up again.

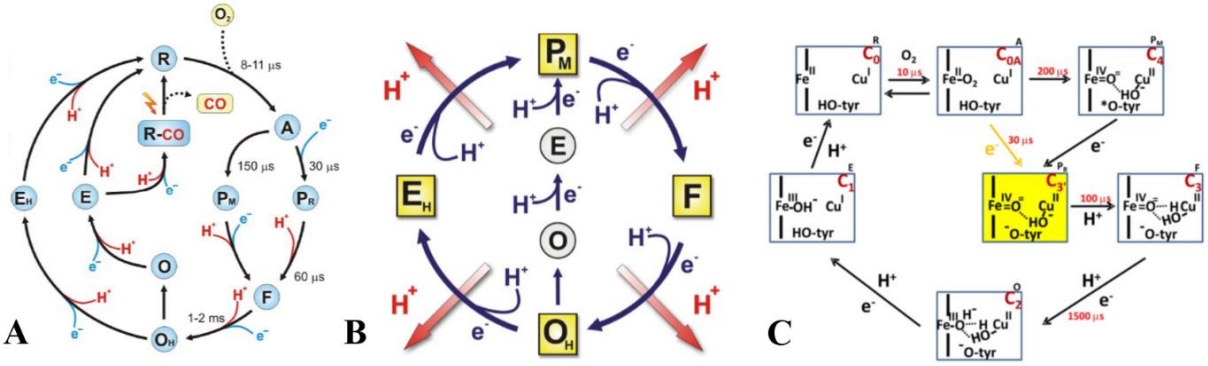

Figure. 1.12. Catalytic cycle of C*c*O. The catalytic cycle of C*c*O is depicted with focus on intermediate states and time ranges (A), proton release (B), and an alternative nomenclature (C). Nomenclature, processes and differences are described in the text. (A) and (B) are adapted from Belevich & Verkhovsky, 2008 [53], (C) from Wikström, 2012 [54].

The measurements corresponding to Fig. 1.10 were started from the O_H state, leading to E_H by single electron injection via a Ru complex. This mechanism is considered as representative for each state transition, but not necessarily transferable one to one, e.g., in terms of transition times, keeping in mind that the destination sites of electrons and protons are different [53]. Hence, varying transition times revealed from different states, regarding, for example, the ones in Fig. 1.12, are not necessarily contradictory. However, these single-electron injection measurements are subjected to certain limitations. They cannot be performed with C*c*O as prepared, but require an activation procedure. The enzyme as prepared is present in the O state (maybe containing little amounts being in the E state) [53]. Bloch *et al.* [55] found that the transition from O via E to R, in opposite to the alternative O_H via E_H to R, is not coupled to proton transfer. Later, the O state was proposed to not be catalytically active at all [56, 25]. Further, Bloch *et al.* [55] concluded that after reduction and reoxidation by O_2 the C*c*O enters the metastable O_H state, which is catalytically fully active and associated with proton pumping when being reduced to E_H and further to R (Fig. 1.12B). If no further electrons are injected, the C*c*O relaxes to the O state again after a certain time (indicated with approximately 30 s at room temperature by Bloch and co-workers [55]). Thus, these experiments require an activation (also called pulsing, referring to the differentiation of pulsed and resting state, which was replaced by O_H and O, respectively), by which the C*c*O is treated with reducing agents and CO to pre-reduce the C*c*O before starting the reaction by CO photolysis and floating with oxygen-saturated buffer (flow-flash method). The CO-modification is displayed in Fig. 1.12 as well, emphasizing the reaction start by simultaneous laser flashing and floating with oxygen [38, 55].

However, this procedure is for some reasons problematic. On the one hand, there are lots of studies indicating C*c*O turnover numbers and hence catalytic activity without upstream activation process (e.g., monitoring cyt *c* degradation), using the C*c*O as prepared [51, 57, 58]. The electron donation by the natural substrate cyt *c* instead of using Ru complexes does not suffice as explanation, since the Ru complexes have been shown to be able to reduce the first electron acceptor within the C*c*O, the Cu_A [38, 59], which indicates a sufficient redox potential. On the other hand, SEIRAS spectra taken after treatment with exemplary mediators used for activation showed significantly altered band patterns compared to spectra taken of non-activated C*c*O, as it is used in electrochemistry [60]. It raises the question whether these modifications alter the observed process entirely compared to the naturally occurring one. The same situation applies for the activation by H_2O_2 treatment instead of applying the flow-flash method, artificially obtaining the P_M or F state as starting point (dependent on the amount of peroxide, see Vygodina & Konstantinov, 1989 [61]), as, e.g., reported by Zaslavsky *et al.*, 2004 [62]. Howsoever, it is not evidenced that the activation actually causes non-natural modifications of the enzymes as well. So, although lots of insights were revealed, basic elusive questions still remain.

Coming back to the proton translocation, there must be special pathways to enable pumping and chemical turnover in rates such high as reported. Fig. 1.7B illustrates two proposed proton pathways, the D and the K channel (named after the conserved aspartate D91 and lysine K319, respectively). The former assumption that the D channel is used by the pumped protons, while the K channel is taken by the chemical ones, turned out to be a misinterpretation. The recent conception is that the D channel, leading to a water-filled cavity, is involved in the uptake of all pumped and at least two of the chemical protons, while the K channel, at the end of which fewer water molecules were found, serves as passage for one or two chemical protons. The exit channel to the P-side is not well understood until today [25]. According to an alternative hypothesis of Yoshikawa & Shimada, 2015 [63], all pumped protons are taken up and released via the H channel, rather distant from the BNC, linked to the chemical reaction by an alternative mechanism that is not described here. In contrast to protons, oxygen – being a small, uncharged molecule – can reach the catalytic center by diffusion; nevertheless, it seems that diffusion alone is too slow to obtain the high turnover numbers, and indeed, hydrophobic paths to the catalytic center were found by X-ray crystallography [41, 42] and confirmed with other experimental [64, 65] and theoretical data [66]. These were assigned to oxygen transport [53].

A special role in terms of C*c*O function is ascribed to cardiolipin, a phospholipid of unusual structure. A cardiolipin comprises two phospholipids that are esterified to a central glycerol via

their phosphate groups, each at one terminal hydroxyl group. A few molecules (3-4 according to Sedlak & Robinson, 2015 [51]) are tightly bound to the C*c*O. During preparation, these cardiolipin molecules remain bound to the enzyme, so it is present in membrane preparations and detergent-solubilized C*c*O micelles. The same was found for other respirational complexes, such as the ATP synthase (see below) and the bc_1 complex [67]. Cardiolipin is not strictly required, as shown with cardiolipin-deficient mutants of *Escherichia coli* [68] and yeast [69], but the activity is reduced to approximately 50 % in case of lipid-free C*c*O. Cardiolipin molecules were found in close vicinity to the D channel, what might suggest a facilitation of proton translocation. Moreover, the dissociation of cardiolipin is accompanied with the dissociation of certain SUs, so cardiolipin seems to be involved in the stabilization of the quaternary structure of the C*c*O [51]. The special backbone of cardiolipin favors the formation of a here not further described acid-anion, resulting in only one negative charge instead of two and an unusually high pK_{a2} value, being around 8, instead of both pK_a values being below 4 as expected without acid-anion formation. It enables the uptake and release of protons, thus forming a kind of proton reservoir directly linked to the membrane-water interface. By lateral motion, cardiolipin is presumed to shuttle the protons, pumped by the enzyme complexes of the respiratory chain, to the ATP synthase. Due to the uptake of protons by cardiolipin, a locally high concentration of protons is achieved, while the pH value and hence ΔpH is rather negligibly altered. Therefore, it was proposed that the proton is rather moved as a charge, employing $\Delta\Phi$ as driving force rather than ΔpH [67]. This further underlines the aforementioned notion that at least on the P-side ΔpH is not significantly altered due to the large volume and the buffer conditions [25]. Indeed, high amounts of cardiolipin were found in prokaryotes that are exposed to so-called uncoupling agents, which diminishes the pH gradient across the membrane, e.g., by introducing proton leakages (see below) [70]. A further function ascribed to cardiolipin is the formation of respiratory supercomplexes. Cardiolipin exhibits a larger binding strength compared to other lipids found in mitochondria, and respiratory complexes can thus be attached to one another via the cardiolipin molecules that are present in their respective binding site [71].

The respiratory chain is summarized regarding the redox potentials in Figure 1.13.

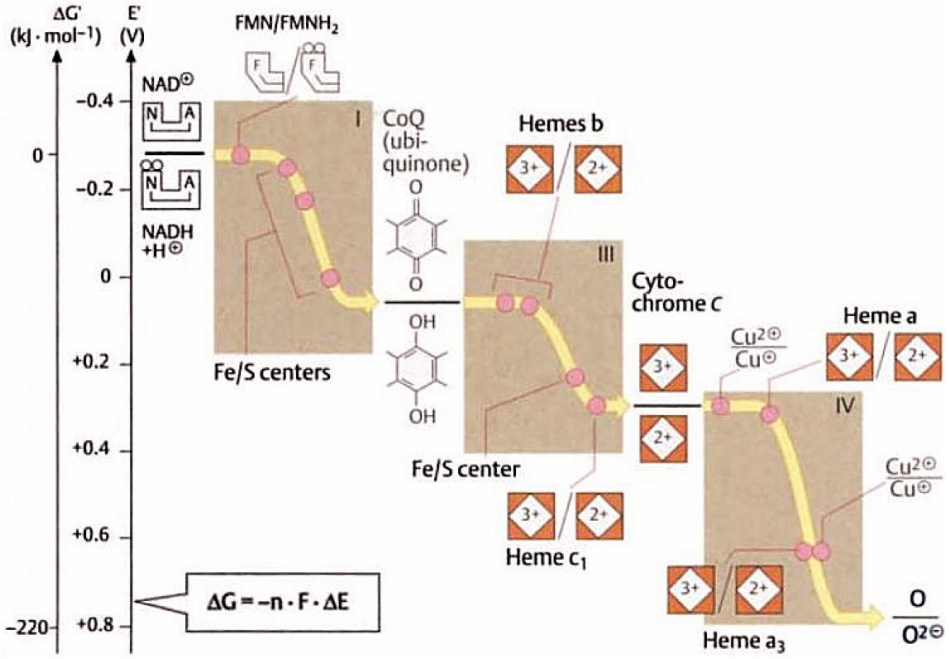

Figure 1.13. Redox potentials of the respiratory chain components. The different components of the redox chain are correlated with their redox potentials. Figure adapted from Koolman & Roehm, 2005 [72].

Complex V – the ATP synthase, F_0F_1-ATPase or ATPase –, shown in Figure 1.14, is coupled to the respiratory chain only by the membrane potential. It uses the energy stored in the electrochemical gradient for the production of ATP. Hence, agents like valinomycin, FCCP, and NH_3 that cancels this gradient are called uncoupling agents, since they uncouple the ATP synthase from the respiratory chain. There are also proteins doing so, such as thermogenin (uncoupling protein 1) [73]. The mechanism and the crystal structure of the ATPase was explored in the 1980s by Paul D. Boyer [74–76] and John E. Walker [77, 78], respectively, and in 1997 they gained the Nobel Prize together with Jens C. Skou, who discovered the first proton pump, the Na^+/K^+-ATPase, in 1957 [79]. It was found that Complex V acts like a mill.

In eukaryotic respiratory chains (and in many bacterial ones), the F-type ATPase is found, which is discussed in the following, although Fig. 1.14 shows an A-type ATPase (with A_0 and A_1 instead of F_0 and F_1) [80]. The ATP synthase consists of two major parts, each consisting of several subunits. The F_0 part is crossing the membrane, while the F_1 part is hydrophilic, protruding to the N-side. The F_0 part takes up protons and channels them back across the membrane (passively, following the electrochemical gradient), and with each channeled proton, a rotational motion is performed. Each of the comprised 12 peptide chains contain a certain carboxyl group. In a relaxed state, this group is deprotonated.

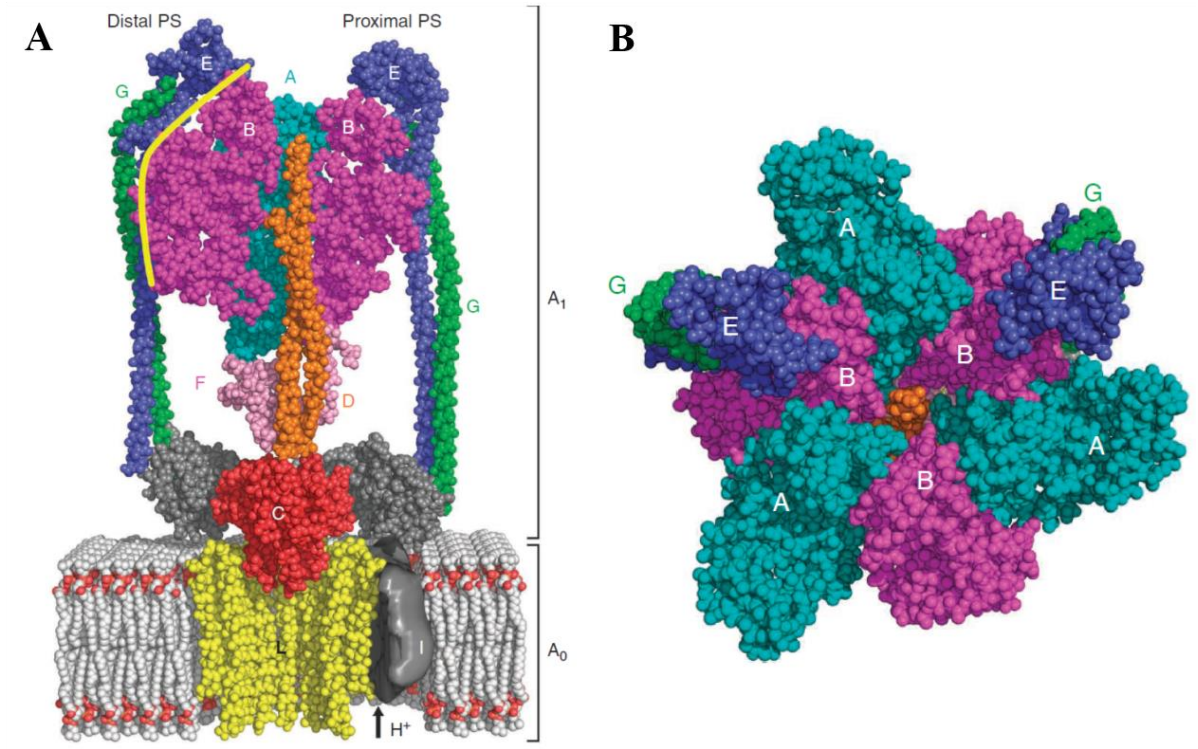

Figure 1.14: ATP synthase. (A) Side view. (B) Top view. The displayed ATPase is an A-type ATPase – in opposite to the eukaryotic F-type ATPases – and the F_0 and F_1 parts of eukaryotes are corresponding to A_0 and A_1 here. Figure adapted from Steward *et al*., 2012 [80].

As soon as the electrochemical gradient exceeds a certain limit, the carboxyl group will be protonated, and the peptide chain changes its conformation towards a tense state. By a rotational movement, the chain relaxes again, thereby channeling the proton. This motion is transferred to the catalytic centers of the F_1 part by a certain subunit ($F_1\gamma$). In 12 steps, thus needing 12 protons, a full circle is performed. The F_1 part is also rotating, but in 120 deg steps. Four protons are needed for each of these steps, and with each step, one of the three steps of the catalytic cycle of ATP synthesis is performed: ADP + P_i (inorganic phosphate) binding, ATP production, and ATP release. Thus, during a full rotation, 12 protons are channeled and 3 ATP are formed theoretically [81]. Measurements obtained minor differences dependent on the organism, yielding rather 3-4 ATP per 12 protons in mitochondria. In studies facing the mechanism in *E. coli*, the theoretical assumption of three could be measured. Eventually, the potential energy of the gradient (also referred to as proton-motive force) is converted into a mechanical, then further into a chemical one by the phosphorylation of ADP. Since the energy of the initial substrate oxidation is coupled to a final phosphorylation, this process in commonly known as oxidative phosphorylation, being one of three major processes of ATP production beside the photophosphorylation (in photosynthesis) and the substrate-level phosphorylation (e.g., in glycolysis). By theoretical calculations, this results in up to 38 ATPs per glucose molecule

(including the yields of glycolysis and citric acid cycle, and provided that the 2 molecules of guanosine triphosphate (GTP) are further converted into ATP), but this might only hold true for prokaryotes, since in eukaryotes the yield is lowered to 30-32 by active transport processes. Thereof, 26-28 ATPs are produced by oxidative phosphorylation at the respiratory electron transport chain, depending on the shuttle that is used to transport the NADH + H^+ produced during glycolysis to the mitochondrial matrix [16, 82]. In practice, final values might be even lower, e.g., due to slight proton leakages that were found in the inner mitochondrial membrane [83]. The energy conversion via an electrochemical gradient as exclusive intermediate is called chemiosmosis, and Peter Mitchell gained the Nobel Prize for its postulation in 1978 [84].

1.3 Reaction center & bc_1 complex of the bacterial photosynthesis

In opposite to the photosynthetic system of green plants, inherited from cyanobacteria, the anoxygenic photosynthesis of purple bacteria is rarer in components, and contains only one photosystem [85]. The employed reaction center (RC) and bc_1 complex were taken from *Rhodobacter sphaeroides*, a phototroph purple bacterium.

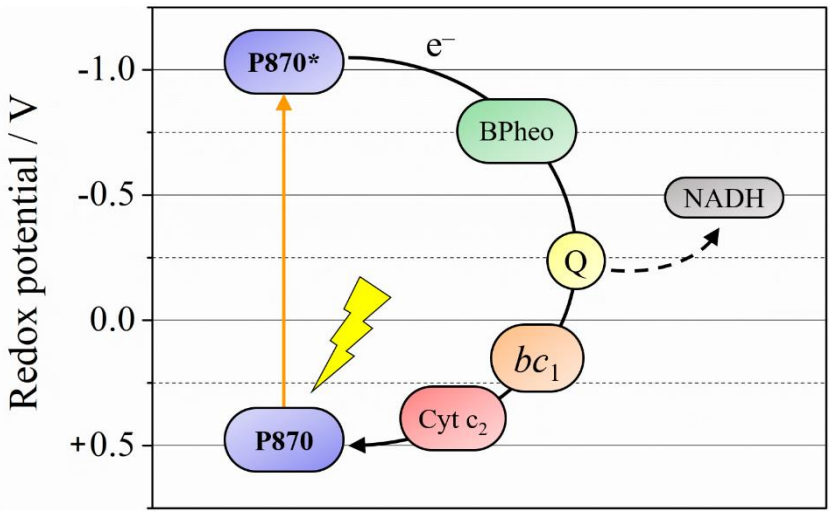

Figure 1.15: Light reaction of the anoxygenic photosynthesis type II in purple bacteria. The components of the anoxygenic photosynthesis type II are depicted schematically with respect to their redox potentials. The flash symbolizes excitation by light. Further description and abbreviations are given in the text. Approximate values taken from Fuchs & Schlegel, 2006 [85].

The bacterial photosynthesis type II (Fig. 1.15), practiced, for example, by *Rh. sphaeroides*, contains only two membrane-bound enzyme complexes, the RC and the bc_1, and only two electron carriers, a hydrophobic one, which is again a ubiquinone, so it is again abbreviated with Q, diffusing within the membrane, and a hydrophilic one, again being cyt *c*, situated in the

aqueous phase [85]. The phylogenetic relationship between these components to the ones of the respiratory chain and details about the structure and nomenclature of, e.g., different quinones, thereof different ubiquinones, or the further differentiation between cytochromes, as it is here cyt c_2, are not discussed in detail to avoid too extensive digression. The interchangeability of bacterial cyt *c* with eukaryotic cyt *c* in terms of *P. denitrificans* C*c*O has been shown, e.g., for bovine cyt *c* [86] and the herein used horse heart cyt *c* [57].

The RC (also referred to as photosystem P870, derived from the absorption maximum of the two bacteriochlorophylls (BChl) *a* in the center) is practicing charge separation using light energy. For this purpose, it contains two bacteriochlorophyll molecules, arranged as special pair, of which one is excited by light energy and forwards an electron to a bacteriopheophytin (BPheo; a pheophytin is a chlorophyll without complexed Mg^{2+}), remaining positively charged ($P870^+$). The light energy mostly is collected by the neighbored light harvesting complexes (LH1 and LH2) and forwarded via Foerster resonance energy transfer, but direct excitation also might occur [85]. To avoid recombination, the electron is quickly (in the order of 10^{-12} s) passed down the redox potential chain to a bound Q (Q_A-site, in the order of 10^{-10} s) and further to a mobile Q at the Q_B-site, which is reduced to the radical $Q^{\bullet-}$ as it happens at Complex I and II of the respiratory chain [87, 88]. A second light excitation (and consequently another electron) is required to form ubiquinol (QH_2), simultaneously taking up two protons, due to which the molecule becomes uncharged again and thus capable to diffuse within the hydrophobic inner membrane space. $P870^+$ is meanwhile reduced by reduced cyt *c* in a cyclic electron transport (see Fig. 1.15 or below) [85]. The electron transport chain within the RC is depicted in Figure 1.16.

As in respiration, QH_2 diffuses to the Q_o-site of the bc_1, where the electrons are accepted, and thus Q is regenerated. A bc_1 monomer, containing all catalytic centers, is shown in Fig. 1.17. In nature, it usually occurs as homodimer. The bc_1 contains several redox centers, namely the hemes b_L and b_H, cyt c_1, and the so-called Rieske protein, also named ISP for iron-sulfur protein, which contains an Fe_2S_2 center within its catalytic unit. These several redox centers are required to split the electron path in two. Cyt c_2, finally accepting the electrons that were brought in by QH_2, is a one-electron carrier. Hence, only one of the two introduced electrons can be forwarded directly to cyt c_2 [89, 90]. (Briefly, cyt c_2 as mobile electron shuttle occurs only in photosynthesis. It is clearly homologue to cyt *c* of the respiratory electron transport chain [91], and – as mentioned before – was unproblematically substituted by horse heart cyt *c* within this work, as, for instance, reported by Witt and co-workers [57].)

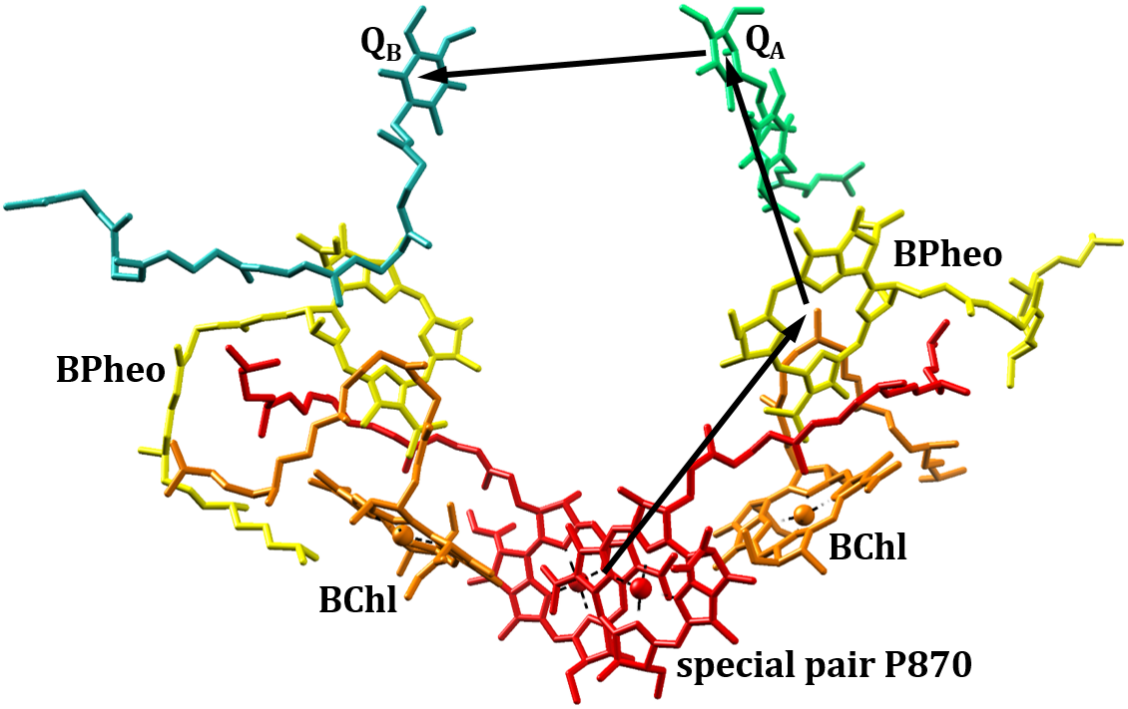

Figure 1.16: Electron transport chain within the photosynthetic reaction center of *Rhodobacter sphaeroides*. BChl: Bacteriochlorophyll (red in case of the special pair, orange in case of neighbored ones); BPheo: Bacteriopheophytin (yellow); Q_A: fixed ubiquinone (green); Q_B: mobile ubiquinone (turquoise); black arrow: electron path. A detailed description is given in the text (PDB file: 2UXJ, resolved by Koepke *et al.*, 2007 [92]). Information taken from Lin *et al.*, 2009 [88].

Taking this path, the electron passes the Rieske protein and cyt c_1 before it is accepted by the mobile cyt c_2. The other electron enters the Q cycle (integrated in Fig. 1.17), taking place within the cyt *b* SU, where it passes the hemes b_L and b_H before it is accepted by another Q that is reduced to $QH^{\bullet-}$. In a second step, another QH_2 binds to the Q_0-site and again one electron enters the Q cycle, reducing the $QH^{\bullet-}$ to QH_2, which is released to the pool at the Q_i-site. Via this cyclic pathway, the oxidation energy of QH_2 is used more efficiently, as it obviously suffices to not only reduce cyt c_2, but also to perform one of the two reduction steps of Q, either from Q to $QH^{\bullet-}$ or from $QH^{\bullet-}$ to QH_2 [89, 90]. $QH^{\bullet-}$ is unstable and favors the formation of the radical oxygen species superoxide (O_2^-) if it remains as semiquinone radical for too long. Indeed, an enhanced superoxide production was measured [93]. For further literature regarding radical formation, controversial points within the Q cycle model, and recent simulation data, see Crofts *et al.*, 2017 [94]. As mentioned above, the bc_1 complexes of the respiratory chain and the anoxygenic photosynthesis are homologue; their basic function, including the Q cycle, is alike [95].

Further, the pool of reduced cyt c_2 serves to refill the electron gap at the RC, and with this step it comes full circle.

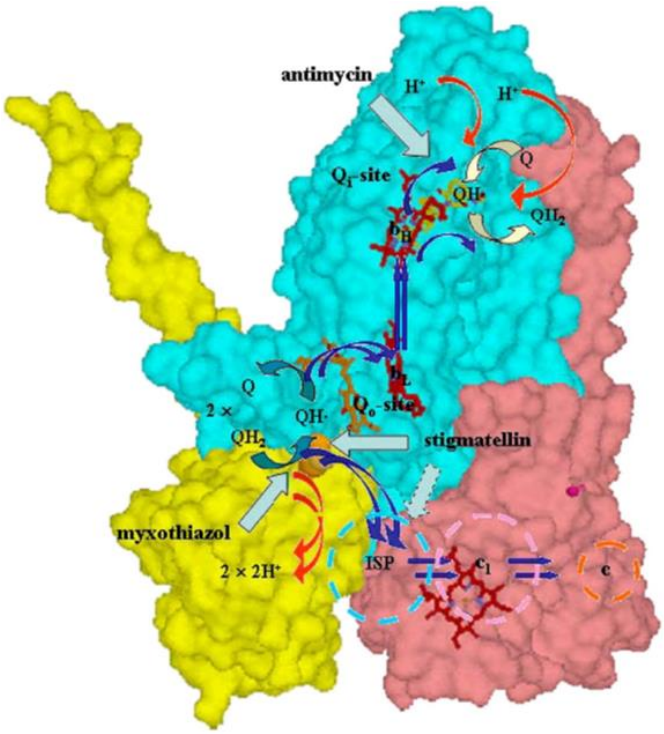

Figure 1.17: bc_1 monomer of *Rh. sphaeroides*, including the Q cycle. The different redox centers and substrates are indicated with respect to their location within the subunits. Electron transitions are indicated by blue arrows, proton motions by red ones. The gray arrows indicate the binding sites of different inhibitors. Further description is given in the text. Figure adapted from Crofts et al., 2008 [89].

As in respiration, an electrochemical gradient $\Delta\tilde{\mu}H^+$ is established over the membrane, driving the ATP production within the ATP synthase. Since light energy is used in this event, the process is called photophosphorylation.

The anoxygenic photosynthesis type II uses – in opposite to the oxygenic photosynthesis – only one photosystem. As indicated in Fig. 1.15, the generated redox potential after the transitions that are supposed to avoid the recombination of $P870^+$ with its electron, is not low enough to produce any reducing equivalents, such as NADPH + H^+. The latter serve to provide electrons with sufficient reduction potential to be used in anabolism. For that purpose, these bacteria are able to additionally use the energy of $\Delta\tilde{\mu}H^+$ to generate redox equivalents at the NADH dehydrogenase ("reverse electron flow"). The lack of electrons is refilled by external electron sources that are not water (e.g., sulfide or sulfur in case of purple sulfur bacteria). If substrates are available, purple bacteria can live photoheterotroph [96, 97].

1.4 Biomimetic membrane systems

Membrane proteins exhibit a hydrophobic surface where they face the inner membrane space and a hydrophilic one towards the aqueous phase. To investigate membrane proteins, their

surrounding needs to be maintained with respect to polarity to avoid their denaturation. There are several approaches to fulfil this condition, e.g., the preparation of cells or compartments thereof. However, working with cells is on the one hand demanding, on the other hand there are lots of other molecules that hinder the investigation of one specific target protein in its sole function. To circumvent this issue, membrane proteins are reconstituted in artificial systems that provide the necessary conditions [98, 99].

An easy-to-use approach and sufficient for many purposes is to solubilize the membrane protein of interest in a detergent micelle, where amphiphilic molecules (exhibiting hydrophilic and lipophilic regions) adhere to the lipophilic protein parts with their lipophilic tails, forming an overall water-soluble micelle that provides a proper environment for the membrane protein. Due to solubility reasons, detergent micelles are self-assembling. In contrast to the phospholipids, they are rather of conical shape, so the micelle is favored over the bilayers and vesicles [100, 101].

As soon as, for instance, transport processes or potential development are investigated, detergent micelles do not suffice anymore. A dense membrane needs to be prepared, mimicking the biological original, and for that purpose, different biomimetic membrane systems were invented. An overview is given in Fig. 1.18. The historically first approach were free-standing lipid bilayer membranes, spanned over an aperture (Fig. 1.18, bottom left) and called painted membranes, according to the respective preparation method. These painted membranes were called black lipid membranes due to their dark appearance in reflected light [102]. This property is caused by destructive interference of the two light beams reflected from the front and the rear leaflet, respectively. It was a first hint of the nanometer-scale thickness [103]. As mentioned before, the abbreviation BLM is not exclusively used for this kind of membranes, but also for biomimetic bilayer lipid membranes in general. After the invention of painted membranes, more preparation techniques resulting in free-standing BLMs were established, being, e.g., folded and tip-dip BLMs. For further literature, see, for example, Hanke & Schlue, 1993 [104], for painted BLMs, Castellana & Cremer, 2006 [105], or Schindler, 1980 [106], for folded BLMs, Coronado & Latorre, 1983 [107], for tip-dip BLMs, and Eray *et al.*, 1994 [108], or Mayer *et al.*, 2003 [109], for apertures and their generation.

More recently, free-standing BLMs were used in combination with modern approaches like microfluidics and lab-on-a-chip systems [110, 111]. Furthermore, they were downsized to nanoscale areas using porous substrates, which was used, for instance, to investigate ion channels [112–114] and to perform single-molecule spectroscopy [115].

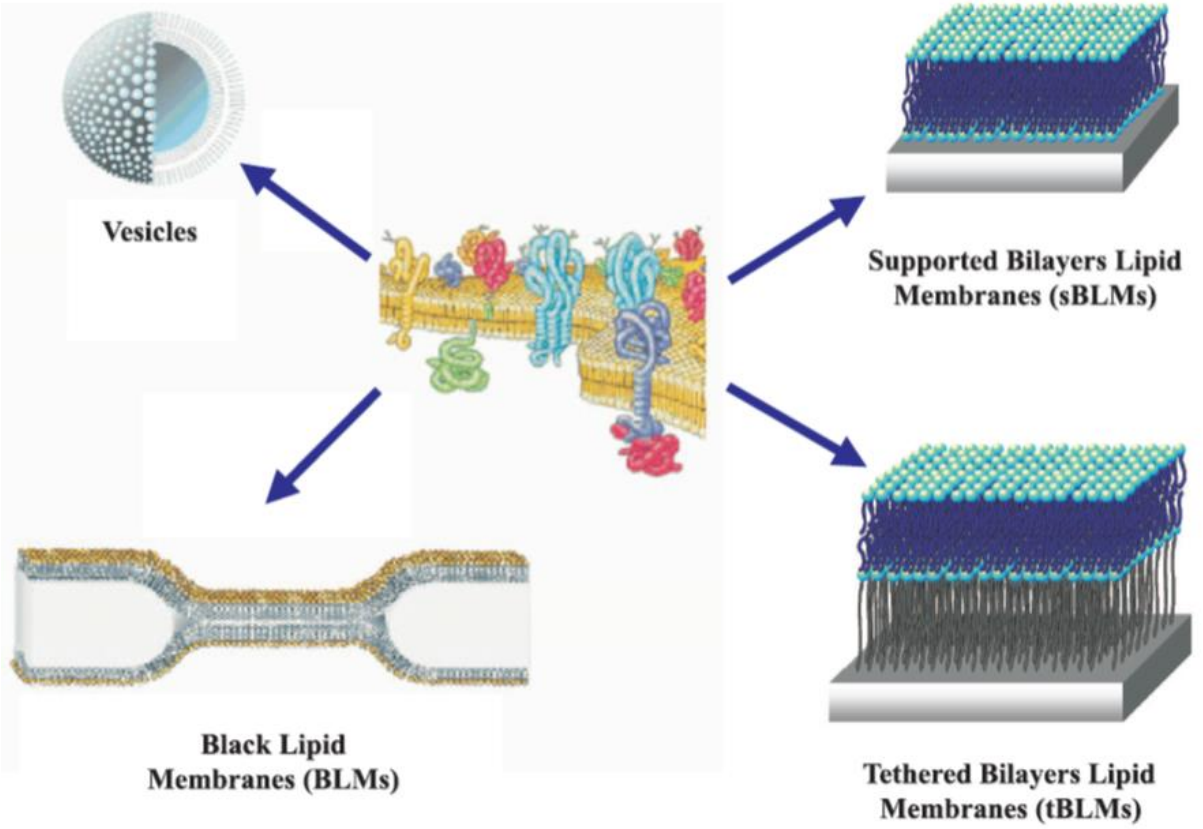

Figure 1.18: Different artificial membrane systems. To mimic biological membranes (center) *in vitro*, several artificial analogues were invented, being, for instance, vesicles (liposomes, top left), black lipid membranes (bottom left), solid-supported bilayer lipid membranes (top right), and tethered bilayer lipid membranes (bottom right). Further description is given in the text. Figure adapted from Friedrich, 2007 [116].

To increase the stability and longevity, supported BLMs (Fig. 1.18 top right) and further tethered BLMs (Fig. 1.18 bottom right) were introduced, both attached to a solid surface, the latter also providing a certain space between the BLM and the solid support, which favors the insertion of transmembrane proteins that might protrude into the aqueous phase or are involved in transport processes and serves as ionic reservoir [117]. Besides stabilizing, it enables to use advanced investigation methods such as atomic force microscopy (AFM) [118]. Further, the solid surface can be utilized itself. Having, for example, a rough gold layer, evanescent-field techniques, such as surface-enhanced infrared absorption spectroscopy (SEIRAS) [119] and surface plasmon resonance spectroscopy (SPR spectroscopy) [120], can be employed, both being introduced in Chapter 2. For further literature, see Heyse *et al*., 1998 [121], Tanaka & Sackmann, 2001 [122], and Knoll *et al*., 2008 [123].

A special case of the tethered membranes are the protein-tethered membranes (ptBLMs). It was found that membrane proteins, exhibiting hydrophobic surfaces where supposed to be located within the membrane, can act as anchors for tethering a membrane themselves. For that purpose, the respective membrane protein of interest, solubilized within detergent micelles, is attached

to a surface in a first step. This attachment, dependent on the applied chemistry, can occur unspecifically, using, for example, active esters that randomly bind amine groups, or in a directed way, using, e.g., his-tag technology. In a second step, a ptBLM is formed upon detergent removal in the presence of lipids. Applying this approach, membrane proteins can be reconstituted in an oriented manner [117, 124].

The described artificial membrane systems are beneficial for plenty of research topics and investigation methods, but are bound to an assisting solid part, being a surface or – in case of the free-standing BLMs – an aperture. Liposomes, also referred to as vesicles (Fig. 1.18 top left), are not dependent on any solid part, mimicking a biological cell or compartment in its shape as free spherical construct in aqueous solution that exhibits no boundaries. Liposomes are self-assembling if dried lipids are exposed to water, or – as aforementioned – if solubilized in detergent upon detergent removal. These self-assembled vesicles are not necessarily unilamellar and differ in size, but there are techniques to like sonication or extrusion, which eventually split the initial multilamellar vesicles into unilamellar ones that are smaller and more uniform in size [101, 125, 126].

Besides employing liposomes in research, they can be used for other purposes, e.g., as drug delivery system. The interior might serve as storage of polar substances, while hydrophobic substances can be taken up in the inner membrane. A large variety of liposomes is employed for the latter purpose, such as stealth liposomes to avoid rapid degradation, or immunoliposomes, equipped with, e.g., antibodies, for targeted delivery [127, 128]. In a further step, biomimetic lipids are even replaced again by artificial polymers that provides desired properties, then referred to as polymerosomes [129].

Liposomes containing reconstituted membrane proteins are called proteoliposomes [130]. Using liposomes, the integration of the respective proteins is again randomly in contrast to ptBLMs, which enable directed insertion. (There are exemptions, such as the ATP synthase, where the direction of insertion is controlled by an extraordinary protein geometry [131], but these are rare cases.)

To combine the size-variable, cell-mimicking spherical shape of liposomes with the strict protein orientation of the ptBLM is a main issue of this thesis, thereby employing the introduced membrane proteins C*c*O, RC and bc_1. The theoretical basics of the applied methods are given in Chapter 2.

Chapter 2 *Methodological Basics*

The methods employed within this thesis has been confocal laser-scanning fluorescence microscopy (abbreviated here with LSM, although that usually stands only for laser-scanning microscopy), surface-enhanced infrared absorption spectroscopy (SEIRAS), Ultraviolet/visible absorption spectroscopy (UV/Vis spectroscopy), dynamic light scattering (DLS), and surface plasmon resonance spectroscopy (SPR spectroscopy). Hence, all analyzation methods are spectroscopic ones, which means that they are based on the interaction of light with matter. Therefore, an overview concerning the fundamentals of light is taken as a basis.

2.1 Fundamentals of light

Pursuant to the principle of the wave-particle duality, light can be described as stream of particles (photons), active with its whole energy at a certain place, and as electromagnetic wave, appearing at different places with different magnitudes. The appearance in measurements is thereby either one or another, never both simultaneously. As a particle, the photon travels uncharged and without mass. Its energy can be correlated with the frequency of the respective wave, being

$$E = h\nu = \frac{hc}{\lambda} = \hbar\omega \ , \tag{2.1}$$

where E is the energy, h is Planck's constant ($h = 6.626 \times 10^{-34}$ Js [132]), ν is the frequency (oscillations per second), c is the propagation speed (in vacuum $c = 3 \times 10^8$ m/s [132]), and λ is the wavelength. Using radian measure, the angular frequency $\omega = 2\pi\nu$ is multiplied with the reduced Planck constant or Dirac constant $\hbar$, being Planck's constant divided by 2π [133, 134].

By division of the middle terms by Planck's constant, it results in the commonly known relation between propagation speed, frequency and wavelength (or angular frequency ω and angular wavenumber $k = 2\pi/\lambda$), being

$$c = \nu\,\lambda = \frac{\omega}{k} \tag{2.2}$$

Regarding the wave-particle duality, the photon is a special case, having no mass assigned. While for light, descriptions either as wave (Huygens) or as "corpuscle" (Newton) reach back to the 17th century, the assignment of a "matter wave" to other particles, such as electrons, was introduced in the dissertation of Louis de Broglie, who earned the Nobel Prize in 1929 for his extension of the concept of the wave-particle duality. For particles having a mass assigned, the so-called de Broglie wavelength calculates according to the de Broglie equation

$$\lambda = \frac{h}{p} = \frac{h}{mv} \,, \tag{2.3}$$

where (in addition to the specification given above) p is the momentum, m is the mass and v is the velocity.

De Broglie derived his equation from the special case of the massless photon, having a momentum of

$$p = \frac{E}{c} \,, \tag{2.4}$$

and generalized the concept with respect to particles exhibiting mass [135]. The experimental confirmation was done by Davisson (Nobel Prize in 1937) and Germer in 1927, within which they observed interference patterns using electrons instead of photons [136].

A practical example, at which the de Broglie equation can be utilized, is electron microscopy. Since the mass of an electron and Planck's constant remain constant, the wavelength of an electron decreases when its velocity increases. Thus, the more the electrons are accelerated, the higher is the resolution (and the more the sample is damaged due to the higher energy, hence especially having biological samples, a compromise needs to be found).

In everyday life, taking place in macroscopic dimensions, the wave-particle duality is of no consequence, since (due to the large mass) the de Broglie wavelengths are extremely small, thus calculations with respect to wave and to particle properties yield the same results, as it is, for example, the case for wave and geometrical optics in macroscopic dimensions [137].

2.1.1 Spectrum and wave equation

The term "light" is confined to electromagnetic waves that can be perceived by eye, and since the spectrum of electromagnetic waves comprises way more – additionally keeping in mind the wave-particle dualism – the headline would be more precisely chosen with "Fundamentals of

electromagnetic waves/photons", whereby the term "photon" is not restricted to light, being in general the quantization of an electromagnetic wave. Throughout the thesis – unless explicitly mentioned – the terms "wave" and "beam" mean an electromagnetic wave and a beam of electromagnetic waves or photons, respectively. An overview of the electromagnetic spectrum is given in Fig. 2.1, additionally indicating the respective causal atomic process.

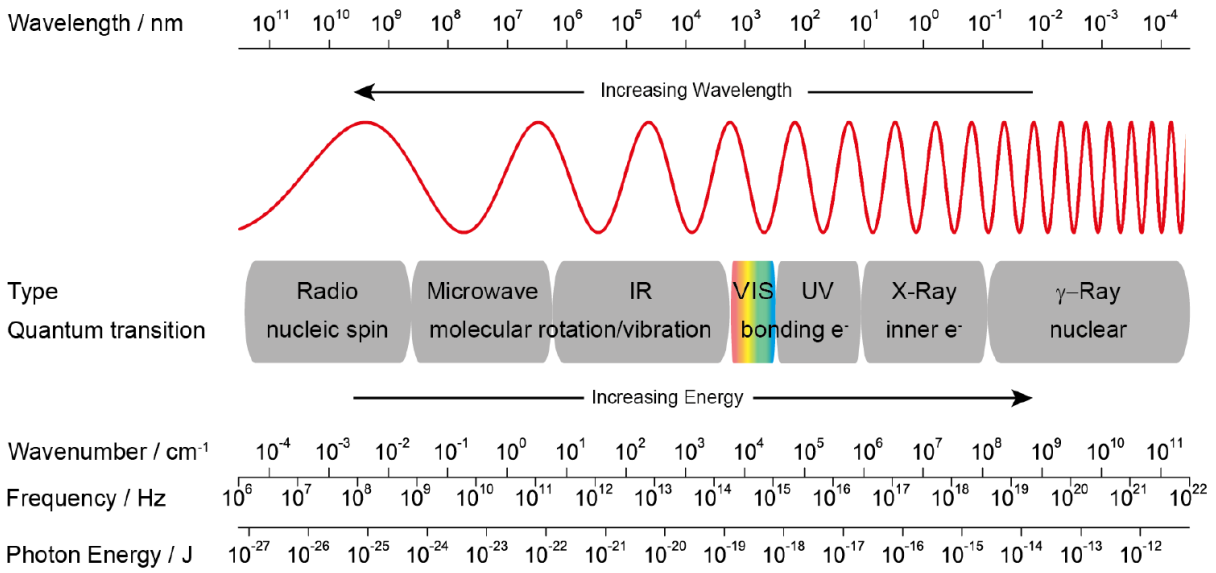

Figure 2.1: Electromagnetic spectrum. Beside the causal atomic interactions (quantum transistions), four common possibilities of wave specification are shown, being the frequency, the wavelength, the wavenumber (being the reciprocal of the wavelength, not to confuse with the angular wavenumber in radian measure), and the photon energy. Figure adapted from Schwaighofer, 2013, PhD thesis [138].

As an example, visible light is able to lift an electron of the outer atomic shell – hence a valence electron – to an energetically higher state. Conversely, by returning to the ground state, the electron emits the released energy as visible electromagnetic wave [134].

Concerning perception, there are three types of color receptors (cone cells) in the retina of the human eye, and their responses to electromagnetic waves of certain, different wavelengths cause the impressions red, green, and blue, respectively. Successively stimulating the three receptors with wavelengths between 400 and 700 nm, each wavelength causes the impression of a color component of the rainbow, which comprises the whole visible spectrum. Moreover, if the receptors for blue (close to 400 nm) and for red (close to 700 nm) light are stimulated, impressions of colors emerge that cannot be expressed by a wavelength, being just a perceptive mixture [139]. These colors are summarized by the umbrella term *purple*, and hence, purple does not appear in the rainbow [140]. The brightness is perceived by another cell type of the retina, the rod cells [139].

Among all types of waves comprised by wave theory, the only ones of importance within this thesis are plane waves. Among those, there are again two different types of waves, the longitudinal and the transversal ones. Longitudinal waves exhibit their oscillations in direction of propagation, such as sound waves. Electromagnetic waves are transversal ones, so both the electric and the magnetic field are directed perpendicular to the direction of propagation. Moreover, the electric and the magnetic field component are perpendicular to each other. A schematic depiction of a transversal plane wave is given in Fig. 2.2.

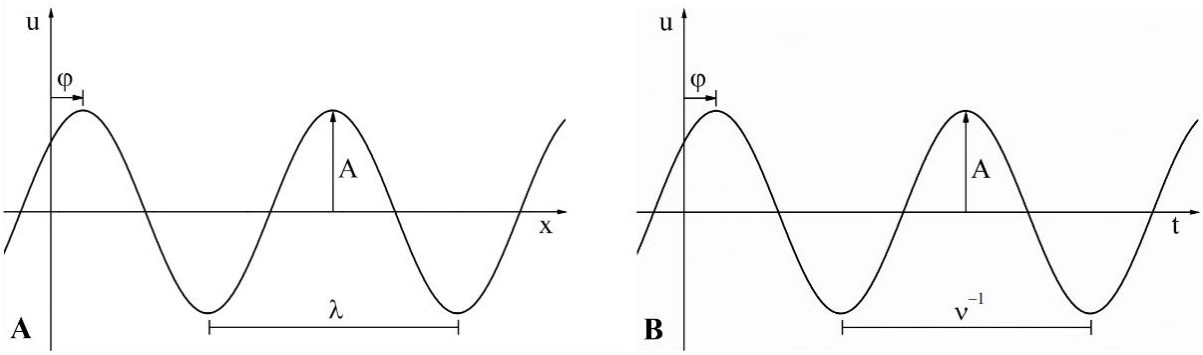

Fig. 2.2: Schematic depiction of a one-dimensional plane wave. Assignment of crucial parameters (λ: wavelength; φ: phase shift; A: amplitude; u: displacement; x: direction in space, in the following expressed as three-dimensional position vector $\vec{r}$) defining a wave in terms of space (A) at a certain point in time, and time (B) at a certain point in space.

An electromagnetic wave travels through space as described by the wave equation (eq. 2.5). Please note that this is for an idealized wave, exhibiting infinite expansion and infinite energy.

$$u(\vec{r}, t) = A\, e^{i(\vec{k}\cdot\vec{r} - \omega t + \varphi)} \tag{2.5}$$

Here, u is the displacement as function of the position vector $\vec{r}$ and the time t, A is the amplitude (as the maximum displacement), e is Euler's number (approximately 2.718 [132]), i is the imaginary unit (square root of –1), k is the wave vector (see below), ω is the circular frequency, and φ is the phase shift [141].

Different waves that encounter each other obey the superposition principle [142].

$$u(\vec{r}, t) = \sum_{j=1}^{n} u_j(\vec{r}, t) \tag{2.6}$$

Hence, the displacement in terms of electric and magnetic field at a certain point in space can simply be added as vector sum. This phenomenon is called interference. To observe a temporally and spatially stable interference (Stationary interference), the waves need to be

coherent, which means that they have a fixed phase relationship, so they equal each other in waveform and frequency, but not necessarily in phase, and hence, their displacement alters in the same way. Absolute coherence is a theoretical construct, so the coherence can be indicated temporally as coherence time or spatially as coherence length (distance the wave propagates within the coherence time). Coherent waves that are in phase interfere constructively, resulting in a wave that exhibits the sum of the single amplitudes. Conversely, two waves can interfere destructively, if they oscillate inversely. In this event, waves that exhibit the same amplitude cancel each other out completely. Destructive interference occurs for waves with a phase shift of half the wavelength, corresponding to odd multiples of π in radian measure, while for constructive interference, the phase shift needs to be an integer multiple of the wavelength, corresponding to even multiples of π. Stationary interference causes characteristic interference patterns, consisting of successive changes of bright and dark areas. If there is no fixed phase relationship, e.g., having waves with different frequencies, there is no stationary interference and the fluctuations cancel each other out in temporal averaging. A border case is the beat, where the amplitude increases and decreases periodically, resulting from the interference of waves oscillating with closely neighbored frequencies [143].

Concerning perception, interference causes the impression of iridescence. Having, e.g., a soap bubble, parts of the light are reflected from the front side of the very thin lipid layer, while other parts pass and are reflected from the backside. The both reflections interfere, so some frequencies interfere constructively and other destructively [144]. The colors of iridescence belong to the structural colors (based on interference), distinguished from colors caused by pigmentation (based on absorption). Combinations occur, e.g., in terms of eye colors, where all colors except from brown are structural ones, while brown is caused by pigmentation [145, 146].

The co-existing description of the wave equation as cosine function

$$u(\vec{r}, t) = A\cos(\vec{k} \cdot \vec{r} - \omega t + \varphi) \tag{2.7}$$

is not used further. A crucial component of the wave equation is the wave vector $\vec{k}$. Its magnitude is the angular wavenumber k (eq. 2.8) and its direction is parallel to the direction of propagation. It is moreover proportional to the momentum (eq. 2.9) [147].

$$k = |\vec{k}| = \frac{2\pi}{\lambda} \tag{2.8}$$

$$\vec{p} = \hbar \cdot \vec{k} \tag{2.9}$$

Since no magnetic materials ($\mu_r \approx 1$, see below) were used throughout this thesis, the focus is permanently set on the electric field component, so the wave equation simplifies to

$$E(\vec{r}, t) = E_0 \, e^{i(\vec{k}\cdot\vec{r} - \omega t + \varphi)} \quad , \tag{2.10}$$

where E is the electric field and E_0 is the amplitude.

The directions of oscillation of the electric and the magnetic field of several waves to each other is described by the wave's polarization. Regarding a single wave, both fields are perpendicular to each other and perpendicular to the direction of propagation, thus perpendicular to the wave vector. If the respective fields of different waves are oscillating in the same direction, the polarization is linear. If the direction of oscillation is rotating at a constant rate, the wave is circularly (or elliptically) polarized, either right circularly (pursuant to the right-hand rule) or left circularly (in left-hand sense). If both is not the case, the wave is unpolarized.

If a linearly polarized electromagnetic wave is impinging on an interface, there are two further possible specifications that are notable. If the electric field is directed parallel to the plane of incidence, which is spread between the wave vector and the orthogonal of the interface, it is called p-polarized, π-polarized or transverse-magnetic(TM)-polarized. If the electric field is directed perpendicular to the plane of incidence, it is called s-polarized (from German "senkrecht", which means perpendicular), σ-polarized or transverse-electric(TE)-polarized [148].

The wave equation is lastly derived from the Maxwell equations (whereas not every solution of the wave equation is a solution of the Maxwell equations, thus re-application into the Maxwell equations is required to ensure), comprising four equations that describe the connection of electric and magnetic fields as well towards each other as with electric charges and currents. Together with the Lorentz force, which describes how a charge in motion is affected by an electric or magnetic field, they explain all phenomena of electrodynamics and are thus the basis of optics and electrical engineering. The Maxwell equations are indicated in eq. 2.11-2.14.

$$\nabla \cdot D = \rho_{ext} \tag{2.11}$$

$$\nabla \cdot B = 0 \tag{2.12}$$

$$\nabla \times E = -\frac{d}{dt} B \tag{2.13}$$

$$\nabla \times H = J_{ext} + \frac{d}{dt} D \tag{2.14}$$

Here, D is the electric flux density, ρ the charge density, B the magnetic flux density, E the electric field strength, H the magnetic field strength and J the electric current density.

The first one describes the charge as source of the electric field, while the second negates magnetic monopoles and describes the magnetic field as source-free. The third one expresses that a change in the magnetic flux density causes an electric vortex field, and the fourth the generation of a magnetic vortex field as consequence of an electric current [141].

2.1.2 Media: The refractive index

For the consideration of electromagnetic waves within different media, a material property needs to be defined that describes the resistance of the medium towards the propagation of an electric and magnetic field, being the permittivity and the permeability, respectively. Thereunto, the permittivity and the permeability of the vacuum has been determined, being $\varepsilon_0 = 8.85 \times 10^{-12}$ F/m [132] and $\mu_0 = 4\pi \times 10^{-7}$ N/A^2 [132], respectively, linked with the vacuum propagation velocity $c_0 = 3 \times 10^8$ m/s [132] by eq. 2.15.

$$\varepsilon_0 \mu_0 = \frac{1}{c_0^2} \tag{2.15}$$

The material's permittivity (ε) and permeability (μ) is then expressed by multiplication of a material-dependent factor with the permittivity and permeability of the vacuum, respectively, described by the equations 2.16 & 2.17.

$$\varepsilon = \varepsilon_0 \varepsilon_r \tag{2.16}$$

$$\mu = \mu_0 \mu_r \tag{2.17}$$

ε_r and μ_r are the relative permittivity and relative permeability, respectively. Beside their material dependence, both are also frequency-dependent (*dispersive*), resulting in a permittivity and permeability function, $\varepsilon_r(\omega)$ and $\mu_r(\omega)$, respectively [148]. If μ_r is approximately 1, materials are referred to as non-magnetic.

Applying these resistance values, the propagation speed in a medium can be determined (and thus the wavelength in a medium, which is changing along with, while the frequency remains unaltered). The ratio between the propagation velocity in vacuum and in a medium is called the refractive index n of the medium, which calculates by means of eq. 2.18.

$$n = \frac{c_0}{c} \tag{2.18}$$

It is directly linked to the permittivity and the permeability via

$$n = \sqrt{\varepsilon_r \mu_r} \ . \tag{2.19}$$

Having a wave packet that comprises different frequencies (each frequency exhibiting a different propagation velocity in a dispersive medium), it travels with group velocity c_g in its entity, thereby forming an overall shape called envelope [148]. These further issues are not applied throughout this work and are thus considered as beyond the scope of this thesis.

When perceiving the impression of brightness by eye (not further considering its tunable sensitivity), the perceived physical quantity is not the electric field directly, but the intensity, being the power divided by the area (in perception, this is the area of the retina). The intensity I is related to the electric field via eq. 2.20. Please note that this applies for a perfectly parallel beam only.

$$I = \frac{c_0 \varepsilon_0 n}{2} |E_0|^2 \tag{2.20}$$

Eq. 2.20 already includes that the fluctuations of the electric field, oscillating with frequencies in the PHz region in case of visible light, cannot be resolved temporally (nor the alternate current frequency of 50 Hz). Instead of constant fluctuations from bright to dark according to the electric field changes from 0 to $|E_0|$, an effective, constant electric field E_{eff} is eventually perceived, related to the amplitude by

$$E_{eff} = \frac{|E_0|}{\sqrt{2}} \ . \tag{2.21}$$

Multiplication with the irradiated area A, it results in the power P.

$$P = |I| \, A \tag{2.22}$$

In a third step, the energy or work of a light beam, irradiating an area for a certain time interval, can be deduced via multiplication with the irradiation time t.

$$W = P \, t = |I| \, A \, t = \frac{c_0 \varepsilon_0 n}{2} |E|^2 \, A \, t \tag{2.23}$$

For a not perfectly parallel beam, which implies that the illuminated area is altering over distance, e.g., having a point source situated within a certain distance, emitting a sphere of radiation (with the sphere surface area $4\pi r^2$), the inverse-square law (eq. 2.24) needs to be

considered in addition. Due to the power distribution over the whole sphere surface area – the latter increasing with distance – the intensity per area decays inversely proportional to the square of the distance r (being the radius of the light sphere) [149].

$$I \propto \frac{1}{r^2} \tag{2.24}$$

2.1.3 Media: Interaction with matter

Since a conductor (in the following put on a level with a metal, since no special cases in that respect are treated within this work) is affected differently by an incoming electric field than a dielectric, the following phenomena needs to be discussed for both cases separately. The behavior of semiconductors is considered as beyond the scope of this work.

In a dielectric, the electron clouds that surround the atomic nuclei are at all times assigned to the respective atoms, also if simultaneously participating in chemical bonds in the case of valence electrons. However, the entity of each electron cloud can be shifted in response to the electric field of an incoming electromagnetic wave, forming a dipole with the non-shifted positive core. The nucleus does not response notably because of its inertia, caused by the way larger mass. The dipole formation is depicted in Fig. 2.3.

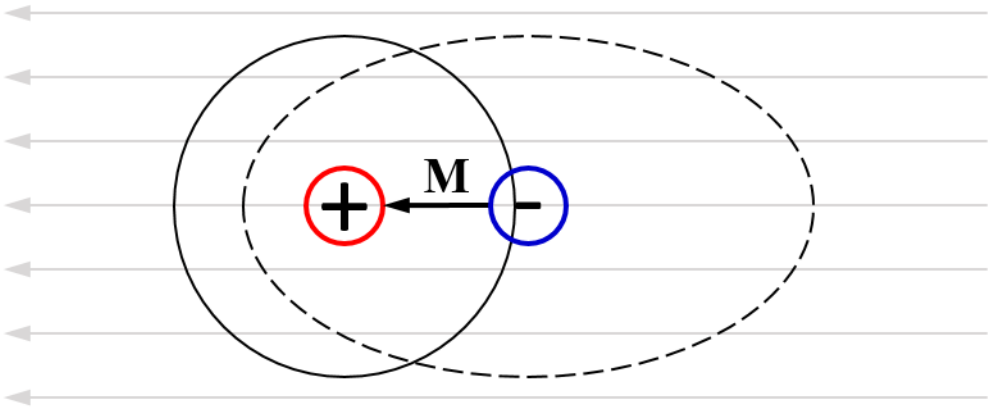

Figure 2.3: Formation of an atomic dipole due to an applied electric field. The atomic nucleus (red circle with assigned positive charge) is surrounded by its electron cloud (solid black circle). If an electric field is applied (gray arrows), the electron cloud shifts (dashed black line, centered by assigned focus of negative charge) in response to the field (and oscillate if the field is alternating), while the core, massive and thus exhibiting way larger inertia, remains at its position. A dipole moment (M) is generated. If the field is cancelled, the original position is recaptured.

Having molecular dipoles, e.g., water molecules, the whole molecule might rotate due to the alternating electric field, causing, for example, the dielectric heating, named accordingly, in a

microwave oven. The dipolar response is limited by the inertia of the affected particles. Molecular response to an alternating field is limited to microwave frequencies, while for ionic or molecular polarization, the infrared region is limiting. Electronic polarization as described above can occur up to the ultraviolet region. Beyond, the permittivity approaches the vacuum permittivity; electron clouds are no longer able to respond due to inertia reasons [141].

In opposite to dielectrics, conductors offer free electrons that are weakly bound by the positive core and tend to leave the atomic entity towards a delocalized electron cloud, behaving like an electron gas in between the lattice of positively charged atomic cores. These electrons are then assigned to the conduction band. The resulting bond type is called metallic bond. The most significant difference between conductors and dielectrics is that the conduction band of metals is partially occupied; the valence and the conduction band overlap. In dielectrics – being insulators in terms of conductivity – there is a band gap between valence and conduction band. The entity of the delocalized electrons (the electron gas) is also referred to as plasma, which holds approximately true, since even though electrons are – due to the still existent binding to the positive core lattice – not as free as ions in a conventional plasma, but on the other hand, they are way less inert than ions because of their far smaller mass.

The crucial value regarding the interaction of electromagnetic waves with metals is the respective plasma frequency. If the oscillating electric field of an electromagnetic field is encountering the electron gas of a metal, the latter will oscillate in its entity. At the plasma frequency, these plasma oscillations are excited resonantly, resulting in the absorption of the electromagnetic wave. The plasma frequency calculates by means of eq. 2.25.

$$\omega_p = \sqrt{\frac{n_e e^2}{m_e^* \varepsilon_0}} \tag{2.25}$$

Here, n_e is the number density of electrons, being the number of electrons divided by the respective volume, e is the electric charge, m_e^* is the effective electron mass (whereby effective mass means the mass the electrons behave to have, different from their real mass when affected by an applied force), and ε_0 is again the vacuum permittivity. Please note that this is an approximation for an infinite ion mass, what is fair enough due to the huge ratio of ion and electron mass.

The refractive index of a metal is directly related to its plasma frequency, being

$$n = \sqrt{1 - (\frac{\omega_p}{\omega})^2} \tag{2.26}$$

The plasma frequency as well as the separated consideration of metals and dielectrics are taken up again in the following parts that deal with absorption, reflection and transmission [150].

2.1.4 Media: Absorption

If electromagnetic waves travel through a lossy medium, the intensity is attenuated due to the by and by absorption of photons. The refractive index of an absorbing medium needs to be expressed by a complex number (and so does permittivity and permeability), being

$$N = n + i\kappa \ , \tag{2.27}$$

where N is the complex refractive index, n is the real part of the complex refractive index, and κ is the imaginary part.

The real part describes the propagation through the medium as discussed before, while the imaginary part describes the absorption. To describe the intensity of a damped wave, another coefficient, the absorption coefficient α, is introduced, which is related to κ.

$$\alpha = \frac{4\pi\kappa}{\lambda} \tag{2.28}$$

On that basis, the intensity of a damped wave can be expressed as

$$I = I_0 \, e^{-\alpha l} \ , \tag{2.29}$$

where *l* is the path length through the absorbing medium. In spectroscopy, absorption is quantified by determining the intensity that passed through a lossy medium. The ratio of detected to initial intensity is called transmittance T. Along with, the extinction coefficient ε, rather used in spectroscopy than α, is introduced.

$$T = \frac{I}{I_0} = e^{-\alpha l} = e^{-2.303\varepsilon c l} = 10^{-\varepsilon c l} \tag{2.30}$$

The Beer-Lambert law, frequently used to determine the absorption or the concentration of a chemical species, can be deduced by applying the negative decadic logarithm [134].

$$A = \varepsilon c l \tag{2.31}$$

Here, A is the absorbance, c is the concentration of the absorbing species and ε is the molar attenuation coefficient. E for extinction and A are widely used synonymous, although extinction, in the proper meaning of the word, includes not only absorption, but all processes

decreasing the intensity, such as scattering, while absorbance does not. The same applies for ε, mostly referred to as extinction coefficient. Another synonym for A is optical density (OD), which might lead to confusion because the term of an optically denser medium is used for a medium that exhibits a higher refractive index. Thus, the term optical density is avoided in the following.

Coming back to the wave equation, a damped wave includes absorption coefficient and path length (with A again for the amplitude).

$$u(\vec{r},t) = A\, e^{-\alpha l}\, e^{i(\vec{k}\cdot\vec{r} - \omega t + \varphi)} = A\, e^{i(\vec{k}\cdot\vec{r} - \omega t + \varphi) - \alpha l} \tag{2.32}$$

As introduced along with the electromagnetic spectrum (Fig. 2.1), the interaction of electromagnetic waves of different spectral ranges with can be assigned to certain state transitions. Absorption thus occurs in the course of several processes, e.g., the above-mentioned dielectric heating, taking place if molecular dipoles are exposed to microwaves, or, as well mentioned above, if the electron cloud of a metal is resonantly excited by the respective plasma frequency. In the following, the absorption of visible light is discussed a bit more extensively.

Absorption of visible light occurs, if the energy of the incoming photon matches the energy needed to lift an electron to a higher energy level, what is dependent on the molecular band structure of the chemical species. The excitation of molecular vibrations and oscillations are caused by the absorption of the neighbored infrared region. The electron transition to higher excitation states is schematically depicted in the *Jablonski diagram* (Fig. 2.4) [134, 151].

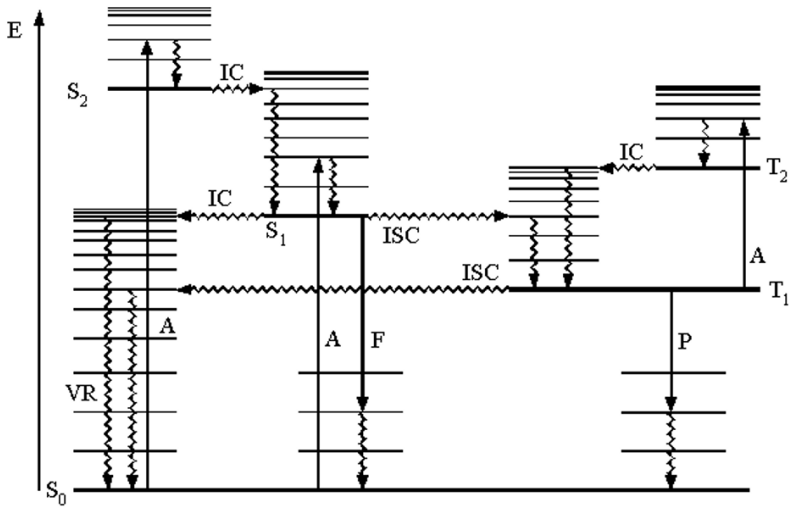

Figure 2.4: Jablonski diagram. The scheme depicts the different possibilities of an energetically lifted electron, having absorbed a photon (A for absorption), to return to the ground state (S_0). These are fluorescence (F), vibrational relaxation (VR) after internal conversion (IC), and, after intersystem crossing (ISC), phosphorescence (P). S_1 and S_2 denote the excited singlet states, T_1 and T_2 the excited triplet states (explanation is given in the text). Figure adapted from Richter, 1998 [151].

Figure 2.4 shows the band structure of a molecule with its ground state S_0 and the excited states S_1 and S_2. Obviously, there is not only one single band, but several sublevels that represent the vibrational modes. Due to the many transition possibilities resulting of the different sublevels, absorption appears in the spectrum as peak (or peaks) of certain broadness. If the energy is not matching a state transition, the wave is transmitted or reflected.

The excited electron is further not remaining in the excited state. There are several possibilities to dissipate the additional energy, and in most cases, it is thermal dissipation. In this event, the electron undergoes an internal conversion (IC) to a highly-excited oscillation level of S_0, and by oscillation, the excess energy is dissipated. Consequently, this is called vibrational relaxation (VR). Some molecules can forward excitation energy non-radiative by means of resonant energy transfer, called Foerster resonance energy transfer (FRET), and in this case, an electron of a neighbored molecule is lifted to the excited state, while the initially excited electron falls back to ground state. That occurs, for example, during photosynthesis, where most of the photons are collected by light-harvesting proteins, which forward the excitation energy to the photosynthetic reaction center. FRET is not depicted in Fig. 2.4. Another possibility is optical emission, i.e., emission of a photon again, while the photon energy is reduced in comparison to the excitation photon due to partial VR. This process is called fluorescence (F) and occurs in the range of 10^{-9} to 10^{-7} s. The distance between absorption and fluorescence maximum is called Stokes shift.

If the electron remains in the S_1 state longer, intersystem crossing (ISC) can occur, which refers to the electron spin. The spin of an electron can accept the values +1/2 (↑, up) and -1/2 (↓, down). Paired electrons cancel each other out, the total spin is zero (↑↓). Thus, only the unpaired electrons need to be taken into account, and in the most molecules, there are none, so the ground state is the above-mentioned singlet (S) state. The name is deduced from the spin multiplicity M, which is just the number of unpaired electrons plus 1. This is 1 for molecules without unpaired electrons. Having one unpaired electron, as, for example, in radicals, M is 2 (duplet, D). In biradicals (e.g., molecular oxygen), M is 3 (triplet, T). In side group metal complexes, it might increase to five (4: quartet, 5: quintet). An ISC thus means that the electron changes its spin, leaving behind two unpaired electrons. The molecule enters the energetically slightly lower T state. A spin reversal is considered as forbidden with respect to the selection rules of quantum mechanics, what does not mean that it never occurs, just that it is kinetically unfavored and usually outdone by faster, “allowed” processes. In T_1, the electron is somehow trapped, since all transitions to dissipate the energy surplus are forbidden. Therefore, it takes longer to emit a photon, usually in the range of µs, but up to hours, what is utilized, e.g., for exit signs.

This emission is called phosphorescence (P). Some molecules are able to dissipate the energy thermally after performing another ISC towards a highly excited vibrational state of S_0. These molecules (e.g., carotenoids in plants) are able to prevent radical formation, which might occur if the electron relaxes by forwarding the excitation energy to a neighbored molecule, which is thereupon entering the T_1 state. By absorption of photons with higher energy, electrons can enter higher excitation states such as S_2. However, these electrons usually perform an IC immediately and return to S_1 by VR [134, 152].

2.1.5 Interfaces: Diffraction

Until now, the discussion of electromagnetic waves was confined to their continuous journey through vacuum or a homogenous medium. If a wave bundle passes an obstacle, it proceeds – besides its straight propagation – also into the geometrical shadow. The wavefront is bent around the obstacle. This process is called diffraction. It can be explained in terms of the Huygens-Fresnel principle, after which every point of a wavefront can be regarded as source of a new spherical wave. The superposition of these secondary waves is resulting in the again in the plane wavefront. At the edge of the hindrance, the secondary wave is not accompanied by another one to superimpose, so it proceeds in a semi-spherical manner within the geometrical shadow. Having a small slit or circular aperture, a planar wave generates a cylindrical or spherical wave behind the hindrance, respectively (depicted two-dimensionally in Figure 2.5A). Discernible diffraction phenomena are only realized, if the slit's dimension is comparable to or smaller than the wavelength. For sound waves, exhibiting wavelengths between 17 cm and 17 m in the audible region, it explains why sound is well to hear through openings like doors or windows, albeit standing in the geometrical shadow. Since lower frequencies are diffracted more strongly than high ones, deep tones are less directed than high ones.

Having two slits in close vicinity, the diffracted light beams interfere with each other, leading to characteristic interference patterns if the light is coherent (with broader pattern the higher the wavelength is). But interference patterns can already be observed having a single slit, what can be imagined by separating the light beam in two half beams that interfere with each other. Interference patterns caused by single-slit diffraction show a characteristic intensity distribution (Fig. 2.5C). The different maxima of constructive interference are numbered with integers in both directions, assigned with negative numbers left of center and with positive ones right of center. The central zeroth order represents the light that passes the obstacle undiffracted; it exhibits the highest intensity, becoming smaller in relation the smaller the slit is. As described

above, interference is constructive, if the phase shift is an integer multiple of the wavelength. The angle under which constructive interference occurs (θ_d) is therefore dependent on the slit's dimension (s), which results in a path difference (Δs) that corresponds to a phase shift by taking the wavelength into account (Fig. 2.5B) [148].

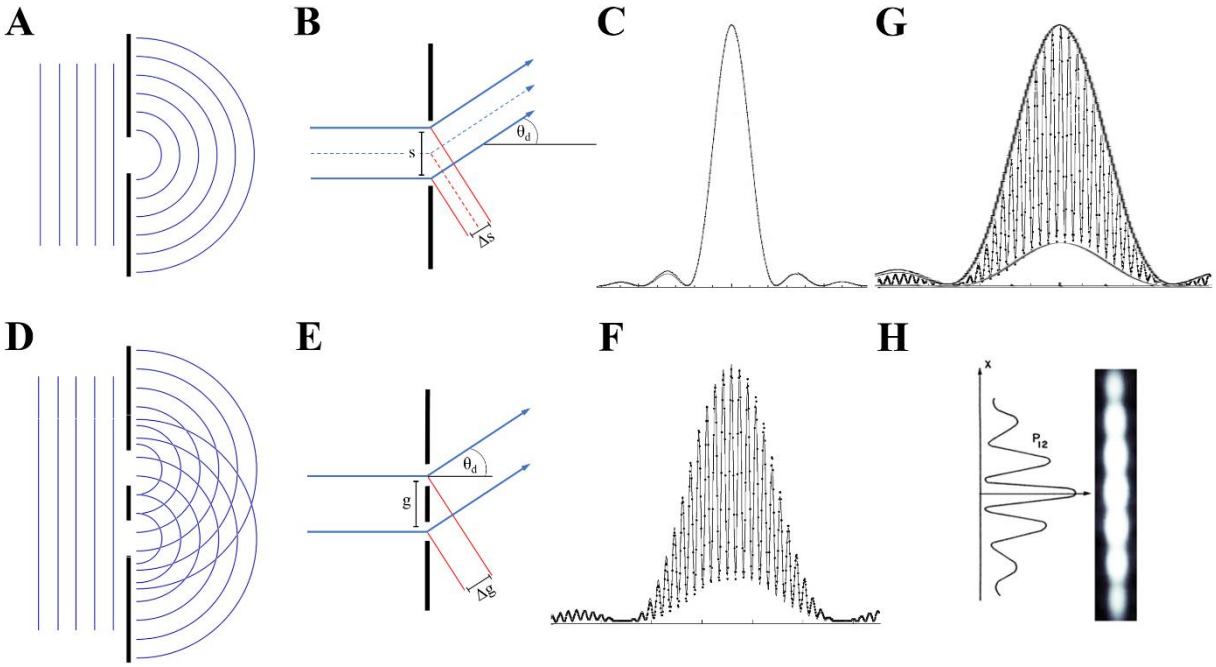

Figure 2.5: Diffraction effects. (A) If coherent planar waves travel through a slit of a size comparable to or smaller than the wavelength, a cylindrical wave emerges due to the diffractive bending, depicted two-dimensionally. (B) A path difference (Δs), corresponding to a phase shift that depends on the wavelength, is emerging for a particular slit width (s) under a particular diffraction angle (θ_d). (C) Intensity distribution caused by a single-slit diffraction pattern. (D) Having two slits sufficiently close to each other, the two cylindrical waves interfere with each other in addition. (E) The beam model of (B) is transferred to the additional interference caused by double-slit diffraction. (F) Intensity distribution caused by a double-slit interference pattern. (G) The double-slit interference pattern is enveloped by a single-slit interference pattern. (H) Exemplary interference pattern of electrons travelling through a double slit. Figures (C), (F), and (G) adapted from Gan & Law, 2009 [153], and (H) from Bach *et al.*, 2013 [154].

So, the angle under which constructive interference occurs calculates according to eq. 2.33.

$$\sin \theta_d = n * \frac{\lambda}{s} , \tag{2.33}$$

where θ_d is the angle of diffraction, n is the diffraction order, hence an integer different from zero (since the waves of the zeroth order pass the obstacle undiffracted), and s is the width of the slit. The position on a screen can further be calculated via the Pythagorean theorem with respect to the screen distance.

For angles of incidence (θ_i) different from zero, the equation must be modified towards

$$\sin\theta_i + \sin\theta_d = n\,\frac{\lambda}{s}\,, \tag{2.34}$$

with θ_i as the angle of incidence.

Having a double slit, the two emerging cylindrical waves interfere additionally with each other (depicted two-dimensionally in Fig. 2.5D), yielding a more complex interference pattern (Fig. 2.5F). The latter is enveloped by the shape of a single-slit interference pattern (Fig. 2.5G), whose interference maxima are obtainable by replacing the width s by the slit distance g (Fig. 2.5E, eq. 2.31). An exemplary diffraction pattern obtained with electrons passing a double slit is shown in Fig. 2.5H. For the double slit, it applies that – besides the slit width – the distance between the slits must be in the size of the wavelength or smaller, too. The patterns become sharper the more slits are arranged periodically. Having multiple periodically arranged slits, it is also denoted as diffraction grating, exhibiting its own periodicity, being the grating period Λ. As further discussed in the section *Surface plasmon resonance spectroscopy*, a diffraction grating is not necessarily composed of slits and works as well in terms of reflection. Diffraction gratings are widely used, e.g., in terms of wavelength splitting in spectrometers, remembering that higher wavelengths are diffracted more strongly. A further application that exploits diffraction, not discussed here, is X-ray crystallography. There, it is utilized that the electrons of, for example, a protein crystal act as diffraction centers for X-rays. Out of the resulting interference patterns, structural information can be obtained [148].

2.1.6 Interfaces: Transmission & reflection

If electromagnetic waves impinge on an interface, they can be either transmitted or reflected. Both is illustrated in Fig. 2.6. Unless the angle of incidence (θ_i) is zero, a beam that is transmitted into another medium, exhibiting a different refractive index, is refracted (blue arrows in Fig. 2.6). If the medium beyond the interface exhibits a higher refractive index, the beam is refracted towards the normal of incidence. If it is lower, refraction occurs away from the normal.

Refraction is described quantitatively by Snell's law.

$$\frac{\sin\theta_i}{\sin\theta_t} = \frac{n_2}{n_1} = \frac{\lambda_1}{\lambda_2} = \frac{c_1}{c_2} \tag{2.35}$$

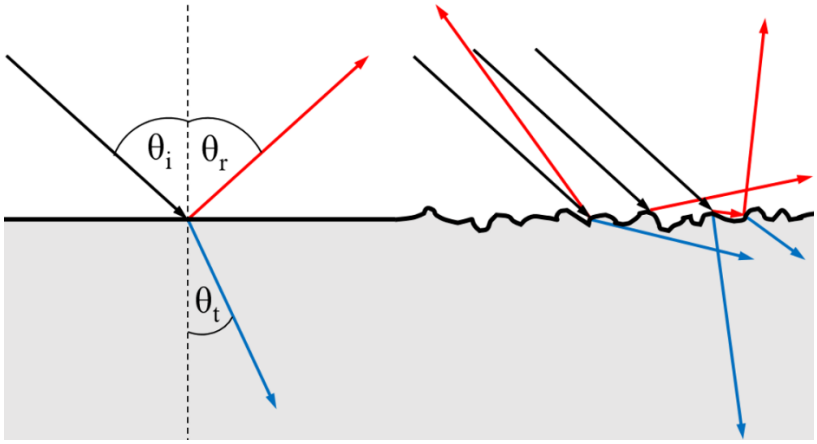

Figure 2.6: Transmission and reflection. A beam of electromagnetic waves that impinges on an interface (black arrows) is transmitted (blue arrows) or reflected (red arrows). For perception, it makes a huge difference whether the surface is smooth (left) or rough (right). In the depicted case, the refractive index of the media displayed in gray is higher than the one of the media displayed in white. Further description is given in the text.

Since the refractive index of a dispersive medium is frequency-dependent, a prism, offering two interfaces, is a second possibility for wavelength separation within a spectrometer besides the grating. (Lenses as tools employing refraction are discussed within the microscopy section.)

In metals, transmission occurs at frequencies above their plasma frequency. In this event, the electrons are not able to oscillate in response to the applied field anymore due to their inertia, so the waves can propagate through. Thus, metals are transparent for those frequencies (e.g., for gamma rays).

Reflection (red arrows in Fig. 2.6) is described by the law of reflection, stating that the angle of incidence equals the angle of reflection (θ_r).

$$\theta_i = \theta_r \tag{2.36}$$

Accompanying phase shifts (e.g., occurring if the refractive index beyond the interface is higher) are only discussed if crucial for the respective method, discussed as of subchapter 2.2.

It makes sense to differentiate between specular and diffuse reflection, the latter often referred to as scattering. The law of reflection applies in both cases. Nevertheless, specular reflection is perceived as mirroring, while diffuse reflection appears white. Gloss is perceived if diffuse reflection dominates, but there is still a notable part of specular reflection. For specular reflection (Fig. 2.6, left), a smooth surface is required. Curvatures are thereby perceived as distortions. Since the subconscious image processing within the human brain is not aware of the law of reflection, the observed picture appears as a virtual one beyond the mirror surface, having the same distance, but being reversed.

The inverse is not the case. Even though a smooth surface is required to obtain specular reflection, diffuse reflection (Fig. 2.6, right) can be caused by both smooth and rough surfaces. That is because parts of the light are transmitted and subsequently reflected at intrinsic crystal edges, due to which, e.g., very smooth marble is still not mirroring. The smoothness is not required on an atomic scale, but for specular reflection, it needs to be in the range of the wavelength, thus the roughness needs to be lower than a micron [148, 155].

For particle sizes in the range of a few wavelength or below, the above-described *geometrical* scattering does not apply any more. It is then replaced by either Mie or Rayleigh scattering. Rayleigh scattering occurs for objects with a size approximately up to 0.2 λ, while geometrical scattering starts at about 2 to 10 λ. In between, Mie scattering takes place. Particles sized in that region exhibit a different scattering cross-section. While for objects that interact with electromagnetic waves in terms of geometrical scattering, electromagnetic waves are almost exclusively scattered backwards, the scattering in forward direction becomes notable for Mie and Rayleigh scattering. Classical examples for Mie scattering are fog and liquids exhibiting turbidity. Even smaller objects – molecules, for example – cause Rayleigh scattering. Here, the scattering angle is furthermore strongly dependent on the wavelength of the respective electromagnetic waves, affecting the scattering cross-section in the fourth power. Thus, the sun appears yellowish, since the blue light is scattered away by the atmosphere's molecules. During dusk and dawn, the path through the atmosphere is longer, so the sun appears red more and more. When looking at the sky (not directly at the sun), a certain angle within the light path is required to arrive at the observer's eye. This condition is only fulfilled for the blue light, while the other spectral parts pass by; therefore, the sky appears blue [156–161]. It needs to be added, that the blue sky during dawn and dusk ("blue hour") is complemented by the absorption of ozone (Chappuis absorption), exhibiting maxima at 575 and 603 nm. Otherwise, the zenith during sunrise and sunset would appear more greenish-yellowish [162]. A combination occurs in the case of opalescence. An opal consists of particles that are big enough to appear as opaque due to Mie scattering, but are small enough to exhibit a recognizably different scattering of blue and red wavelength. So, the opal is appearing bluish opaque from the side, while the transmitted light is reddish [163].

Rayleigh scattering is elastic. In seldom cases, the scattered photon is of less energy than the incoming one, leaving the molecule in a vibrationally excited state (Stokes scattering). Also, it can have more energy, leaving a formerly vibrationally excited molecule in the ground state (Anti-Stokes scattering). These processes, summarized as inelastic Raman scattering, are described more in detail within the infrared absorption spectroscopy subchapter. Other types of

scattering, such as Compton scattering, which occurs in the case of high-energy photons, are not further discussed [164].

Above their plasma frequency, metals are highly reflective. The impingement of the electric field causes an oscillation of the electron plasma (oscillating with its plasma frequency, but non-resonantly), thereby generating an inverse wave that is reflected, following the law reflection. The penetration depth is thus very low for these frequencies [150].

The plasma frequency of most metals is in the UV range, so specular reflection can occur within the whole visible spectrum. For that reason, mirrors are mostly made of aluminum or silver, evaporated on the backside of a protective glass plate. In the case of gold, violet light is already partially absorbed, but not because of its plasma frequency. The yellowish color (and the reddish of copper) is caused by interband transitions of inner electrons that change their orbitals, in case of gold from 5d to 6sp [165, 166]. The plasma frequencies of gold (ω_p = 2.180 PHz; corresponding wavelength in vacuum and hence approximately in air: λ = 138 nm) and copper (ω_p = 1.914 PHz; λ = 157 nm) do not differ a lot from, for example, silver (ω_p = 2.183 PHz; ω_λ = 137 nm) [167]. By contrast, white and red gold are just alloys containing silver and/or copper in addition [168].

2.1.6.1 Total reflection and the evanescent wave

If a beam of electromagnetic waves undergo a refractive index change, there is a part of transmitted and a part of reflected waves (quantitative description follows). But, under certain circumstances, the wave bundle can be totally reflected. This happens if it enters a medium with a lower refractive index, thereby exceeding the so-called critical angle (θ_c). Total internal reflection is utilized in optical fibers, which forwards electromagnetic waves almost lossless due to this process.

By entering a medium with a higher refractive index, refraction occurs to the normal of incidence. Conversely, light is refracted away from the normal in the opposite case. Under a certain angle, being the critical angle, the beam is refracted parallel to the interface. By further increasing the angle of incidence, the beam is refracted back into the medium it is coming from. Obviously, in this case, it is no longer refracted, but reflected, and since there is no change of medium anymore, there is no angle of refraction; instead, the law of reflection applies. The fact that the electromagnetic wave is nevertheless penetrating the second medium is discussed

subsequently. The critical angle can be calculated using Snell's law, knowing that the angle of refraction needs to be 90 deg.

$$\frac{n_2}{n_1} = \frac{\sin\theta_c}{\sin 90°} = \sin\theta_c \leftrightarrow \theta_c = \arcsin\left(\frac{n_2}{n_1}\right) \tag{2.37}$$

In addition to the reflected wave, an evanescent wave emerges beyond the interface in case of total reflection, which is crucial for spectroscopic techniques like surfaced-enhanced infrared absorption spectroscopy and surface plasmon resonance spectroscopy. An evanescent wave differs from a damped wave significantly. A damped wave is oscillating temporally (resulting in its frequency) and spatially (yielding its wavelength) like a non-damped wave, only the amplitude decays exponentially over distance. An evanescent wave is only oscillating over time (thus having a frequency), but not spatially. Spatially, it is just exponentially decaying (and is hence not a travelling wave anymore). Mathematically spoken, the evanescent wave is purely imaginary [169, 170].

Having total reflection, the reflected wave is not leaving the interface exactly at the position where it was impinging. That was assumed already by Newton, but proven experimentally by Goos and Hänchen in the forties of the twentieth century using TM-polarized light. In Fig. 2.7 it is depicted schematically as drawn by Goos & Hänchen in 1947 [171].

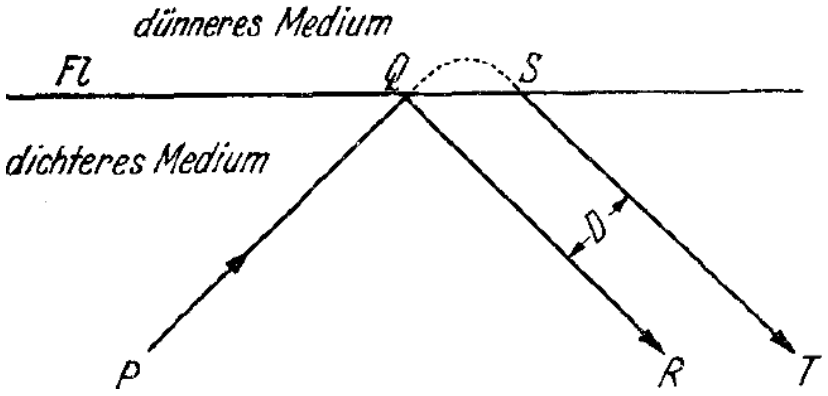

Figure 2.7: Possible courses of a reflected light beam. An incoming light beam is assumed to either take the path QR or ST. Further explanation is given within the text. "Dünneres Medium": optically thinner medium in terms of refractive index; dickeres Medium: optically thicker medium). Figure adapted from Goos & Hänchen, 1947 [171].

In opposite to the above-described metallic reflection under non-critical angles, where the beam is indeed QR-reflected, under critical angle conditions the light beam was reflected taking the ST path. The QS shift is therefore called Goos-Hänchen shift. As drawn in Figure 2.7, the light beam seems to be reflected at an imaginary plane of reflection parallel to the real interface,

situated at the cross section of PQ and ST. Exceeding the critical angle, the wave is split into a travelling wave and the evanescent one. The travelling wave is travelling along the surface, while an evanescently decaying field is generated perpendicular to the surface [171].

When totally reflected at the interface, the interference of the incoming and the reflected wave cause a standing wave and an evanescent field (with the same frequency) emerges beyond, both illustrated in Fig. 2.8 [172].

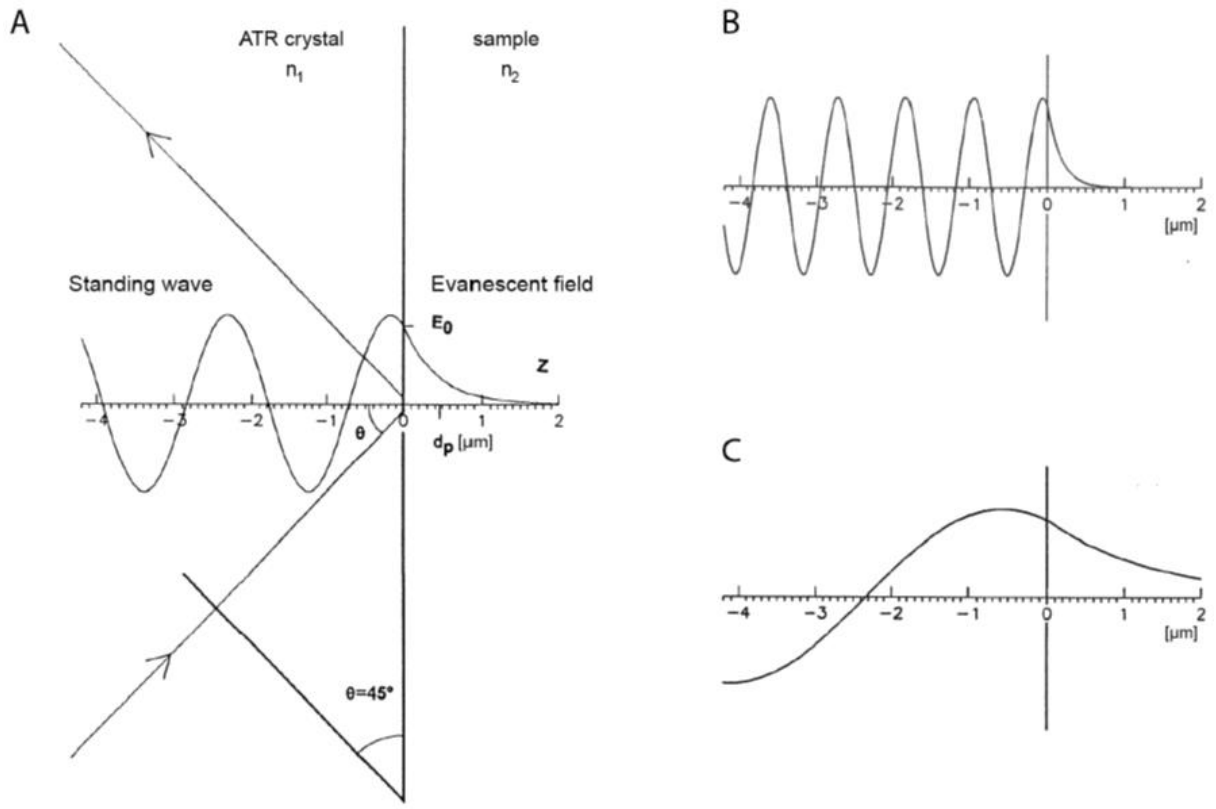

Figure 2.8: Standing wave and evanescent field caused by a totally reflected beam. (A) An incoming wave impinging under a 45 deg angle is causing a standing wave directly in front of the interface. Beyond the interface, an evanescent field is exponentially decaying, also referred to as evanescent wave. The amplitude equals the displacement of the standing wave on the front side. The exponential decay caused by a wave of short wavelength (B) is compared to one of longer wavelength (C). Figure adapted from Schwaighofer, 2013 [138].

The penetration depth (d_p) of the evanescent wave, specifying the distance over which the electric field decreases to the value of 1/e (37 %) of the initial intensity, is dependent on both the wavelength and the angle of incidence. It calculates by means of eq. 2.38 [169, 172].

$$d_p = \frac{\lambda}{2\pi n_1 \sqrt{\sin^2(\theta_i) - \left(\frac{n_2}{n_1}\right)^2}} \tag{2.38}$$

Usually, there is no net transport of power due to the evanescent field. All the energy that penetrates the medium behind the interface is given back to the travelling wave that is finally reflected. But there are exemptions, being consequences of interactions within the penetration depth. Since the certain amount of energy, which is consumed by the interaction, is missing within the totally reflected beam, these type of reflection is called attenuated total reflection (ATR). A possible interaction might be absorption due to absorbing molecules situated within the penetration depth of the evanescent field. This effect is exploited in ATR-infrared absorption spectroscopy (ATR-IR). Another interaction is the resonant excitation of surface plasmons, exploited in surface plasmon resonance (SPR) spectroscopy. Both are explained in detail in the respective sections [170, 171, 173].

A further notable exception, at which indeed energy is transported, is frustrated total internal reflection (FTIR, not to confuse with Fourier transform infrared spectroscopy). It occurs, if a third medium, exhibiting a higher refractive index than the second, is placed within the penetration depth of the evanescent field. Then, an electromagnetic (travelling) wave can be outcoupled into the third medium, and the total reflection is – ideally spoken – completely prevented. This process is also called optical tunneling, since eventually photons tunnel through the low-refractive index barrier. The angle under which the tunneled photons are outcoupled equals the angle of incidence [174]. Such a sandwich structure is utilized, e.g., for beam splitters. Within a microscope, beam splitters enable imaging while simultaneously observing the sample through the ocular.

2.1.6.2 Quantitative description: The Fresnel equations

The quantitative description of the shares of electromagnetic waves that are reflected and transmitted, respectively, is given by Fresnel's formulae. In hindsight, they were shown to be deducible from boundary conditions of the Maxwell equations, describing an interface that exhibits neither charge nor current. The derivation was implemented only after their formulation by Fresnel; he died four years before Maxwell's birth. Fresnel's formulae treat s- and p-polarized waves separately (with the absorption included via the complex refractive index N). In all cases, plane waves, a flat interface without edges, and homogenous media are assumed. In their most general description, the Fresnel equations are displayed by eq. 2.39-2.42.

$$\left(\frac{E_t}{E_0}\right)_p = t_p = \frac{2\,N_1\cos\theta_i}{N_2\frac{\mu_1}{\mu_2}\cos\theta_i + N_1\cos\theta_t} = \frac{2\,N_1\,N_2\cos\theta_i}{N_2^2\frac{\mu_1}{\mu_2}\cos\theta_i + N_1\sqrt{N_2^2 + N_1^2\sin^2\theta_i}} \quad (2.39)$$

$$\left(\frac{E_r}{E_0}\right)_p = r_p = \frac{N_2\frac{\mu_1}{\mu_2}\cos\theta_i - N_1\cos\theta_t}{N_2\frac{\mu_1}{\mu_2}\cos\theta_i + N_1\cos\theta_t} = \frac{N_2^2\frac{\mu_1}{\mu_2}\cos\theta_i - N_1\sqrt{N_2^2 + N_1^2\sin^2\theta_i}}{N_2^2\frac{\mu_1}{\mu_2}\cos\theta_i + N_1\sqrt{N_2^2 + N_1^2\sin^2\theta_i}} \quad (2.40)$$

$$\left(\frac{E_t}{E_0}\right)_s = t_s = \frac{2\,N_1\cos\alpha}{N_1\cos\alpha + N_2\frac{\mu_1}{\mu_2}\cos\beta} = \frac{2\,N_1\cos\alpha}{N_1\cos\alpha + \frac{\mu_1}{\mu_2}\sqrt{N_2^2 + N_1^2\sin^2\alpha}} \quad (2.41)$$

$$\left(\frac{E_r}{E_0}\right)_s = r_s = \frac{N_1\cos\alpha - N_2\frac{\mu_1}{\mu_2}\cos\beta}{N_1\cos\alpha + N_2\frac{\mu_1}{\mu_2}\cos\beta} = \frac{N_1\cos\alpha - \frac{\mu_1}{\mu_2}\sqrt{N_2^2 + N_1^2\sin^2\alpha}}{N_1\cos\alpha + \frac{\mu_1}{\mu_2}\sqrt{N_2^2 + N_1^2\sin^2\alpha}} \quad (2.42)$$

Here, E is the electric field with the indices t for transmitted, r for reflected and 0 for the incoming one, t and r are the transmission and reflection factor, respectively, each with the indices s for s-polarization (TE) and p for p-polarization (TM), θ_i is the angle of incidence and at the same time – since equal – the angle of reflection, θ_t is the angle of refraction, μ is the permeability coefficient (equaling μ_r each, since μ_0 is cancelled out; nevertheless, the several r-indices might lead to confusion), and N is the complex refractive index. The media are specified by the indices 1 and 2. The right term further expresses θ_t via θ_i by applying Snell's law.

There are a lot of special cases that are not outlined here: If the media are nonmagnetic (so $\mu_r \approx 1$ and thus $\mu \approx \mu_0$), all μ-parameters cancel out each other; if the media are not absorbing (so $\kappa = 0$), N can be replaced by n, and if further (in combination with the aforementioned) the angle of incidence is zero, it is just

$$r_s = \frac{n_1 - n_2}{n_1 + n_2} = -r_p \quad (2.43)$$

$$t_s = \frac{2n_1}{n_1 + n_2} = -t_p\,. \quad (2.44)$$

A required addition to consider unpolarized light is that every arbitrary wave can be expressed as a superposition of a perpendicular and a parallel polarized wave. This is expressed by the vector sum

$$\vec{E} = (E_0)_s \, \vec{e}_s \, e^{i(\vec{k}\cdot\vec{r} - \omega t + \delta_s)} + (E_0)_p \, \vec{e}_p \, e^{i(\vec{k}\cdot\vec{r} - \omega t + \delta_p)} \quad , \tag{2.45}$$

where $\vec{e}_{s \text{ or } p}$ is the unit vector for the respective polarization and $\delta_{s \text{ or } p}$ is the respective phase shift.

Fresnel's formulae are given with respect to the electric field. The widely used quantities reflectance (or reflectivity) R and transmittance (or transmissivity) T refer to the reflected and transmitted power, respectively. The power was defined earlier (eq. 2.22 and associated). The aforementioned equation needs to be slightly modified by multiplication with cos θ_i (again applying the law of reflection to replace θ_r) or θ_t, respectively, to specify A, the beam cross section, correctly with respect to the beam projection occurring at the interface for angles different from zero.

$$P_r = I \, A \cos\theta_i = \frac{\varepsilon_0 c_0 n_1}{2} |E_0|^2 \, A \cos\theta_i \tag{2.46}$$

$$P_t = I \, A \, \cos\theta_t = \frac{\varepsilon_0 c_0 n_2}{2} |E_0|^2 \, A \cos\theta_t \tag{2.47}$$

As mentioned within the respective paragraph, the effective value of the electric field is already included (see eq. 2.20 & 2.21). In case of reflection, this additional term is cancelled out, while for transmission, it needs to be considered. Moreover, regarding reflection, the medium is not changed at all, so no change of the refractive index occurs. For transmission, this change occurs.

The reflectance and transmittance, respectively, calculates by means of the equations 2.48 & 2.49.

$$R = \frac{P_r}{P_0} = \frac{\frac{\varepsilon_0 c_0 n_1}{2} |E_r|^2 \, A \cos\theta_i}{\frac{\varepsilon_0 c_0 n_1}{2} |E_0|^2 \, A \cos\theta_i} = \frac{|E_r|^2}{|E_0|^2} = |r|^2 \tag{2.48}$$

$$T = \frac{P_t}{P_0} = \frac{\frac{\varepsilon_0 c n_2}{2} |E_t|^2 \, A \cos\theta_t}{\frac{\varepsilon_0 c n_1}{2} |E_0|^2 \, A \cos\theta_i} = \frac{n_2 \cos\theta_t \, |E_t|^2}{n_1 \cos\theta_i \, |E_0|^2} = \frac{n_2 \cos\theta_t}{n_1 \cos\theta_i} |t|^2 \tag{2.49}$$

Please note that absorption is included via the complex refractive indices appearing in r and t, and again, s- and p-polarization needs to be treated separately (eq. 2.39-2.42).

As result of the conservation of energy, the sum of reflectance, transmittance and absorbance is 1 [141, 148, 149].

$$R + T + A = 1 \tag{2.50}$$

2.2 Confocal laser-scanning fluorescence microscopy

The confocal laser-scanning fluorescence microscope (abbreviated here with LSM, although this usually stands only for laser-scanning microscopy) is basically a light microscope, also referred to as optical microscope, with several expansions. The crucial aspect of an optical microscope is the resolution, not the magnification. The resolution is defined by the smallest distance two objects may have to be distinguishable [175]. In continuation of the *Fundamentals of light* part, one could imagine a diffraction grating, at which the resolution indicates the smallest distance two ridges may have to be separately discernable. If the resolution is not sufficient, no magnification will enable to discriminate the two ridges, which then will appear as one. It will just display the putative single ridge larger. The magnification is theoretically unlimited, since each magnified picture can be magnified again. The resolution is limited, since – if two ridges of the exemplary grating are in closest vicinity – diffraction will occur. Resolution limits usually refer to the findings of Abbe, Helmholtz, and Rayleigh. All of them found diffraction as limiting criterion, and eventually their results are relatively similar (see below). Although rather unknown, diffraction was indicated as limiting for microscopic resolution before by Verdet in 1869 [176]. Abbe published his achievements in 1873, indeed using the discriminability of the ridges of a diffraction grating [177, 178]. He stated that for resolving the grating lines sufficiently, at least the first diffraction order maximum needs to be collected beside the main (zeroth) one. (The zeroth diffraction order maximum is often denoted as “Airy disc”, the complete pattern as “Airy pattern”, named after George B. Airy, who firstly calculated the diffraction pattern of a point source in 1835 [175, 179].)

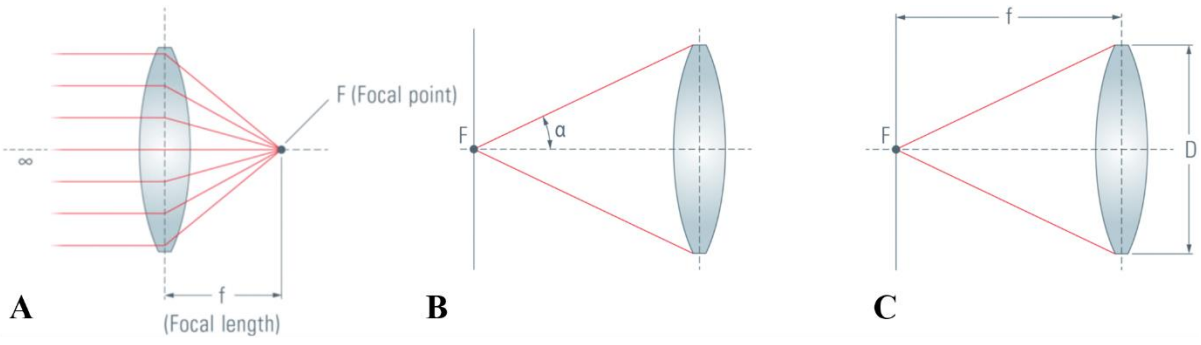

Figure 2.9: Converging lens. A converging lens focuses a parallel light beam to a focal point (F), and the higher the optical power of the lens is – dependent on curvature and refractive index –, the smaller is the focal length (f) (A). In a microscope, the numerical aperture (NA), a critical value for estimating the resolution, is defined as the product of the refractive index of the medium between sample and lens and the maximum angle, under which light of the sample can be collected by the objective lens (α, measured with respect to the optical path), shown in (B). By contrast, in photography, the aperture is indicated by the f-number, defined by the ratio of the focal length divided by the lens diameter (D), inversely resulting in small number for large apertures (C). Figure adapted from Rühl, 2012 [180].

To collect the first diffraction order maximum, the following numerical aperture is of crucial important.

Light is focused by a converging lens, exhibiting a convex shape. Such a lens is depicted in Fig. 2.9. In a microscope, the lens that focuses the light coming from the sample – thus the critical one in terms of resolution – is called objective lens [180]. Due to refraction of a collimated (thus parallel) light beam at the curved lens surfaces, a focal point emerges for each converging lens. The focal length is dependent on the curvature and on the refractive index of the lens; its inverse is called optical power. To collect the first order maximum of the diffracted light, the ratio of lens diameter and focal length, called (numerical) aperture, must be as large as possible. In photography, this is indicated by the f-number, being the ratio of the focal length divided by the lens diameter. In microscopy, the numerical aperture (NA) is defined by the sinus of the aperture angle (α, specified with regard to the optical path) multiplied by the refractive index of the medium between lens and sample (n_m) [175, 180].

$$\mathrm{NA} = n_m \sin\alpha \tag{2.51}$$

Second – keeping in mind that longer wavelengths are diffracted stronger – the resolution limit depends on the wavelength of the imaging light [180].

Additionally to his findings concerning numerical aperture and wavelength, Abbe described a resolution enhancement by utilizing grazing angle illumination instead of a parallel light beam. In modern microscopes, this is – besides increasing the light intensity – implemented by the condenser, a further lens system between lamp and specimen [181]. The condenser also exhibits a numerical aperture, finally resulting in the commonly known formula for the highest achievable resolution (d). Please note that the effective NA of the condenser cannot exceed the one of the objective [182], so eq. 2.52 indicates indeed the maximum possible resolution by specifying the right term, while the middle term can be applied to any other combination of condenser and objective lens.

$$d = \frac{\lambda}{\mathrm{NA}_{\mathrm{condenser}} + \mathrm{NA}_{\mathrm{objective}}} = \frac{\lambda}{2\ \mathrm{NA}_{\mathrm{objective=condenser}}} \tag{2.52}$$

However, for reasons of better contrast, the condenser's NA is usually chosen to be two thirds of the objective's one [182].

In opposite to common notion, Abbe did not mention the refractive index of the space between lens and sample (but only the sinus of α) [177, 178], but it is assumed that he already exploited the implied possibility. To increase the NA, the air between specimen and lens can be replaced by an immersion oil that exhibits a higher refractive index. Since the sinus of α is obviously smaller than 1, the immersion oil is necessary to achieve an NA of approximately one, which is implied in Abbe's literal resolution limit of "half the wavelength of blue light" (translated from German) [177]. Nowadays, numerical apertures of up to 1.4 can be achieved. Abbe considered the replacement of the eye by a detector that would be able to detect shorter wavelength (and smaller intensity differences) than the naked eye [177, 178].

Only one year later (1874), Helmholtz published almost the same results, additionally providing a mathematical description, what was omitted by Abbe himself. These descriptions, however, assumed an illuminated sample ([183], translated and accessible in [184]).

In the same year, Rayleigh published about microscopy [185], and finally stated his Rayleigh criterion for self-luminous samples, saying correspondingly that the zeroth diffraction order of a light source (e.g., regarding double stars in astronomy) needs to be located at least within the first diffraction minimum of the one aside to be able to resolve [186]. In 1896, Rayleigh discussed the microscopic resolution extensively [187]. Based on the above-mentioned minimum distance between two luminous objects, the analog for optical microscopy was derived, yielding as resolution limit

$$\mathrm{d} = \frac{0.61\,\lambda}{\mathrm{NA}}\ . \tag{2.53}$$

Hence, although to differentiate between illuminated and self-luminous specimens, the results are similar. The practical implementation is further hindered by lens imperfections (discussed below), what was already mentioned by Rayleigh in terms of spherical and chromatic aberrations, in respect of which he was confident that they would be eliminated by more advanced microscopic objectives to a certain extend [185–187].

Several improvements – such as the mentioned increase of the numerical aperture (what would yield a resolution limit of 0.36 λ for an NA of 1.4 and the acceptance of lower contrast) – were implemented, but until the advent of super-resolution (fluorescence) microscopy, which was theoretically described in 1994 by Hell and Wichmann [188] and rewarded with the Nobel Prize for Hell, Betzig and Moerner in 2014, these limitations held true. (Theoretically, the limit of diffraction and the Abbe limit for non-luminous specimens still hold true, however, they were circumvented.)

Abbe already mentioned that a single luminous source would be resolvable in much higher resolution, since no diffraction would occur [177, 178]. As described above, this was implemented more than hundred years later in terms of super-resolution microscopy (RESOLFT, STED), offering resolutions up to 6 nm by achieving that only one fluorophore within a diffraction limited area gives a signal [189]. To that, the approximate position of the fluorophore was required, which was overcome later by techniques such as STORM and (F)PALM, too [190–192]. Apart from light microscopy, higher resolutions were achieved by utilizing shorter wavelengths, as it is the case for the de Broglie wavelength of highly accelerated electrons, and for X-rays [193].

The specimen is imaged already magnified within the microscope. Afterwards, it is again magnified by the eyepiece. The magnification of a converging lens is dependent from its distance to the object [180]. A summary of possible cases is given in Fig. 2.10.

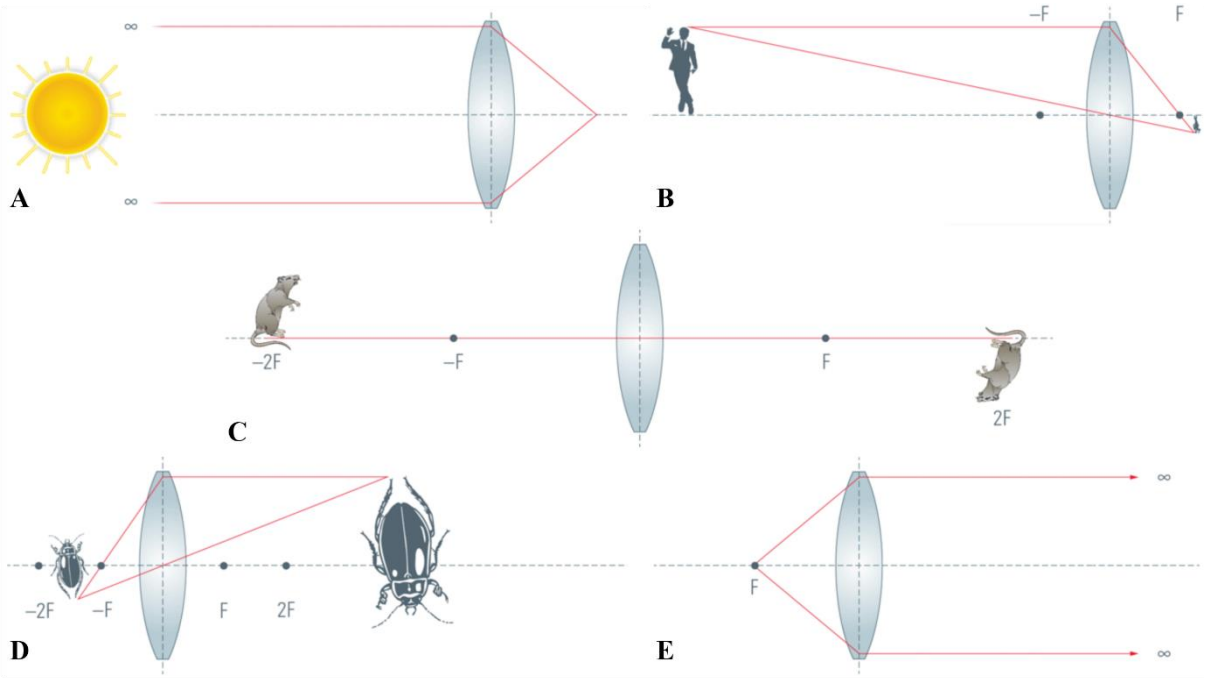

Figure 2.10: Depiction of an object by a converging lens. Description is given in the text. Figure adapted from Rühl, 2012 [180].

If the object can be regarded as infinitely far away, the incoming light is focused at the focal point, what – as described above – actually defines the focal point (Fig. 2.10A). If the distance from the lens is exceeding twice the focal length, it results in demagnification (Fig. 2.10B). For a distance of twice the focal length, the object is depicted in original size (Fig. 2.10C), while for a distance between the single and the double focal length, the object is imaged magnified (Fig. 2.10D), as it is the case for the objective lens in a microscope. Being situated at the focal

point, there is no image, since the beams are leaving the lens parallel to each other (Fig. 2.10E). However, since the eye lens is able to focus these beams again, projecting them on the retina, the object is indeed depicted magnified. These pictures (which could not be projected on a screen without additional lenses) are called “virtual images”, and such an image is produced by the eyepiece of a microscope, since the latter focuses on the intermediate image projected by the objective lens. Hence, a virtual image is – in opposite to a real image – finally not inverted. For even closer objects, the rays diverge, producing a virtual image in magnified expression behind the object [180]. Since the human eye lens is imaging upside down – being a converging lens – the image is projected right side up at the retina, but during image processing by the brain, retina images are inverted (since usually upside down), so microscopic pictures are perceived upside down. The schematic beam path is of an optical microscope is given in Fig. 2.11.

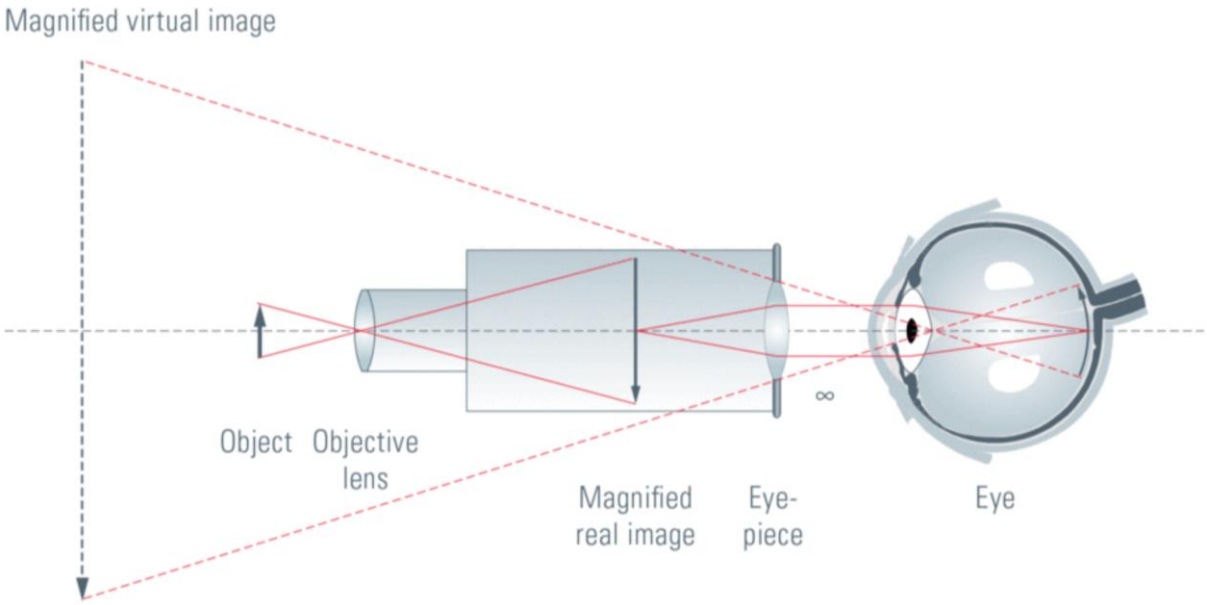

Figure 2.11: Schematic depiction of the light path within a microscope. The object is imaged by the objective lens in magnified expression within the focal length of the eyepiece. Hence, the object must be placed between the single and the double focal lens of the objective. The eyepiece is then producing a virtual image, depicted on the very left, which can only be seen with the help of the eye lens, focusing the parallel light beams on the retina. Figure adapted from Rühl, 2012 [180].

A light microscope comprises more than two lenses. On the one hand, the condenser consists of some, on the other hand, there are aberrations, also called imaging errors or imaging defects. To minimize those, several lenses are required, one principal converging lens and at least one (but mostly more) to compensate imaging errors. Since the schematic pictures above are idealized, they do not exhibit aberrations. Conversely, for real lenses, there are several.

A real lens does not exhibit the same optical power over its entire extend, which is neglected in schematic drawings by using a representative line. Instead, the optical power usually increases with the distance to the optical axis (symmetry axis of the system). Thus, there is not one focal point, but several, and a point source appears like a small circle. This lens defect is called spherical aberration. The same applies in principle for the different frequencies of white light, which are differently refracted due to the dispersion of the lens material, eventually resulting in a chromatic aberration (due to which different focal points emerge for different wavelength). If the object is not situated within the optical axis, the effective lens shape is not symmetric any more (resulting in the so-called sagittal and meridional planes), so the object (or light source) is projected distorted. This effect is called astigmatism, and together with the spherical aberration, it is also named “coma”, since circular light sources away from the optical axis exhibit kind of a tail like comets do. There are several more, and all these aberrations are corrected as much as possible in high-class microscopes by using lens systems that are more complex than just having two converging lenses [194].

Throughout this work, the employed kind of microscopy was fluorescence microscopy. (Although an additional light microscopy channel was provided, mounted in the classical way with a white light source situated below the sample, so light microscopy pictures could be recorded simultaneously.) Since there was no technique applied that enables to switch off the neighbored fluorescence sources and hence recording a single fluorescence emitter that is not affected by diffraction, the same laws in terms of resolution and magnification applied as described for the “normal” light microscope. A general difference in fluorescence microscopy is the necessity to illuminate the specimen, but to collect the fluorescence only. Therefore, a light source is required to excite of the fluorophores within the respective spectral region of absorption, which is not to be imaged, while a secondary light source, being the fluorophores, needs to be imaged. The setup which was utilized was an epifluorescence microscope, meaning that the excitation source, i.e., a laser in this case, is not situated below the sample, but takes the same way through the objective as the fluorescence signal does.

The advantage of the epifluorescence setup towards an excitation from below is that the excitation laser light is shining away from the detector. (Another one is that the excitation is focused on the currently imaged area by the objective lens, which avoids photo-bleaching of fluorophores that are not imaged in the respective moment.) Nevertheless, a part of the excitation light is reflected. For this reason, a sophisticated system of optical filters is required to provide that only the fluorescence emission reaches the detector, while the (laser) excitation light does not. Filters are more commonly used than monochromators to separate the excitation

wavelength (e.g., in the case of multi-line lasers). These filters do not necessarily prevent from characteristic Raman scattering peaks (see above, *Transmission & reflection*), e.g., originating from the solvent, so these peaks might need to be identified beforehand without fluorophore. Even though Raman scattering occurs seldom, it might become intense enough here, especially having weak fluorescence emitters, whose quantum yield (ratio of emitted to absorbed photons) is low [195]. The basic setup of an epifluorescence microscope is schematically shown in Fig. 2.12.

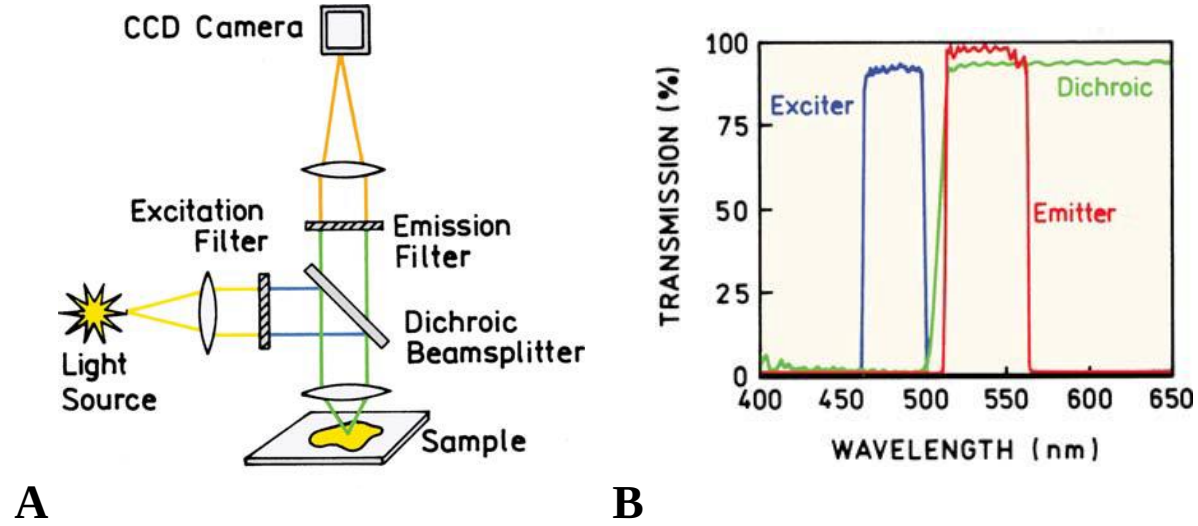

Figure 2.12: Basic epifluorescence microscope setup with principal filters. (A) The epifluorescence configuration utilizes a dichroic mirror to reflect the excitation light onto the specimen. For imaging, the excitation light is reflected away, while the fluorescence emission is transmitted. To ensure the selectivity, a band pass filter is mounted in front of the detector. The excitation filter is chosen with respect to the desired laser wavelength, if there are more than one available, or allows the transmission of certain wavelengths of a white-light source. (B) The transmission spectra of an exemplary combination of filters and the dichroic mirror is displayed. Figure adapted from Lakowicz, 2006 [195].

There are two major kinds of optical filters, the absorptive and the dichroic ones. The absorptive ones consist of stained glass, absorbing a certain wavelength range (and thus heat up). The dichroic filters are interference filters, utilizing the constructive interference of certain wavelengths and the destructive one of others. This is done by optical coatings, being thin films evaporated on top of a transmitting glass substrate. The same effect was described before in terms of structural coloration, e.g., having a soap bubble. Since at both interfaces light is partially reflected and transmitted, the concept works also for reflection, not only for transmission. Please note that the phase shift of 180 deg, which occurs for reflection at an interface, if the refractive index beyond is higher, might lead to inverse phase conditions for constructive and destructive interference, respectively. By choosing the material (and hence the

refractive index), the thickness, and the number of layers, optical properties can be designed as desired. In opposite to the absorptive filters, interference filters do not heat up [195].

Common filter types are short pass filters, which enable only wavelengths below a certain limit to pass, long pass filters, doing the same for wavelengths longer than the cut-off wavelength, band pass filters, allowing only a certain wavelength (range) to pass, and notch filters, which reject a certain wavelength (range). The dichroic mirror in Fig. 2.12 can therefore be regarded as long pass filter with a cut-off wavelength of around 500 nm. For certain properties, several filters might be used in combination. The passband of a band pass filter is tunable by changing the angle of incidence, albeit usually used at normal incidence.

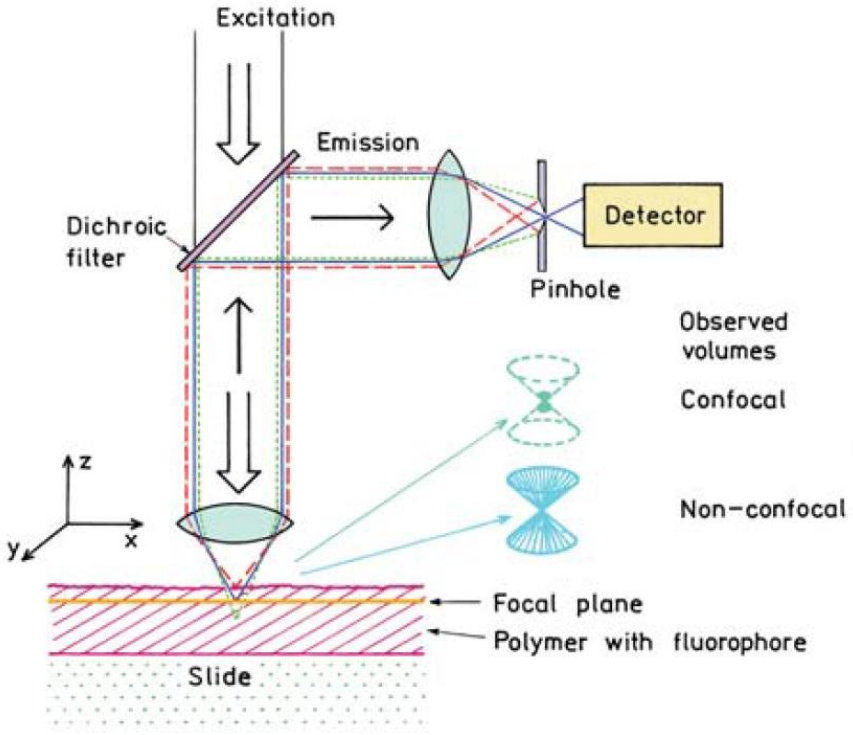

Figure 2.13: Schematics of a confocal epifluorescence microscope. The light paths of excitation and emission are inverse compared to Fig. 2.12. After reflection at the dichroic mirror, the emission is focused again by a converging lens. A pinhole is situated at the focal point, rejecting all the emission that is not originating of the respective focal plane within the sample, which is here again out of focus. Thus, only the emission emerging in the focal plane is imaged, not the entire emission induced by the excitation light cone. Figure adapted from Lakowicz, 2006 [195].

Neutral-density filters, used to attenuate the intensity independent from the wavelength (therefore *neutral*), follow a different working principle. Here, a thin metal film is deposited on the transmitting filter material, whereat the transmission intensity varies with the thickness of the film. It is usually indicated by the optical density OD (see above, *Absorption*), meaning that for an OD of 1 and 2, the transmittance is 10^{-1} and 10^{-2}, thus 10 % and 1 %, respectively. Due

to the low penetration depth of light impinging on metals, these layers need to be in range of tens of nanometers, while the interference filter thin films are rather in the range of hundreds of nanometers (therefore in the range visible wavelengths).

Having polarized light for excitation, it can also be excluded by a polarizer, since fluorescence is unpolarized. However, since the equally polarized component of the fluorescence is rejected along with, it goes along with signal intensity losses. Having polarized light, the intensity can be gradually attenuated by a polarizer as well, becoming lower the more the polarizer is adjusted to the respective other direction of polarization [195].

Having a confocal microscope, the light path situation in terms of excitation and emission is inverse (Fig. 2.13). Here, the dichroic mirror reflects the emission towards the detector, while the excitation beam is transmitted. Since the excitation light passes the objective, the sample is illuminated by a cone of light (more precisely a double cone, as the light is further passing the focal point), additionally providing the grazing angle illumination described by Abbe. The whole double cone volume is thereby excited. In a confocal microscope, the fluorescence signal is once more focused by a converging lens between the dichroic mirror and the detector, this time on a pinhole. The latter needs to be automatically adjusted with respect to the focal plane within the sample, providing that only the emission coming from the focal plane is passing the pinhole, while the emission originating from planes below or above exhibit a different focal length and therefore does not reach the detector. The resolution along the vertical axis is nevertheless lower than in horizontal direction, but reduces to approximately twice the excitation wavelength. This is especially essential if the fluorophores are concentrated in a certain sample location. Then, the ratio of fluorescence emission to undesired Raman scattering (emerging within the whole volume that is excited) is drastically improved [195].

Due to the focused excitation, the sample needs to be scanned row by row. If time-resolved measurements are performed, this is limiting in terms of temporal resolution. In comparison to the time it takes the laser beam to return to the respective area again, other effects are negligible. The increase of the scanning speed and thus temporal resolution correlates with a decrease of spatial resolution (since the laser speed is increased by dividing the specimen area in less pixels), and thus – dependent on the respective purpose – a compromise between spatial and temporal resolution needs to be found.

2.3 Dynamic light scattering

Dynamic light scattering (DLS) is employed to determine the size of small particles in solution. A notable limitation is that the particle is – due to the evaluation technique – assumed to be spherical.

In DLS, a laser shines light on a sample, which consists of solved or solubilized particles in a liquid, thereby causing light scattering. As described earlier (subchapter *Transmission & reflection*), having particles in the size range of (macro)molecules or colloids, this is Rayleigh scattering (and it results in the upper limit of this method, being around 250 nm), thus causing light reflections in all directions with equal distribution (implying spherical particles). Having a large number of scattering centers in a solution or suspension, the scattered light beams will interfere with each other. The usage of laser light, being monochromatic and coherent, simplifies the resulting interference patterns and therefore the evaluation, since the wavelength is unique and known (here, Raman scattering occurs too seldom to cause any problems). Due to the motion of the observed particles and consequently the scattering centers, which follow the Brownian motion, fluctuations of brightness will occur, since the interference pattern is permanently changing. By analyzing these fluctuations over time, conclusions about the particles' velocity can be obtained [196, 197]. For this purpose, a second order autocorrelation function ("self-correlation"; a function is correlated to itself at different points in time) is applied, described by eq. 2.54 [197].

$$g(\tau) = \frac{\langle I(t)\, I(t+\tau)\rangle}{\langle I(t)\rangle^2} \tag{2.54}$$

Here, g is the second order autocorrelation function, I(t) is the intensity at time t, and τ is the respective delay time with respect to which the correlation takes place.

If the correlation of the measured values between different points in time is not purely accidentally, the data points of the autocorrelation function are as well not randomly spread. Since the particles move, the similarity of the single functional values decreases with elapsed time, which occurs in an exponential manner. The smaller the particles are, the faster the correlation decreases due to quicker motion and the faster the resulting exponential function decays. For monodisperse particles (particles of the same size and shape), this function would be mono-exponential, and by fitting the autocorrelation function accordingly, the diffusion

coefficient D can be obtained, which is a measure of the particles' mobility, derived from the covered distance per time and hence from their velocity [196, 197].

For such a monodisperse sample, the correlation function can be fitted with eq. 2.55.

$$g(\tau) = B + \beta\, 10^{-2\Gamma\tau} \tag{2.55}$$

Here, B is the baseline value, hence the limit towards infinite decay times, β is the value for $\tau = 0$, and Γ is the decay rate. The latter is connected to the diffusion coefficient D via the magnitude of the scattering vector q, specifying the change of the wave vector of the incident light due to scattering.

$$\Gamma = |\vec{q}|^2 D = q^2 D \tag{2.56}$$

The scattering vector can be described by

$$q = \frac{4\pi n_s}{\lambda} \sin\left(\frac{\theta_q}{2}\right) . \tag{2.57}$$

The scattering angle θ_q is spanned between the light paths of the scattered light (in direction of the detector) and the excitation laser beam, and n_s is the refractive index of the solvent, which is preferably non-absorbing, so the refractive index is not complex [197].

The obtained diffusion coefficient can further be used to calculate the hydrodynamic radius r_h (also called Stokes radius), which indicates the radius of a hypothetical solid sphere that exhibits the same diffusion properties as the investigated particle. The related equation is the Stokes-Einstein equation [197].

$$r_h = \frac{k_B T}{6\pi\eta D} \tag{2.58}$$

Here, k_B is the Boltzmann constant ($k_B = 1.38 \times 10^{-23}$ J/K [132]), T is the temperature, and η is the viscosity of the liquid.

For monodisperse, spherical (therefore isotropic) particles, the determination of the radius is straightforward, angle-independent and of high accuracy. For anisotropic particles (being of any shape except from a sphere), the approach implies deviations from the real size already from the beginning. In this case, the correlation is not angle-independent, and an optimum needs to be found. If a high-quality analysis is desired, several determinations at different angles of incidence need to be performed [196].

Having a solution or suspension of polydisperse particles, the fitting function is the superposition of several mono-exponential decay functions, each corresponding to a certain particle size, and the result is a particle size distribution. If necessary, the fitting function needs be found by numerical approximations. Multi-angle DLS is strongly required, since for some angles, large scattering intensities of one class of particle sizes will outplay others, and vice versa.

There are several obstacles which impede accurate DLS measurements. Multiple scattering must be avoided, which limits DLS to low concentrations, especially for larger particles or particle mixtures that exhibit larger differences in terms of their refractive indices. The diffusion might be hindered by collisions (also resulting in the necessity of applying low concentrations) or electrostatic attraction (whereas the latter can be suppressed by salt addition). Aggregation of particles would lead to a wrong size estimation, since many particles are observed as one, while preventing (or necessary) detergent micelles are measured as part of the particle, moreover affecting the overall refractive index [196]. To overcome these difficulties, there are many sophisticated techniques, but within this work, only rough estimations were performed, later supported by the results of other kinds of measurements.

2.4 Ultraviolet/visible spectroscopy & Michaelis-Menten kinetics

UV/Vis spectroscopy (UV/Vis) is a standard tool to determine the concentration of chemical species in solution based on their absorption, thereby employing the visible and ultraviolet (and possibly the very near infrared) spectral region. Since absorption is difficult to determine itself, a UV/Vis spectro(photo)meter detects the transmission and calculates the absorption by comparison with the irradiated light intensity. The physics of attenuated waves, absorption and transmission is discussed above within the *Fundamentals of light* section, but briefly summarized, light intensity is decreasing exponentially due to absorption, in this case of visible or near ultraviolet radiation, which interacts with the valence electrons of atoms and molecules. To yield a linear proportionality towards the concentration, the negative decadic logarithm is applied to the transmittance value, leading to the Beer-Lambert law, revisited from eq. 2.30 & 2.31 [134].

$$A = -\log(T) = -\log\left(\frac{I}{I_0}\right) = \varepsilon c l \tag{2.59}$$

The path length *l* is usually normed to 1 cm, and in cm it is applied in contrast to normal SI standards. The proportionality constant, being the extinction coefficient ε, is material-dependent and dispersive, thus changes with frequency. Differences in terms of small shifts (approximately ± 2-3 nm) can occur, e.g., in response of the solvent; then the peak value is to prefer over the accurate wavelength indication given by extinction coefficient tables, so the peak value of ε is to apply to the peak value of A. Non-target absorbances and differences in the light paths, if employing a multiple beam path spectrometer, are subtracted by reference and baseline measurements, respectively.

For larger particles, scattering becomes a notable hindrance. Then, as mentioned before, absorption is no longer the only source of extinction, and being accurate, the term absorbance would no longer hold true. However, practically these terms are used synonymously. For Rayleigh scattering at small molecules as discussed in terms of sky coloration for the earth's atmosphere, the path length is too short to obtain remarkable influences. Nevertheless, for bigger particles (e.g., colloids), Rayleigh scattering may contribute notably to the extinction, being more pronounced the shorter the wavelength. By Rayleigh and – having even bigger particles – Mie scattering, the applicability of UV/Vis spectroscopy is finally limited in terms of particle size. This theoretical description is given rather with respect to the practical use in terms of concentration determinations of biological samples (e.g., proteins), usually exploiting comprised chromophoric molecules, or comparative scattering analyses using reference particles. For a deeper discourse, which might include the assignment of molecular band transitions to spectral regions or a sound knowledge concerning elementary organic bond absorption, taking place in the far and vacuum UV region, see, for example, Gauglitz & Vo-Dinh, 2005 [134].

Another purpose of using UV/Vis spectroscopy within this work was the determination of kinetic constants via the concept of Michaelis-Menten kinetics, so this is briefly discussed in the following.

The Michaelis-Menten theory is used to determine kinetic constants, like the substrate affinity and the maximum possible turnover value of enzymes, deduced from their initial reaction rates at different substrate concentrations. It is crucial for comprehension that the initial reaction rate of an enzyme is decreasing at lower substrate concentrations, and the maximum possible reaction rate might be drastically undercut [16].

An enzymatic reaction can be divided in the following steps: A substrate is bound by an enzyme, together forming an enzyme-substrate complex, followed by the formation of the product,

resulting in an enzyme-product complex, and finally the release of the product. To every step, kinetic constants in forward and backward direction can be assigned.

$$E + S \underset{k'_1}{\overset{k_1}{\rightleftharpoons}} ES \underset{k'_2}{\overset{k_2}{\rightleftharpoons}} EP \underset{k'_3}{\overset{k_3}{\rightleftharpoons}} E + P \tag{2.60}$$

Here, E is the enzyme, S is the substrate, ES is the enzyme-substrate complex, EP is the enzyme-product complex, P is the product, and the k values are the reaction rate constants [16].

The reaction rate constants k assign the reaction rates of forward and reverse reaction to the concentrations of the involved reactants, including the concentrations of the products, being the reactants of the back reaction. Once an equilibrium is reached, back and forward reactions still occur permanently, but with the same rate, so no net concentration changes occur anymore. A simple equilibrium reaction would be

$$xA + yB \leftrightarrow zC + D \ . \tag{2.61}$$

At equilibrium, this results in the following equation:

$$k_f\,[A]^x\,[B]^y = k_r\,[C]^z\,[D] \tag{2.62}$$

Here, A is a chemical species, [A] is the concentration of A, also often denoted as c(A), and so it is for B, C, and D; x, y, z are the stoichiometric numbers, and k_f and k_r are the rate constants for the forward and the reverse reaction, respectively. The reaction rate constant for the forward reaction is also often denoted with k_+ or just k, then the reverse reaction is indicated as k_- or k', respectively. The chemical equilibrium of a reaction is described by the law of mass action, specifying the ratio of reactants and products at this point:

$$K = \frac{[C]^z\,[D]}{[A]^x\,[B]^y} = \frac{k_f}{k_r} \tag{2.63}$$

K is therefore called equilibrium constant [198].

In this case, a simplification was applied by setting stoichiometric numbers instead of activities as exponents (the chemical activity includes the differences between ideal and real solutions, so the activity can be imagined as effective concentration, deduced from the chemical potential of the respective chemical species), since for the given case of enzymatic reactions, it holds approximately true.

Considering the major principle that a system aspires to its lowest-energy state, the concept of an equilibrium reaction seems to be unlikely, since often a lower energy is assigned to one or

the other species of a reactant-product pair, but it can be easily explained by the course of Gibbs free energy (same as free enthalpy) of an equilibrium reaction, which includes also the concentrations of each species of a reactant-product pair. The latter is not equaling the energy of a system directly, but it can be seen as a measure of driving force, and the system will aspire to the state of its lowest Gibbs free energy value. This is illustrated for an equilibrium reaction by Fig. 2.14 [198].

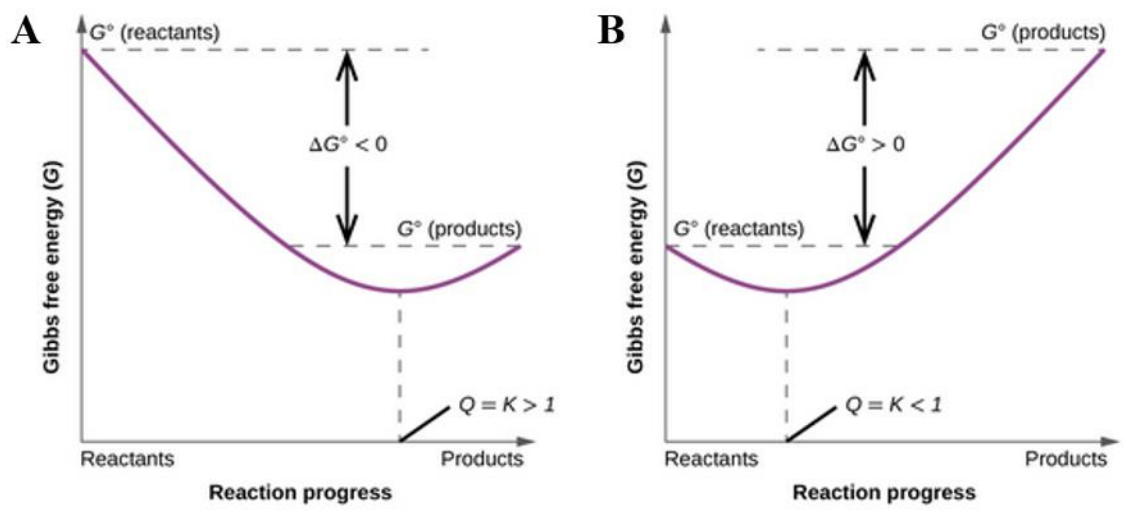

Figure 2.14: Description of the chemical equilibrium in terms of Gibbs free energy. (A) Exergonic reaction. (B) Endergonic reaction. Explanation is given in the text. Figure adapted from Petrucci *et al.*, 2016 [198].

The law of mass action can be directly contextualized with ΔG via

$$K° = e^{-\frac{\Delta G_m^\circ}{RT}} , \tag{2.64}$$

where K° and G° are the respective values of K and G at standard conditions (temperature: T = 273.15 K = 0 °C, pressure: p = 1013.25 hPa, activity of all species: a = 1), and G_m is the molar free energy, which is the Gibbs free energy divided by the amount of substance, so ΔG_m° is the molar Gibbs free energy at standard conditions [198]. Further discussion, such as the temperature dependence of rate constants given by the Arrhenius equation, are considered as too digressive.

The kinetic description of enzymatic reactions by the Michaelis-Menten theory implements a few simplifications, reducing the six rate constants to only three. First, the intermediate step of the enzyme-product complex was not taken into account, since for the overall process of generating a (free) product, it is not of importance whether the product is formed quickly and slowly released afterwards, or if it is formed slowly and then released instantly. Second, the

reverse reaction of P to ES was considered to be negligible, what is only valid if a vast amount of energy is released ($\Delta G << 0$), but then it would be no equilibrium reaction anymore, and moreover it is not the case in biological systems, or if the product concentration is very low compared to the substrate concentration ([P] << [S]). Since in measurements following the Michaelis-Menten concept only the initial moments of a reaction are observed (not the equilibrium state), the reaction products are indeed still present at very low concentrations compared to the substrates, hence the latter is justified. The remaining is comprised by eq. 2.65 [16].

$$E + S \underset{k_r}{\overset{k_f}{\rightleftharpoons}} ES \xrightarrow{k_{cat}} E + P \tag{2.65}$$

Here, k_f and k_r are commonly used for substrate binding and unreacted dissociation, while the third constant is specified with k_{cat}, being the maximum catalytic activity. Applying the maximum catalytic activity to eq. 2.65 implies that the turnover in any case occurs at the same rate. Further, lower concentrations are turned over more slowly, since the collision frequency of substrate and enzyme is lower. At the equilibrium state, the reverse reaction rate is no more negligible (hence the concept does not apply anymore), but equals the forward reaction rate. No more net turnover is possible. The emergence of notable reverse reactions is known as product inhibition, which can only be overcome by further reaction or transport of the product [16].

In a further step, the enzyme concentration is set to be constant (which follows the enzyme definition, according to which it works as a catalyst, being unaffected by the reaction) and much smaller than the substrate concentration. Both is usually the case. On these conditions, the Michaelis-Menten equation can be inferred of four differential equations that are directly derived from the law of mass action, which was modified by G. E. Briggs and J. B. S. Haldane [199], being

$$v_0 = \frac{d[P]}{dt} = \frac{v_{Max}\,[S]}{K_M + [S]}\ . \tag{2.66}$$

Here, v_0 is the initial reaction rate, v_{Max} is the maximum reaction rate (of all participating enzymes, see below), [S] is the substrate concentration and K_M is the Michaelis-Menten constant [16]. The Michaelis-Menten constant K_M calculates by means of the above-mentioned rate constants.

$$K_M = \frac{k_r + k_{cat}}{k_f} \tag{2.67}$$

It is widely used as a measure of the substrate affinity (the lower K_M, the higher the substrate affinity of an enzyme), being the concentration at which the initial reaction rate (v_0) is half the maximum reaction rate (v_{Max}). The maximum reaction rate (performed by all enzymes included in a reaction) can be correlated with the maximum catalytic activity of a single enzyme via division by the enzyme concentration.

$$k_{cat} = \frac{v_{Max}}{[E]} \tag{2.68}$$

k_{cat}, the maximum catalytic activity, is also called only catalytic activity or turnover number [16].

Sometimes, the enzyme efficiency is quantified by the ratio of k_{cat} to K_M. For the most efficient enzymes (e.g., fumarase), exhibiting values between 10^8 and 10^9, the reaction can be considered as diffusion-limited. The ratio is also known as specificity constant, especially when comparing different substrates. The higher this value, the more one substrate is preferred over the others [200]. It is not unusual in practice that also enzymes exhibiting a higher reaction order, hence possibly converting more than one substrate into more than one product, or performing additional activities that are coupled to the reaction (e.g., proton pumping, as discussed repeatedly in Chapter 1), are characterized in terms of Michaelis-Menten kinetics nonetheless. For examples, see Witt *et al.*, 1995 [57], or Czapla *et al.*, 2012 [201].

2.5 Infrared absorption spectroscopy

In the following section, the field of infrared absorption is discussed stepwise towards the utilized technical combination, which would be overall abbreviated tr-FT-ATR-SEIRAS, meaning time-resolved Fourier transform attenuated total reflection surface-enhanced infrared absorption spectroscopy. Throughout the text, the respective commonly used abbreviations, being FTIR, ATR-SEIRAS, and tr-SEIRAS, are used.

2.5.1 Molecular vibrations

As described before, the absorption of electromagnetic waves is due to the excitation of certain quantum transitions. For UV/Vis, that concerns the outer electrons. Infrared (IR) radiation causes molecular rotations and vibrations. Hence, IR spectroscopy is sometimes referred to as

vibrational spectroscopy. The range is divided in near (λ = 1-2.5 µm), mid (λ = 2.5-25 µm), and far (λ = 25-250 µm) infrared, abbreviated NIR, MIR, and FIR, respectively. In contrast to UV/Vis spectroscopy, in IR spectroscopy the wavelength is commonly replaced by the wavenumber (not to confuse with the angular wavenumber, used, e.g., in eq. 2.2 & 2.8), being the number of waves per meter, but in spectroscopy commonly per centimeter. The subdivisions are then defined as FIR = 40-400 cm^{-1}, MIR = 400-4,000 cm^{-1}, and NIR = 4,000-10,000 cm^{-1}. If FIR radiation is absorbed, relatively weak bonds like hydrogen bonds start to vibrate, and so do heavy atoms. In the MIR region, stretching and bending transitions within a molecule are excited (fundamental modes), and in the NIR range, overtone vibrations can be observed. In addition, combinations of MIR transitions can be excited [202, 203].

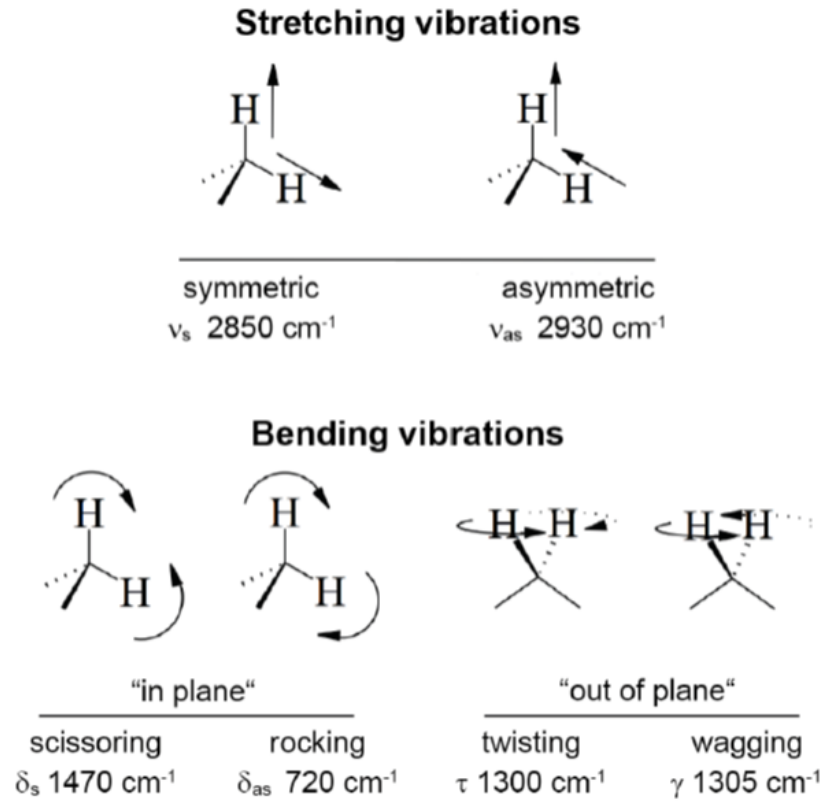

Figure 2.15: Vibrational modes of a methylene bridge. Stretching and bending of bonds cause a displacement of atoms and might also alter the angle in between, the bond length, and the relative position to each other. Figure adapted from Schwaighofer, 2013 [138].

The number of possible rotational and vibrational modes can be deduced regarding the degrees of motional freedom. Since there are three directions in space, a molecule consisting of N atoms has 3N of degrees of motional freedom. Three of them describe the motion of all atoms in one of the three translational directions, while another three are the rotations of the whole molecule around one of the three principal axes. For vibrational movements, 3N-6 possibilities exist due

to superposition of single vibrations that change bond lengths and/or angles in between them [202, 203]. The possibilities of vibrational motion are summarized in Fig. 2.28.

Hooke's law describes the energy of vibrational states, deduced from the harmonic oscillator model.

$$V_{iv} = h\nu_i \left(v_i + \frac{1}{2}\right) \tag{2.69}$$

Here, V_{iv} is the vibrational energy state, h is Planck's constant (see eq. 2.1), ν_i is the fundamental frequency, and v_i is the vibrational quantum number of the i^{th} mode. Harmonic modes of vibration allow only values of v_i of +1 and -1, but due to combinations and the occurrence of overtones, the vibrations are better described by non-harmonic Morse-type potential function [202], which is considered as beyond the scope of this work. Analog to the formerly described absorption of visible light, which occurs if an outer electron is energetically lifted to an excited state, infrared radiation is absorbed by a molecule, if the molecule (or the residue of a molecule) is energetically lifted to the next higher vibrational state, usually from the ground state to the first vibrationally excited state. The relevant criterion of a molecule (or residue) to be infrared active is – described by selection rules of quantum mechanics – that the dipole moment (μ) is changing along the normal coordinate (q), described by eq. 2.70.

$$\left(\frac{\partial \mu}{\partial q}\right)_0 \neq 0 \tag{2.70}$$

The exact amount of excitation energy needed – leading to an absorption peak within a spectrum of continuous infrared illumination – is not only depending on the involved mass and the bond type, but is moreover based on electron donation to and acceptance from the surrounding, respectively, and vibrational coupling. Nevertheless, for an approximation, the first ones are sufficient to know [204].

Infrared absorption can be appropriately supplied by Raman spectroscopy, where the polarizability (α) change along the normal coordinate is observed, described by eq. 2.71.

$$\left(\frac{\partial \alpha}{\partial q}\right)_0 \neq 0 \tag{2.71}$$

Raman spectroscopy is based on inelastic scattering, at which the emitted wave does not equal the incoming one in energy, as it would be the case having Rayleigh scattering (see above, *Transmission & reflection*). In Raman spectroscopy, molecules are excited – usually by a

monochromatic laser in the region of NIR, VIS, or near UV – and thus lifted to a virtual state energetically higher than the ground and the first vibrational state, from which they fall back immediately. In the majority of cases, they fall back to the ground state again, thus are scattered elastically. In seldom cases, the energy amount that is set free is smaller than the absorbed one; the scattering is inelastic. Hence, a certain amount of energy remains within the molecule, causing vibration. Inelastic scattering is also referred to as Raman scattering. It causes the respective molecule to indirectly reach the first vibrationally excited state, what would be possible directly using infrared excitation. Conversely, vibrating molecules that are excited might fall back to the ground state, so the energy release is larger compared to the excitation energy. These two sub-processes are called Stokes and anti-Stokes scattering, respectively [202, 203]. Both are depicted in Fig. 2.16.

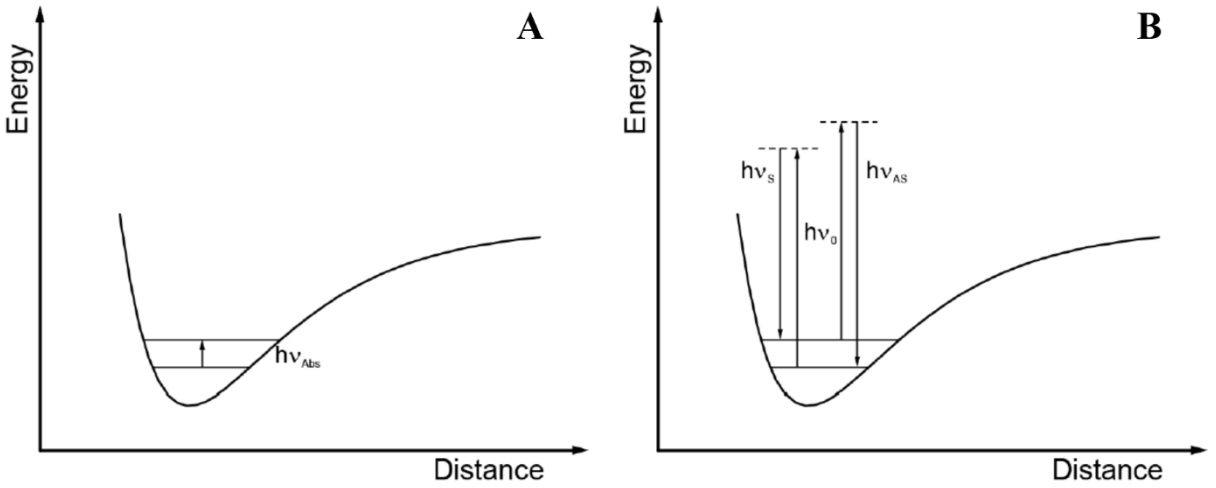

Figure 2.16: Direct and indirect excitation of the first vibrationally excited state. Infrared absorption (A), being the direct way of excitation, is depicted in comparison to the indirect way via the rarely occurring Stokes and anti-Stokes scattering (B). Abbreviations: $h\nu_{Abs}$: energy difference between ground and first excited vibrational state; $h\nu_0$: energy difference to the virtual state; $h\nu_S$: energy amount released during Stokes scattering; $h\nu_{AS}$: energy amount released via anti-Stokes scattering. Figure adapted from Schwaighofer, 2013 [138].

2.5.2 Fourier transform infrared absorption spectroscopy

In opposite to UV/Vis spectroscopy, IR spectroscopy is not performed by using a grating or prism to obtain single wavelengths of a broad-band source, which are scanned for absorption one by one. That is because the infrared region is way larger than the UV/Vis region, so the spectrum acquisition would take too long. (And wavelength separation behind the sample, which enables to record all wavelengths simultaneously, would not result in a sufficient spectral resolution assuming reasonable device dimensions.) Besides time-consuming, the samples

would heat up strongly. Sensitive samples could be damaged, and in case of proteins, denaturation might occur. Recent setups are thus based on the interferometer, conceived at the end of the 19th century by Michelson [205], which is schematically presented in Fig. 2.17.

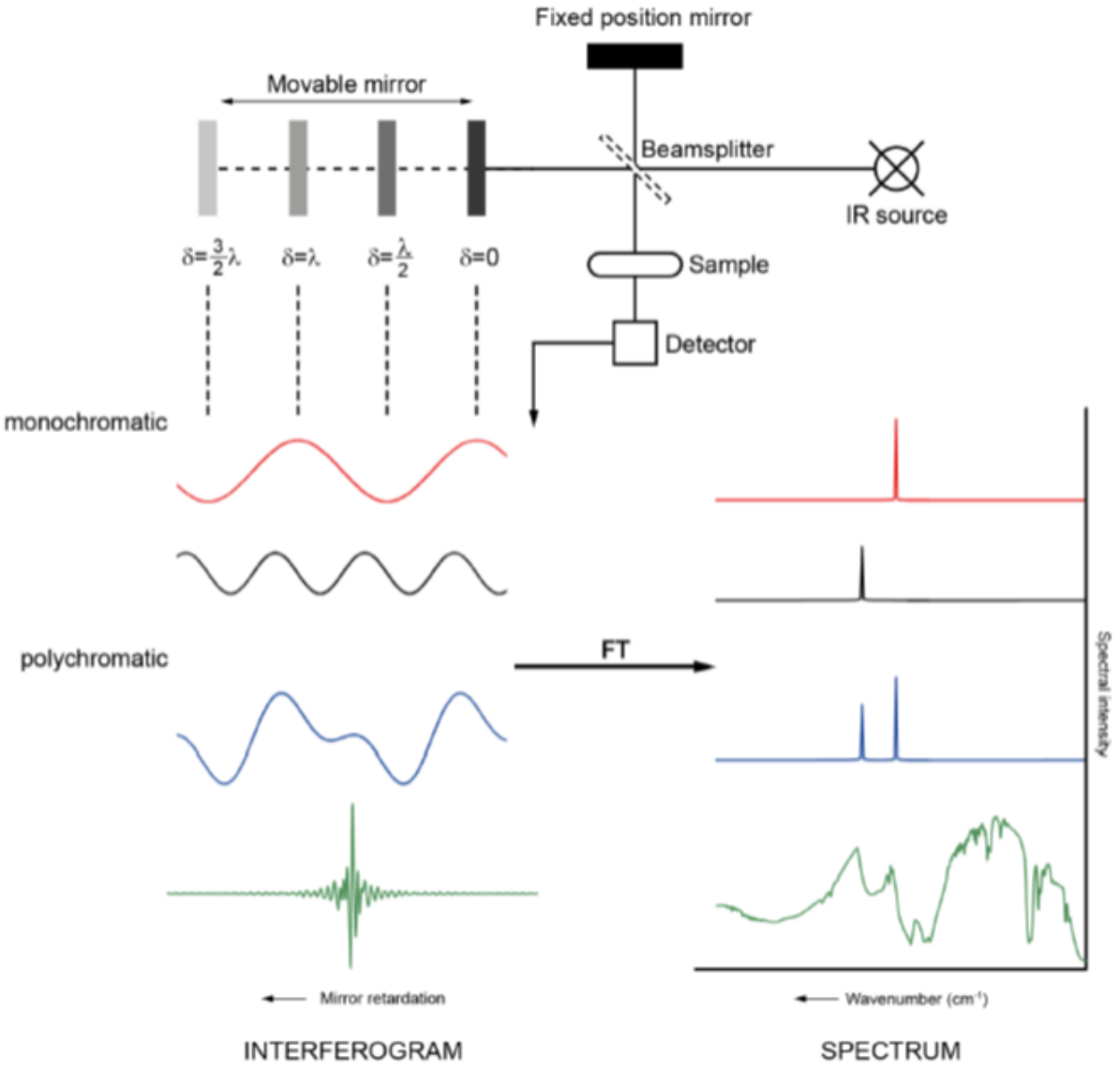

Figure 2.17: Working principle of an interferometer. The Michelson-interferometer (top) is described within the text. Moreover, exemplary interferograms (bottom left) and the resulting spectra, obtained by Fourier transform (bottom right), are shown. Figures adapted from Schwaighofer, 2013 [138].

The Michelson-interferometer consists of a source, i.e., an IR source in this case, a beam splitter, dividing the radiation in two parts (each 50 %), a movable mirror in-line with the source reflecting the transmitted share of the IR radiation, and a fixed one perpendicular to the optical axis, reflecting the reflected share. On the fourth side, the radiation passes through the sample and subsequently reaches a detector. Due to the beam reflection at the moveable mirror, mostly adjusted via a piezo element, different interference patterns emerge for different retardation

lengths. The latter, indicated with δ in Fig. 2.17, is the distance from the closest possible (δ = 0) to the actual position of the moveable mirror and back. If the dimensions of the light path exceed the coherence length of the excitation beam, a correction plate can be additionally mounted on top of the beam splitter [206].

The interferogram can be converted into a spectrum again by Fourier transform. Since the fast Fourier transform, which reuses preliminary results and thereby saves time, was rediscovered and further developed to the recently best-known algorithm as late as 1965 by Cooley & Tukey [207], the usage of this method in infrared absorption spectroscopy is way more recent than the invention of the interferometer itself.

Using monochromatic light, the interferogram can be described as a single cosine function (see red and black line in Fig 2.17), while polychromatic light (blue line for two, green line – as typical interferogram – for plenty of wavenumbers), provided by a continuous light source, can be expressed as sum of cosine waves, each assigned to a single wavenumber. Therefore, the spectrum can be recovered again using the following function describing the brightness B as function of the retardation length δ, while the intensity I appears as a function of the frequency ν [206].

$$B(\delta) = \int_0^{\infty} I(\nu) \cos(2\pi\delta\nu)\, d\nu \tag{2.72}$$

For a retardation length of zero, all interferences are constructive, which is called center burst, describing the maximum intensity. To obtain the IR spectrum in usual presentation, assigning the absorbance to the wavenumber, the intensity is obtained by using eq. 2.73., deduced from eq. 2.72. The frequency can then be replaced by the wavenumber by using eq. 2.2 and subsequent conversion of the wavelength into the wavenumber, the latter being the reciprocal of the wavelength [206].

$$I(\nu) = \int_{-\infty}^{+\infty} B(\delta) \cos(2\pi\delta\nu)\, d\delta \tag{2.73}$$

After doing so for sample and reference, the reference-corrected absorbance calculates according to eq. 2.74.

$$A = -\log\left(\frac{I_{Sample}}{I_{Reference}}\right) \tag{2.74}$$

Applying this procedure, abbreviated FTIR for Fourier transform infrared (absorption spectroscopy), the sample acquisition can be performed way faster by simultaneously

measuring all wavenumbers, circumventing the above-described disadvantages. It is called the Fellgett or multiplex advantage. Moreover, known as Jacquinot or throughput advantage, the otherwise resolution-defining slit is not necessary, allowing the use of a higher radiation power that results in a better signal-to-noise ratio. A third one is the Connes or calibration advantage: If a laser continuously determines the exact mirror position – resulting in a highly precise wavenumber assignment – plenty of measurements can be reliably correlated and averaged to one spectrum, improving the signal-to-noise ratio even more, still in a rapid manner [206, 208, 209].

2.5.3 Attenuated total reflection infrared absorption spectroscopy

The principle of total (internal) reflection, leading to the phenomenon of attenuated total reflection (ATR), is described above in the subchapter *Total reflection and the evanescent wave*, so it is only briefly repeated: If an electromagnetic wave (i.e., IR radiation in this case) is impinging on an interface to a less refractive medium under an angle greater than the critical angle, an evanescent field emerges behind the interface, decaying in close vicinity to the latter. The penetration depth can be calculated according to eq. 2.38. If no interaction occurs, the irradiated power is completely transferred back to the totally reflected beam. Conversely, if interaction occurs, such as infrared absorption, energy is transferred and thus lacking within the reflected beam, which is then attenuated. Out of the reflected light, information about the occurred absorption can be obtained, as well qualitatively as quantitatively.

ATR-IR was firstly described in 1960 and 1961 by Harrick and Fahrenfort, respectively [173, 210]. Utilizing attenuated total reflection, IR spectroscopy is no longer confined to liquid samples, but becomes capable of sampling high concentrations (not sufficiently transmitting anymore) and insoluble or solid analytes as well as specimens that are bound to a surface (possibly providing surface-enhancement). ATR-IR has become the major IR technique in several fields, e.g., in surface chemistry [169]. For comparability with old IR spectroscopy databases, special ATR correction algorithms are required, since the positions of the band maxima are indeed identical, but smaller wavenumbers produce broader and more intensive peaks due to the wavenumber-dependent penetration depth (see eq. 2.38). Hence, having smaller wavenumbers, the absorbance is higher in comparison, since the evanescent field interacts with a greater sample volume. More complex correction algorithms also include the refractive index of the ATR crystal and the angle of incidence, which are influencing the band intensities as well via the penetration depth [211].

Usually, the IR beam is reflected multiply within the mostly trapezoidal ATR element. The number of reflections (N) is thereby directly proportional to the length (l) and inversely proportional to the thickness (t) of the crystal.

$$N = \frac{l}{t} \cot \theta_i \tag{2.75}$$

For a given ATR element, the number of reflections can be increased by increasing the angle of incidence. On the one hand, a larger number of reflections causes increased absorption, on the other hand, the absorption at each single reflection site is lowered, since the penetration depth decreases for increasing angles of incidence. If critical, the optimum needs to be found.

The ATR crystal needs to be chosen with respect to the given conditions. It should be hard, so that the sample can be applied firmly pressed to achieve good contact. Moreover, it should be inert and have no infrared absorption bands itself. The inertness must be especially given towards the solvent, and obviously, the crystal's material needs to be insoluble towards the solvent. It must be as transmitting as possible to not lose intensity, and the refractive index must be higher than the one of the sample. Moreover, the better matching the refractive indices are, the higher is the resulting penetration depth (also deducible from eq. 2.38) [169, 172]. If desired, the surface can be functionalized, e.g., with regard to immobilize proteins. If so, the material must be chosen with respect to the desired modification (albeit usually not the ATR element itself is functionalized, but a slide on top; nevertheless, slide and ATR element should be of the same material.) The most common materials are summarized in Table 2.1. Within the thesis, only quartz glass was used.

Table 2.1: Common materials of ATR elements. Table adapted from Schwaighofer, 2013 [138].

Material	Usable range (cm^{-1})	Refractive index	Comments
SiO_2 / Quartz	55,000 – 4,000	1.43	Hard and inert
Al_2O_3 / β-alumina	55,000 – 1,800	1.7	Very hard and inert
BaF_2	50,000 – 840	1.45	Water soluble
CaF_2	50,000 – 1140	1.41	Slightly soluble in water
$C_{diamond}$	45,000 – 2,500 1,650 – 200	2.4	Very hard
ZnSe	20,000 – 500	2.4	Toxic in contact with acids
Si	8300 – 660	3.5	Hard
Ge	5,500 – 600	4.0	Insoluble in water
TlBr-TlI / KRS-5	20,000 – 250	2.4	Toxic, soft

2.5.4 Surface-enhanced infrared absorption spectroscopy

To enhance the absorption up to 1000-fold, surface-mediated enhancement effects can be utilized [202]. This technique is called surface-enhanced infrared absorption spectroscopy (SEIRAS). The morphology of such a surface, usually being a metallic thin film structured with nanoparticles, strongly influences the enhancement factor. Two mechanisms have been revealed to be causal for the enhancement effect, a chemical one and an electromagnetic one. The chemical one is still rather unsolved, but also found to be not that crucial for the enhancement. Charge oscillations between the molecular orbitals and the surface electrons are held responsible for this rather subordinate effect [212, 213].

The chemical effect is surpassed by far by the electromagnetic one, which can be well explained with localized surface plasmons (LSPs). Ellipsoid islands that are way smaller than the wavelength of the impinging radiation and closely beside each other have been reported to cause the largest enhancement factors [214, 215]. The electric field of incoming infrared radiation with its amplitude E_{IR} induces a dipole moment p within the nanoparticles, which is linearly proportional the polarizability α and the volume V of the spheroid [212, 215].

$$p = \alpha V E_{IR} \tag{2.76}$$

The induced dipole generates an electric field in close proximity of the particle, whose amplitude is

$$E_{localized} = \frac{2p}{l^3} \ . \tag{2.77}$$

With the third power of the distance l in the denominator, the field turns out to be strongly localized [212, 215]. Since the LSP-generated localized electric field is oriented perpendicular to the surface, only the vibrational components exhibiting their dipole changes perpendicular to the surface are enhanced. (Fig. 2.18) [213].

The physics behind LSPs is an extensive topic by itself, but the fundamentals of (resonant) surface plasmon excitation are discussed in the following subchapter *Surface plasmon resonance spectroscopy*.

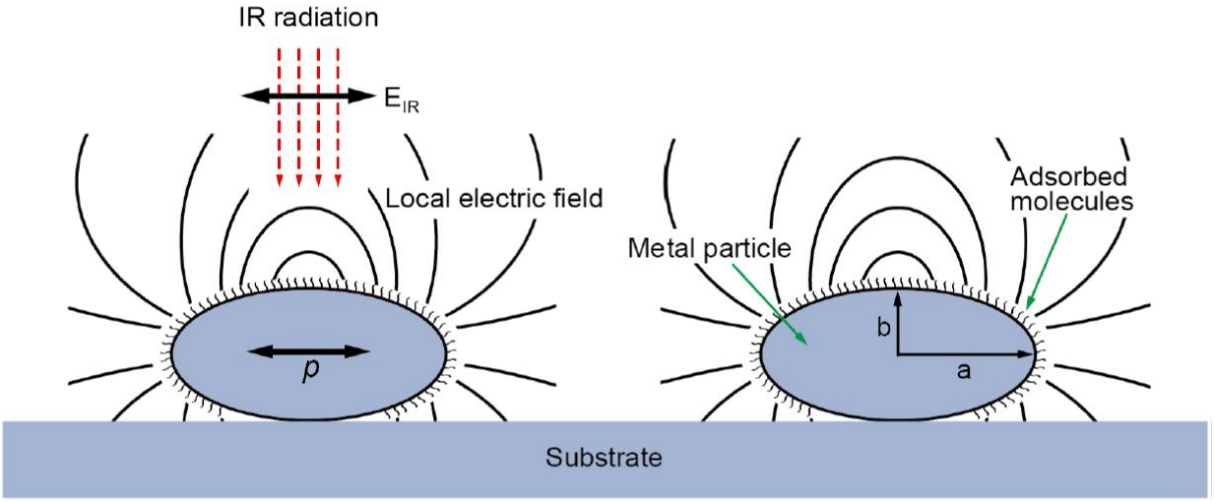

Figure 2.18: Electric field caused by localized surface plasmons. Description is given in the text. Figure adapted from Schwaighofer, 2013 [138].

2.5.5 Time-resolved infrared absorption spectroscopy

Changes in dynamic systems, such as changes due to redox reactions, which are associated with modifications of IR-relevant groups, can be resolved temporally by successive acquisition of spectra, resulting in time-resolved (abbreviated with the prefix tr-) measurements, predominately either performed by the rapid-scan or the step-scan technique.

The rapid-scan approach is based on normal spectra acquisition, done successively over a certain period. Usually, an entire interferogram is taken during one cycle of the moveable mirror. Afterwards, the next cycle is measured, representing the second point in time. In this approach, the velocity of the mirror is significant in terms of temporal resolution, governed by mechanical limitations. A conventional tr-IR spectrometer is capable of the acquisition of 25 spectra per second, yielding a temporal resolution of 40 ms [202]. In 1999, the conventional rapid-scan setup was outreached by the so-called cube corner retroreflector that replaces the translational optical element by a rotating one. Here, a better temporal resolution of up to 166 spectra per second can be achieved, corresponding to approximately 6 ms [216]. A striking advantage towards the step-scan setup is the possibility to measure irreversible processes [202, 217].

The approach used here was the step-scan technique. It reduces the mirror motion to a minimum by acquiring all spectra assigned to one retardation length over the desired period, before changing δ and proceeding with all spectra of the second mirror position. That allows for way higher temporal resolution – being in the range of nanoseconds – but, on the other hand, the

step-scan approach can be utilized for reversible reactions only. If this is provided, only the speed and sensitivity of the detectors, the related instruments, and the memory of the FTIR element are limiting [202, 217].

2.5.6 Infrared absorption spectroscopy of proteins

Structural information of proteins can be obtained well by IR spectroscopy due to the highly IR active peptide bond, which connects one amino acid to the next, thereby forming the peptide backbone [204]. By replacing the C_α-atoms of a dipeptide with terminating methyl groups, N-methylacetamide is obtained (Fig. 2.19). The relatively big methyl group in comparison to possibly terminating hydrogens is necessary to provide the same chemical morphology as found in proteins, requiring a trans-N-methylacetamide instead of a cis-configured one. Several possible vibrational interactions of this molecule can be assigned to IR-spectroscopic bands, and moreover, having a polypeptide, these can be further interpreted, yielding information about the infrared absorption behavior of secondary structures, which constrains the vibrational freedom of single bonds differently.

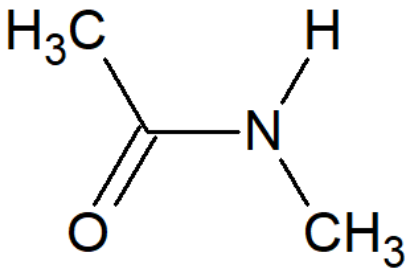

Figure 2.19: N-methylacetamide. The depicted molecule represents a peptide bond, terminated with methyl groups at the positions where usually the C_α-atoms are situated in a protein.

Table 2.2: IR absorption bands caused by the peptide bond. Table adapted from Schwaighofer, 2013 [138].

Designation	Approximate frequency (cm^{-1})	Nature of vibration
A	3300	N–H stretching, in resonance with overtone (2x amide II)
B	3100	
I	1650	80 % C=O stretching, 10 % C–N stretching, 10 % N–H bending
II	1550	60 % N–H bending, 40 % C–N stretching
III	1300	30 % C–N stretching, 30 % N–H bending, 10 % C=O stretching, 10 % O=C–N bending, 20 % other
IV	625	40 % O=C–N bending, 60 % other
V	725	N–H bending
VI	600	C=O bending
VII	200	C–N torsion

The nine IR band positions assigned to the peptide (synonymous to amide) bond are summarized in Table 2.2 [218]. Of major importance concerning the determination of secondary structures is band I, which might be either compared to structurally well-known proteins using special pattern-recognition calculations or fitted with component bands [218]. To identify the respective band components, band narrowing can be performed with the help of first-derivative spectra or Fourier-self deconvolution [219]. Another possibility is utilizing modulated excitation, which provides the possibility of phase-sensitive detection, enabling the separation of overlapping bands [220]. The absorption bands assigned to different secondary structures are collected in Table 2.3.

Table 2.3: IR absorption bands caused by secondary structures. Table adapted from Schwaighofer, 2013 [138].

Secondary Structure	Band position in H_2O (cm^{-1})		Band position in D_2O (cm^{-1})	
	Average	Extremes	Average	Extremes
α-helix	1654	1648-1657	1652	1642-1660
β-sheet	1633	1623-1641	1630	1615-1638
β-sheet	1684	1674-1695	1679	1672-1694
Turns	1672	1662-1686	1671	1653-1691
Disordered	1654	1642-1657	1645	1639-1654

Since most proteins are situated within an aqueous environment, they are surrounded by large amounts of O–H bonds provided by the water molecules. These O–H bonds strongly overlaps with the amide I band (1650 cm^{-1}), being located at 1640 cm^{-1}. To circumvent this obstacle, the water is replaced by deuterium oxide (D_2O), whose O–D bond absorbs at 1200 cm^{-1}. As already mentioned within the *UV/Vis spectroscopy* section, band positions are influenced by the solvent. For the amide II band, predominately caused by N–H bending, this shift is large (from 1550 cm^{-1} to 1450 cm^{-1}), but it is still sufficiently far away from the O–D absorption, while the amide I band, mainly consisting of C=O interactions (80 %), shifts only about 5 to 10 cm^{-1} [202]. The solvent exchange evokes new uncertainties, since it cannot be unequivocally assumed that the respective proteins of interest withstand this treatment completely unaltered [221]. Several possibilities are discussed in literature concerning this strategy, dealing with changes in structure and function [222], denaturation [223, 224] and affected salt bridges [204]. Sheridan *et al.* [225] and Farver *et al.* [226] explicitly name proteins exhibiting internal electron transfer as vulnerable towards the deuterium oxide treatment.

2.6 Surface plasmon resonance spectroscopy

A surface plasmon is a collective electron oscillation at the interface of a metal and a dielectric [227]. To briefly clarify the notions: A plasmon is the particle assigned to a plasma oscillation (also called Langmuir wave) in terms of the wave-particle dualism, as the photon is for an electromagnetic wave. The term plasma describes charged particles in free motion, also including the conduction band electrons of a metal. The plasmon, comprising all electrons that are oscillating, can be considered as a quasiparticle. A quasiparticle is assigned to a microscopically complicated system, if the latter is behaving like a different (only theoretically existing) particle that moves in free space. An example for a quasiparticle – assigned for simplification and behaving like it was a particle – is an electron hole in a valence band, which can be treated as a positive charge, or an electron moving through a semiconductor, which is hindered in its motion by the other components. It can be regarded as electron with an effective – therefore different – mass travelling through free space. The electron with the assigned effective mass (it has not) is hence the quasiparticle of the real electron [228, 229]. In that way, the plasmon comprises the entity of oscillating electrons.

Besides propagating surface plasmons, which are described in the following, there are localized surface plasmons (LSPs), in the case of which the collective surface electron oscillation (of the delocalized conduction band electrons only) is confined to nanoparticles of sizes smaller than the wavelength of the excitation light. The latter play an important role if large field enhancements are required. Both are possible to excite by light, resulting in the term surface plasmon polaritons (SPPs), whereat a polariton is another quasiparticle that describes the coupling of electromagnetic waves with electric (or magnetic) dipoles [230]. In contrast, volume plasmons, also referred to as bulk plasmons, being collective oscillations of delocalized electron clouds within the bulk of a metal, are not excitable by light. (Bulk plasmon polaritons have been reported for metamaterials [231, 232], but this is by far beyond the scope of this thesis.) The only type relevant within this thesis are propagating surface plasmon polaritons, herein referred to as surface plasmons (SPs) only.

2.6.1 General conditions of surface plasmon excitation

As mentioned before, SPs occur at the interface between a metal and a dielectric. Two conditions needs to be fulfilled for SP excitation. First, the metal must provide free electrons,

i.e., the aforementioned delocalized electron cloud of the conduction band, under conditions they are able to respond to an incoming electromagnetic field (regarding their inertia that hinders responding at frequencies higher than the respective plasma frequency). This implies a negative real part of the metal's permittivity, the latter being material- and frequency-dependent (see above, *Fundamentals of light*). (The case of heavily doped semiconductors, exhibiting a negative real part and allow for SP excitation as well [233], are left out here.) Conversely, the permittivity's real part of the dielectric, which does not provide the aforementioned property, is positive (which is sometimes expressed as a change of sign across the interface). An SP can be regarded as damped wave travelling along that interface. So, second, to provide the conditions for a travelling wave along the surface, the absolute value of the metal's real part (of the permittivity) needs to be larger than the one of the dielectric [170]. (This can be mathematically derived by means of eq. 2.80; otherwise, the vector component in this direction becomes purely imaginary.) Combining both criteria (briefly: $\mathrm{Re}\{\varepsilon_{metal}\} < -\mathrm{Re}\{\varepsilon_{dielectric}\}$), it results in general usability limits of metals in terms of SP excitation, which is illustrated for exemplary metals in Fig. 2.20.

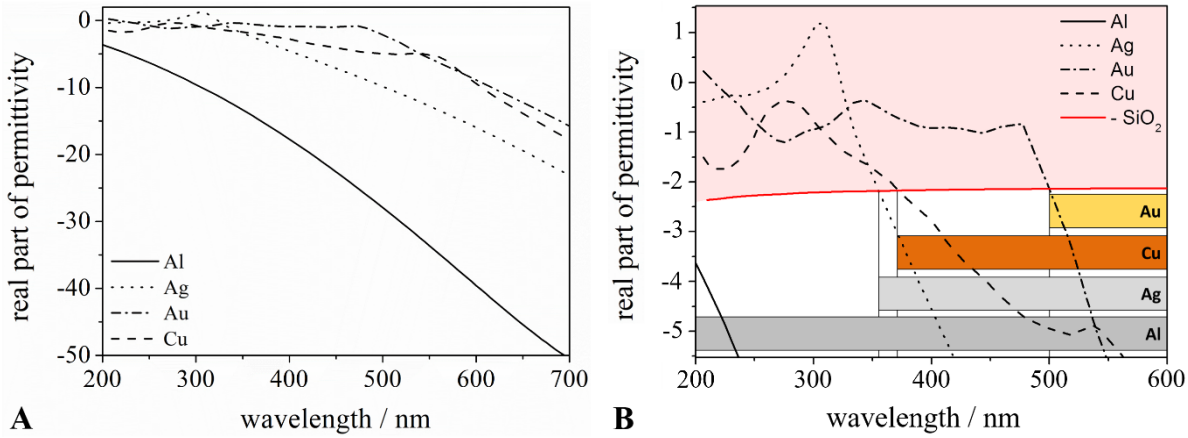

Figure 2.20: Usability of different metals in terms of surface plasmon (SP) excitation. (A) The real part of the complex permittivity is assigned to the wavelength of an incoming electromagnetic wave. (B) Zoom in (A): The intersections of the permittivity curves of the metals and the negative one of an exemplary dielectric (i.e., fused silica in this case) results in usability limits of the exemplary metals to excite SPs. Values are taken from McPeak et al., 2015 (Al) [234], Babar & Weaves, 2015 (Ag, Au, Cu) [235], and Malitson, 1965 (fused silica) [236], accessed online via the refractive index database [237].

These basic requirements restrict, for instance, gold, being one of the most utilized metals in the field of plasmonics, to wavelengths above 500 nm, and silver at least to the visible range.

Under certain conditions, SPs can be excited *resonantly*, which is crucial to exploit plasmonic oscillations in terms of spectroscopic applications (and hence, it is called surface plasmon

resonance (SPR) spectroscopy). To have a look at exemplary spectra beforehand, see Fig. 2.26 and related text.

2.6.2 Resonant excitation of surface plasmons

To resonantly excite an SP, frequency and momentum of the incoming electromagnetic wave need to match the ones of the SP [170]. As described above, the momentum can be expressed via the wave vector k, being connected by reduced Planck constant.

$$\vec{p} = \hbar \cdot \vec{k} \tag{2.9}$$

Since SPs are directed parallel to the surface, and the general physics behind resonant SP excitation remain the same if the phenomenon is treated two-dimensionally (by setting y = 0, with the z-component perpendicular to the interface), the crucial wave vector component of the incoming light that needs to match is the one in x-direction. (In the following, vector arrows are left out in terms of the wave vector.)

$$k_x = k \sin\theta_i = k_{SP} \tag{2.78}$$

However, the momentum of the incoming light – propagating through air – can never satisfy this condition; it is too low. To overcome this issue, two fundamental approaches exist. The first one is related to the principle of attenuated total reflection (ATR, see above, *Total reflection and the evanescent wave*), and the consequential spectroscopic application is therefore called ATR-SPR spectroscopy [170].

2.6.2.1 Evanescent wave-coupling: ATR-SPR

The wave vector, briefly repeated by means of eq. 2.2, can be expressed as

$$k = \frac{\omega}{c} = \frac{2\pi}{\lambda} \ . \tag{2.2}$$

The propagation speed c in a medium can be expressed by means of the refractive index and the vacuum propagation velocity, as defined by eq. 2.18, resulting in

$$k = \frac{\omega}{c_0} n = k_0 n \ , \tag{2.79}$$

which obviously displays that, for a given frequency, the momentum of the incoming light can be increased by increasing the refractive index. There are several high-refractive index glasses that can be utilized for that purpose.

Out of this solution for the momentum increase, two new problems arise. On the one hand, having an interface of glass and metal leaves no space for sampling, when it comes to applications. On the other hand, by increasing the refractive index of one of the interfacing materials, the required SP momentum increases along with.

To solve these constraints finally, a third layer, situated at the backside of the metal, needs to be introduced. This third layer can be connected in terms of SP coupling via the evanescent wave, emerging if the critical angle is exceeded. The critical angle and the principle of total reflection were introduced in the respective section *Total reflection and the evanescent wave*. Briefly summarized: If the critical angle (of incidence) is exceeded, the electromagnetic wave is split into a travelling wave along to the surface and an evanescent wave perpendicular to the surface, penetrating the adjacent medium with a certain penetration depth (see eq. 2.38), before being totally reflected. For that reason, the light needs to be TM-polarized to have an electric field component perpendicular to the interface. For the third layer, the same conditions apply in terms of resonant SP excitation as for the first one: It needs to have a positive real part with an absolute value smaller than the one of the metal. This condition is usually satisfied for air and water, which allow for sampling. Moreover, on the backside, the momentum required for resonant SP excitation is not increased due to the high-refractive index glass at the front. Eventually, the momentum, respectively k_x, can be increased at the front side by utilizing a high-refractive index glass (usually a prism), so that it is possible to fulfill the matching conditions to resonantly excite an SP at the backside, to which it is coupled via the evanescent field that penetrates the spacing metal layer, if the latter is thin enough. Since, besides the momentum, the frequency needs to match as well, the matching conditions for a certain k_x apply only at one particular wavelength. In a last step, k_x can be tuned towards a particular wavelength by adjusting the angle of incidence.

This rather figurative explanation can be underpinned by a mathematical one, employing the dispersion relations of the incoming light and the SP, each of them for both interfaces. The dispersion relation assigns the circular frequency to the wave vector (keeping in mind that both are required to match), and hence, cross sections of the dispersion relations imply that the conditions required for resonant excitation are fulfilled [170]. Exemplary dispersion relations are shown in Figure 2.21.

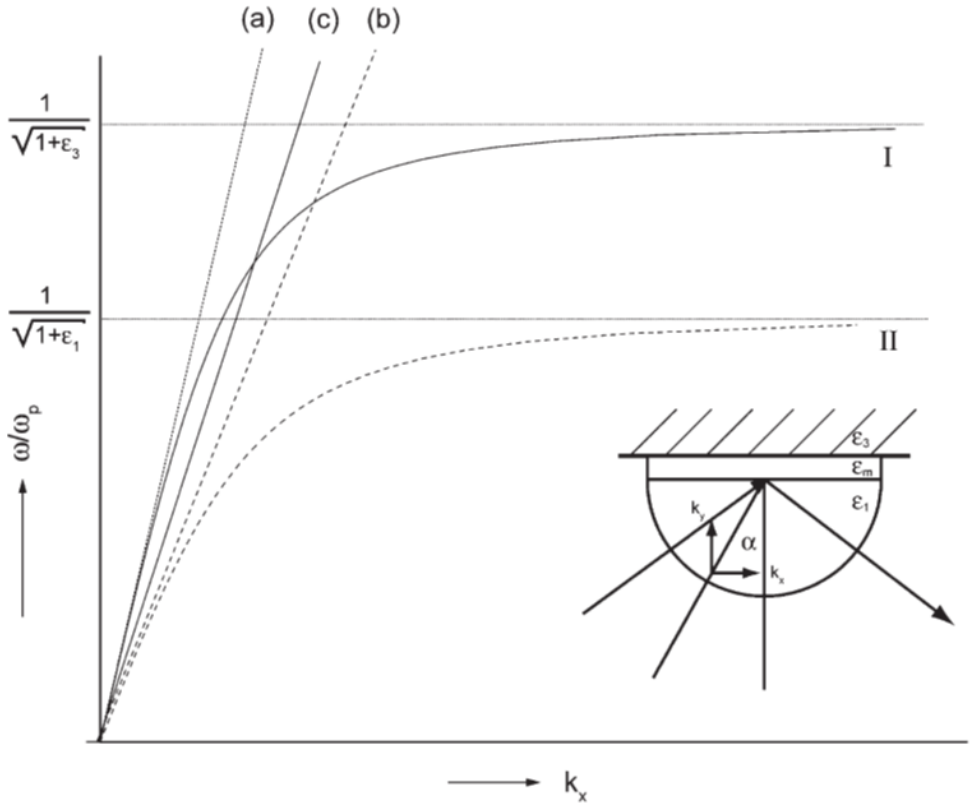

Figure 2.21: Dispersion relations of surface plasmons and light. The circular frequency of a wave is assigned to its wave vector in x-direction. Since air, as well as the commonly used glasses, exhibit almost no or little dispersion, the respective dispersion relations are close to linearity. The dispersion relations are given for the sample side (I: SP, (a): light) and the prism side (II: SP, (b): light), with the permittivities ε_m for the metal, ε_1 for the prism, and ε_3 for the sample side medium. The line (c) indicates a possible realization of (b) by adjusting the angle of incidence. The associated experimental setup is depicted as inlay, with α for the angle of incidence and y as the direction perpendicular to the surface, corresponding to θ_i and z, respectively, in the text. Figure adapted from Schasfoort & Tudos, 2008 [170].

Figure 2.21 illustrates two pairs of dispersion relations. The curves a and b are the dispersion relations of an electromagnetic wave propagating through air and a high-refractive index glass, respectively, which are described by eq. 2.79 (with $k = k_x$ for an angle of incidence of 90 deg, also denoted as grazing angle). I and II display the respective SP dispersion relations, mathematically described by

$$k_{SP} = \frac{\omega}{c_0}\sqrt{\frac{\varepsilon_m \varepsilon_{1\text{ or }3}}{\varepsilon_m + \varepsilon_{1\text{ or }3}}} = k_0\sqrt{\frac{\varepsilon_m \varepsilon_{1\text{ or }3}}{\varepsilon_m + \varepsilon_{1\text{ or }3}}}\,, \qquad (2.80)$$

with ε_m as the permittivity of the metal, ε_1 as the permittivity of high-refractive index glass, and ε_3 as the permittivity of the backside medium, which is air in this case. Please note that this is already deduced from resonance conditions, which is, for example, lucidly derived from Fresnel's equations in Schasfoort & Tudos, 2008 [170]. For the dispersion relation pairs I/a and II/b, there are no intersections, so it is not possible to resonantly excite an SP at the respective

front side of the sandwich structure. Nevertheless, by means of the evanescent wave, the light with enhanced momentum can resonantly excite an SP at the backside, depicted as intersection of the dispersion relations I and b. The intersection I/b implies an angle of incidence of 90 deg (hence $k = k_x$), which is not possible to implement. By adjusting the angle of incidence, k_x is tuned downwards (see eq. 2.78), thereby realizing any line c. It further implies that for a given wavelength, resonant SP excitation occurs at a single angle of incidence only, while, conversely, for a given angle, the intersection takes place at a particular wavelength. The asymptote, to which the SP dispersion relations converge, is called surface plasma frequency, being

$$\omega_{SP} = \frac{\omega_P}{\sqrt{1 + \varepsilon_{1\text{ or }3}}}\ , \tag{2.81}$$

which is approximately ω_P divided by the square root of two for air [170].

Actually, two geometries were described that realize resonant SP excitation by means of evanescent wave-coupling: the Otto [238] and the Kretschmann/Raether [239] configuration. Both are displayed in Fig. 2.22. The Kretschmann/Raether geometry is much more versatile, hence it was taken as basis so far. It describes the aforementioned adequately thin metal film, which is evaporated directly onto the prism (or, in practice, rather onto a glass slide of the same material, tightly pressed onto the prism using a refractive index-matching immersion liquid to provide a seamless junction). The SP is resonantly excited on the backside of the metal film as described.

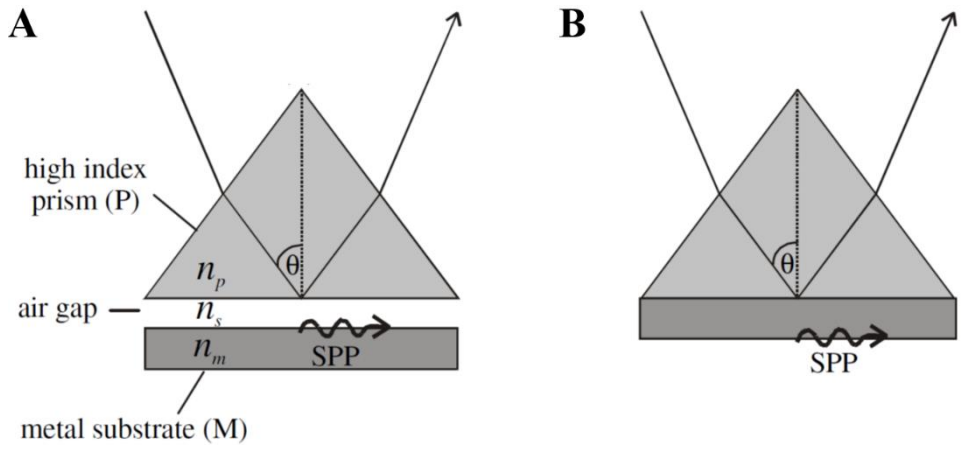

Figure 2.22: Otto (A) and Kretschmann/Raether (B) configuration. The Otto configuration utilizes a narrow air gap to transport the enhanced momentum of the incoming light via the total reflection-mediated evanescent field. Hence, the SPP is excited resonantly at the front side of the metal film. In the Kretschmann/Raether geometry, the metal film is attached to the prism directly. The evanescent field of the momentum-enhanced light is exciting the SPP at the backside of the metal film. Figure adapted from Hibbins, 1999 [240].

Considering the Otto geometry, a thin air gap is situated between the metal and the prism, so the evanescent wave penetrates this gap. The SP is thus resonantly excited at the front side of the metal (which is not to confuse with the aforementioned statement that an SP cannot be resonantly excited at the front side of the sandwich structure, which corresponds to the prism/air interface here). However, this approach is mechanically demanding because of the air gap dimensions that are required to place the metal sufficiently close to the prism, ensuring that it is situated within the penetration depth of the evanescent field [240]. At the same time, this limits the sample channel in terms of dimensions.

Before proceeding with SPR spectroscopy aspects, the second possibility of resonant SP excitation is outlined.

2.6.2.2 Grating-coupled SPR

The second possibility to resonantly excite SPs is utilizing a diffraction grating. As described before (see *Diffraction*), consecutively numbered diffraction orders emerge due to interference as soon as light is diffracted by a grating. In terms of the wave vector, this results in an enhancement that can be mathematically expressed by the addition of the grating vector (k_g) for each diffraction order, the latter describing the conditions under which constructive interference is realized (see, e.g., Bragg or von Laue conditions in crystallography [228]). The wave vector of the SP consequently needs to equal the sum of the wave vector of the incoming light and the grating vector [230, 240].

$$k_{SP} = k_x + m\,k_g = k_0\,n_d \sin\theta_i + m\,\frac{2\pi}{\Lambda} \qquad (2.82)$$

Here, m is the diffraction order, n_d the refractive index of the dielectric, and Λ the grating period.

Since the light of the zeroth order is not affected by diffraction, there is no additional momentum, and accordingly, the right side of eq. 2.82 is reduced to k_x in this case, implying that zeroth order SPs cannot be resonantly excited by the zeroth diffraction order light (Fig. 2.23B, discussed below). Due to the emergence of higher diffraction orders, resonant SP excitation is possible, which is illustrated by the dispersion relations of grating-coupled SPs (Fig. 2.23B), based on an exemplary linear, sinusoidal grating (Fig. 2.23A) [240].

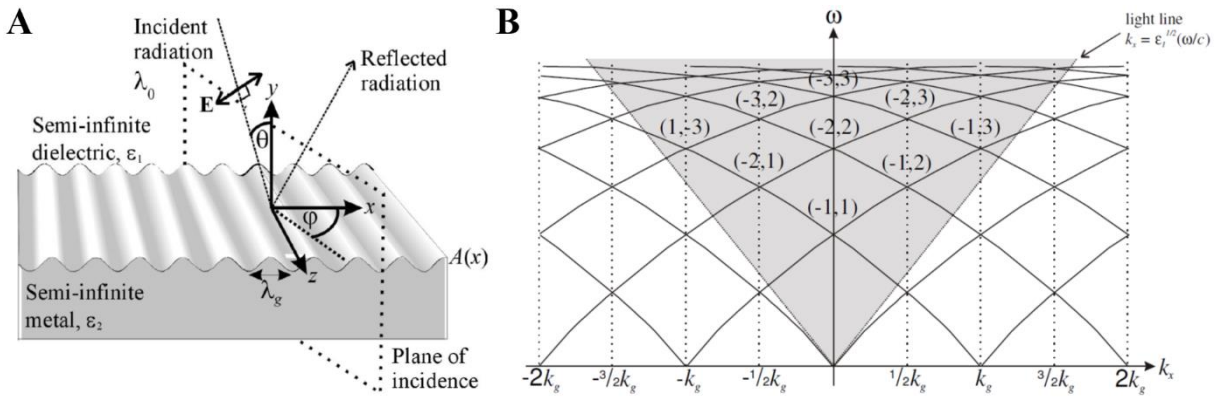

Figure 2.23: Diffraction grating and associated dispersion relations. (A) A schematic linear, sinusoidal grating is depicted with assigned parameters, including the additional azimuthal angle φ, spanned between the plane of incidence and the grating ridge course. Again, y- and z-directions are reversed compared to the text, and Λ is denoted as λ_g. The permittivities of the dielectric and the metal, being ε_1 and ε_2 here, correspond to ε_d and ε_m within the text, respectively. (B) Dispersion relations for grating-coupled SPs with an azimuthal angle of φ = 0, assigning the circular frequency to multiples of the grating vector. The shaded area can be realized, confined by the light line at grazing angle. Figures adapted from Hibbins, 1999 [240].

Having a linear, sinusoidal grating (Fig. 2.23A), there is an additional angle that matters besides the angle of incidence, i.e., the azimuthal angle φ. It describes the angle between the plane of incidence and the grating groove direction. If it is 90 deg, there is no diffraction effect, since (for TM-polarized waves, as depicted) the electric field component is directed parallel to the grating ridges. The opposite applies for TE-polarized light. Having a crossed grating, there is no direction parallel to the grating, implying that TM- as well as TE-polarized light can be used for resonant SP excitation [230, 240].

The dispersion relations shown in Fig. 2.23B are indicated for an azimuthal angle of 0 deg (and assumed planarity, see below). Again, the shaded area indicates the possible realizations of the light line, limited mathematically by an angle of incidence of 90 deg (and practically a bit below). The zeroth diffraction order SP dispersion relation does not intersect any possible light line, being in accordance with eq. 2.82, which predicts no momentum enhancement for the zeroth diffraction order light. However, there are several possibilities to satisfy the matching conditions mediated by other diffraction orders, even at normal incidence. As depicted, more than one intersection emerges for a particular light line, resulting in resonance features at more than one wavelength for a certain angle of incidence. Vice versa, above a lower frequency limit, SP resonances can be observed at one or more angles of incidence, theoretically limited by the surface plasma frequencies, but in practice rather due to the diminishing intensities associated with the involved higher diffraction orders (however, newer techniques are capable to overcome this issue, see Cai and co-workers [241]). Intersections of the SP dispersion relations, emerging at multiples of $k_g/2$, indicate SP coupling, due to which SPs mediated by different diffraction

orders merge and result in a single resonance feature in the spectrum (see below). At normal incidence, the respective plus and minus diffraction orders couple to each other [240].

At the point of having an azimuthal angle unlike 0 deg or crossed gratings with unequal periodicities, the y-direction cannot be neglected any more. (Strictly speaking, due to the corrugation, the geometry is moreover not planar as assumed, but for small amplitudes (of the corrugation), the given equations and the planar dispersion relations hold approximately true [240]). With emerging y-direction, the SP wave vector needs to be calculated by means of the Pythagorean theorem, as lucidly depicted by Bauch, 2014, exemplified by a crossed grating (Fig 2.24). For simplicity reasons, only crossed gratings that exhibit the same periodicity in x- and y-direction are considered [230].

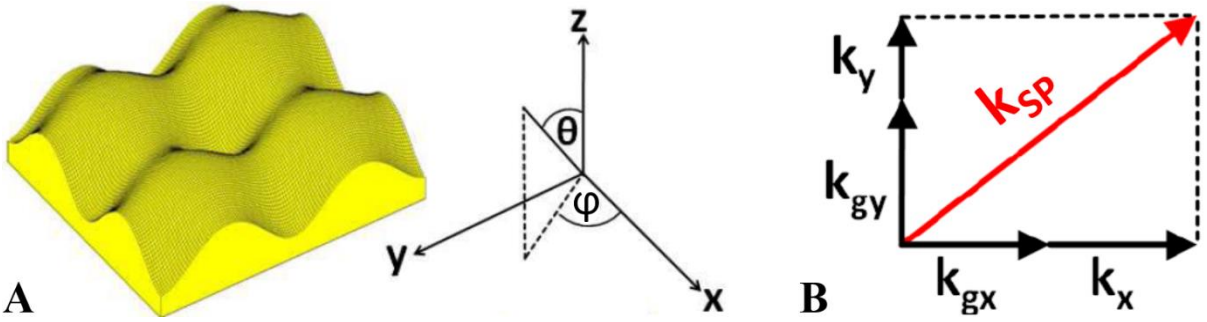

Figure 2.24: Vector diagram for grating-coupled SP excitation. (A) A schematic crossed grating is depicted with assigned coordinate system and angles. (B) The SP wave vector is expressed by the in-plane components of k_0 and the grating vectors in two dimensions. Figure adapted from Bauch, 2014 [230].

According to the vector diagram shown in Fig. 2.24, eq. 2.82, specified for an azimuthal angle of φ = 0 deg, becomes

$$k_{SP} = \sqrt{(k_{gx} + k_x)^2 + (k_{gy} + k_y)^2} \tag{2.83}$$

with the components

$$k_x = k_0\, n_d \sin\theta_i \cos\varphi \ , \tag{2.84}$$

$$k_y = k_0\, n_d \sin\theta_i \sin\varphi \ , \tag{2.85}$$

$$k_{gx} = m\frac{2\pi}{\Lambda} \ , \text{and} \tag{2.86}$$

$$k_{gy} = n_{diff}\frac{2\pi}{\Lambda} \ . \tag{2.87}$$

Here, n_{diff} is – as m – the respective integer diffraction order, with the subscript to differentiate from the refractive index in general (n) and from the refractive index of the dielectric (n_d).

Vice versa, the required periodicity of the grating can be deduced, being for normal incidence

$$\Lambda = \frac{\lambda \sqrt{m^2 + n_{diff}^2}}{\sqrt{\frac{\varepsilon'_m \, \varepsilon_d}{\varepsilon'_m + \varepsilon_d}}} \, . \tag{2.88}$$

Here, the introduced permittivities ε_1 and ε_3 of the required sandwich structure using the ATR approach simplify to ε_d of the only involved dielectric in reflectivity measurements [230].

In summary, grating-coupled resonant SP excitation does not require total reflection conditions, hence lower angles than the critical one can be realized and even normal incidence. Furthermore, it enables resonant SP excitation at the interface the light is impinging on, so it does not require three layers enclosing two interfaces. If the metal film is thin enough, transmission SPR can be realized as well, potentially resonantly exciting SPs at both interfaces, which is not possible to implement via ATR-SPR. (However, there are more advanced structures related to the conventional ATR configuration, which make it possible after all, as extensively discussed by Berini, 2009 [242], but this is considered as beyond the scope of this fundamental description.) Even though reflectivity attenuation might be measured in grating-coupled SPR spectroscopy as well, it is not referred to as ATR-SPR, since ATR is a set expression related to the phenomenon occurring above the critical angle. An adequately rough surface might be sufficient for resonant excitation as well, since it acts as a superposition of gratings. Although already observed by Wood at the beginning of the twentieth century [243, 244], deeper understanding and implementation took its time, so the usage of grating-coupled SPR in terms of sensors was not preceding the approaches of Kretschmann and Raether (and Otto) [170].

2.6.3 Spectroscopic application

To describe the spectroscopic application of resonant SP excitation adequately, there is one parameter missing, namely a measure how distant an analyte may be situated from the surface to still influence the SP properties. As a consequence of resonant plasma oscillation, the electric field intensity in closest vicinity is strongly enhanced, evanescently decaying with increasing

distance. An exemplary simulation, adapted from Bauch, 2014 [230], is depicted in Fig. 2.25, showing the electric field intensity assigned to the distance from the relevant surface, once for the resonance angle and once for another angle off the resonance conditions.

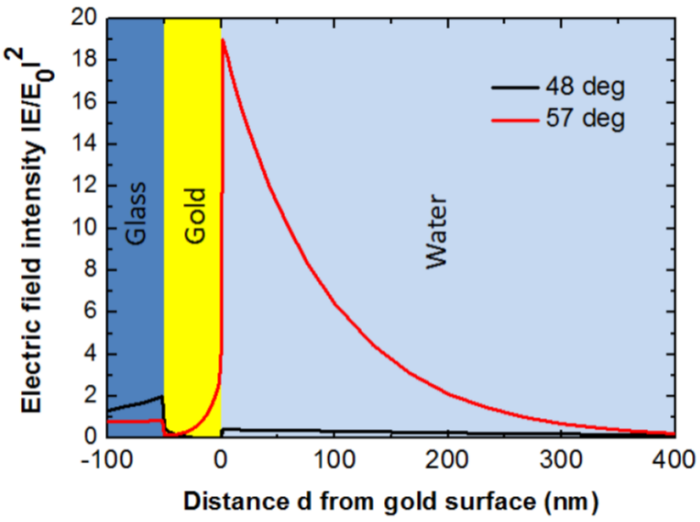

Figure 2.25: SP-mediated electric field enhancement. Electric field intensities are assigned to the distance from the relevant interface of a Kretschmann/Raether geometry. The evanescent field intensity course is shown for the resonance angle (57 deg) and an off-resonance angle (48 deg). The simulation was performed assuming an excitation wavelength of 633 nm and a gold layer of 50 nm thickness. Figure adapted from Bauch, 2014 [230].

As illustrated by the simulation of Bauch [230], displayed in Fig. 2.25, the evanescent electric fields associated with off-resonance conditions are negligible. Regarding resonant excitation at the gold/water interface, the electric field is enhanced by the factor 19 compared to the incoming field intensity, and decays with increasing distance. While the field is notably penetrating the water, it decays rapidly within the metal. The penetration depth d_{SP} (to distinguish from d_p, describing the penetration depth of the evanescent wave under total reflection conditions, see *Total reflection and the evanescent wave*) calculates by means of eq. 2.89. Again, the penetration depth indicates the distance after which the field is decreased to a value of 1/e, being approximately 37 % [230, 240].

$$d_{SP} = \frac{1}{k_z} = \frac{\lambda}{2\pi}\sqrt{\frac{|\varepsilon'_m| + \varepsilon_3}{\varepsilon^2_{m\text{ or }3}}} \tag{2.89}$$

Here, k_z is the z-component of the wave vector (the one perpendicular to the interface), and the denominator of the square root needs to be specified with ε_m and ε_3 for the penetration depth within the metal and the dielectric, respectively.

On this basis, the sensor application is straightforward: Due to the resonant SP excitation, light is absorbed and hence, the reflection or transmission is attenuated (or at best completely prevented) under a certain angle of incidence that provides matching condition in terms of the wave vectors at a given frequency. If changes occurs within the penetration depth of the SP-mediated field, e.g., the binding of an analyte to an accordingly functionalized surface (see below), the overall refractive index is altered and hence, the resonance angle (or the resonance wavelength at a certain angle) is changed [170, 230].

Typical ATR-SPR spectra and the effect of a refractive index change at the sample side are depicted in Fig. 2.26A. After exceeding the critical angle, up to which the reflectivity is increasing with increasing angle (inset), the reflectivity is constant at a value that is in practice not necessarily 100 %. At the resonance angle, the reflectivity is attenuated and, at optimum, completely prevented, resulting in a reflectivity dip. The simulation was done for a silver layer of 54 nm thickness, mounted in Kretschmann/Raether configuration with a triangular prism of the high-refractive index glass N-LASF9, using an excitation wavelength of 488 nm. The refractive index of pure water is 1.3355 at this wavelength [245]. Due to small changes in the refractive index, notable changes in the resonance angle were predicted. By monitoring the change of the resonance angle over time (Fig. 2.26B, A and B indicating the respective resonance angles), kinetic measurements can be performed. Depending on the setup geometry, it might be more advantageous to record the reflectivity change over time at a fixed angle within the linear course at the dip edge, which would be realized, e.g., at 57 deg in the case that is illustrated by the solid line in Fig. 2.26A. Kinetic curves as displayed in Fig. 2.26B can, for example, be used to determine affinity constants of antibodies after functionalizing the chip surface with the respective antigen [170].

The efficiency of resonant SP excitation exhibits an optimum in terms of the thickness of the metal layer, which is both dependent on the material and on the excitation wavelength (keeping in mind that the permittivity, respectively the refractive index, is frequency-dependent anyway). The SPR spectrum was simulated using the same parameter as in Fig. 2.26A, this time fixing the refractive index to the one of water and varying the thickness. For thicknesses below and above the optimum, being 54 nm in this case, the reflectivity dip becomes shallower, while for thicknesses below, it becomes broader in addition. In gray, the same geometry was simulated for an excitation wavelength of 633 nm. Still, the optimum thickness is 54 nm, but, as an example, for 1500 nm, it changes to 47 nm. Nevertheless, taking into account that the optimum thickness of an aluminum layer at 488 nm is 14 nm, it turns out to be rather material-dependent. As the gray curves display, the resonance angle might slightly change in addition.

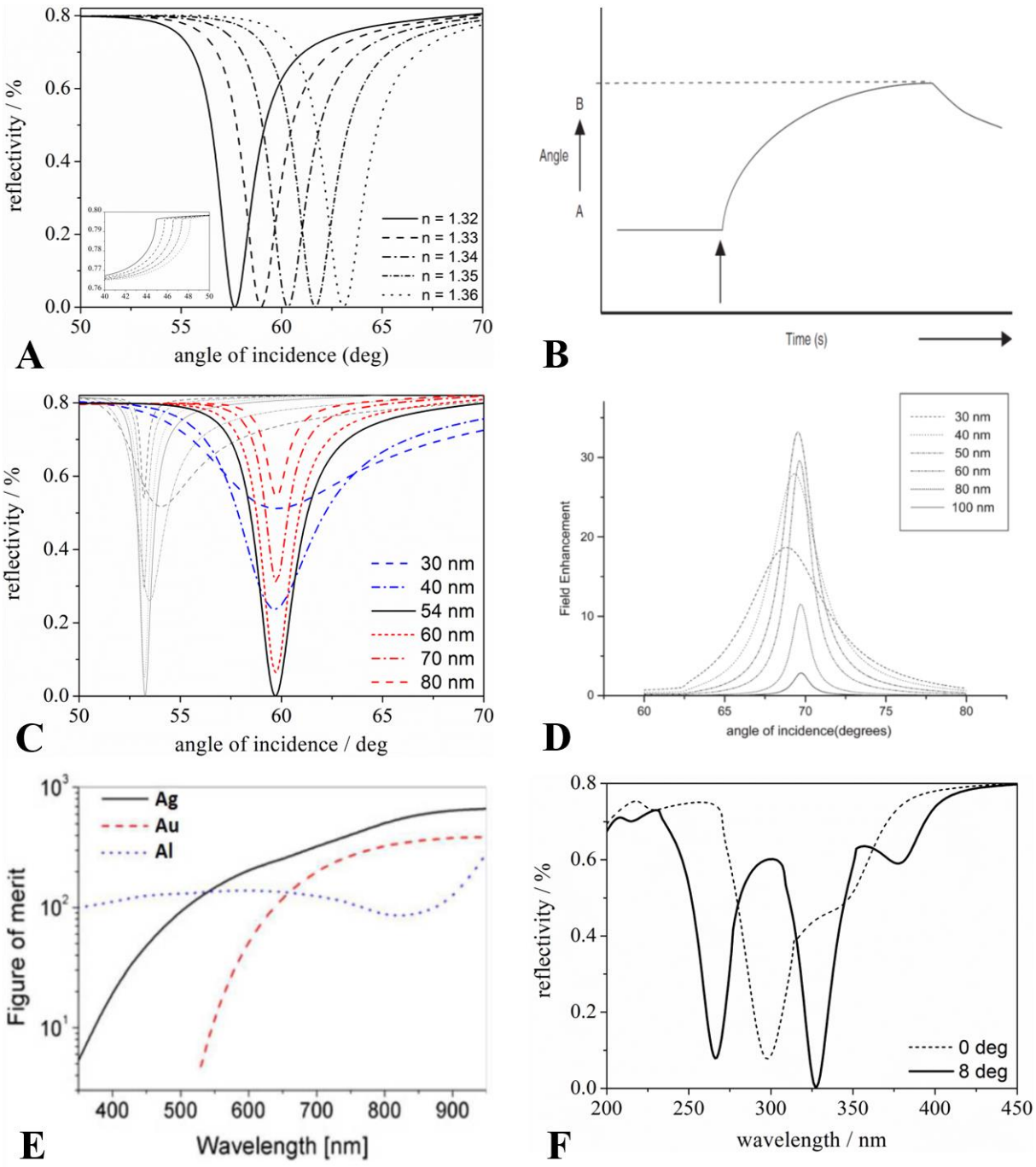

Figure 2.26: Surface plasmon resonance-mediated spectral features and quality factor. (A) The reflectivity course was simulated as function of the angle of incidence for slightly different refractive indices of the sample side medium, simulated for a silver layer of 54 nm thickness on top of a triangular prism made of the high-refractive index glass N-LASF9, mounted in Kretschmann/Raether configuration, excited by 488 nm. Refractive indices close to the one of water were chosen. (B) Schematic kinetic measurement, monitoring the resonance angle change over time. (C) The simulations of (A) were repeated for different thicknesses of the silver layer, fixing the refractive index of the sample side to the one of water. The colors serve for better clarity only and are specified by the key. The gray curves results from the same geometry, but with an excitation wavelength of 633 nm. (D) The electric field enhancement is assigned to the angle of incidence for different thicknesses of a gold layer. (E) Quality factor of different metals in the visible range and slightly beyond. (F) Simulation of a grating-coupled SPR spectrum at normal incidence and 8 deg. A crossed aluminum grating with a grating period of Λ = 200 nm in both x- and y-direction on top of an exemplary photoresist substrate with a refractive index about 1.5 and high transparency was taken as basis, illuminated by a white light source. (A) and (C) were simulated using WinSpall, (F) was simulated using PCGrate, (B) and (D) are adapted from Schasfoort & Tudos, 2008 [170], and (E) is adapted from Bauch, 2014 [230]. Permittivity values were taken from McPeak et al., 2015 (Au, Ag) [234], Palik, 1985 (Al) [246] the manufacturer's catalog (N-LASF9 glass) [247], and Hale & Querry, 1973 (H_2O) [245], accessed via the refractive index database [237] or integrated in the simulation software.

In Fig. 2.26D, the thickness of a gold layer, interfacing with water, is investigated concerning the SP-mediated field enhancement assuming an excitation wavelength of 700 nm. (Due to the lack of parameters, the Figures 2.26A and C could not be simulated in accordance.) An enhancement factor of more than 30 was predicted for the optimum thickness at an angle close to – however slightly aside from – the resonance angle. (The slightly different angular position of the reflectivity minimum is on account of the phase behavior at resonance, having a non-ideal metal, which is not outlined here; see, for example, Liebermann & Knoll, 2000 [248].) The most advantageous metal to achieve field enhancements as high as possible can be chosen according to the so-called quality factor (Q, also referred to as figure of merit), which is specified for the most commonly used metals in SPR spectroscopy over the extended visible range in Fig. 2.26E. For a flat surface, it calculates by means of eq. 2.90 [230, 233].

$$Q_{SP} = \frac{\varepsilon_m'^2 + \varepsilon_m' \, \varepsilon_3}{\varepsilon_m'' \, \varepsilon_3} \tag{2.90}$$

If the absolute value of the metal's real part of the permittivity exceeds the permittivity of the dielectric by far ($|\varepsilon_m'| >> \varepsilon_d$), eq. 2.90 simplifies to

$$Q_{SP} = \frac{\varepsilon_m'^2}{\varepsilon_m''} \, . \tag{2.91}$$

So, roughly, the smaller the absorption of a metal is (represented by the imaginary part of the permittivity), the greater is the electric field enhancement and the narrower the reflectivity dips [248]. The evanescent field can be used in terms of fluorescence enhancement. The related spectroscopic method is called surface-plasmon field-enhanced fluorescence spectroscopy (SPFS). Because of potentially way higher enhancement factors, LSP excitation at metal nanoparticles plays an important role, for which Q is calculated differently [230, 233]. Exploiting fluorescence enhancement, the optimum distance of the analyte to the metal surface changes from closest possible vicinity to a certain distance due to quenching by the metal. However, SPFS is a large topic by itself, and it was not applied within this work. For further literature, see, for instance, Liebermann & Knoll, 2000 [248], in terms of SPFS in general, and Bauch & Dostalek, 2013 [249], focusing on LSPs in particular. Altogether, SPFS was shown to provide a better sensitivity than SPR spectroscopy, namely by orders of magnitude.

In contrast, Fig. 2.26F shows reflectivity curves assigned to the wavelength, obtained by simulations of grating-coupled resonant SP excitation. Here, a crossed aluminum corrugation

on a reasonable substrate (due to preparatory reasons, a photoresist needs to be applied between the glass slide and the metal grating, which is – for reasons of simplicity – only described by its refractive index of approximately 1.5 here) with a grating period of $\Lambda = 200$ nm in both directions, interfacing with water, was investigated. Due to the different underlying mechanism, a reflectivity grating can be as thick as desired, thereby avoiding transmission losses. For transmission SPR, a thin layer providing sufficient transmission is required. The simulation assumed a 20 nm thick aluminum layer, which would be adequate to employ for transmission SPR spectroscopy. The simulation results show – unlike the ATR-SPR simulations – multiple resonance features. Using eq. 2.88, the first order SPs are expected at 300 nm at normal incidence, keeping in mind that in this case plus and minus first order plasmons couple (see Fig. 2.23B). Indeed, a dip can be observed at around 300 nm. Further in accordance with Fig. 2.23B, by increasing the angle of incidence, the plus and minus first order plasmons split because of less coupling, which can be seen as well in Fig. 2.26F for the angle of incidence of 8 deg. The additional features, red-shifted in comparison, result from the rear side of the aluminum film, since light is partially transmitted and in turn partially reflected at the opposite side. These resonances is predicted to be located at 331 nm for normal incidence (see eq. 2.88), which is in accordance with the simulation, considering that the features of both interfaces are superimposed. By increasing the angle, the minus first order SP remains hidden, since it is covered by the way more pronounced plus first order SP feature originating from the front side. The plus first order feature can be observed at around 380 nm. Both are way less pronounced because of the intensity distribution. Having an aluminum film, being a good mirror material and consequentially highly reflective, the largest share of the incoming light is reflected at the front, while only a small part reaches the rear side, exciting an SP at the aluminum/photoresist interface. The irregularities slightly above 200 nm might be due to second order SPs. Admittedly, the present case is somewhat unnecessarily complicated, but it was taken over from the actually employed grating structure, which is revisited within the results part. On the other hand, it displays the complexity of grating-coupled SPR spectroscopy, eventually resulting in enhanced possibilities. A further enhancement, the multi-diffractive grating, which exhibits multiple grating periods, was presented by Adam & co-workers [250]. The detection of resonance-mediated phase shifts, on the one hand providing increased sensitivity, on the other hand requiring a more complicated setup, is not outlined here (see, e.g., Schasfoort & Tudos, 2008 [170], or, as a more recent research article, Zeng *et al.*, 2013 [251]), as well as closer analyses of sensitivity issues, the outcoupling of light, and the temperature dependence of resonant SP excitation.

A special focus when it comes to spectroscopic application needs to be set on the choice of the metal. A strong argument for using gold is its chemical stability, which is much greater than the one of silver that is – although belonging to the noble metals as well – vulnerable to oxidation by traces of hydrogen sulfide within the normal room climate. Silver, on the other hand, is the best SPR material in terms of performance in the visible and IR range [252]. Besides, gold cannot be used below approximately 500 nm due to the general conditions described initially. In spite of the inertness of gold, both can easily be modified by thiol-terminated molecules, which covalently bind to the gold or silver surface, enabling various kinds of further functionalization via bifunctional linker molecules [253]. In the UV spectral region, aluminum is likely the most reported material (whereat, for example, indium was utilized as well, see Mishra et al., 2011 [254]). As a base metal, it oxidizes immediately after getting in contact with air. Nevertheless, it can be used due to passivation. As soon as subjected to oxygen, a thin aluminum oxide (alumina, Al_2O_3) passivation layer is formed on top, protecting the aluminum below. Being passivated, it is comparable to a noble metal concerning further reactions. The influence of the alumina layer on SP-mediated spectroscopic features was investigated by Ono and co-workers (Fig. 2.27) [255].

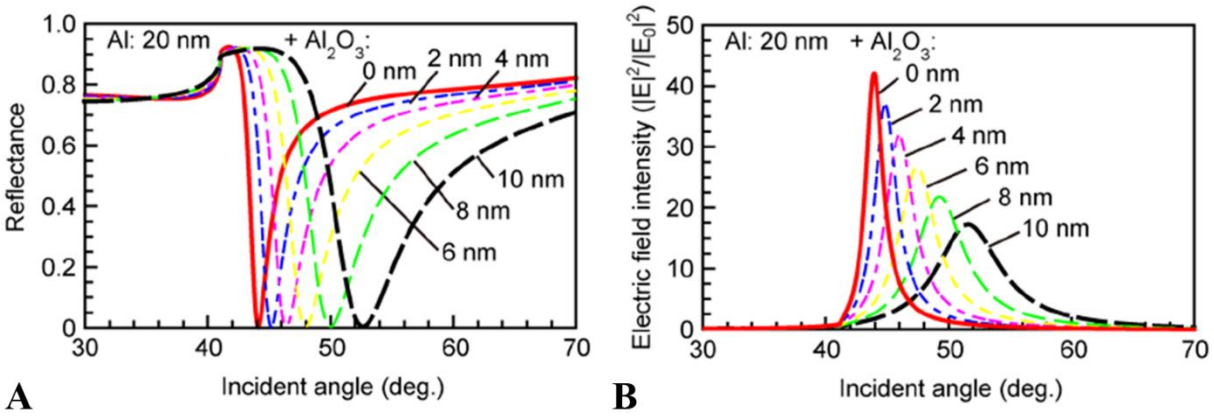

Figure 2.27: Influence of alumina passivation layers on SP excitation. Simulations of the reflectance (A) and the electric field intensity (B) are shown, based on a 20 nm-thick aluminum film covered by differently thick alumina layers. Figure adapted from Ono *et al.*, 2013 [255].

As depicted in Fig. 2.27, the resonance angle was predicted to shift towards higher angles with increasing thickness of the alumina layer, while the reflectivity dip broadened, albeit not becoming shallower. The electric field enhancement was shown to decrease with increasing thickness (shifting along with resonance angle). However, Ono and co-workers indicated the naturally occurring alumina layer with 4-10 nm, while several others found it to be rather 2-3 nm only [256–258]. Hence, they concluded that the passivation layer does not influence the properties of aluminum in terms of SPR applications in a notably hindering way. In terms of

fluorescence-related applications, they even claimed it to be of advantage, since the alumina layer prevents quenching [255]. Concerning surface functionalization, the aluminum oxide layer enables silane-terminated linkers to covalently bind.

Dependent on the deposition method, adhesion layers, mostly chromium or titanium, might be required for each of the three metals. This is discussed, e.g., by Ekgasit *et al.* [259], while surface functionalization is discussed more extensively in Wijaya and co-workers [253]. Other materials are, at least in the wavelength region discussed throughout this thesis, mostly outperformed by those three (such as copper, which can neither keep up with gold in terms of stability, nor with silver in terms of performance, or with aluminum in terms of UV-suitability). Alternative materials with putatively better properties are a current issue in research [233, 260, 252]. However, although this comprises a lot of materials, including alkali metals, nitrides, silicides, heavily doped semiconductors, and graphene as well as poor metals like indium and thallium, and derived oxides like indium tin oxide, these seem to be either tailored to other purposes (since the field of plasmonics comprises way more than the outlined spectroscopy application) or not yet sufficiently developed in terms of performance or easy usability.

Concerning the glasses, it needs to be mentioned that the most high-refractive index glasses become highly absorbing and fluorescing within the UV spectral range [247], so lower-refractive alternatives like fused silica needs to be used, which, in turn, do not necessarily suffice in terms of the refractive index for a conventional ATR setup, which is a major issue to overcome within this work.

II Proteo-Lipobeads

A novel platform to investigate strictly oriented membrane proteins in their functionally active form

Chapter 3 *Introduction*

About 55 % of all approved pharmaceuticals target on membrane proteins (MPs), corresponding to 60 % among protein targets (Fig. 3.1) [261]. Therefore, MP-related investigations are not only a topic of mere basic research. Due to their hydrophobic transmembrane segments, MPs need to be solubilized by a detergent. But, since the biological membranes are meant to separate compartments in a tight manner, the function of MPs (herein excluding the membrane-associated enzymes) is often correlated with a transport across a dense membrane [262], and hence, the sole solubilization with the help of detergents does not suffice. A biological membrane is further required to investigate MPs and related diseases.

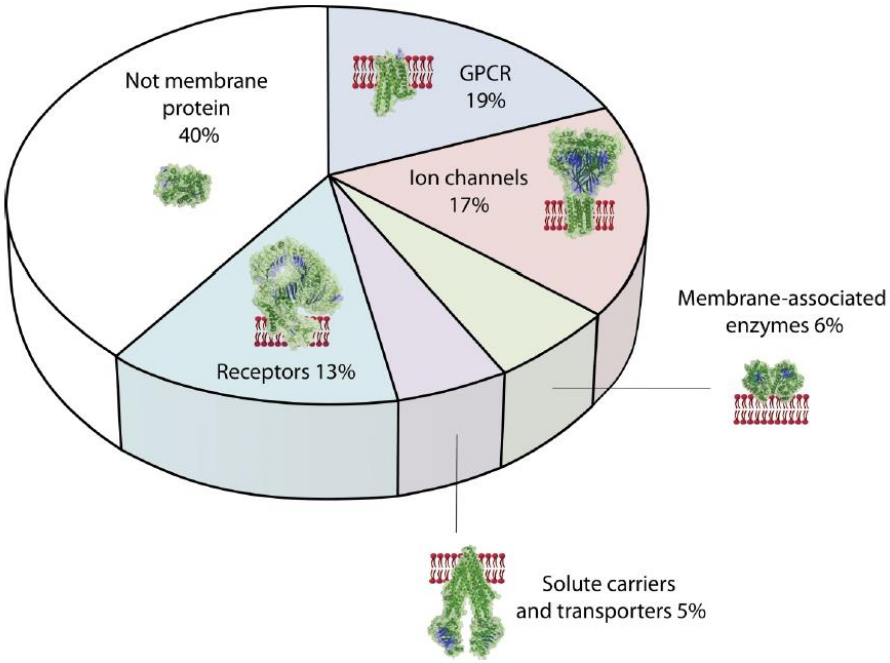

Figure 3.1: Protein targets of pharmaceuticals. The pie chart illustrates the drug targets among proteins, of which 60 % are membrane proteins (MPs) or at least membrane-associated proteins. This corresponds to 55 % of the overall drug targets. Figure adapted from Tiefenauer & Demarche, 2012. [261].

To overcome this issue, there are two fundamental approaches: Either cells or compartments thereof can be prepared from their natural origins [263], or a biomimetic membrane can be established to investigate the respective MP of interest in an *ex vivo* environment [262]. Since a cell, and as well its compartments, is closely packed with a large multitude of different proteins (and the membranes are complex assemblies themselves, including a variety of

different lipophilic molecules), the preparation of those is – besides demanding – associated with another difficulty, namely to extract the signal rendered by the MP of interest from the background of hundreds of other components.

Regarding biomimetic lipid membranes (BLMs) as a surrogate of live cells, several approaches were presented to the recent day, mainly differing in being either solid-supported or not [100, 105].

Liposomes are not solid-supported and mimic the biological cell by being a spherically shaped membrane compartment that is taken up in solution (although cells are usually attached to elements of the cytoskeleton, thus being not that freely diffusing). Proteins can be integrated to form proteoliposomes, but still the random integration of proteins is an issue of proteoliposomes, which effects the more stable polymerosomes in the same way [129, 130]. To monitor transport processes, it can be determined on a case-by-case basis, at which ratio a protein of interest orientates in the favored direction [264, 265]; however, it would be more straightforward to insert MPs in an oriented manner.

Regarding solid-supported membranes, this issue was overcome at last, especially addressing the protein-tethered membranes (ptBLMs) [117]. Inter alia, the well-established polyhistidine(his)-tag technology can be utilized to provide an oriented insertion of MPs into a ptBLM. But, nevertheless, those planar BLM offer boundaries and are limited in investigation techniques due to the solid support.

The presented work hence aims at combining both approaches towards a spherically shaped, therefore proteoliposome-like biomimetic model membrane system that allows for oriented MP insertion and thus expands the possibilities in MP research (Fig. 3.2). Thereby, the objective is not to replace both of the aforementioned techniques, which are perfectly suitable for, e.g., drug delivery in the case of liposomes or polymerosomes [127, 128, 266], while, on the other hand, any surface-enhanced technique, such as surface-enhanced infrared absorption spectroscopy (SEIRAS), even requires an – in this case enhancing – surface [119].

To overcome the orientation issue by simultaneously avoiding a solid support, a central particle was employed to form a ptBLM around a small, spherical, and moreover functionalized core. Named with respect to its center, the presented approach is called proteo-lipobeads (PLBs). By choosing the beads, the PLB size can be tailored to the desired measurement devices, using micrometer-sized cores for microscopic analyses and nanoparticles for UV/Vis spectroscopy. The further components are at optimum interchangeable to constitute a modular system. Then

MPs (if carrying a his-tag), lipids, and molecules to monitor the observed changes like, for example, fluorescent labels, can be freely chosen to mimic the investigated situation as well as possible. Even going further, PLBs are not confined to a single type of proteins, but might be capable to encapsulate more complex enzyme systems.

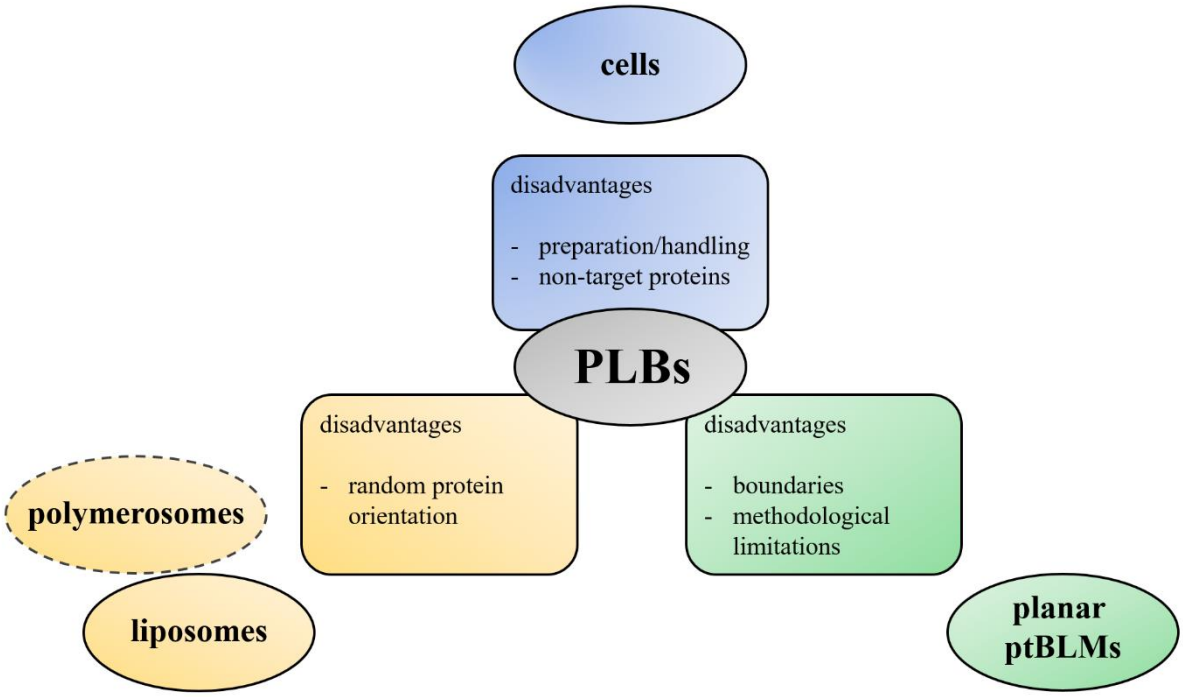

Figure 3.2: The concept of proteo-lipobeads (PLBs). PLBs are designed to overcome certain limitations associated with existing biomimetic model membrane systems.

In any case, the reported approach aims to represent not only a binding assay, but a functional integration of MPs into a dense membrane, capable of conducting a quantifiable net transport of chemical species across the lipid bilayer. A crucial point among others is to present an easy-to-use and low-cost approach (especially compared to cell culture-based approaches), capable of being applied in high-throughput assays, and thus holding potential to, e.g., pre-test promising active substances to be sorted out before going into clinical studies.

Besides applied science, basic research questions could be addressed as well, remembering, for instance, the discussed elusive questions in terms of the employed model proteins cytochrome *c* oxidase (C*c*O) [267] and the cytochrome bc_1 complex [268], which are frequently addressed by monitoring the redox status of its active site components [22, 59]. Choosing nanometer-sized central beads, PLBs could well be small enough to serve as a platform for these issues by being used in UV/Vis spectroscopy.

Chapter 4 *Materials & Methods*

This section lists any used equipment, i.e., devices, chemicals, proteins, software, labels, etc., including its origin. Furthermore, all preparation techniques and device-related evaluation techniques are outlined. The frequent specification of prepared volumes instead of giving the final concentrations only is due to the usage of several commercially available components of a certain volume, like dialysis tubes, flow cells, or UV/Vis spectroscopy cuvettes. In any case without exemption, water means purified water (18.2 MΩ/cm, see *Devices*).

4.1 Materials

4.1.1 Beads

- Agarose beads: Thermo Scientific HisPur Ni-NTA Resin, 50−150 µm, purchased from Fisher Scientific, Schwerte, Germany. Storage occurred at 4 °C
- Silica (silicon dioxide, SiO_2) beads: Nickel nitrile tri-acetic acid (Ni-NTA)-functionalized silica nanoparticles (NPs) (diameters: 25, 50, 100, and 120 nm; concentration: 25 mg/mL, quantity: 3.5 x 10^{13} beads per mg), obtained from Kisker Biotech, Steinfurt, Germany. If not explicitly mentioned, NPs with 25 nm diameter were used. The NPs were stored at room temperature.

4.1.2 Proteins

- Cytochrome *c* oxidase (C*c*O) from *Paracoccus denitrificans*: The C*c*O was kindly provided by the group of <content not available in online version> of the Goethe University in Frankfurt am Main, Germany. It was delivered including all cofactors necessary to operate, additionally containing a polyhistidine(his)-tag genetically engineered to the C-terminus of subunit I. The C*c*O was expressed and purified according to Dürr *et al.*, 2008 [269].

- Photosynthetic reaction center P870 (RC) of *Rhodobacter sphaeroides*: The RC was kindly made available by <content not available in online version> of the University of Illinois, IL, USA. The genetically modified version with a 7-his-tag at the C-terminus of the M-subunit was expressed by a strain that was allocated by the group of <content not available in online version> of the Stanford University, CA, USA, (see Goldsmith & Boxer, 1996 [270]), prepared and purified as described in Kirmaier *et al.*, 2002 [271]. It was obtained containing all associated pigments.
- Cytochrome bc_1 complex (bc_1), systematically named coenzyme Q : cytochrome *c* – oxidoreductase or ubiquinol : cytochrome *c* oxidoreductase: The bc_1 was provided by the group of <content not available in online version> as well, equipped with all associated cofactors and his-tagged at the C-terminus of the cytochrome *b* subunit. Expression and purification were done pursuant to Guergova-Kurvas *et al.*, 1999 [272].
- Cytochrome *c* (cyt *c*) from horse heart was purchased from Sigma-Aldrich, Steinheim, Germany.
- Light harvesting complex II (LHCII): The LHCII was expressed and purified in the group of <content not available in online version> of the Johannes Gutenberg University in Mainz, Germany, by myself. The apoprotein LHCP of *Pisum sativum* with a 6-his-tag attached to the C-terminus was expressed by the strain JM101 of *Escherichia coli*. The associated pigments were extracted as total extract from *Pisum sativum* according to Paulsen *et al.*, 1993 [273]. The reconstitution of the apoprotein and the associated pigments to functional LHCII monomers was done pursuant to Paulsen *et al.*, 1990 [274]. Finally, the LHCII monomers were trimerized to functional LHCII trimers according to Rogl *et al.*, 2000 [275]. A detailed description is given in Geiss, 2012 [276].

4.1.3 Lipids

- 1,2-diphytanoyl-sn-glycero-3-phosphocholine (DiPhyPC)
- *E. coli* polar lipid extract: The lipids were chloroform:methanol-extracted and partitioned against deionized water. Afterwards, the chloroform phase was concentrated, yielding a concentrated total extract. For the polar lipid extract, the total extract was precipitated with acetone and again extracted with diethyl ether. It consisted of 67 % phosphoethanolamines, 23.2 % phosphoglycerols, and 9.8 % cardiolipins.

Both were purchased from Avanti Polar Lipids (Alabaster, AL, USA).

DiPhyPC was used in most cases because of its stability. *E. coli* polar lipid extract was used to prove the ability of preparing functionally active PLBs with lipids different from DiPhyPC and at the same time choosing one that is close real-life membrane compositions. If not explicitly mentioned, DiPhyPC was used.

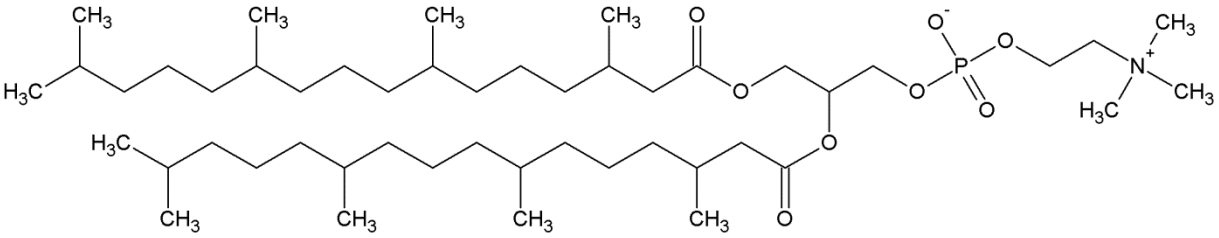

Figure 4.1: Chemical structure of 1,2-diphytanoyl-sn-glycero-3-phosphocholine (DiPhyPC).

4.1.4 Labels

All labels except from di-4-ANBDQBS (see below) were purchased from Invitrogen, Carlsbad, CA, USA (today Thermo Fisher Scientific, Waltham, MA, USA). The related product information was obtained from the Thermo Fisher Scientific homepage [277–281]. A summary of excitation wavelength and channel settings is given in Table 4.2.

- NBD-PE (1,2-dioleoyl-sn-glycero-3-phosphoethanolamine-N-(7-nitro-2-1,3-benzoxadiazol-4-yl) (ammonium salt)): The FRET (Förster resonance energy transfer) pair component NBD-PE was used without the corresponding FRET partner in terms of early proof of principle measurements, not exploiting its FRET pair-related properties. Its absorption maximum is located at 460 nm, therefore it could be excited with the 458 nm Ar laser line. The emission was recorded at 520-570 nm (maximum at 535 nm).

pH-sensitive

- Fluorescein DHPE (1-(8-((3',6'-dihydroxy-3-oxo-spiro(isobenzofuran-1(3H), 9'-(9H)xanthen)-5-yl)amino)-3-hydroxy-8-thioxo-2,4-dioxa-7-aza-3-phosphaoct-1-yl)-1,2-ethanediyl ester, P-oxide): Fluorescein DHPE is a pH-dependent fluorescent dye that intercalates into the outer leaflet of bilayer membranes by means of its lipophilic DHPE anchor. If the pH value decreases, the fluorescence intensity decreases as well. It was excited with Ar laser light of the wavelength 488 nm (absorption maximum at

485 nm). The fluorescence emission was collected at 500-600 nm (in earlier experiments at 492-610 nm).

- 5-(and-6-)-carboxy SNARF-1 (SNARF, Benzenedicarboxylic acid, 2(or 4)-[10-(dimethylamino)-3-oxo-3H-benzo[c]xanthene-7-yl]) is a water-soluble (but vulnerable towards hydrolysis), pH-sensitive fluorescent dye, whose emission maximum changes not only in intensity, but in its peak wavelength, too (580 nm at pH = 6, 640 nm at pH = 9). SNARF was excited at 514 nm with an Ar laser and the fluorescence was recorded using two channels, one at 550-610 nm and the other at 620-700 nm.

potential-sensitive

- di-8-ANEPPS (ANEPPS; di-8-butyl-amino-naphtyl-ethylene-pyridinium-propyl-sulfonate): The fluorescence dye ANEPPS was used for early staining experiments only, without utilizing its potential-sensitive properties. It was replaced by the red-shifted ANBDQBS later. It was excited by the 488 nm line of a multiline Ar laser. The fluorescence was recorded at 600-670 nm (peak maximum at 640 nm).
- di-4-ANBDQBS (ANBDQBS, 4-(1-[2-(di-n-butylamino)-6-naphthyl]-4-butadienyl)-1-(4-butylsulfonate) quinolinium betaine): ANBDQBS was kindly provided by <content not available in online version> (UConn Health, Department of Cell Biology, University of Connecticut, Farmington, CT, USA), synthesized according to Matiukas et al., 2006 [282]. ANBDQBS is a red-shifted version of ANEPPS, which was excited at 633 nm, while the emission was recorded at 685-790 nm, in earlier measurements at 651-794 nm (fluorescence maximum at 740 nm).
- FRET pair CC2-DMPE/DiSBAC$_2$(3): The exact chemical structure was not indicated by the provider, but CC2-DMPE was described to be a membrane-bound coumarin-phospholipid, acting as FRET-donor, while DiSBAC$_2$(3) was outlined as a mobile, negatively charged, hydrophobic oxonol, acting as FRET acceptor. This so-called Voltage Sensor Probes (VSP) were developed for high-throughput measurements of ion channels in terms of drug delivery systems, assuming that the membrane potential in most cells is outside positive until depolarization occurs due to the activity of the respective ion channels. In the resting state, i.e., before depolarization, the negatively charged oxonol DiSBAC$_2$(3) resides as close to the extracellular membrane side as its hydrophobic character allows, thus being in close vicinity to CC2-DMPE, which is anchored in the outer leaflet via the DMPE that acts as anchor. The close proximity enables FRET. As soon as depolarization occurs, DiSBAC$_2$(3) follows the inverted

potential gradient and moves away from the acceptor, thus interrupting the energy transfer. This results in a stronger donor and a weaker acceptor fluorescence. The maxima of the donor and acceptor fluorescence are indicated with 460 nm and 580 nm, respectively, so the channels were set to 440-480 nm and 565-620 nm. The excitation wavelength was 405 nm, emitted by a diode laser.

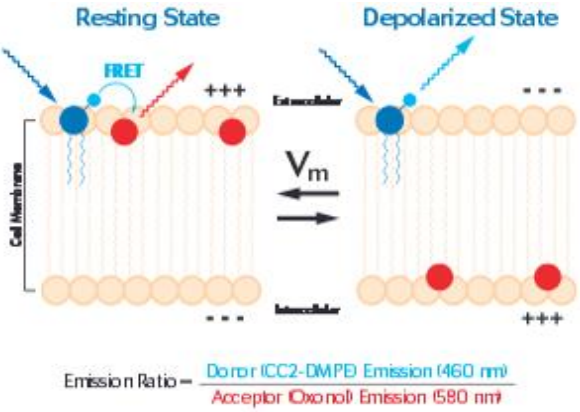

Figure 4.2: Working principle of the FRET-pair CC2-DMPE/DiSBAC$_2$(3). Figure adapted from the data sheet, available on the homepage of Thermo Fisher Scientific [281]. Further description is given in the text.

4.1.5 Ruthenium complex for light activation

The ruthenium complex, subsequently denoted as Ru$_2$C, was kindly provided by <content not available in online version> of the University of Arkansas, Fayetteville, AR, USA. The preparation process was carried out employing Ni-catalyzed coupling similar to Johansson et al., 2000 [283], but instead of 5-chlorobipyridine, the commercially available 5-chlorophenanthroline was used, yielding [(2,2′-bipyridine)$_2$Ru(diphenanthroline)Ru(2,2′-bipyridine)$_2$](PF$_6$)$_4$ instead of [(2,2′-bipyridine)$_2$Ru(quaterpyridine)Ru(2,2′-bipyridine)$_2$](PF$_6$)$_4$.

The absence of monomers was checked using ESI-MS (electrospray ionization mass spectroscopy). The absorption maximum was located at 453 nm (see below for the spectrum, Fig. 4.5)

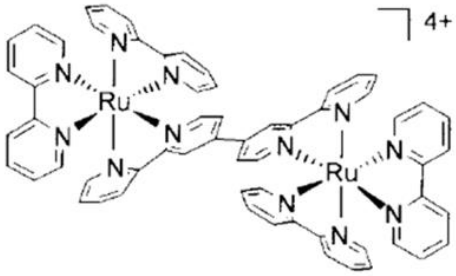

Figure 3.3: Chemical structure of the ruthenium complex [(2,2'-bipyridine)$_2$ Ru(2,2':4',4'':2'',2'''-quaterpyridine)Ru(2,2'-bipyridine)$_2$], with (PF$_6$)$_4$ as counterion. Figure adapted from Johansson et al., 2000 [283].

4.1.6 Software & PDB files

- ACD/ChemSketch was used to draw chemical structures.
- AutoCAD was used to draw beads, spherical membranes of PLBs, and ATR crystals.
- Citavi 6 was used for reference management.

- Leica Application Suite Advanced Fluorescence (LAS AF) Lite was the integrated software to operate the Leica confocal laser-scanning fluorescence microscope (see *Devices*) and to perform the first, software-related evaluation steps.
- Microsoft Office was used for text work (Word), math operations (Excel) and figure arrangements (Power Point).
- OPUS 7 was used for the analyzation of infrared (IR) spectroscopy data.
- Origin Lab 8.5 was used for evaluation processes like plotting, math operations etc.
- PDB files for protein and lipid modelling:
    - 2UXJ: Reaction center of *Rhodobacter sphaeroides* (Koepke *et al*., 2007) [92]
    - 2QJK: bc_1 complex of *Rhodobacter sphaeroides* (Esser *et al*., 2008) [284]
    - 2B4Z: Cytochrome *c* from bovine heart (*Bos taurus*) (Mirkin *et al*., 2008) [33]
    - 1QLE: Cytochrome *c* oxidase from *Paracoccus denitrificans* (Harrenga & Michel, 1999) [36]
    - dppc64: Lipid bilayer, including water molecules (Marrink *et al*., 1998) [285]

  a.-d. were accessed online via the Protein Data Bank (http://www.rcsb.org) [286, 287].

  e. is available via http://people.ucalgary.ca/~tieleman/download.html [288].

  All other molecules were drawn with ACD/ChemSketch and, if necessary, post-processed with USCF Chimera.

- Rhino 3D was used to finish and render the spherical components in PLB drawings.
- UCSF Chimera was used for the modelling of proteins, membranes and small molecules.

4.1.7 Devices

- Balance: ABT 120-5DM precision balance (Kern & Sohn, Balingen, Germany)
- Centrifuge: Heraeus Fresco 21 (Thermo Fisher Scientific, Waltham, MA, USA)
- Confocal laser-scanning fluorescence microscopy: Upright Leica TCS SP5 II microscope, equipped with a 10x dry objective (Leica, HC PL APO 10x/0.40 CS), several excitation lasers (diode laser, $\lambda = 405$ nm; multiline Ar laser: $\lambda = 458$ nm, 488 nm, and 514 nm; diode-pumped solid-state laser: $\lambda = 561$ nm; HeNe laser: $\lambda = 633$ nm), and a white light source (Leica Microsystems, Wetzlar, Germany)

- Dynamic light scattering: Zetasizer Nano ZS (Malvern Instruments, Worcestershire, UK)
- Evaporator: Vacuum thermal evaporator HHV Edwards Auto 306 (HHV, Crawley, UK)
- Fluorescence imaging plate reader: FlexStation 3 Multi-Mode Microplate Reader (Molecular Devices, San Jose, CA, USA), contracted out to SB Drug Discovery, Glasgow, UK
- Halogen lamp: Fiber-lite DC 950 (Dolan Jenner Industries, Boxborough, MA, USA)
- Infrared absorption spectrometer: Custom-made setup (see below) based on a FT-IR spectrometer VERTEX 70v (Bruker, Ettlingen, Germany), equipped with a L11316-12 Xe flash lamp module, connected via an A7969-08AS lightguide and an A11690 connector (Hamamatsu Photonics, Hamamatsu, Japan) and an as well custom-made flow cell.
- Magnetic stirrer with heatable plate: MR Hei-Tec (Heidolph Instruments, Schwabach, Germany)
- pH electrode: Seven Multi (Mettler Toledo, Columbus, OH, USA)
- Polisher: PHOENIX 4000 from Buehler (Lake Bluff, IL, USA), used with the polishing cloths TexMet P, VerduTex, MicroCloth and MetaDi Supreme, and polycrystalline diamond suspension of a grain size of 9 µm, 3 µm, and 1 µm
- Thermoshaker: PCMT Thermoshaker with Cooling for Microtubes and Microplates (Kemomed, Kranj, Slovenia)
- Ultrasonic bath: Elmasonic S10 (Elma Schmidbauer GmbH, Singen, Germany)
- UV/Vis spectrophotometer: Hitachi U-2900 (Hitachi, Tokyo, Japan)
- Vortex mixer: Vortex-Genie 2 (Scientific Industries, Bohemia, NY, USA)
- Water purification: Arium Pro UV water purification system (Sartorius Stedim Biotech, Göttingen, Germany)

4.1.8 Utensils

- Cuvettes for UV/Vis spectroscopy: Disposable poly(methyl methacrylate) (PMMA) cuvettes, light path: 10 mm (Carl Roth, Karlsruhe, Germany); 2 quartz glass cuvettes for measurements below 350 nm: Hellma 10-QS, light path: 10 mm (Hellma Analytics, Müllheim, Germany)

- Cuvettes for Dynamic Light Scattering: Disposable polystyrene cuvettes, volume: 1 mL (Carl Roth, Karlsruhe, Germany)
- Dialysis tubes: Float-A-Lyzer dialysis tubes (MWCO: 500-1000 Da, volume 5 mL) (Carl Roth, Karlsruhe, Germany)
- Flow cells: µ-slide I 0.6 Luer (ibidi GmbH, Planegg/Martinsried, Austria)
- Gel filtration: PD-10 Sephadex gel filtration columns (G-25 M) (GE Healthcare, Little Chalfont, UK)

The common lab equipment like pipettes, pipette tips, syringes, glassware etc. were taken from available stocks and are not listed in detail.

4.1.9 Chemicals

All chemicals, unless explicitly mentioned, were purchased from Sigma-Aldrich, Steinheim, Germany.

- 3,3'-Dithiopropionic acid (DTP)
- 3-(carboxy)-2,2,5,5-tetramethyl-1-pyrrolidinyloxy, 3-carboxy-2,2,5,5-tetramethyl-1-pyrrolidinyloxy, free radical (3-carboxy-PROXYL, 3-CP)
- 3-Mercaptopropyltrimethoxysilane (MPTES) (ABCR, Karlsruhe, Germany)
- Aniline
- Argon, compressed (Westfalen AG, Münster, Germany)
- Bio-beads (SM-2 Resin, 20-50 mesh) (Bio-Rad Laboratories, Vienna, Austria)
- Carbonyl cyanide 4-(trifluoromethoxy)phenylhydrazone) (FCCP)
- Dimethyl sulfoxide (DMSO, dried over a molecular sieve)
- Dipotassium hydrogen phosphate (K_2HPO_4)
- Dithiobis(nitrile tri-acetic acid butylamidyl propionate) (DTNTA) (Dojindo Laboratories, Kumamoto, Japan)
- Ethanol absolute for analysis (pro analysi, p.a.)
- Gold granules (Mateck, Juelich, Germany)
- Gold(III) chloride hydrate ($HAuCl_4$ x H_2O)
- Hydrochloric acid (HCl, 37 %)
- Hydroxylamine hydrochloride (NH_2OH x HCl)
- Imidazole (1,3-Diaza-2,4-cyclopentadiene)

- n-Dodecyl-β-D-maltoside (DDM)
- Nickel(II) chloride ($NiCl_2$)
- Nitrogen, liquid and compressed gaseous ($N_{2(l)}$, $N_{2(g)}$) (Westfalen AG, Münster, Germany)
- Potassium chloride (KCl)
- Potassium ferricyanide (potassium hexacyanoferrate(III), $K_3Fe(CN)_6$)
- Sodium dithionite (sodium hydrosulfite, $Na_2S_2O_4$)
- Sodium hydroxide (NaOH, anhydrous pellets)
- Tris(hydroxymethyl)aminomethane hydrochloride (Tris-HCl)
- Ubiquinone-10 (2,3-dimethoxy-5-methyl-6-all-*trans*-decaprenyl-1,4-benzoquinone, coenzyme Q_{10}, subsequently abbreviated UQ resp. UQH_2 for ubiquinol)
- Water (18.2 MΩ/cm), purified by an Arium Pro UV purification system (Sartorius Stedim Biotech, Göttingen, Germany)
- Valinomycin (1 mg/mL in DMSO, 0.2 µm filtered)

4.2 Methods

Since the respective kind of device (i.e., centrifuge, microscope, spectrophotometer) was represented once or originated from the same manufacturer, being of the same type, the assignment to the entries in the devices or utensils lists are unambiguous and hence, device types and origins are not mentioned within the *Methods* part. Used or common abbreviations are also outlined in the *Materials* lists.

4.2.1 Universal procedures

As of the next subchapter, preparation procedures and analyzation techniques are divided in agarose-PLBs and silica-PLBs, which differ too much to be outlined by a single legible section. Here, all preparations and analyses are described that are required in both cases.

4.2.1.1 Buffer solutions

The buffer solutions described here are afterwards only mentioned abbreviated to provide easier reading. Hence, the abbreviated expression implies equality in any respect, as well including pH value, pH adjustment etc.

- DPK buffer: DPK buffer (the original meaning of this in the laboratory established abbreviation escaped my notice) was made of 50 mM K_2HPO_4 and 100 mM KCl, adjusted to pH = 8. It was prepared as 10-fold stock solution, adjusted to the pH value of 8 using 5 M NaOH. The DPK buffer was the first choice for PLB preparation, since a high ionic strength stabilizes membranes. When proceeding with light activation of the C*c*O via a Ru complex, the buffer was changed to THK (see below), because high ionic strengths inhibits the Ru complex binding at the respective binding site. Thenceforward, the THK buffer became the standard buffer used in all further experiments performed within the covered pH range, except from IR spectroscopy, at which previously published studies using DPK buffer were adopted.
- DDM/DPK buffer: DDM/DPK buffer comprised the same ingredients as the DPK buffer, only containing 0.1 % of DDM in addition. Thereunto, a stock solution, of 10 % (w/v) DDM, dissolved in purified water, was used. The buffers containing DDM were used to keep membrane proteins and lipids solubilized prior to membrane formation. Afterwards, only DDM-free buffer was used to prevent the anew solubilization of the membrane lipids.
- THK buffer: 5 mM of Tris-HCl, 35 mM KCl, prepared as 10-fold stock solution and adjusted to pH = 8 using 5 M NaOH. The potassium chloride was used to provide a certain ionic strength that favors the membrane stability. The concentration was chosen as compromise between a lower one that might destabilize the membrane and a higher one that inhibits the binding of the Ru complex used to activate the C*c*O by light. To remain comparable, the THK buffer replaced the DPK buffer also if no light activation was performed.
- DDM/THK buffer: THK buffer with 0.1 % DDM. The DDM stock solution and its purpose is described within the DDM/DPK section.
- Citrate/THK buffer: To measure pH calibration curves in a range of pH = 3-10, which is not covered by Tris alone, 40 mM of citrate were added to THK buffer (see above).

The pH adjustment was done with 5 M NaOH towards the alkaline and 10 % HCl towards the acidic direction.

- Acetate buffer: 50 mM sodium acetate at pH = 5.5, adjusted with 1 M NaOH, used for the functionalization of the ATR crystal surface in infrared spectroscopic measurements.

4.2.1.2 Aliquots

The protein stock solutions obtained by the cooperation partners (see *Proteins* section) were aliquoted in portions of 50 µL of 10 µM. The concentration was determined by UV/Vis spectroscopy as described below. The buffer was in any case DDM/THK to avoid precipitation or damage by uncontrolled pH changes, e.g., as a result of acidification via air CO_2, forming carbonic acid in aqueous solution. Due to strong dilution prior usage, buffer exchanges were not implemented. The initial stock of C*c*O aliquots, used for silica-PLBs, turned out to have a concentration of 7 µM.

4.2.1.3 Preparation of cytochrome c *solution*

Cyt *c* from horse heart was obtained as solid powder in oxidized state. Around 30 mg were weighted and dissolved in 1 mL of THK or DPK buffer. At this point, it served as oxidized cyt *c* solution.

Reduced cyt *c* was prepared by adding a narrow spade point of sodium dithionite, intermixed by vortex mixing. The reduction takes place instantly after addition, which was clearly visible due to the rapid color change from dark to light red. To avoid too high concentrations of dithionite, two additions were preferred over adding a larger amount at once.

After that, the dithionite was removed by applying the sample to a PD-10 Sephadex gel filtration column. Subsequent collecting was done manually and with naked eye. The deep red droplets were taken up by an Eppendorf tube. The collected volume did not exceed 1 mL to avoid unnecessary dilution.

The concentrations of both solutions were determined by means of UV/Vis spectroscopy (see below).

4.2.1.4 Determination of protein concentrations

The protein concentration was determined by UV/Vis spectroscopy. The used standard PMMA cuvettes provided a path length of 1 cm and transmitted down to 340 nm, which was sufficient for the protein concentration determinations. The spectral range was 350-750 nm, only in case of the RC, spectra were taken up to 820 nm (main maximum at 802 nm). If required, the samples were diluted to a extinction of less than 1 at the wavelength of interest. A reference channel was present, and the reference spectrum was automatically subtracted. A baseline was recorded at the beginning of each session and subtracted manually during downstream evaluation.

In case of cyt *c*, the RC and the LHCII, the concentration could be regularly determined by using the Beer-Lambert law (eq. 4.1) and the extinction coefficients given in Table 4.1.

$$A = \varepsilon c d \tag{4.1}$$

Here, A is the absorbance (sometimes denoted as E for extinction), ε the extinction coefficient, c the concentration, and d the path length. For a detailed discussion, see *Chapter 2: Absorption*, with the Beer-Lambert law as eq. 2.31.

In case of C*c*O and bc_1, difference spectra of reduced and oxidized enzymes had to be calculated. For reduction, a few grains of sodium dithionite were admixed by gentle inversions. Due to the immediate reduction, the sample had to be measured directly afterwards, as the dithionite hydrolyzed shortly after getting in contact with water, and the hydrolysis product strongly superimposed the spectra due to huge absorption. To ensure that the amount of dithionite was sufficient to completely reduce the protein of interest, more grains were be added step by step, until no changes occurred any more.

For oxidation, potassium ferricyanide ($K_3[Fe(CN)_6]$) was used, also by admixing a few grains. The ferricyanide spectrum widely overlapped others at shorter wavelengths, but in all mentioned cases, the desired wavelength was not within the affected region. It turned out that the samples were already oxidized by time, so if samples were scarcely available, they were measured untreated to obtaining the spectra of the oxidized states and afterwards reduced with dithionite as described above to record the spectra of the reduced sample. This was, for example, the case if formerly attached proteins were eluted again from proteobeads to determine the amount of protein that was attached.

To calculate the difference spectra, the values of A were firstly subtracted as described in Table 1. The result was then used as A in the Beer-Lambert law (eq. 4.1).

Table 4.1: Extinction coefficients of the used proteins.

Protein	ε_λ [$mM^{-1}\,cm^{-1}$]	Reference
Cytochrome *c* (reduced)	$\varepsilon_{550\,nm} = 27.7$	Margoliash & Frohwirt, 1959 [289]
Cytochrome *c* (oxidized)	$\varepsilon_{528\,nm} = 11.2$	Margoliash & Frohwirt, 1959 [289]
Cytochrome *c* oxidase	$\varepsilon^{\,reduced-oxidized}_{606-630\,nm} = 23.4$	Ludwig & Schatz, 1980 [290]
Reaction Center P870	$\varepsilon_{802\,nm} = 288$	Straley et al., 1973 [291]
Cytochrome bc_1 complex	$\varepsilon^{\,reduced-oxidized}_{562-575\,nm} = 25.6$	Hielscher et al., 2009 [292]
Light Harvesting Complex II	$\varepsilon_{670\,nm} = 546$	Butler & Kühlbrand, 1988 [293]

4.2.2 General PLB preparation scheme

Due to their differences in size, agarose-PLBs and silica-PLBs were prepared and analyzed differently. Therefore, the methodological description is divided in two separated parts. To give a general overview, the process of PLB formation is depicted schematically in Figure 4.4.

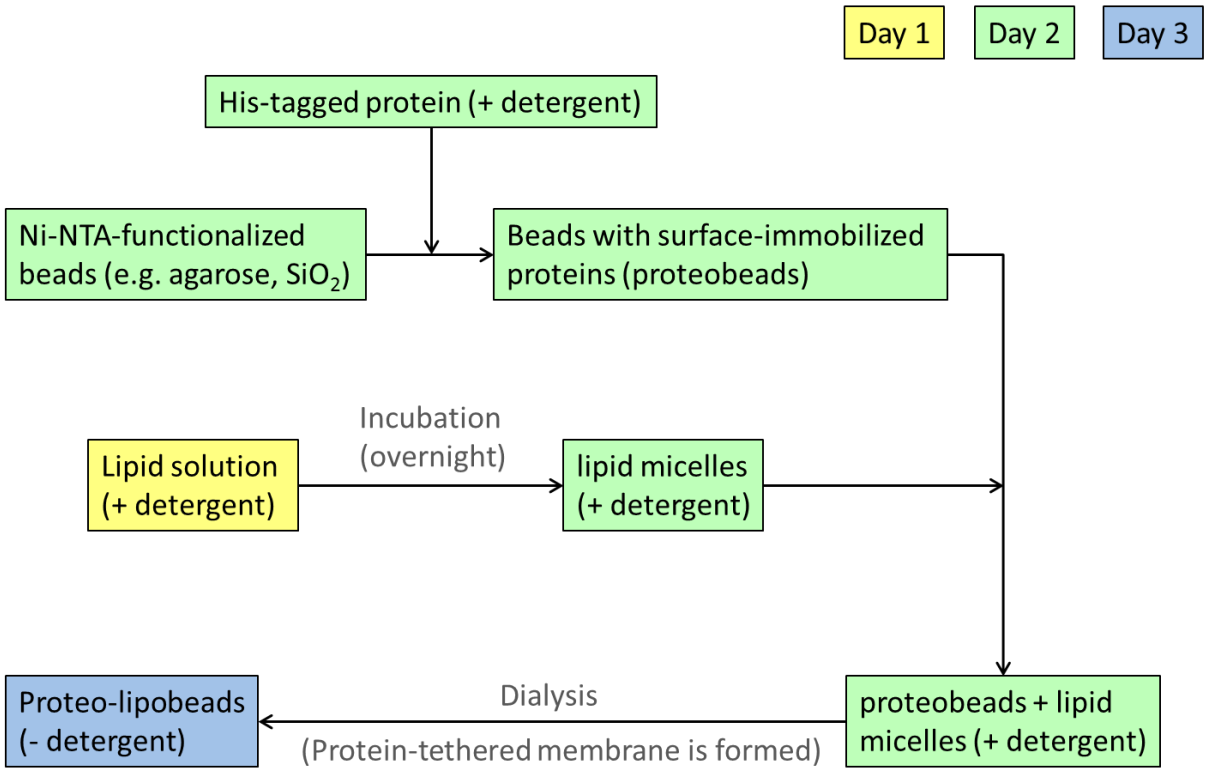

Figure 4.4: Scheme of the PLB preparation procedure.

Please note that the detergent removal by dialysis was not twenty-twenty, but turned out to be sufficient.

4.2.3 Agarose-PLBs (incl. comparative ptBLM measurements)

4.2.3.1 PLB preparation

4.2.3.1.1 Preparation of the lipid suspension

DiPhyPC was obtained as chloroform solution at a concentration of 10 mg/mL. A stock solution was prepared by evaporating the chloroform under a stream of nitrogen in a glass pear-shaped flask. If needed, UQ was added to the lipid stock solution prior to the chloroform evaporation. To that end, the UQ powder was dissolved in chloroform at a concentration of 1 mg/mL and then added to the lipid solution at a ratio of 0.153 mg per mg DiPhyPC. The dried DiPhyPC was re-suspended in THK or DPK buffer at a final DiPhyPC concentration of 1 mg/mL (0.153 mg/mL UQ, if added), corresponding to 1.182 mM (and 177.36 mM UQ), by vigorous treatment on the vortex mixer and subsequent welling in a 30-40 °C warm water bath for 2 hours. Afterwards, the suspension was again thoroughly vortexed for 10 min. The stock solution was stored at -20 °C until needed.

In case of the *E. coli* polar lipid extract, which was obtained as powder, a chloroform solution was made at a concentration of 1 mg/mL. In the following, it was treated like the DiPhyPC. A combination of *E. coli* lipid mixture and UQ was not used.

To obtain the required lipid micelle suspension, the lipid stock solution was thawed and rapidly vortexed for 10 min. Thereafter, the respective membrane-forming lipid was added to DDM/THK or DDM/DPK buffer at a final concentration of 40 µM. If UQ was added to the DiPhyPC stock solution, its final concentration was 6 µM. Keeping in mind that the volume of the dialysis tube is limited to 5 mL, the recommended volume of lipid micelle suspension for one PLB preparation is 3.5 mL. With respect to the aforementioned detail, the used volumes are specified in the PLB preparation protocol. The same applies later for UV/Vis spectroscopy and fluorescence microscopy measurements because of the volumes of standardly used cuvettes or flow cells. The lipid suspension was incubated overnight at 4 °C.

4.2.3.1.2 Protein attachment / Formation of proteobeads

500 µL of homogenously suspended agarose beads were taken out of the bottle as obtained from the supplier. Repeated rinsing was performed by adding 1 mL of buffer, centrifugation (1 min, 1.5 x 10^3 g), discarding the supernatant and refilling with 1 mL of buffer. This was done three times with THK and afterwards three times with DDM/THK buffer. After the last refill, the agarose bead pellet was re-suspended and 5 x 10^{-10} mol of the desired protein were added within 50 µL of a 10 µM stock solution aliquot. In the special case of PLBs encapsulating two different species of protein, an aliquot of each were premixed (to provide an equal distribution in case of a rapid binding process) and then added, hence the final quantity of each was 5 x 10^{-10} mol, while the total protein amount was 10^{-9} mol. After an incubation time of 2 hours during gentle pivoting on a thermoshaker (fixed on top lying to provide better mixing), the rinsing process described above was repeated three times with DDM/THK buffer to remove unbound as well as nonspecifically adsorbed proteins. The resulting agarose beads with attached, still DDM-solubilized proteins are subsequently called proteobeads.

4.2.3.1.3 Determination of the amount of immobilized protein

To determine the amount of the finally attached protein, a proteobead sample was centrifuged (1 min, 1.5 x 10^3 g), then the pellet was re-suspended in 425 µL DDM/THK buffer that contained 300 mM of imidazole in addition to remove the his-tagged protein from the Ni^{2+} again. After an incubation time of 1 hour on a gently pivoting stage (of a thermoshaker), the procedure including incubation was repeated once. The supernatants were collected and unified. To avoid agarose beads within the light path of the UV/Vis spectrometer, the unified supernatants were centrifuged once more as described above. Only 800 µL of the supernatant were collected this time. The volume was chosen with respect to the size of the UV/Vis cuvettes and to avoid unnecessary dilution, so the final volume of 800 µL was just enough to perform the one UV/Vis determination (with untreated sample as oxidized one), which is described in detail in the UV/Vis section.

4.2.3.1.4 Dialysis / Formation of PLBs

A dialysis tube was filled with the proteobead suspension after rinsing and welling for half an hour filled with water. Then, 3 mL of the lipid micelle suspension, containing 40 µM DiPhyPC or *E. coli* polar lipid extract (and possibly 6 µM UQ), which had been incubated overnight at 4 °C, were added. In early experiments, PLBs were stained with NBD-PE. In this case, NBD-PE was dissolved in chloroform (1 mg/mL) and added to the lipid micelle suspension directly prior filling the dialyses tube at a final concentration of 12.2 µM. By careful inversion, the sample was mixed. The sample was subjected to dialyses in 1 liter of DDM-free THK buffer at room temperature while gently stirring with a magnetic stir bar. The dialysis took place for 24 hours, within which the buffer was exchanged three times, namely after 2, 4 and 10-14 hours. The third dialysis period, i.e., the overnight step, took place in 2 L of THK buffer.

After completion, the sample was re-suspended, removed from the tube with the help of the provided plastic pipette and stored at 4 °C. Concerning the durability of the PLBs, please see the corresponding *Results & Discussion* part. In general, except from the durability tests, the PLBs were used within the same week or discarded. To remove PLB samples, the pipette tip was dipped into the deposit, which was settled over time, then imbibing the desired volume like it was a solution.

4.2.3.2 Determination of the PLB mass within a sample

For later calculations it was crucial to differentiate between PLB deposit and pellet. The deposit of PLBs was settled over time. Samples of deposited PLBs were taken out of the storage vessel by dipping the pipette tip into the deposit. The deposit was containing a lot of buffer and the PLBs could be imbibed by the pipette like a solution. The deposit was less dense and presumably, the removal did not damage the PLBs. So, this was done to further use the PLBs in an intact condition. To determine the mass of PLBs within the PLB deposit, 40 µL of PLB deposit, corresponding to the volume of a standard sample measured by LSM within a 400 µL flow cell, were centrifuged harshly at 5.25 x 10^3 g for 10 min, then the supernatant was removed carefully. This was repeated several times, until the more or less dry pellet (not possible to imbibe any more) remained. This dry condition was actually easy to differentiate from the fluid-like deposit condition. The mass of PLBs was determined by weighing beforehand and afterwards. The same was done with agarose beads, using 500 µM of the re-suspended bead

stock according to the initial volume for a standard PLB preparation. The dry pellets were not further used.

4.2.3.3 Deep-freezing of agarose-PLBs

For durability tests, PLBs were deep-frozen. Before freezing, 10 % (v/v) DMSO was added to prevent the formation of ice crystals that might perturb the membrane and protein integrity. Since DMSO is able to penetrate the membrane, this applied also for the interior of the PLBs. The tube containing the PLBs was placed inside a deware and then flooded with liquid nitrogen to avoid Leidenfrost phenomena. (Vaporized nitrogen forms an insulating layer between the sample and the liquid nitrogen. By rapidly pouring the liquid nitrogen over the sample, the gaseous layer is supposed to be displaced quickly by liquid nitrogen to provoke amorphous freezing.) Unfortunately, critically slow temperature and thus phase transitions potentially leading to harmful crystal formation will occur nevertheless when thawing. For that reason, the addition of DMSO was considered to be indispensable. Further storage occurred at -20 °C. One batch was shock-frozen immediately after preparation and stored at -20 °C, another was stored at 4 °C. Samples were measured (by confocal laser-scanning fluorescence microscopy, see below) directly after preparation and after two weeks of storage (which implies that one of the immediately measured samples underwent a freeze-thaw cycle, while the other simultaneously represented the freshly-prepared status, being at preparation, i.e., room temperature).

4.2.3.4 Confocal laser-scanning fluorescence microscopy

4.2.3.4.1 Preparation of the Ru complex solution

C*c*O activation by light occurred via Ru_2C, which is described in the respective *Materials* section. Therefore, a stock solution of 2.5 mM Ru_2C in acetonitrile was prepared. Moreover, to refill the electron holes, a 500 mM stock solution in ethanol of the sacrificial electron donor aniline was made. To prevent proton release from the latter, which would distort quantitative analyses, a stock solution of 50 mM 3-CP in methanol was prepared. Finally, one part of each stock solution was mixed with 7 parts of THK buffer. All of the solutions were stored at 4 °C. In any case, the solutions were protected from light as well as possible. The volume applied to a sample of 400 µL was 10 µL.

4.2.3.4.2 PLB staining & treatment with uncoupling agents

Most of the employed label molecules interact with the membrane, e.g., the ones that intercalate into the outer leaflet like fluorescein DHPE and ANBDQBS, which have a lipophilic anchor molecule attached (for details concerning the dye molecules, please see *Labels* in the *Materials* section). For that reason, it is not reasonable to mention final dye concentrations, since this would relate to the initial concentrations of dye molecules to the 400 µL of flow cell content. Those dyes would, in contrast, not distribute equally within the flow cell, but accumulate inside or attached to the membrane (and the residuals of lipophilic solvents) of an uncertain volume. Because of this unequal distribution, these fluorescence dyes exhibit negligible fluorescence emission in aqueous solution [294], which was of advantage in terms of signal-to-background ratio and effective concentrations.

If uncoupling agents were used to verify the presumed membrane denseness or as negative control measurements, the 40 µL of PLB deposit mentioned below were incubated in 1 mL of the respective buffer containing 0.5 µM valinomycin and 1.2 µM FCCP for 30 min at room temperature before staining.

Fluorescein DHPE, ANEPPS & ANBDQBS

In case of fluorescein DHPE, a stock solution was prepared in chloroform at a concentration of 1 mg/5 mL. It was stored at -20 °C.

In case of ANEPPS and ANBDQBS, the stock solution was made of ethanol, but otherwise at the same concentrations and storage conditions.

In each case, 20 µL of the respective stock solution were added to 40 µL of PLB deposit, which was taken up in 940 µL of the respective buffer before. The PLB suspension containing the dye molecules was incubated for 20 min at room temperature during rapidly shaking, lying flat on the shaking plate of a thermoshaker. Afterwards, the chloroform, if contained, was separated. Since it is significantly denser than the aqueous suspension, the latter was imbibed immediately after the chloroform had settled. Small residuals of chloroform turned out to not harm the sample. The PLBs were washed three times in dye-free THK buffer by centrifugation (1.5×10^3 g), removal of the supernatant and refill with buffer. Since the PLB content was considered in calculations later, not losing any PLBs was preferred over precise supernatant removal, hence only 800 µL were removed of each 1 mL added. Due to the aforementioned negligible

fluorescence in aqueous solution of these labels, putative excesses of free dye molecules did not result in strong background signals.

After the last rinsing, only the corresponding volume of buffer was removed to obtain a final volume of stained PLB suspension of 400 µL minus 40 µL for cyt *c* and 10 µL for Ru_2C/aniline/3-CP solution, if one or both were needed.

FRET pair CC2-DMPE/DiSBAC$_2$(3)

The FRET pair CC2-DMPE/DiSBAC$_2$(3) was opened and dissolved like described in the manual available at the homepage of Thermo Fisher Scientific [281]. After it had reached room temperature and was tapped to settle the contents, the flasks containing 1 mg of powder were carefully opened while wrapped in a wet tissue to avoid electrostatic charging, due to which the powder might be dropped out unintendedly. The powder was dissolved by adding 233 µL of DMSO to CC2-DMPE and 191 µL to DiSBAC$_2$(3), followed by vigorous vortex mixing for 1 min, ultrasonication for 1 min and incubation inside a 37 °C warm water bath for 1 min. The contents were transferred into Eppendorf tubes, having a concentration of 5 mM CC2-DMPE and 12 mM DiSBAC$_2$(3), respectively. The stock solutions used for labelling were obtained by diluting both solutions with DMSO to a final concentration of 500 µM, which were devided in reasonable portions to avoid unnecessarily many freeze-thaw events, and stored at -20 °C.

40 µL of PLB deposit were diluted to 380 µL with the desired buffer. 16 µL of CC2-DMPE stock solution were added, then the PLBs were incubated for 30 min lying on the shaking plate of a thermomixer. Subsequently, the PLBs were rinsed only once as described before (1 min of centrifugation at 1.5 x 10^3 g, discarding the supernatant, refilling with to the initial volume), prior to the addition of 4 µL of DiSBAC$_2$(3). Afterwards, incubation and rinsing (once) were repeated. Subsequently, the respective volume of buffer was removed to obtain a final volume of 400 µL minus 40 µL for cyt *c* and 10 µL for Ru_2C/aniline/3-CP solution, if one or both were needed.

NBD-PE

NBD-PE was added during the PLB preparation, see *Dialysis / Formation of PLBs*. Since it was only used for staining purposes, 40 µL of stained PLB deposit were diluted to 400 µL.

SNARF

A stock solution of 1 mM SNARF was prepared in water-free DMSO. 40 µL of PLB deposit were stained by 20 µM SNARF in a final volume of 400 µL. Due to the risk of hydrolysis, the labelling occurred directly prior the flow cell preparation.

Antibody Staining

The antibody staining was done prior to this work by <content not available in online version>. It is mentioned here for two reasons: First, it is presented in a shared publication that resulted from collaboration in other published results. Second, it is shown to compare with later results (see LHCII-based staining) and to be comprehensive in terms of the measurements that were performed with PLBs. Briefly summarized, a polyclonal primary immunoglobulin G (IgG)-antibody originating from rabbit that bound specifically to both SU I and II was applied to C*c*O-based PLBs. In a second step, a Cy5-conjugated secondary antibody was attached to the primary IgG. The Cy5 label was excited with light of a HeNe laser, emitting at 633 nm. The fluorescence emission was detected at 650-700 nm. To compare protein and lipid staining, the Cy5-labelled C*c*O encapsulated in PLBs was monitored in the presence and absence of ANBDQBS, respectively.

PLB staining by co-reconstitution of the LHCII

The LHCII auto-fluorescence (due to the associated chlorophyll pigments) was exploited to visualize protein and lipid parts separately on one image by recording the fluorescence emission via different channels. Therefore, the LHCII was co-reconstituted with another protein as described in the respective section. Afterwards, samples were labelled with the desired dye as described in that section. The channel settings are given in Table 3.1. The images were superimposed, which can be done by means of the LSM software LAS AF Lite.

4.2.3.4.3 Flow cell preparation

The samples were measured in disposable flow cells, which are specified in detail in the *Material* section. The stained PLB suspension was spiked with cytochrome *c* if necessary. For that reason, a 200 µM stock solution of both reduced and oxidized cytochrome *c*, dissolved in the respective buffer, was prepared according to the respective section. 20 µL of each stock solution were added to the PLB suspension (yielding a final concentration of 10 µM each), simultaneously achieving a final volume of 400 µL (corresponding to the flow cell volume) in

any case. The sample was injected into the flow cell with a cannula-free syringe that matched the aperture size of the flow cell. The flow cell was closed with the enclosed closures and, if desired, additionally by wrapped with parafilm. In any case, the filled flow cells were transported light-protected in a box to harm the fluorophores as slight as possible.

4.2.3.4.4 Measurements

Imaging

The excitation and recording wavelengths (abbreviated λ_{ex} and λ_{rec}, the latter sometimes referred to as λ_{em}) for each single fluorophore are collected in Table 4.2. Round brackets indicate alternative settings of early experiments. Squared brackets give the single recording wavelength used in the FLIPR assay. Slashes separate the wavelength ranges of two channels used simultaneously. All lasers were integrated in the LSM microscope. The bright field channel was activated in addition at all times.

Table 4.2: Excitation and recording wavelengths of the labels. For description see text.

Label name	Excitation wavelength	Channel wavelength range
Fluorescein DHPE	488 nm	500-600 nm (492-610 nm)
ANEPPS	488 nm	600-670 nm
ANBDQBS	561 nm (633 nm)	685-790 nm (651-794 nm)
NBD-PE	458 nm	520-570 nm
FRET donor: CC2-DMPE	405 nm	440-480 nm [460 nm]
FRET acceptor: $DiSBAC_2(3)$	405 nm	565-620 nm [590 nm]
SNARF	514 nm	550-610 nm / 620-700 nm
LHCII	488 nm	650-700 nm
Cy5	633 nm	640-680 nm

Images were recorded with a scanning resolution of 1024 x 1024 pixel. In case of time-resolved measurements, the scanning resolution was intentionally lower (684 x 684 pixel) to obtain a higher temporal resolution. That resulted in a temporal resolution of 1.3 s per image.

Triggering of enzyme activity

The activity of the bc_1 complex was induced by UQH_2 that was produced by the RC, which is, as photosynthetically active protein, excitable by light. So, the proton pumping activity that was finally measured was indirectly activated by white light. To that end, a 150 W halogen lamp was used and placed in closest vicinity of the sample. The effective intensity was not determined, but turned out to be likely not the limiting factor (see *Results & Discussion*). The excitation periods with the halogen lamp can be deduced from the results (in most cases several intervals of 60 s).

The C*c*O was as well activated by light via the Ru complex (Ru_2C), which binds at the cyt *c* binding site and is able to forward electrons to the C*c*O upon light excitation (absorption maximum at 453 nm) [38]. As mentioned before, the Ru_2C was applied together with an excess of aniline as sacrificial electron donor and 3-CP to prevent proton release from aniline, which would distort the measurements that aims to determine proton transport rates across the membrane via fluorescein fluorescence emission intensity [62]. The preparation of this solution is described above. At first, the inducement was also achieved by the halogen lamp like described above in terms of the RC. Later, it was realize that the imaging laser itself (488 nm) is capable to excite Ru_2C at the edge of the emission peak (Fig. 4.5). The effective intensity as possibly limiting factor is discussed in the *Results & Discussion* part. Eventually, the 488 nm laser was used to excite both the fluorescein and the Ru_2C. If another label was used, the 488 nm laser was used for excitation additionally. On the one hand, the laser excitation was preferred since it avoided illumination artefacts and was expected to be better reproducible in terms of effective intensity, and, on the other hand, this kind of excitation would occur in addition anyway. (The RC excitation via laser failed because of its near infrared maximum at 870 nm, at which no laser was available, nor was any that corresponded to smaller absorption peaks of the RC.)

Bleaching controls were performed without Ru_2C and without co-reconstituted RC, respectively. Control measurements related to the sealing properties of the membrane, hence to correlate measured effects to protons translocated across the membrane, was done by adding the uncoupling agents valinomycin and FCCP at concentrations of 0.5 and 1.2 µM, respectively.

In addition, the proposed cooperation of RC and bc_1 was checked by control measurements without cyt *c*.

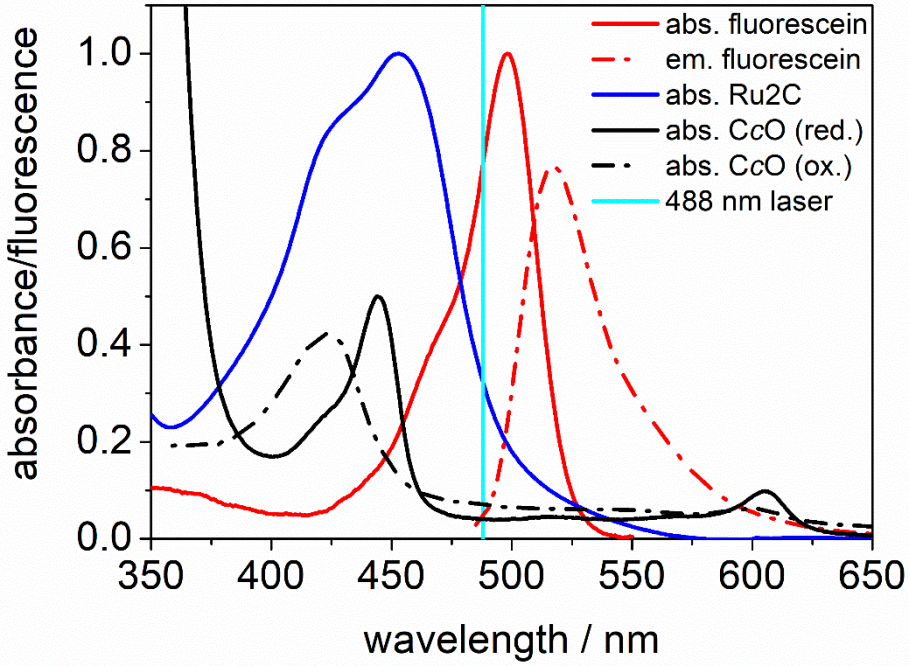

Figure 4.5: Spectra of the components used in Ru_2C excitation measurements. Qualitative representation, values are arbitrary. Figure published in Geiss *et al.*, 2017a [295].

The spectra of the components involved in the measurements using Ru_2C excitation is summarized in Figure 4.5. The small differences of the spectra assigned to the C*c*O oxidation state were not presumed to distort the results, since in any case the fluctuations of spectral changes due to reduction and reoxidation exceeded the temporal resolution by far.

4.2.3.4.5 Software-related evaluation

The superimposition of different channels and the integration of a scale bar was an installed function of the software that could be added using the respective button.

The time-resolved measurements were evaluated by plotting the fluorescence emission intensities as a function of time. To obtain the intensities assigned to the membrane region (remembering that the fluorophore is located outside in the case of the anchored labels fluorescein DHPE, ANBDQS and ANEPPS), "regions of interests" (ROIs) had to be specified at both sides of each PLB membrane (ROI_{out}, ROI_{in}). The implementation of the latter is depicted in Figure 4.6.

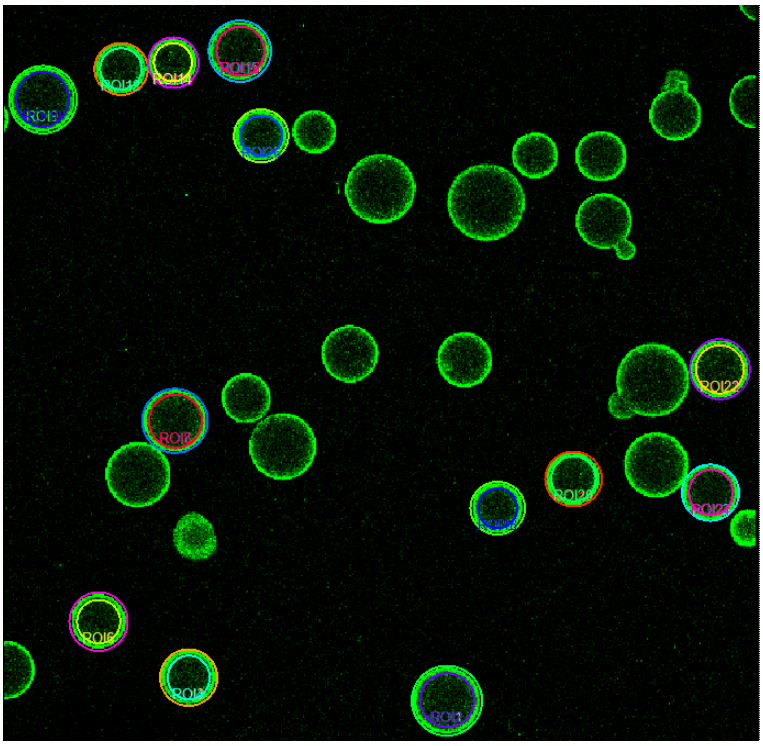

Figure 4.6: Measurement software-related evaluation of intensity courses. The representative sample was stained with fluorescein DHPE. To obtain the intensity changes at the outside of the membrane (where the fluorophore is located), "regions of interests" (ROIs) were specified, one at the outer edge of each PLB (ROI_{out}) and one at the inner one (ROI_{in}).

For each ROI, the intensity data over time could be exported as Microsoft Excel file. Since the intensities were displayed as average intensities (I_{av}), the pixel count (PC) needed to be exported as well. The intensities assigned to the PLB membranes were then calculated via equation 4.2.

$$I_{membrane} = I_{av}(ROI_{out})\ PC(ROI_{out}) - I_{av}(ROI_{in})\ PC(ROI_{in}) \qquad (4.2)$$

This was done for each time point of each PLB. Afterwards, the average of usually 10 PLBs was calculated and plotted vs. time. The initial intensity at t = 0 was normalized to 1 to provide comparability. If the measurement curves started with a plateau, a reasonable amount of data points were averaged to set the plateau to I = 1.

4.2.3.5 Fluorescence imaging plate reader assay

The fluorescence imaging plate reader (FLIPR) assay was contracted out to SB Drug Discovery (Glasgow, UK). The PLBs were deep-frozen using liquid nitrogen as described in the respective section and sent on dry ice. There, a high-throughput assay was performed using 96-well plates to investigate the potential response of C*c*O-PLBs due to reduced cyt *c* activation over a range

from 0 to 100 µM of cyt *c*. (The activation could not be done using the Ru_2C complex due to spectral overlap with the FRET pair). The potential was measured by monitoring the fluorescence intensities of the FRET pair CC2-DMPE/$DiSBAC_2(3)$ at 460 and 590 nm, respectively. The implementation and evaluation was done according to the protocol of SB Drug Discovery that is usually applied in case of such standard high-throughput assays commonly performed for transporter and ion channel screening in whole cell recordings [263, 296, 297]. The aim of this measurements was to test the applicability of PLBs in high-throughput assays, while the finally obtained EC_{50} value does not provide any useful direct information.

4.2.3.6 Surface-enhanced infrared absorption spectroscopy

The experiments described here were performed by the exchange internship student <content not available in online version> (Indian Institute of Technology Kanpur, Uttar Pradesh, India). The experimental part is nevertheless comprised by this thesis, since these measurements were performed as control experiments towards the above-mentioned LSM measurements and further on, the evaluation, discussion and publication within a bigger picture was done by myself, with the kind advice of <content not available in online version> of the University of Vienna, Austria.

4.2.3.6.1 Preparation of the two-layered gold surface

The trapezoid single-reflection silicon ATR (attenuated total reflection, see *Reflection* in the *Theory* part) crystal surface was polished at first using four different polishing cloths in consecutive order, i.e., TexMet P, VerduTex, MicroCloth and MetaDi Supreme, and then with polycrystalline diamond suspension with a grain size of 9 µm, 3 µm, and 1 µm. The polished trapezoidal AFM crystal was cleaned in an ultrasonic bath for 15 min with ethanol. To anchor the gold layer, the crystal was immersed in a 10 % ethanolic MPTES solution for 1 h. Subsequently, it was thoroughly rinsed with ethanol, dried in a stream of argon and baked at 100 °C for another hour. When cooled down to room temperature, it was immersed in water and subsequently dried in a stream of argon again.

By electrochemical evaporation, a gold film of 25 nm thickness was deposited. Afterwards, the surface was rinsed with ethanol and then dried under a stream of argon. In a second step, gold nanoparticles were grown on top of the gold layer. The AFM crystal was immersed into 50 mL

of a 0.4 mM aqueous hydroxylamine hydrochloride (NH_2OH x HCl) solution. 500 µL aqueous 0.3 mM gold(III) chloride ($AuCl_3$) was added 5 times in intervals of 2 min. To terminate the growth process, the sample was removed from the growth solution, rinsed with water and dried gently with argon. The resulting two-layered gold surface provides a rough gold nanoparticle surface that enables surface enhancement. The procedure was adapted from Nowak *et al.*, 2009 [298].

4.2.3.6.2 Immobilization of the protein & ptBLM formation

According to the technique described previously by Nedelkowski *et al.*, 2013 [119], the RC, carrying a 7-his-tag at the C-terminus of subunit M (what was of importance, since the cytochrome *c* binding site is thus, although different from nature, directed to the outside of the membrane; hence, it was accessible for the later added cyt *c*) and bc_1, poly-his-tagged at the C-terminus of the cyt *b* SU (so the cyt *c* binding side was as well pointing outside), were attached to the surface. For 20 h, the gold surface was submerged in a water-free DMSO solution (kept water-free by storing over a molecular sieve, taken out with a syringe by piercing the cannula through the closing membrane at the bottle opening) containing a mixture of 2.5 mM DTNTA and 7.5 mM DTP. After rinsing with ethanol and water, the sample was immersed in solution of 40 mM $NiCl_2$, dissolved in acetate buffer, for 30 min. Excess $NiCl_2$ was removed by thorough rinsing with water. The Ni^{2+}-NTA-functionalized crystal was dried with argon again and then mounted to the measurement chamber inside the spectroscope. It was rehydrated again with DDM/DPK buffer, which was fed into the flow cell. RC and bc_1, as well solubilized in DDM/DPK buffer, were added at a final concentration of 100 nM each and incubated at 28 °C for 4 h. The removal of unbound and nonspecifically bound proteins was effected by rinsing with DDM/DPK buffer.

The preparation of the DiPhyPC/UQ suspension is described in *Preparation of the lipid suspension* within the PLB preparation section. It was applied via the flow cell. Subsequently, the DDM was removed by the addition of bio-beads to the lipid/detergent suspension to form a ptBLM. Depending on the flow cell volume, a larger volume might be required. Finally, 100 µM cyt *c* were added (50 µM reduced, 50 µM oxidized) to serve as electron shuttle between RC and bc_1.

4.2.3.6.3 Measurements

Surface-enhanced infrared absorption spectroscopy (SEIRAS) measurements were performed at the custom-made setup displayed in Fig. 4.7, based on a VERTEX 70v Fourier transform infrared (FTIR) spectrometer as described in the *Devices* section. (Some parts were integrated to enable electrochemical excitation, which was not used here.) The flow cell was mounted on the trapezoid single-reflection silicon ATR crystal that was functionalized as described above. The infrared light beam was coupled in at an angle of incidence of $\theta = 60$ deg. According to the principles of ATR, transversal electric(TE)-polarized light (also referred to as s- or σ-polarized) does not penetrate the gold layer. Therefore, all measurements were performed with transversal magnetic(TM)-polarized light (same as p- or π-polarized light). The intensity of the totally reflected IR beam was measured using a photovoltaic mercury cadmium tellurite (MCT) detector, which was cooled with liquid nitrogen. The excitation of the RC was performed with a Xe flash lamp.

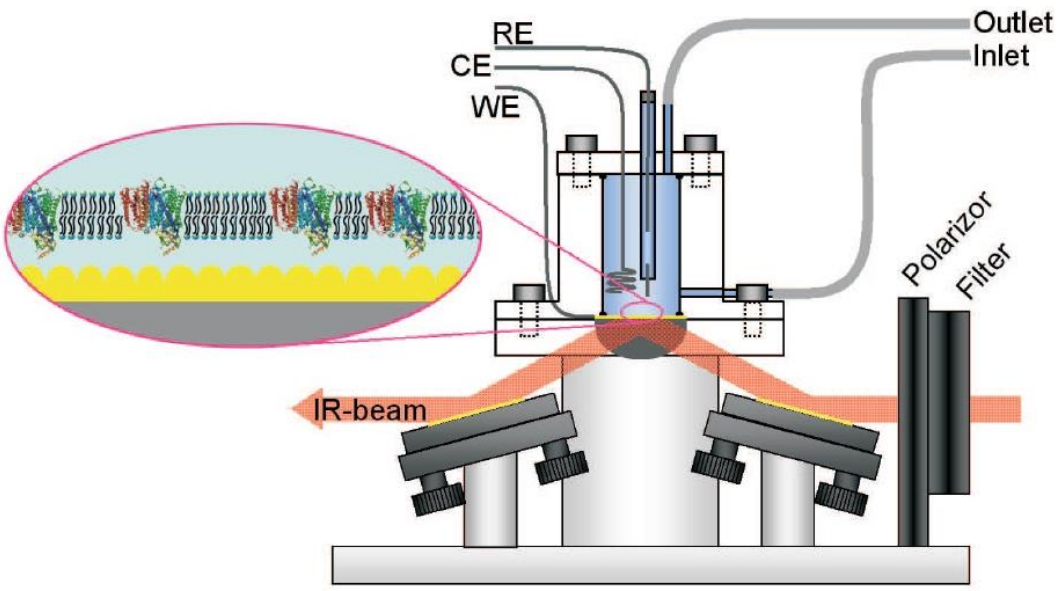

Figure 4.7: Schematic drawing of the custom-made IR-setup. Description is given in the text. RE: Reference electrode; CE: Counter electrode; WE: Working electrode. All of those electrodes were not used (no electrochemical activation was performed). Figure adapted from Friedrich, 2007 [116]

During all measurements, performed at 28 °C, the sample chamber housing was purged with dry CO_2-free air to remove both water vapor and carbon dioxide from the light path. The spectral resolution was 4 cm^{-1} using the Blackham-Harris three-term apodization and a zero-filling factor of 2. Interferograms were measured in double-sided mode and transformed into spectra by means of the power mode of Fourier transform.

4.2.3.6.4. Measurement-related evaluation

Fourier transform to obtain spectra out of interferograms was implemented by the IR spectrometer software without any additional steps. The evaluation of integral absorbances and all further steps to obtain the final matrices corresponding to the plots shown in the *Results & Discussion* section were done by the exchange internship student <content not available in online version> (Indian Institute of Technology Kanpur, Uttar Pradesh, India) and <content not available in online version> of the University of Vienna.

4.2.4 Silica-PLBs

4.2.4.1 PLB preparation

The preparation of PLBs based on silica nanoparticles (NP) followed the same principle as the agarose-based PLB preparation (Fig. 4.4). Nevertheless, a few differences exist because of the size difference. Since the NPs (mainly) used for PLB preparation were 25 nm in diameter, sedimentation would not occur during the above-mentioned centrifugation steps. Due to the different size, the investigation methods were completely different ones (while the agarose-PLBs are too big for UV/Vis spectroscopy, the silica-PLBs are too small for optical microscopy). Thus, both are distinguished in terms of the *Methods* part as well. Silica-PLBs were only prepared encapsulating C*c*O. Again, certain volumes are mentioned because of the utensils used later.

4.2.4.1.1 Preparation of the lipid suspension

The lipid suspension was prepared like described in the respective part within the *Agarose-PLB* section. Only the needed volume was less, so preparation of 1.5 mL was sufficient. To prepare silica-PLBs, only DiPhyPC was used as membrane lipid, in any case without UQ.

4.2.4.1.2 Protein attachment / Formation of proteobeads

The NPs were obtained at a concentration of 25 mg/mL. To finally use 6 mg of NPs, the stock solution (stored at room temperature) was diluted 2:3 with DDM/THK buffer to a concentration

of 16.7 mg/mL, having 1 mg NPs in 60 µL. To 360 µL of this dilution, 300 µL of a 7 µM C*c*O suspension (6 of the aforementioned aliquots, see *Aliquots*) were added and incubated for 2 h of gentle pivoting on a thermoshaker. As mentioned before, the rinsing of silica-PLBs was not possible with the available centrifuges, so the proteobeads were taken unrinsed, expecting unbound proteins to be precipitated when the detergent was removed, especially when PLBs were drastically diluted in DDM-free buffer in terms of the kinetic measurements, thereby likely undercutting the critical micelle formation concentration (CMC).

4.2.4.1.3 Dialysis / Formation of PLBs

The 660 µL of proteobead solution were applied to a dialysis tube, the 840 µL of the lipid suspension were added. The dialysis was done exactly following the steps described in the *Agarose-PLB* section. The final volumes were determined by weighing beforehand and afterwards. In this case, due to the volume of the dialysis tubes, the preparation of twice the PLB amount was feasible.

4.2.4.2 Determination of PLB size and occupancy

The C*c*O concentration encapsulated in silica-PLBs could be determined directly employing UV/Vis spectroscopy due to the small size, without the necessity to detach the C*c*O from the bead surface, as required for agarose-PLBs.

The spectra were recorded in disposable PMMA cuvettes with 1 cm light path (sample volume should be at least 700 µL) and a spatial resolution of 1 nm. The spectral range was 350-750 nm. In case of the NPs, spectra were measured using a quartz glass cuvette to be able to record as of 250 nm. A reference channel was present; the reference spectra were automatically subtracted. A baseline was recorded at the beginning of each session and subtracted afterwards manually. Specifications concerning the time-resolved measurements are given in the following section *Michaelis-Menten kinetics*.

At first, spectra of the NPs (25, 50, 100, and 120 nm in diameter) were recorded at a concentration of 4 mg/mL in DDM/THK buffer. Then, spectra of solubilized C*c*O, C*c*O-proteobeads and C*c*O-PLBs were measured, adjusting the PLB concentration to 4 mg NPs (calculated by means of the initial concentration and the dilution factors during preparation) per mL and a calculated concentration of C*c*O of 1.4 µM (if 100 % would have bound). Spectra of

C*c*O in reduced and oxidized state, respectively, were measured according to the section *Determination of protein concentration* within the *Universal procedures* chapter. The same protocol was applied in case of C*c*O-proteobeads and C*c*O-PLBs as well. The reduction (while, as mentioned, aliquoted C*c*O turned out to be oxidized over time) did not seem to be hindered by the membrane. Furthermore, the difference spectra of C*c*O-PLBs minus C*c*O and C*c*O-PLBs minus 50 nm NPs were calculated to roughly estimate the proteobead and PLB-size by comparing the scattering share with the spectra of differently-sized NPs.

Last, different amounts of C*c*O (0.43, 0.86, and 1.29 nmol per mg NPs) were added during preparation (0.43 nmol per mg NPs corresponded to the standard amount in the above-described preparation procedure and was used in all other experiments) to roughly estimate the maximum C*c*O occupancy. Therefore, volumes were kept the same, while higher concentrated C*c*O aliquots were used that were prepared of the C*c*O stock solution.

4.2.4.3 Dynamic Light Scattering

To double check the size of the NP-based proteobeads and PLBs, DLS measurements were performed. These measurements were done by <content not available in online version>, but were discussed and published collaboratively, so they are mentioned here.

All DLS measurements were performed at a scattering angle of 173 deg, using disposable rectangular polystyrene cuvettes of 1 mL sample volume. The 25 nm NPs were measured before and after protein immobilization (then being proteobeads) in DDM/DPK buffer, diluted to a concentration of 1 mg/mL NPs, and after dialysis (becoming PLBs) in DPK buffer diluted to the same concentration. Since a rough determination was considered to be sufficient, different scattering angles and further refining adjustments and measurements were not performed.

4.2.4.4 Kinetic measurements pursuant to Michaelis-Menten kinetics

To determine kinetic constants (i.e., in this case, the Michaelis-Menten constant K_M, as a measure of substrate affinity and the catalytic activity k_{cat}), measurements according to the Michaelis-Menten theory (see *Theory*) were performed.

For Michaelis-Menten kinetics-based (MMK) measurements, the absorbance at 550 nm (maximum of reduced cyt *c*) was recorded over. time. The measurement time was 60 s. The

needed cytochrome *c* solutions were made by dilution in the respective buffer (see below), while the stock solution was prepared following the respective protocol within the *Universal procedures* section

Dilutions of solubilized C*c*O and proteobeads were made with DDM/THK buffer and those of PLBs in THK buffer. Cyt *c* was diluted in the same buffer in each case. The final cyt *c* concentrations were 0.5, 0.75, 1, 2.5, 5, 10, 15, 20, and 25 µM. The enzyme concentrations were chosen in a way that cytochrome *c* oxidation was more or less linear within the first 60 s, following the kind advice of <content not available in online version> of the University of Frankfurt am Main, Germany. This was achieved with 0.2 nM for solubilized C*c*O, 0.6 nM for proteobeads and 2 nM for PLBs. Different concentrations did not matter, since K_M is concentration independent and k_{cat} includes division by the enzyme concentration. The total sample volume was 1 mL in each case. The cytochrome *c* solution was added, immediately admixed by two times of up-down pipetting, then the cuvette was placed in the sample holder as fast as possible, the absorbance value was auto-zeroed and the measurement was started. With employed concentration, absorbances have never been out of the sensitive range of the detector. Due to mixing procedure, the first seconds (approximately 2 or 3, not more), were not recorded, but due to the linearity within the first 60 s, this did not make a difference (since finally the slope is required for further evaluation).

As a measure of membrane denseness, the so-called respiratory control ratio (RCR) was calculated. For that reason, PLBs containing valinomycin (which makes the membrane leaky for potassium ions) and FCCP (same for protons) were prepared. Stock solutions of valinomycin and FCCP were prepared in DMSO and ethanol at concentrations of 18 and 40 µM, respectively, and stored at 4 °C. Valinomycin and FCCP were added to the PLB samples at final concentrations of 0.5 and 1.2 µM, respectively, and incubated at room temperature for 30 min. Again, the effective concentration cannot be specified, since both substances accumulates within the membranes of uncertain volume. Afterwards, MMK measurements were performed as described above. The C*c*O concentration in this case was 0.6 nM.

For reproducibility reasons (with regard to variations between different preparations), all states of C*c*O bound to NPs (proteobeads, PLBs, and PLBs with valinomycin and FCCP) were performed not only repeatedly, but also out of three different PLB preparations. To control the accuracy of the method, solubilized C*c*O, originating from one batch, was measured three times as well.

Chapter 5 *Results & Discussion*

Briefly repeated, the desired features of proteo-lipobeads (PLBs) are the following:

I. The structure of a PLB needs to fulfil two criteria:
   a. Each membrane protein of interest can be bound, as long as it contains a his-tag at the desired terminus to enable the directed reconstitution in a lipid bilayer membrane (which is not necessarily limited to natural lipids, but the thesis is confined to these). The thesis demonstrates on four proteins.
   b. The membrane needs to be dense, so that penetration of chemical species, which are rejected by a natural cell or mitochondrial membrane, is avoided.

II. The protein embedded in this kind of membrane maintains its functionality. A simple binding assay is not aimed, but a platform to investigate the protein function.

III. By varying the PLB cores, PLBs can be suited in size to allow for the desired investigation technique.

IV. The PLB components and possibly required additional tools like marker dyes are exchangeable, constituting a modular system.

V. The PLB format allows for storage and high-throughput assays.

Fulfilling these goals, PLBs should be a versatile tool to

I. study proteins embedded in their native membrane environment without any issues of different orientations or background signals of non-target proteins, furthermore enabling the investigation of transport processes. In providing these functions, active components that influence those proteins could be investigated as well.

II. be a low-cost and easy to handle alternative to cell cultures

III. enlarge the ptBLM concept due to their spherical shape, offering no boundaries and allow for investigation techniques that are hindered by fixed surface.

In doing so, the approach should serve applied science as well as basic research, whereas the focus during conception was on applied sciences, such as drug pre-testing.

Chapter 5A *Agarose-PLBs*

A core of agarose in the size range of 50 to 150 µm in diameter was chosen to allow for confocal laser-scanning fluorescence microscopy (LSM), thereby providing a notable inner reservoir of aqueous medium within the agarose.

5A.1 Structure

For PLB imaging as well as for functional assay, potential- or pH-sensitive fluorescent labels were used. These dyes, which are introduced in detail in the *Materials & Methods* section, are conjugated with a lipophilic tail that is designed to intercalate in the outer leaflet of a lipid bilayer, anchoring the fluorescent dye residue in close vicinity to the outer membrane surface. Due to accumulation, they exhibit negligible fluorescence in aqueous solution. While the PLB in its entity can be imaged with a standard light microscope, these pictures do not contain any information about the membrane, which is way too thin to be resolved by light microscopy, its denseness or the protein pumping activity. It is possible to image the agarose beads as well as the readily prepared PLBs, but it is not possible to distinguish between them. The proposed PLB structure is depicted in Fig. 5A.1. Fluorescence as well as light microscopic images are shown in Figure 5A.2.

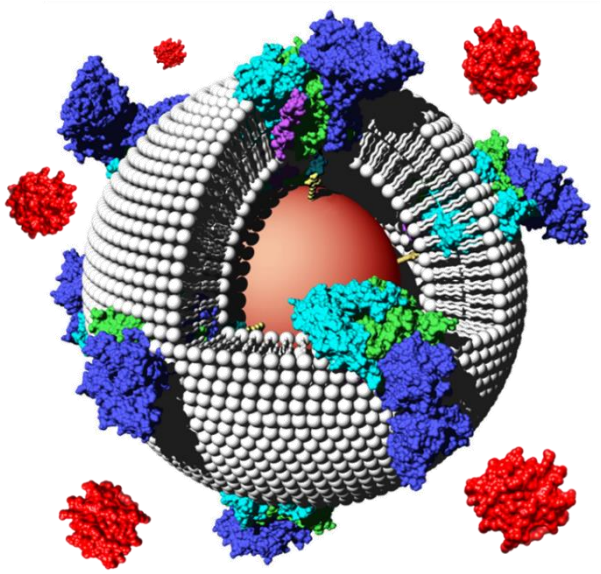

Figure 5A.1: Scheme of a C*c*O-PLB. The agarose core is depicted in light red, the Ni-NTA residues in yellow, the membrane lipids in white, the cytochrome *c* oxidase (C*c*O) subunits in blue to green (his-tag in petrol), and the substrate cytochrome *c* (cyt *c*) in bright red. Scheme published in Geiss *et al.*, 2017a [295].

In Fig. 5A.2A, PLBs are imaged by light microscope as filled circles. Special features could not be distinguished, and the raw bead material is looking the same (not shown). In Fig. 5A.2B, the putative PLBs are recorded via the label fluorescence and appeared as light, unfilled circles, which was assumed due to the confocal way of imaging (see Fig. 5A.3).

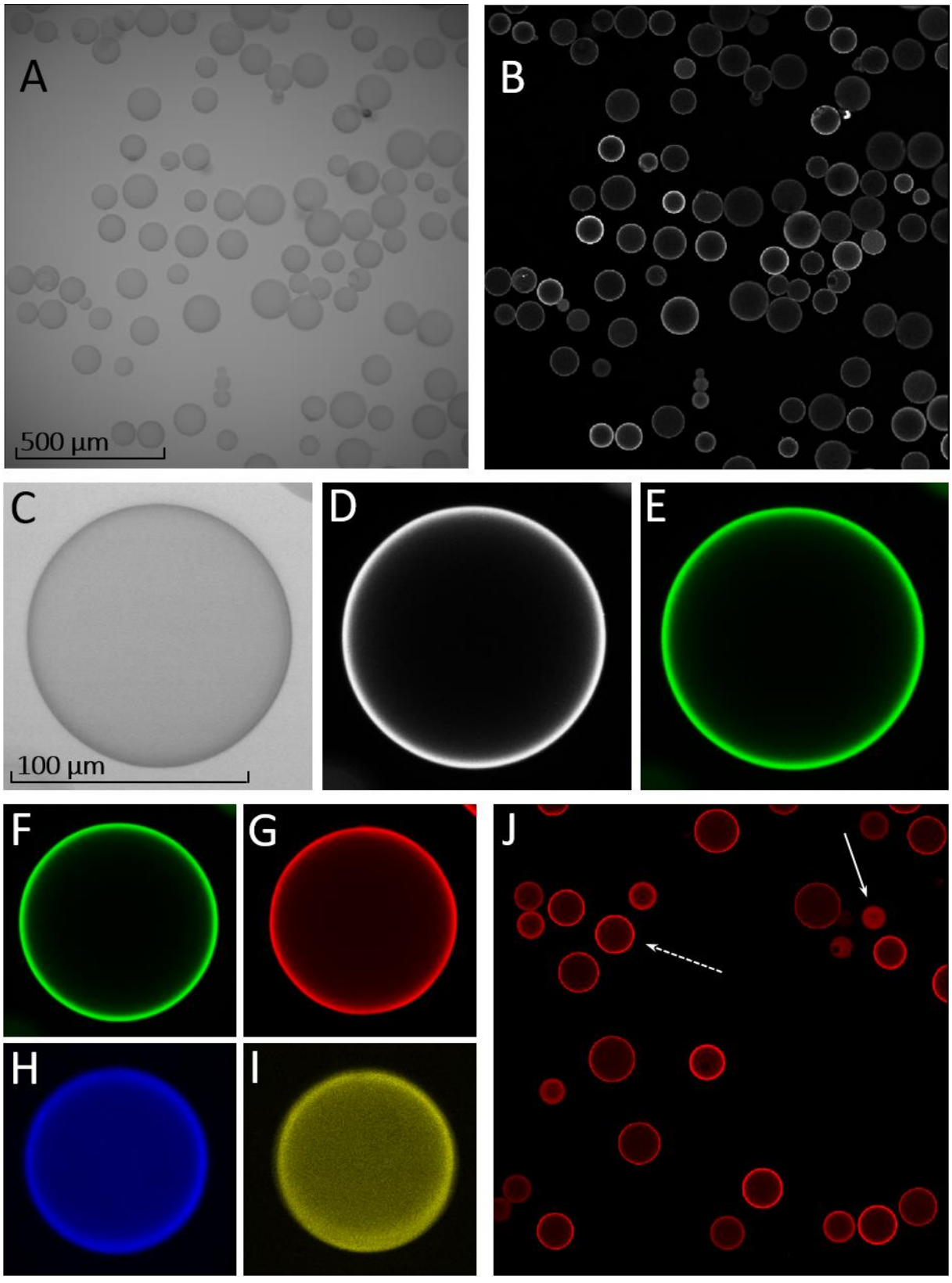

Figure 5A.2: Confocal laser-scanning fluorescence microscopy (LSM) images of agarose-PLBs, encapsulating C*c*O in DiPhyPC membranes, re-suspended in 5 mM Tris-HCl/35 mM KCl buffer, pH = 8 (THK buffer). (A) Light microscopy image of the PLB suspension labeled with fluorescein DHPE. (B) Fluorescence image of the same sample. (C) Single PLB, labeled with fluorescein DHPE, imaged by light microscopy. (D) Fluorescence image of the PLB depicted in (C). (E) Another depiction of the same PLB, subsequently colored by the imaging software according to the fluorescein absorption spectrum. (F-G) Used coloration chosen with respect to the respective absorption spectra: fluorescein-DHPE ($\lambda_{ex}/\lambda_{rec}$: 488/500-550 nm) (F), di-4-ANBDQBS ($\lambda_{ex}/\lambda_{rec}$: 561/685-790 nm) (G), FRET pair donor CC2-DMPE ($\lambda_{ex}/\lambda_{rec}$: 405/440-480 nm) (H), and FRET pair acceptor DiSBAC$_2$(3) ($\lambda_{ex}/\lambda_{rec}$: 405/565-620 nm) (I). (J) ANBDQBS-labeled PLBs, appearing as filled (solid arrow) and unfilled (dashed arrow) light circles, respectively, which is discussed in the following.

Having agarose bead diameters of 50-150 µm, the spatial resolution in top-down direction is high enough to image only a PLB slice. Considering that the label molecules are designed to intercalate in the lipid phase only, a signal of the membrane is expected exclusively. (The thickness of the membrane, however, cannot be determined, since the lateral resolution is not high enough, so the fluorescence signal emitted be a nanometer-sized structure is depicted as large as a structure of the minimum size that can be resolved. Due to the vertical resolution, it is even a bit lower, since the thickness of each PLB slice is not infinitely thin.) The lipids are arranged seemingly well-ordered around the bead, penetrating the agarose in a marginal manner. The fluorescence coming from the buffer was indeed negligible, indicating that the dye was accumulating within the lipid phase as assumed (while the polar dye itself is assumed to be located outside the membrane). Due to the preparation protocol, adopting a protocol to prepare a protein-tethered lipid bilayer membrane (ptBLM) [117], this also hints to the presence of proteins that act as anchor for the ptBLM during preparation. The diameter of 50-150 µm was validated, whereas this is not of particular importance. A detailed evaluation of the size distribution was not performed.

Fig. 5A.2C displays a PLB imaged with the light microscope function magnified, while Fig. 5A.2D shows the fluorescence image of the same PLB. In Fig. 5A.2E, the signal intensity, displayed in grayscale, because the detector detects only incoming photons without distinction, is secondarily colored by the program with respect to the spectral position of the fluorescence signal, which is detected at 500-550 nm in case of fluorescein DHPE, corresponding to the perception of green. By comparison, the fluorescence origin could be assigned to the outer edge the agarose bead.

The Figures 5A.2F-I display PLBs that were stained with the mainly used label molecules, being the pH-sensitive fluorescein DHPE in Fig. 5A.2F, the potential-sensitive ANBDQBS in Fig. 5A.2G, and the FRET pair donor CC2-DMPE (Fig. 5A.2H) and acceptor DiSBAC$_2$(3) (Fig. 5A.2I), respectively. The color code is used throughout the thesis with excemptions regarding the results of first co-authored publication, which was published before clear color definitions were decided [299]. The specifications of excitation wavelengths and recording wavelength ranges are given in the figure caption. In contrast to the other shown dyes, both components of the FRET pair penetrated the membranes as well as the agarose core notably. Nevertheless, within the putative membrane region, the fluorescence signal is significantly stronger in case of the donor and at least slightly stronger in case of the acceptor. For reasons of legibility, the full names of the herein abbreviated label and lipid molecules are given in the *Materials* section only.

Figure 5A.2K emphasizes the different appearance of PLBs as filled (solid arrow) and empty (dashed arrow) circles, respectively. This could be explained with the focus in z-direction (Fig. 5A.3). As of Fig. 5A.3, lowercase letters were used if the respective figures were published in this way.

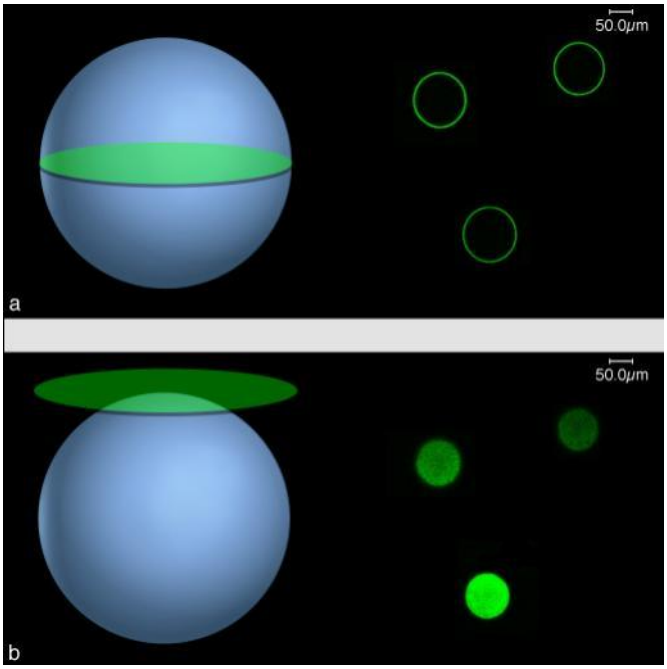

Figure 5A.3: Influence of the confocal way of imaging on the PLB appearance. (a) PLBs were imaged after adjusting the focal plane to the equatorial plane of the PLBs. (b) PLB images focusing the polar region. The PLBs (protein: C*c*O, lipid: DiPhyPC) were labeled with ANEPPS and re-suspended in 50 mM K_2HPO_4/100 mM KCl buffer, pH = 8 (DPK buffer). Figure published in Frank *et al*., 2015 [299]. Scheme drawn and image recorded by co-workers. Lowercase letters were used according to the published illustration.

As mentioned before, there is a finite resolution in z-direction. An exemplary scheme is given on the respective left in Fig. 5A.3a and B. Hence, if a pole region of a PLB is in focus, the fluorescence signal shows a filled circle (Fig. 5A.3b). If the imaged plane is located around the equatorial plane, fluorescence coming from the pole regions is excluded due to the confocal way of imaging (Fig. 5A.3a). To validate this hypothesis, the PLBs shown in Fig. 5A.3 were imaged once in the equatorial and once in the polar plane by adjusting the focal plane in z-direction. Please note that the displayed green slice representing the focal plane is not to scale. It is too thin. For that reason, the PLBs imaged in their polar region were not of such a small diameter as it would be expected regarding the scheme. Using the FRET pair, fluorescence was recorded in the equatorial plan, too, indicating that dye molecules had indeed penetrated the membrane (see Fig. 5A.2H and I, which were recorded in equatorial plane). Further discussion concerning the deduced membrane denseness and applicability of the FRET pair is given below. Fig. 5A.3 was made by co-workers of the respective publication [299].

To further elucidate the presence of proteins, particularly with regard to the effect they have on ptBLMs by providing their lipophilic surfaces as a scaffold (see, e.g., Giess *et al*., 2004 [117], or Friedrich *et al*., 2007 [300]), lipids were added to agarose beads without attached proteins (Fig. 5A.4). The recordings shown in Fig. 5A.4 were taken by co-workers shortly before this work was started. They are shown and discussed here nevertheless, because they were published in collaboration. In Figure 5A.4a, a PLB with putative protein-tethered membrane is shown. Its appearance is sharp-edged (as mentioned before: the thickness in the image is defined by the resolution, not by the actual thickness of the membrane) and strongly fluorescent. In the absence of C*c*O, the fluorescence signal showed a blurry layer around the agarose bead, way less intensive (which might be due to the larger distribution area) and much less defined (Fig. 5A.4b). The lipid area around the agarose bead – even it was not tested functionally – was not considered as a membrane, but as an unorganized lipid phase that adheres to the bead surface. The hypothesis of agarose bead penetration was not preferred because of the lack of fluorescence originating from the core region. The beads of Fig. 5A.4a and b are hence presumed to be of different diameters.

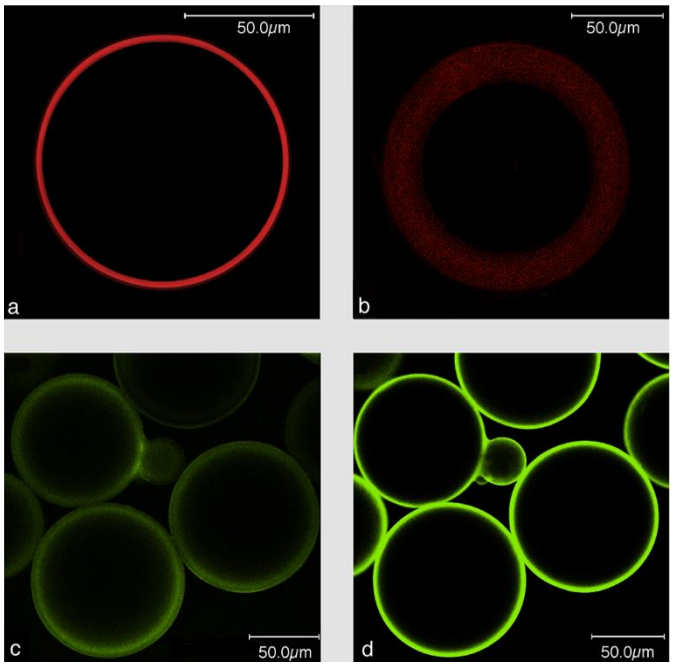

Figure 5A.4: LSM images of PLBs and agarose beads in the presence and absence of C*c*O, respectively. Antibody staining of C*c*O. (a) C*c*O-based PLBs were prepared as described in the *Materials & Methods* section, forming a ptBLM by attaching DDM-solubilized C*c*O and subsequent removal of the detergent in the presence of DiPhyPC via dialysis in DPK buffer. (b) The PLB protocol was implemented without the addition of C*c*O. (a) and (b) were labeled with NBD-PE. (c, d) PLBs were prepared as described for (a) and afterwards stained with a primary IgG antibody, which was designed to specifically bind to the C*c*O subunits (SUs) I and II. A Cy5-conjugated secondary antibody was used as fluorescent label. The PLBs were additionally labelled via the lipid phase using ANBDQBS. Both emitters were monitored via different channels. The channel specification could not be obtained anymore. (c) was denoted as displaying the antibody staining, (d) was reported to show the ANBDQBS fluorescence. Figure published in Frank *et al*., 2015 [299]. Samples prepared and images taken by co-workers. Lowercase letters were used according to the published illustration.

The presence of proteins, i.e., C*c*O in this case, was investigated by antibody staining, implemented by treating the PLBs with a non-labeled primary antibody. Subsequently, a fluorescently labeled secondary antibody, which was conjugated with a Cy5 dye molecule, was applied. Fig. 5A.4c shows a somewhat weaker fluorescence signal as recorded before, which is not meaningful without any reference, since neither the number of actually bound fluorescent molecules were adjusted to be equal (cy5 to ANBDQBS), nor the different quantum yield and the broader recording range of ANBDQBS was taken into account in a quantitative manner. Qualitatively, the significant fluorescence signal shown in Fig 5A.4c was considered to originate from the labeled antibody that has bound to the C*c*O, proving the the presence of proteins and lipids that were situated at comparable sites. However, later on, channels and emission spectra were found to be overlapping, so – even if not presumed – the fluorescence signal displayed in Fig. 5A.4c could theoretically originate from ANBDQBS as well, while the difference in intensity might be due to the narrower recording range. Cy5 was monitored at 640-680 nm, while ANBDQBS was recorded at 651-794 nm. Both were excited with a HeNe laser emitting at 633 nm. The spectral situation is depicted in Fig. 5A.5.

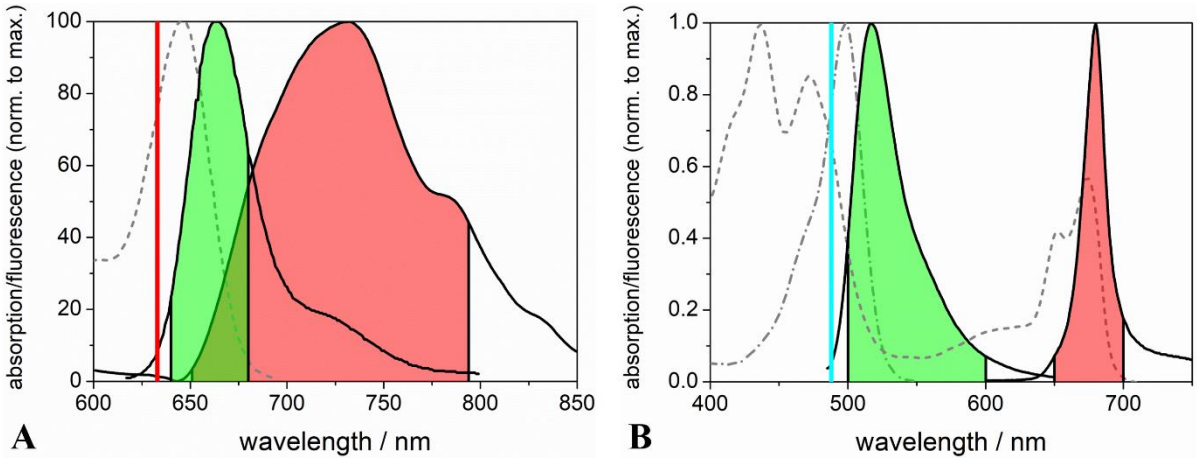

Fig. 5A.5: Spectra of protein and lipid labels. To image proteins and lipids separately, the lipids were labelled using dyes with conjugated lipophilic anchor tail as described before, while the protein share was monitored by antibody staining and auto-fluorescent proteins, respectively (see text). (A) Green integrals indicate the channel adjusted to monitor Cy5 fluorescence, which was attached to a secondary antibody that was designed to bind to a primary antibody, the latter binding to SU I and II of the C*c*O. The associated black solid line specifies the emission spectrum of Cy5. The red integral depicts the recording range of the channel that was employed to monitor the ANBDQBS fluorescence, while, again, the associated black solid line indicates the emission spectrum of ANBDQBS. The dashed gray line depicts the absorption spectrum of Cy5, while the absorption spectrum of ANBDQBS was not provided. The red line indicates the 633 nm excitation HeNe laser. (B) Briefly, according to the description given for (A): Green integral: fluorescein-recording channel; red integral: channel to record LHCII auto-fluorescence; associated black solid lines indicate the respective emission spectra. Dashed and dashed-dotted gray lines specify the absorption spectra of LHCII and fluorescein, respectively. Cyan line: 488 nm excitation Ar laser. Absorption and emission spectra of fluorescein were taken as representative for fluorescein DHPE. Fluorescein spectra were taken from the manufacturer's homepage [301]. Spectra of ANBQBS were provided by the group of <content not available in online version>, University of Connecticut, CT, USA. Spectra of the LHCII were taken from the data of Geiss, 2012 [276].

As a more elegant approach (since no protein labeling was required), and since the settings used for the experiments shown in Fig. 5A.4c and d were not as elucidating as desired, the light harvesting complex II (LHCII) of green plants, in this case *Pisum sativum*, which is fluorescing by itself, was used to form PLBs. PLBs were stained with fluorescein-DHPE, so excitation of both could be implemented with the 488 nm laser (see. Fig. 5A.5B), whereas the emission was detected by separate channels again, this time without spectral overlap. The fluorescein fluorescence was recorded at 500-600 nm, while the LHCII fluorescence was monitored at 650-700 nm. Fluorescein is not fluorescing in the latter spectral range [278], while the LHCII exhibits no green fluorescence (again Fig. 5A.5B) [276]. The results are shown in Figure 5A.6.

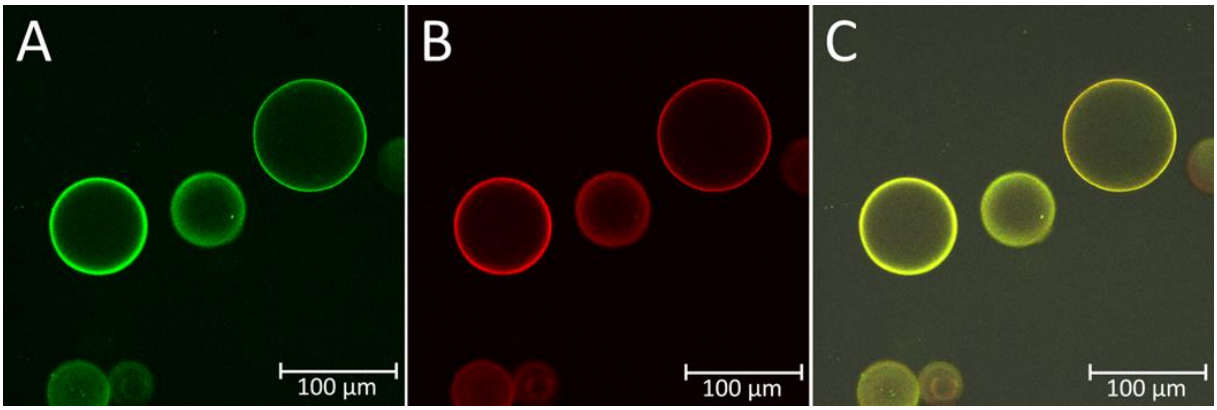

Figure 5A.6: LSM images of PLBs encapsulating the fluorescent light harvesting complex II (LHCII) of green plants, additionally labeled with fluorescein DHPE. (A) The fluorescein fluorescence was recorded at $\lambda_{ex}/\lambda_{rec}$: 488/500-600 nm. (B) The LHCII fluorescence was imaged at $\lambda_{ex}/\lambda_{rec}$: 488/650-700 nm. (C) Superposition of both images. Figure published in Geiss *et al.*, 2017b [302].

Fig. 5A.6A indirectly indicates the lipid share of the PLBs via the membrane-anchored fluorescein DHPE, while Fig. 5A.6B shows the protein share via the LHCII auto-fluorescence. In the superposition (Fig. 5A.6C), the presence of both, located at the same sites at the bead edges (with respect to the above-mentioned resolution issues that applies for single proteins as well), is evidenced, yielding a yellow color by superimposing red and green images.

Altogether, the assumed PLB structure is confirmed in a first qualitative step. Statements concerning the sealing properties of the alleged bilayer, its actual presence as bilayer and the enzyme functionality cannot be made so far.

5A.2 Enzyme activity and membrane denseness: qualitative statements

To determine the functionality of the reconstituted enzymes and the presence of a dense membrane, another property of the used dye molecules beside the membrane intercalation was taken advantage of, being the pH and potential sensitivity, respectively.

The first measurements, enabling to qualitative statements only, were performed with fluorescein DHPE, belonging to the pH-sensitive dyes. As soon as the pH value of the surrounding solution decreases, the fluorescence intensity decreases along with. Therefore, it is beneficial that the dye only intercalates into the outer leaflet of the membrane, so the signal decrease would not be compensated by an increase of dye molecules located inside. This specification was, by the way, not verified by specially tailored experiments, but was in accordance with any following results.

Following the theory, protons are pumped across the membrane as a consequence of C*c*O activity, in this case releasing them to the outside (which is dependent on the his-tag position in this artificial approach, not on the direction it is natively oriented). So, a drop of pH value, followed by an intensity decrease of the label, was presumed.

The addition of cyt *c* was not advantageous with regard to the evaluation technique. Even though these measurements were carried out in flow cells, the required flow to add cytochrome *c* during the measurements moved the PLBs, and that made the evaluation impossible in the way it was done. Instead, a Ruthenium complex (Ru_2C, see *Materials & Methods* for structural details), was utilized. Ru_2C binds electrostatically at the cyt *c* binding site. For that reason, the ionic strength of the buffer was drastically decreased by using Tris instead of phosphate buffer (≈ 39 % uncharged at pH = 8, ≈ 61 % carrying a single positive charge, see eq. 5A.5), and a much lower amount of KCl. So, the DPK buffer (50 mM K_2HPO_4, 100 mM KCl, pH = 8) was replaced by the THK buffer (5 mM Tris-HCl, 35 mM KCl, pH = 8), exclusively used hereinafter. The buffer concentration was lowered as well to increase the effect on the fluorescein. A certain ionic strength was kept nevertheless, since it was reported to increase the membrane stability [303]. Activated by light, Ru_2C forwards electrons to the C*c*O, hence reduces it [38, 59]. The electron wholes were refilled by aniline, what was added in large excess. The potential proton release of aniline – which would falsify the results – was compensated by the addition of 3-carboxy-PROXYL (3-CP) [62]. The composition is described within the *Materials & Methods* section and in the figure caption of Fig. 5A.7. (The Ru_2C concentration was chosen to be approximately in 10-fold excess towards the C*c*O concentration).

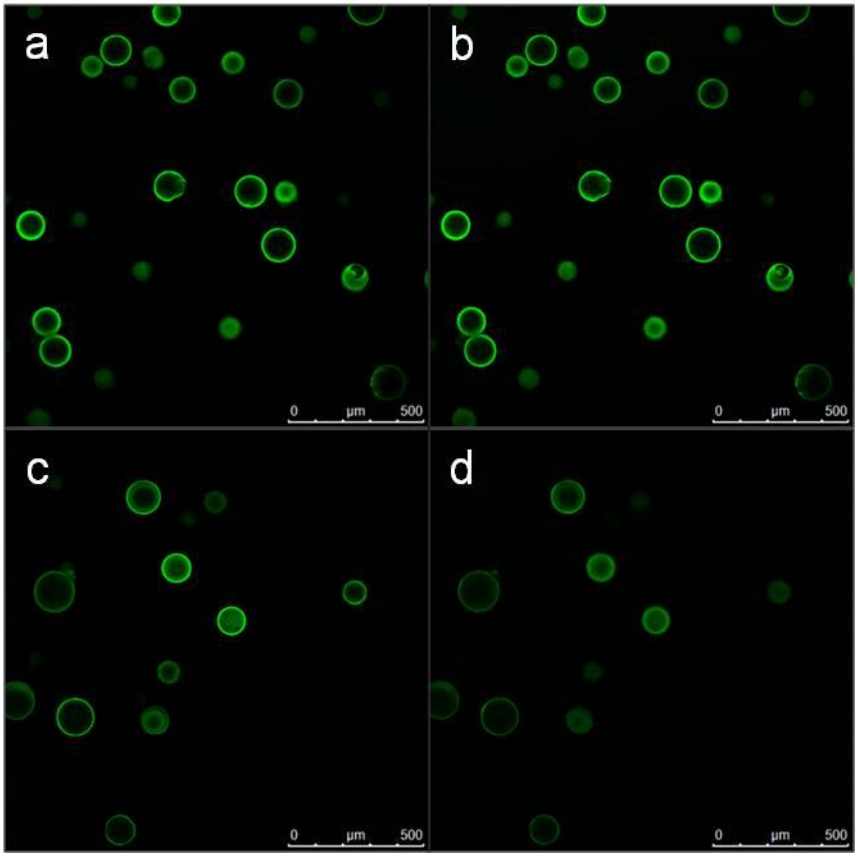

Figure 5A.7: Cytochrome *c* oxidase was illuminated in presence and absence of 62.5 µM Ru_2C, 12.5 mM aniline, and 1.25 mM 3-CP (Ru_2C/aniline/3-CP), respectively. C*c*O-PLBs without Ru_2C/aniline/3-CP before (a) and after (b) light excitation for 40 s, and with Ru_2C/aniline/3-CP before (c) and after (d) excitation, in THK buffer (5 mM Tris-HCl, 35 mM KCl, pH = 8). Figure published in Frank *et al.*, 2015 [299]. Lowercase letters were used according to the published illustration.

Figure 5.A7a and b show PLBs of approximately the same intensity. No change during the illumination was expected, since the C*c*O cannot be excited by light without containing Ru_2C. In Figure 5.A7c and d, Ru_2C was present, and a considerably lower intensity was observed even by eye in Fig. 4.7d, which was explained by the proton pump activity of C*c*O that lowered the outside pH value and hence the fluorescence intensity of fluorescein DHPE. The results were thus in good agreement with the a priori expectations. To monitor the changes more objectively, images were taken over time, following the intensity course before, during and after illumination. Images were taken every 1.3 s, limited by the imaging process of the laser-scanning microscope (depends on the time until the imaging laser is at the respective pixel again). To achieve this temporal resolution, the spatial resolution was reduced to 684 x 684 pixel instead of having 1024 x 1024. The evaluation process to obtain intensity curves assigned to elapsed time is described in detail in the *Materials & Methods* chapter.

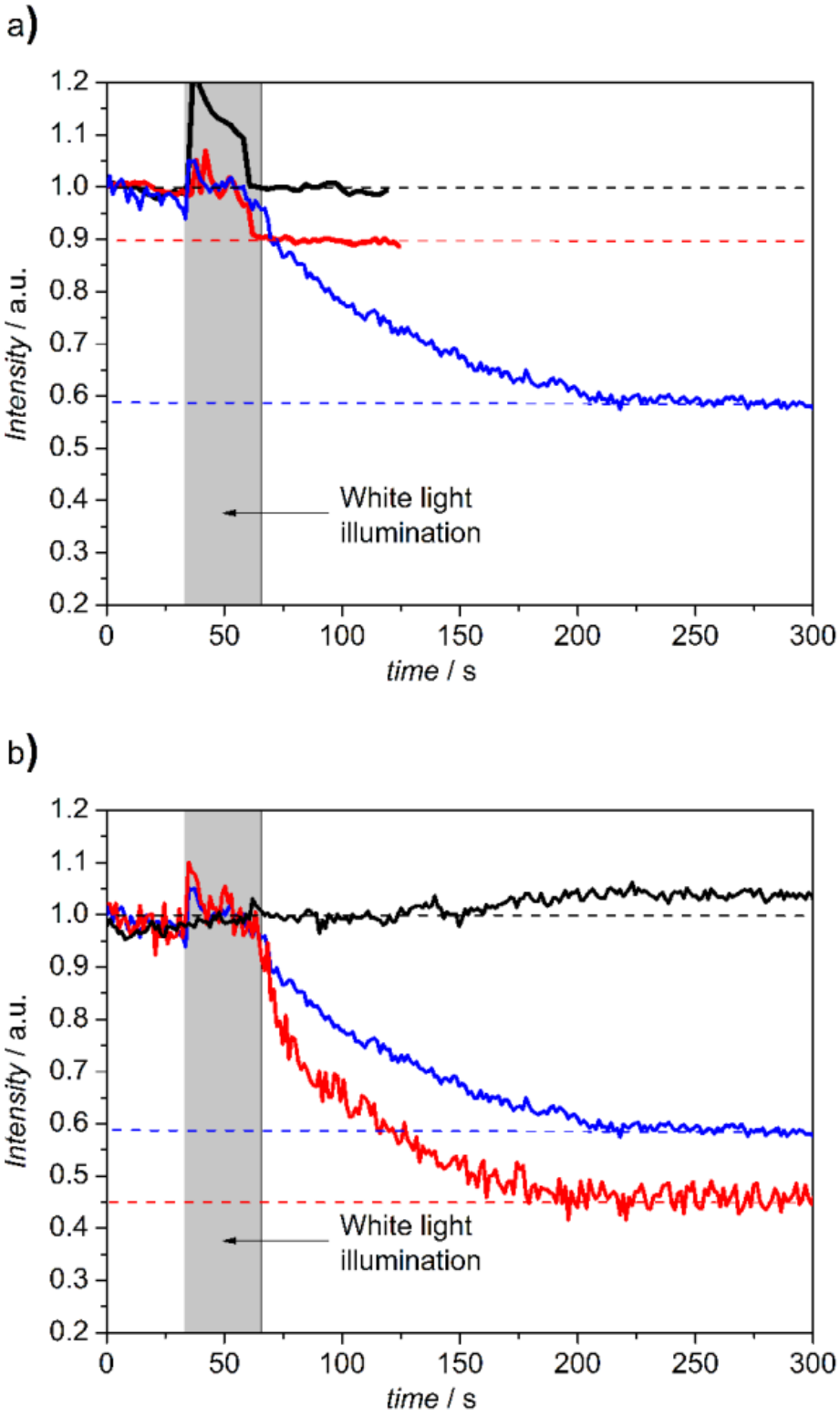

Figure 5A.8: Intensity changes due to white light illumination. (a) Fluorescein DHPE-labeled C*c*O-PLBs, resuspended in THK buffer, were illuminated by a halogen lamp for 40 s after 30 s of monitoring the initial fluorescence with (red) and without (black) Ru_2C/aniline/3-CP. Another sample of C*c*O-PLBs were re-suspended in unbuffered 40 mM KCl solution at pH = 8, then spiked with Ru_2C/aniline/3-CP and illuminated the same way (blue). (b) The unbuffered sample of (a) was compared to samples re-suspended in 40 mM KCl solution containing 0.5 µM valinomycin (red), and 0.5 µM valinomycin in combination with 1.2 µM FCCP (black), respectively. The initial fluorescence intensities were normalized to 1. Figure published in Frank *et al.*, 2015 [299]. Lowercase letters were used according to the published illustration.

Briefly, the fluorescence signal assigned to the membrane area was evaluated exclusively by defining regions of interest (ROIs) manually. The obtained intensities (provided by the software in arbitrary units) of ten PLB membrane areas were averaged and normalized to 1 at t = 0 for reasons of comparability. Please note that these measurements (Fig. 5A.8) were considered as qualitative evidences for enzyme activity nevertheless, since it only assigns a change of arbitrary fluorescence intensity units to an arbitrarily chosen period. Later quantitative estimations included specifications of the actual pH changes and turnover numbers of the reconstituted enzymes.

The fluorescence intensity courses recorded over time are shown in Fig. 5A.8. In any case, the period during the white light illumination is distorted by illumination artefacts (light of the halogen source that was scattered into the objective). Before the putative excitation, all curves of Fig. 5A.8a and b except from the black ones, serving as negative controls in both cases (without Ru_2C in Fig. 5A.8a and spiked with valinomycin and FCCP in Fig. 5A.8b, see below) showed little intensity decreases already. After the obscured illumination period, the sample without Ru_2C remained at the initial intensity level, while the buffered sample evened out at approximately 90 % of the initial intensity. Both were recorded only for one more minute after the white light illumination occurred, whereby the level seemed to be evened out. Th unbuffered sample, recorded for 5 minutes in total, showed a further intensity drop to a limit of approximately 58 %. The sample containing valinomycin showed an even steeper intensity drop to approximately 45 % of the initial intensity, while the one spiked with both valinomycin and FCCP showed no decrease of intensity.

Concerning the discussion of the results presented in Fig. 5A.8, some additional comments are requisite, since the perception of these results had changed after publishing the short communication Frank *et al.*, 2015 [299], and the findings were corrected in parts by a newer publication (Geiss *et al*., 2017a [295], see below). The white light illumination should be causal for any changes in intensity except from possible additional bleaching effects by the imaging laser, which would have affected all samples in the same way. On that basis, it was somewhat surprising that all curves but the black ones showed little intensity losses during the time before the putative excitation already. Since the effect was not very pronounced and the alleged effects occurred nevertheless, this was overlooked. Later, it was realized that the imaging laser, emitting at 488 nm, can excite the Ru complex itself. At this time, these little initial effects attracted attention, and a better way of excitation was found. By utilizing the imaging laser for simultaneous excitation, artefacts accompanying the white light illumination could be avoided in later experiments. As mentioned before, the period of illumination could not be evaluated,

since the signal was partially superimposed by the detectable spectral share of scattered white light. The distortion by illumination effects was more pronounced regarding the measurements shown in Fig 5A.8a, which can be explained by the initial fluorescence intensity of the fluorescein. The more intense the target signal is, the less artefact signals are pronounced in the average signal of several PLBs. For that reasons, attempts to subtract these artefacts were not successful. It was also questioned, why intensity changes (regarding the blue and red curve in Fig. 5A.8a and b, respectively) occurred that time-shifted, contradicting the assumption of direct turnover of the C*c*O. After identifying the additional source of excitation, the results were not contradicting a direct proton release any longer, since the excitation obviously was not terminated along with the white light illumination.

However, some interpretations of the results displayed in Fig. 5A.8 retained their validity. The black line in Fig. 5A.8a represents the sample without Ru_2C/aniline/3-CP. After a signal increase during white light illumination because of illumination artefacts, the intensity returned to its initial value. Due to the lack of Ru_2C, the C*c*O could not be excited and hence did not pump any protons. Consequently, neither the pH value of the surrounding solution nor the fluorescence intensity decreased. Considerable bleaching effects were not monitored.

The sample containing Ru_2C/aniline/3-CP, represented by the red line in Fig. 5A.8a, decreased in intensity during white light excitation to approximately 90 % of the initial value. After reviewing the results, a further decrease was expected retrospectively due to the Ru excitation by the laser, which was not visible. On the basis of these results solely, it remained enigmatic. However, without being able to validate the following for the results shown above, later experiments showed a clear and reproducible excitation of buffered samples with the imaging laser, but in a larger time scale. Hence, a longer record time might have been required to recognize little changes. It was further pursued, shown and discussed as of Fig. 5A.10. Without any buffer, only containing 40 mM KCl, the intensity decreased further, advancing towards approximately 60 % of the initial intensity (Fig 4.7A, blue curve). Hence, it was concluded that the Ru_2C was sufficiently excited, leading to C*c*O proton pumping activity and thus to a decrease of pH value, accompanied by a decrease of fluorescein fluorescence intensity, as expected. The limit formation at approximately 50-60 % could be explained with the increasing membrane potential, consisting of both a chemical and an electrical component. The chemical component arises from the concentration gradient of protons, which can be translated in a difference in pH (ΔpH) values across the membrane, while the electrical component ($\Delta\Phi$) is due to the charge generation accompanied by proton transport, each one carrying a positive charge. Altogether, it is also referred to as electrochemical potential ($\Delta\tilde{\mu}H^+$; please note that this

expression refers to the chemical potential of protons only). With increasing gradient, the active transport against both components of the membrane potential is hence more and more impeded. There are three more putative reasons for the limit formation, being on the one hand the increasing distance from the pH optimum of the C*c*O and on the other hand the pH range, within which the fluorescein can respond to changes of pH value (after attaining its minimal fluorescence emission, occurring if all protonation sites of all fluorescein molecules are protonated, the fluorescence intensity cannot decrease any more, although the pH value can). Moreover, it turned out that a linear intensity change of the fluorescein in this range would require an exponentially increasing release of protons, thus a curve of such a shape would be simply a logical consequence. But, to avoid extensive anticipation, the discussion of this limit, as well as the C*c*O activity within an unbuffered medium, is pursued along with the respective results, shown as of Fig. 5A.10. Up to here, the changes in signal intensity as a consequence of light excitation (distinguished from bleaching or other non-target effecs by means of the negative control measurement without Ru_2C) confirmed the functional incorporation of C*c*O within PLBs qualitatively (hence not yet revealing any turnover numbers).

The measurements shown in Fig. 5A.8b were performed to assess the membrane denseness qualitatively. For that purpose, two chemical agents, valinomycin and FCCP (carbonyl cyanide 4-(trifluoromethoxy)phenylhydrazone) were used, making the membrane leaky for potassium ions and protons, respectively. If only valinomycin was added (red line in Fig. 5A.8b), the intensity decrease was enhanced. Following a faster course, a limit was attained at around 45 % of the initial intensity after about 200 s. Conversely, the sample containing both valinomycin and FCCP (Fig. 5A.8b, black line) did not show any decrease of signal, but a slight increase. Assuming that the C*c*O is inhibited by the increasing electrochemical potential, the addition of valinomycin would enhance the fluorescence decrease, since the potassium ions. An increasing chemical gradient in terms the potassium ions might stop this process at a time, but initially, the membrane is relieved in terms of the electrochemical potential, and so is the C*c*O in terms of proton pumping. It confirmed the presence of a dense membrane to a certain extent, since there would be no effect in case of a membrane that leaks already in terms of potassium ions. (By the way, the lower limit of the sample containing valinomycin indicated the membrane potential as limiting rather than the pH optimum of the C*c*O or the ability of the fluorescein DHPE to respond, since an influence of valinomycin on the latter is unlikely. However, a more detailed discussion follows.) Usually, valinomycin is used to prove a dense membrane together with FCCP. If the activity of an actively transporting enzyme, which is embedded in a membrane, is significantly enhanced due to their addition, the membrane is considered as dense;

otherwise – having a leaky membrane – no membrane potential would emerge, so the uncoupling agents could not enhance the pump rate by relieving the enzyme in terms of the potential. The ratio of a membrane protein's turnover (involved in active transport processes) with and without valinomycin and FCCP is called respiratory control ratio (RCR). It is a measure of membrane denseness, whereby a value considerably larger than 1 indicates a sealing membrane [304]. In this conventional way, this was performed on silica-based PLBs, following the cytochrome *c* oxidation by UV/Vis spectroscopy and hence not influencing the measured quantity directly by the addition of FCCP (see *Chapter 5B*). Here, FCCP would have the opposite effect, since protons are causal for the detection. Due to the consequential redistribution of protons by means of the FCCP, the sample spiked with the latter was expected to serve as a negative control.

Indeed, an enhanced effect could be observed in presence of valinomycin, while in the presence of both substances, the sample showed no effect at all, assuming the slight increase rather to be an unspecific drift. Hence, the established ptBLM provided a notable hindrance for protons and potassium ions. So, although the curve shape could also be explained by the fluorescein response (which was not known at the time these results were evaluated and published) as described below, the enhanced response of the sample containing valinomycin evidenced the presence of a membrane potential as outlined, if limiting or not.

Altogether, the first measurements confirmed qualitatively the proposed structure as well as the preservation of the enzyme's function. Moreover, the membrane was observed to act as barrier for protons and potassium ions. The acidification due to light excitation indicated the actual presence of a lipid bilayer. In a multilayer system, the C*c*O would only be present within the inner lipid layer due to the his-tag immobilization, while the fluorescein, added after PLB preparation, should only be located in the outer one. Having received the displayed results, it seemed unlikely to have lipid multilayers, offering additional barriers between C*c*O and fluorescein.

The results obtained so far were published as short communication in the journal *Soft Matter*. (Only the results concerning the durability of PLBs within the *Supplementary Information* have not been discussed yet. This will be done along with more recent results to supply those.) The publication is presented in the following.

(As an aside: The water-soluble, pH-sensitive dye SNARF, which was chosen because of its property to not only change the fluorescence intensity, but as well the spectral position of the maximum, turned out to be not suitable at all, since it penetrated the beads in spite of its hydrophilic character for reasons unknown. Although measurements might have been possible to implement neverthess, this enigmatic penetration was considered as an insecure basis. The results are shown in Fig. 5A.9.

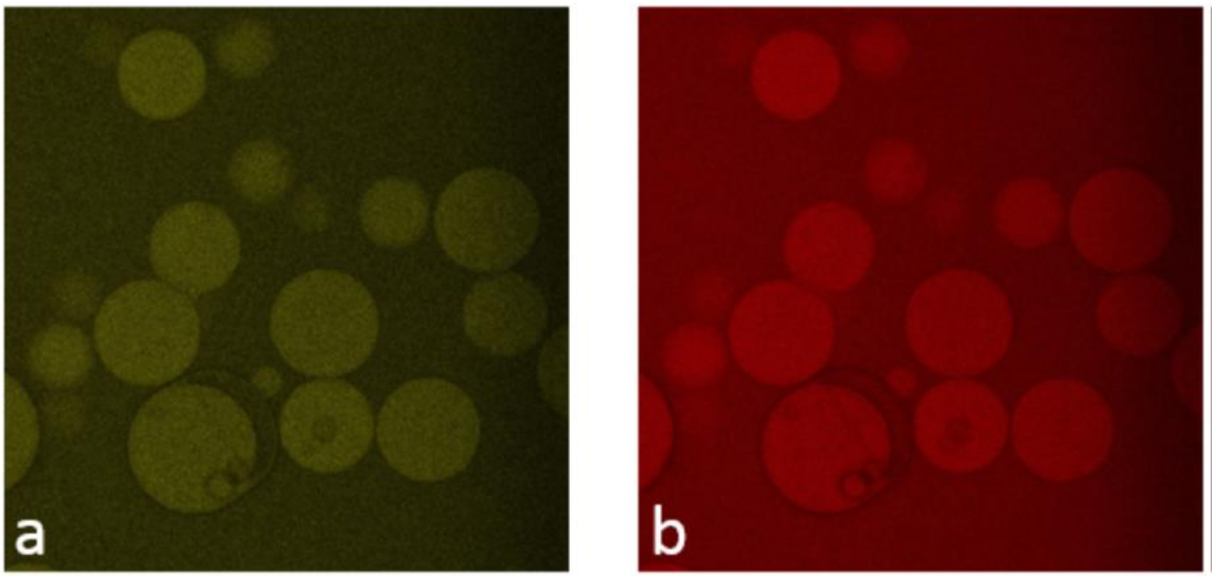

Figure 5A.9: LSM images of C*c*O-PLBs in THK buffer containing 20 µM of the water-soluble, pH-sensitive dye SNARF. (a) Channel 1: $\lambda_{ex}/\lambda_{rec}$: 514/550-610 nm. (b) $\lambda_{ex}/\lambda_{rec}$: 514/620-700 nm. Figure published in Frank *et al.*, 2015 [299]. Lowercase letters were used according to the published illustration.

Fig. 5A.9a shows the channel that captured the fluorescence with regard to the fluorescence maximum at pH = 6 (λ_{max}: 580 nm), while Fig. 5A.9b represents the channel chosen with respect to the emission maximum at pH = 9 (λ_{max}: 640 nm). Originally meant to facilitate the pH change detection, it was later considered to be unnecessarily complicated (like the unintended excitation with two sources, laser and halogen lamp).

To quantify the C*c*O turnover, the fluorescein response was finally employed, thereby exciting the Ru_2C with the imaging laser at 488 nm. SNARF was not further used at all.)

P. FRANK, B. SIEBENHOFER, T. HANZER, A. F. GEISS, F. SCHADAUER, C. REINER-ROZMAN, B. DURHAM, L. M. LOEW, B. LUDWIG, O.-M. H. RICHTER, C. NOWAK, AND R. L. C. NAUMANN: **Proteo-lipobeads for the oriented encapsulation of membrane proteins**. *Soft Matter* 11 (2015) pp. 2906–2908. doi: 10.1039/c4sm02646b.

Publication I

<content not available in online version>

<content not available in online version>

<content not available in online version>

<content not available in online version>

<content not available in online version>

<content not available in online version>

<content not available in online version>

<content not available in online version>

<content not available in online version>

<content not available in online version>

5A.3 Enzyme activity and membrane denseness: quantitative statements

As discussed above, the 488 nm Ar laser is suitable not only for imaging but also for the excitation of the Ru complex. In doing so, artefacts originating from the additional white light source could be completely avoided. The results are shown in Fig. 5A.10.

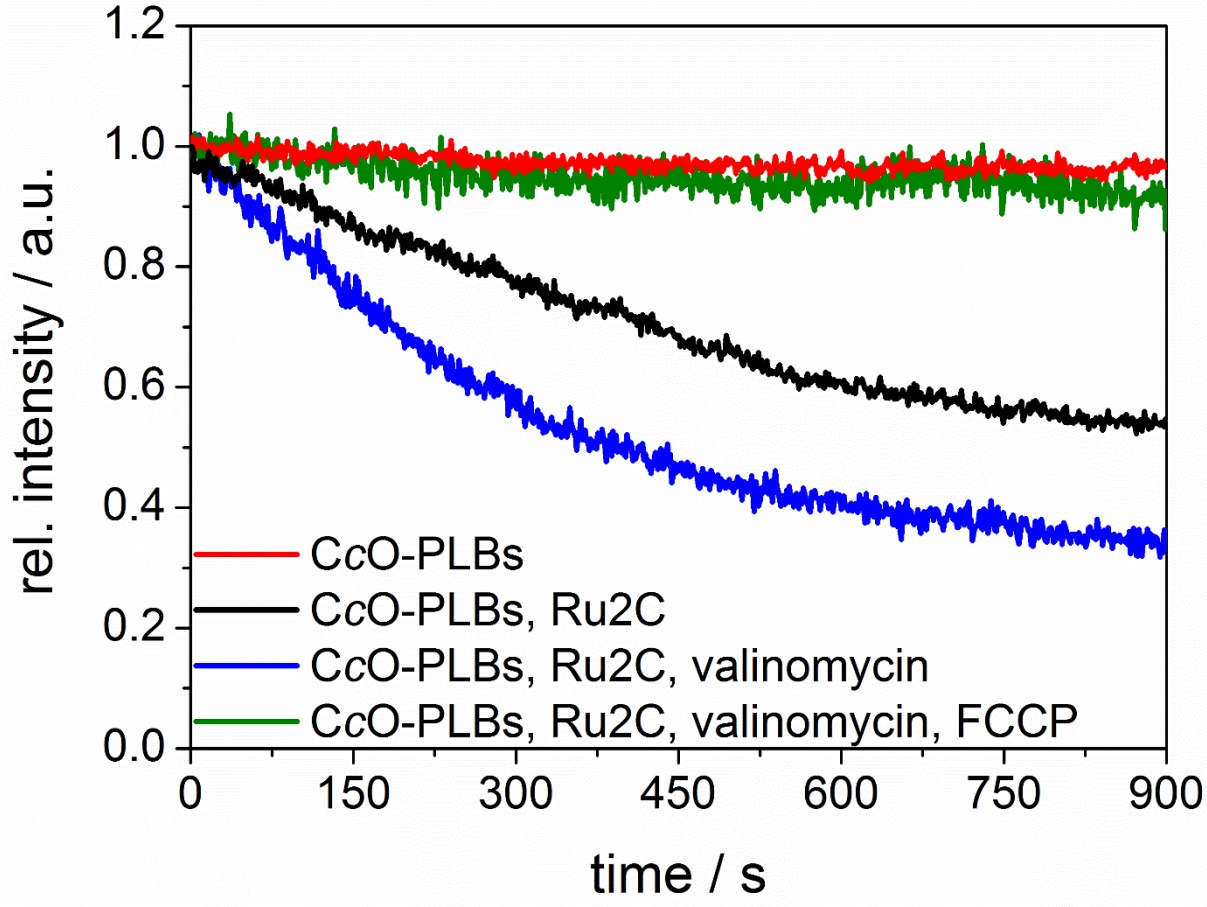

Figure 5A.10: Intensity changes of fluorescein DHPE attached to C*c*O-PLBs over time. C*c*O-PLBs were imaged by LSM and evaluated as described above. All samples were re-suspended in THK buffer. Fluorescence intensity changes are plotted versus excitation time in the absence (red) and presence (black) of Ru_2C/aniline/3-CP (referred to as Ru2C in the legend). The samples that additionally contained valinomycin alone and in combination with FCCP are represented by the blue and green curve, respectively. The initial fluorescence intensities were normalized to 1. Figure published in Geiss *et al.*, 2017a [295].

Figure 5A.10 shows the fluorescence intensity course detecting fluorescein fluorescence similar to the measurements displayed in Figure 5A.8. The sample without Ru_2C/aniline/3-CP (red line) showed almost no intensity loss, as it was observed for the corresponding sample in Fig. 5A.8. The final value was 97 %, and the difference to the initial value was assigned to bleaching. Therefore, this sample, which served as a negative control, enabled to subtract the bleaching effect to obtain the target effect only.

In the presence of Ru_2C, aniline and 3-CP, the intensity dropped to 55 % (black line). This significant decrease could be observed although all the samples contained 5 mM of Tris buffer. Again, the effect was enhanced regarding the sample containing valinomycin, but no FCCP (blue line). Here, only 35 % of the initial intensity was retained after 15 minutes. Both seemed to approximate to a limit exponentially, which they did not attain until the measurement time was over. While enhanced by valinomycin only, the effect was completely abolished in additional presence of FCCP (green line). The latter sample showed a similar intensity course as the negative control (end value: 93 %).

Qualitatively, the argumentation of Fig. 5A.8 can be adopted completely. The behavior of the buffered sample, which remained unclear, in the beginning because the signal was covered by the aforementioned illumination artefacts and afterwards because the measurement was carried on too shortly, could now be evaluated. The assumed effect can also be observed in buffered surrounding, while the 5 mM Tris did not completely compensate the acidification (see below for a detailed analysis), which suggested a notably large pumping activity. An unbuffered sample is displayed in Fig. 5A.14, further postponed because the following quantification process facilitates the argumentation why the unbuffered measurements were discarded at last.

To quantify both pH decline and C*c*O activity, a calibration curve was measured, translating the fluorescein intensity in pH values (Fig. 5A.11).

The intensity of the fluorescein labels did indeed decrease with decreasing pH value. The intensities at different pH values were used to fit a calibration function. In doing so, the fluorescence intensities were translated into pH values. Since the intensities of the samples – keeping in mind that the samples were adjusted to pH = 8 – were normalized to an initial value of 1, the same normalization (assigning the value 1 to pH = 8) was applied to the calibration function. A sigmoidal shape was assumed, having two limits; one, if all protonation sites of all fluorescein molecules are protonated, representing the lower limit, and another one, if all of them are deprotonated, representing the upper one. Indeed, there are four protonation steps comprising seven structural variants, which are described in detail in Martin & Lindqvist, 1975 [305].

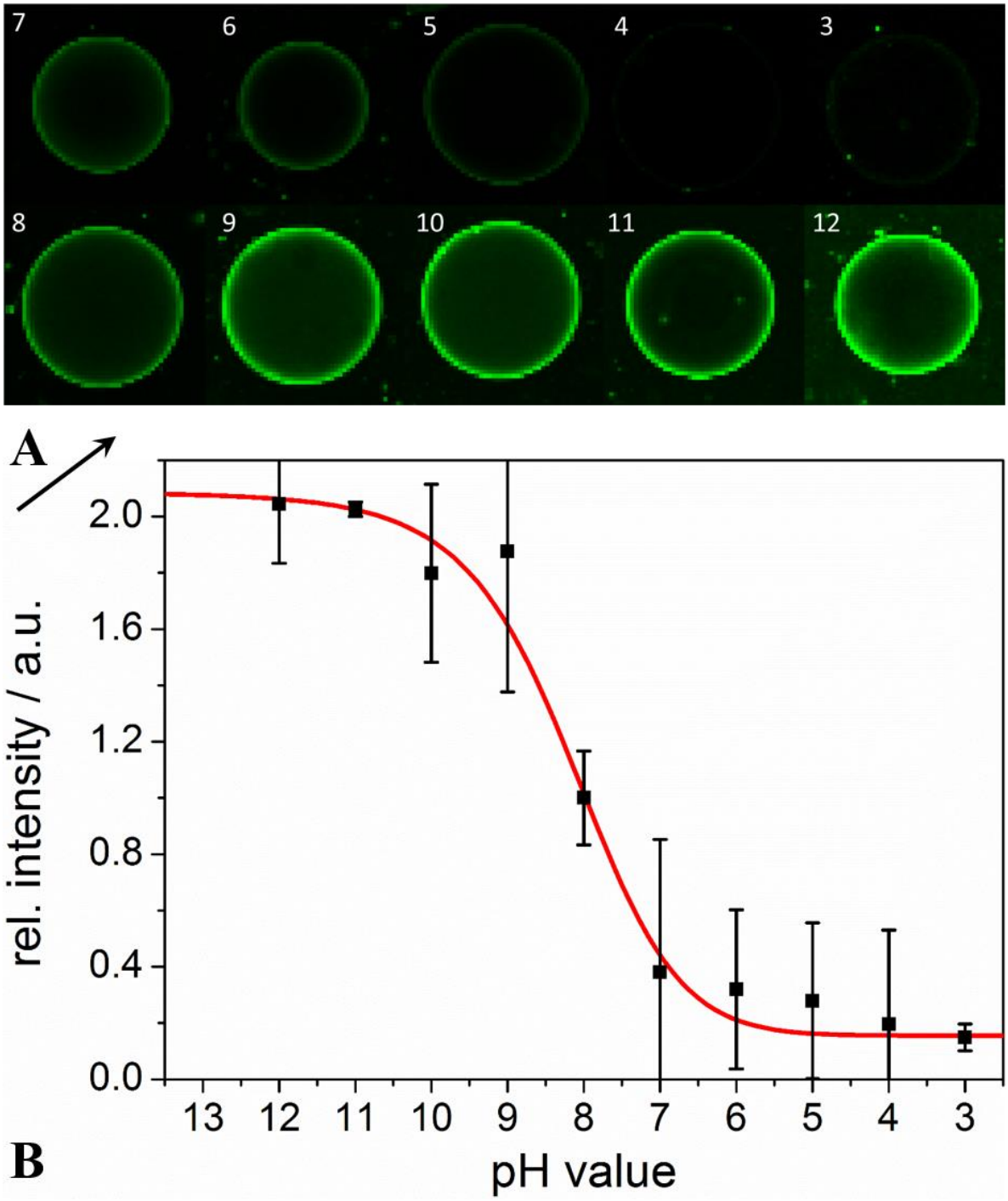

Figure 5A.11: Calibration plot assigning the fluorescence intensity of fluorescein DHPE to the pH value. Fluorescein DHPE-stained C*c*O-PLBs were suspended in THK buffer additionally containing 40 mM citrate and adjusted to the indicated pH values, ranging from 3-12, in steps of integer pH values. (A) LSM images at different pH values, specified in the respective image. (B) The average intensity values of ten PLBs at each pH value were fitted with a sigmoid function. Afterwards, the calibration function was normalized to 1 at pH = 8. Figure (B) published in Geiss *et al*., 2017a [295]. Please note that the figure caption there was erroneously not updated concerning the buffer.

The pH dependence was nevertheless described by a continual transition without potential plateaus, since the measuring points did not allow for a reasonable fit that is more complex. This simplification was considered to be fair enough, especially because the aforementioned

publication by Martin & Lindqvist indicated only one main protonation step (dianion to monoanion) down to a pH value lower than 6, suggesting that these additional plateaus are located in the very low pH range, which might be slightly discernible in calibration plot, but not to validate with these slight hints, moreover having a rather large standard deviation in comparison. Hence, for the majority of the investigated range (as of pH ≈ 5), a single protonation step seemed reasonable to assume. Fig. 5A.12 shows the measurements of Fig. 5A.10, this time assigning the pH value to the excitation time.

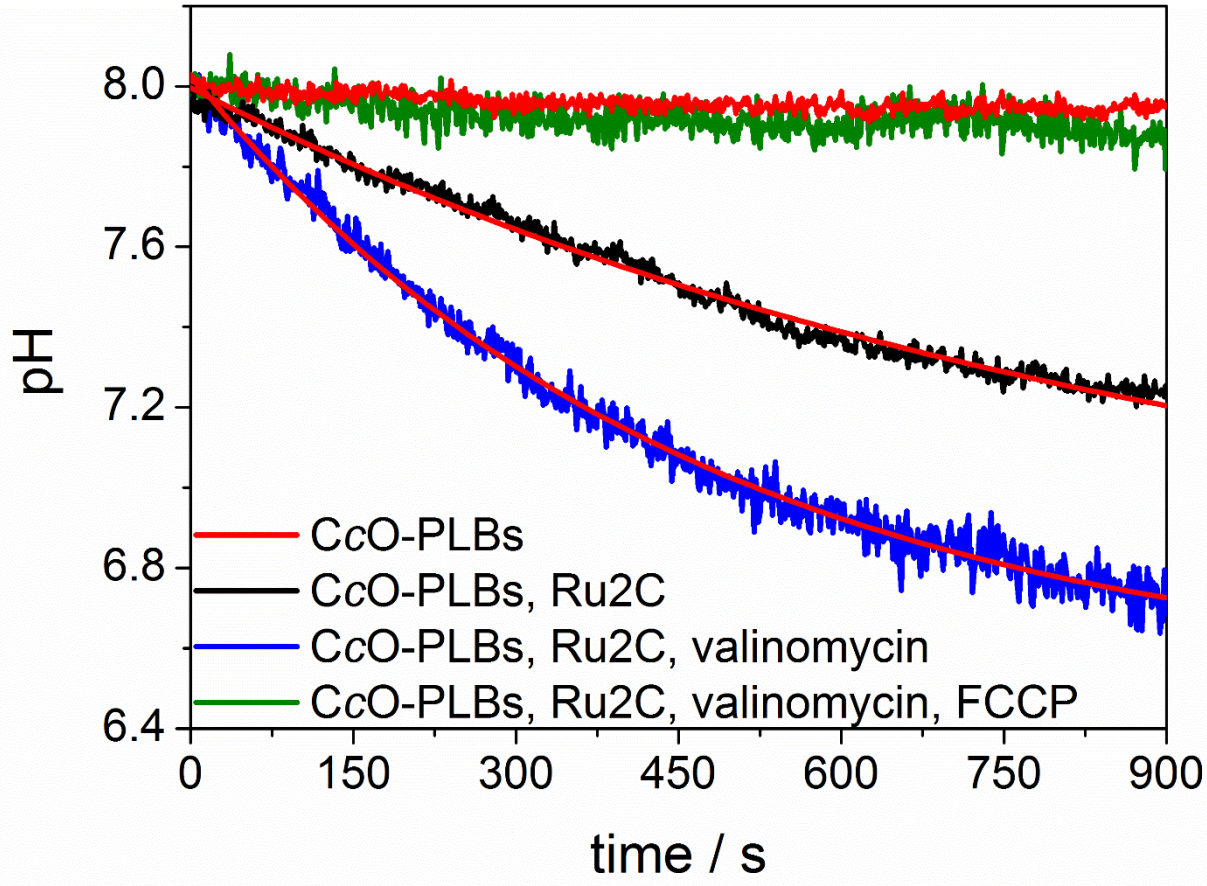

Figure 5A.12: Change of the pH value over time, monitored by PLB-bound fluorescein DHPE fluorescence. The intensities of Fig. 5A.10 were translated into pH values applying the calibration function plotted in Fig. 5A.11. Before applying the calibration curve, the intensity curve sample without Ru_2C/aniline/3-CP (red line in Fig. 5A.10) was subtracted from the intensities of the samples containing Ru_2C/aniline/3-CP (black curve in Fig. 5A.10) and those of the sample containing valinomycin in addition to Ru_2C/aniline/3-CP (blue curve in Fig. 5A.10) to subtract intensity losses assigned to bleaching. The pH curves were fitted exponentially (red lines). Figure published in Geiss *et al.*, 2017a [295].

After translating intensities in pH-values, the measured data could be fitted exponentially. The fits are displayed as red line, while the residual color code is the same as in Fig. 5A.10. Please note that the intensity curve of the negative control measurement without Ru_2C/aniline/3-CP was subtracted from the ones containing Ru_2C/aniline/3-CP and Ru_2C/aniline/3-CP/valinomycin to eliminate the bleaching effects.

For the quantification of the C*c*O turnover, only the initial moment is of interest, since it is unaffected by the electrochemical potential, which emerges over time due to C*c*O activity. Hence, the slope – corresponding to $\Delta pH/\Delta t$ – at time point 0 needs to be determined at first.

The exponential fit function was,

$$pH(t) = Ae^{R_0 t} + y_0 \ . \qquad (5A.1)$$

Its first derivative is thus

$$pH'(t) = R_0 Ae^{R_0 t} \ . \qquad (5A.2)$$

The designation of the parameters as A, R_0, and y_0 was adopted from the fitting program, which was Origin Pro 8.5. The obtained values by fitting and the calculated $pH'(0)$, the latter giving the initial pH change per time, are summarized in Table 5A.1.

Table 5A.1: Obtained fitting parameters and initial pH changes. Table adapted from Geiss *et al.*, 2017a [295].

	R_0	**A**	**y_0**	$(\Delta pH/\Delta t)_{ini} = \lvert pH'(0)\rvert$
- valinomycin	-0.00109	1.26858	6.72793	0.00138
+ valinomycin	-0.00217	1.51896	6.50977	0.00330

To determine the number of pumped protons, the number of protons in the surrounding solution was calculated before and after the changes given in the very right column of Table 5A.1. In the respective solution, not only the protons that were bound to water needed to be considered, forming H_3O^+, $H_5O_2^+$, and so on. Although those are defining the pH value, the protons are distributed between all proton-binding chemical species, being the fluorescein itself and, most of all, the buffer. To obtain the number of pumped protons, the initial protonation of all the three reservoirs outside the PLBs needs to be factored in. Later on (see Fig. 5A.21), it could be shown that the distribution of the pumped protons within the whole flow cell volume by means of diffusion happened that quick that the equilibrium set in – regarding the temporal resolution – instantaneous. Hence, the monitored effects were shown to not be a net sum of pumped and redistributing protons, but the change within the whole flow cell volume.

For the water share, the number of protons corresponding to the pH value can be calculated by means of the pH value definition, being the negative decadic logarithm of the proton concentration, mathematically described by equation 5A.3.

$$[H^+] = 10^{-pH} \tag{5A.3}$$

The volume of the solution was determined by the flow cell volume of 400 µL subtracted by the PLB volume. To receive the latter, PLBs were centrifuged harshly and the supernatant was removed, until the PLBs attained a dry condition. The PLB mass was determined by weighing beforehand and afterwards (described in detail within *Materials & Methods*) The internal water reservoir of the agarose was presumed to be bound too strongly by capillary forces. The volume was determined to be 12.3 µL of the 40 µL deposit that was applied during sample preparation (average value of three determinations). The volume between agarose cores and membrane was considered to be negligible, yielding a volume of the surrounding solution of 387.7 µL. The number of additional protons could be determined straightforward by subtracting the calculated number of protons (concentrations multiplied by the volume and the Avogadro constant, being 6.022 x 10^{23} molecules per mole) before (pH = 8) and after the obtained initial pH value change per second (pH = 8 – ΔpH_{ini}). Potential-caused inhibitions within the first second were neglected. The number of protons pumped and taken over by the water phase turned out to be 7.5 x 10^9 and 1.8 x 10^{10} absence and presence of valinomycin, respectively.

For fluorescein DHPE (being in the validity range with a pK_a value of 6.7 for the monoanion, prevalent as the corresponding acid in the regarded pH value range [305]) and Tris, the Henderson-Hasselbalch equation was used [1].

$$pH = pK_a + \log_{10}\frac{[A^-]}{[HA]} \tag{5A.4}$$

To determine the ratio of protonated and deprotonated species, it results in

$$10^{pK_a - pH} = \frac{[HA]}{[A^-]}\ . \tag{5A.5}$$

Here, pK_a is the negative decadic logarithm of the acid dissociation constant of the respective protonation step, [HA] is the concentration of the protonated species, and $[A^-]$ is the concentration of the deprotonated species.

So, the percentage of protonated molecules could be calculated (having, for example, a ratio of 1.5 (to 1), it means that 1.5 of 2.5 parts of the molecules are protonated, being 60 %). Again,

the number of bound protons can be obtained by comparing the share of protonated molecules before and after the initial pH change multiplied by the applied concentration, the volume, and the Avogadro constant. For the given case (without valinomycin), it turned out that 0.08 % of the Tris molecules had been protonated within the investigated initial second, corresponding to 8.8 x 10^{14} protons. So, it turned out that the number of protons within the water and bound to the fluorescein are negligible in comparison to the ones bound by the Tris buffer (which is actually the purpose of a using a buffer), even if it was assumed that all fluorescein DHPE molecules were incorporated in the membrane (not likely due to the chloroform:membrane distribution during the staining process). Against this backdrop, a considerable number of protons possibly taken up by amino acid residues of C*c*O seemed to be unlikely, especially regarding the large excess of Tris molecules towards proteins. The same applies for the tightly bound cardiolipin that is retained during preparation, whereas DiPhyPC protonation does not occur at all at pH values above 4 [306].

To estimate the number of proteins bound to PLBs, the latter were eluted with imidazole from exemplarily prepared proteobeads after rinsing, and then determined by UV/Vis spectroscopy using the Beer-Lambert law (see *Materials & Methods*, eq. 4.1). The obtained spectra are shown in Fig. 5A.13.

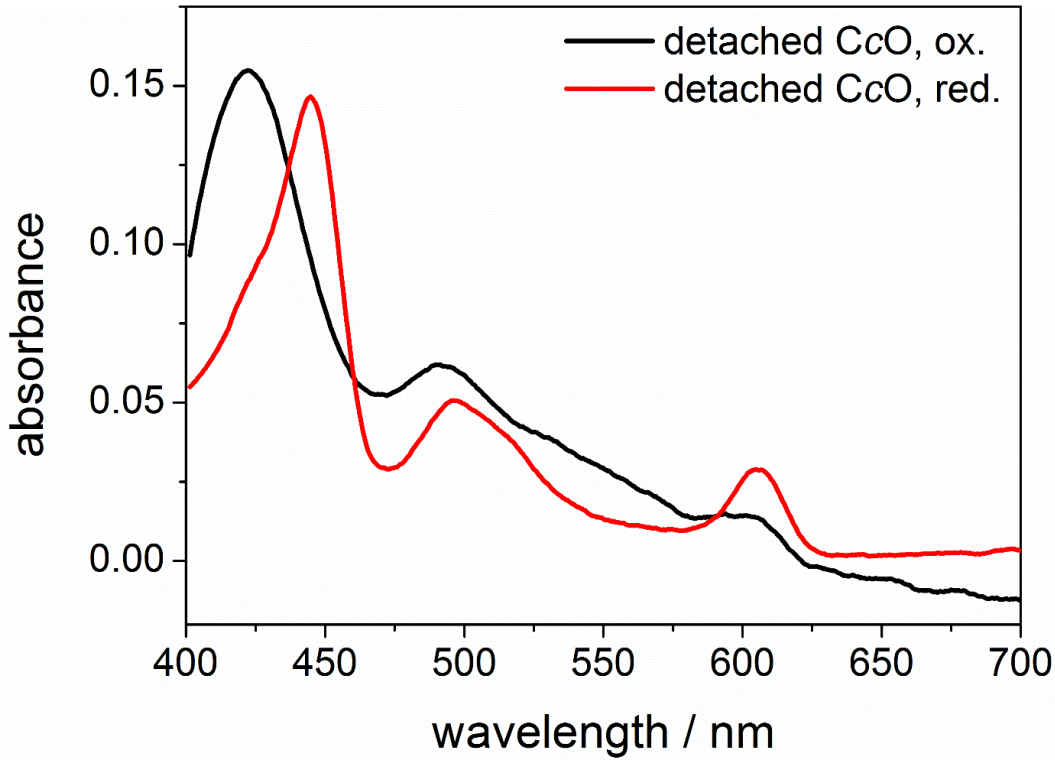

Figure 5A.13: Determination of the C*c*O concentration eluted from proteobeads. After the preparation of exemplary C*c*O proteobeads, proteins were eluted by treatment with 300 mM imidazole (in THK buffer) and measured by UV/Vis spectroscopy. Afterwards, a few grains of sodium hydrosulfite were added to reduce the C*c*O and measured again. Figure published in Geiss *et al*., 2017a [295].

The detached C*c*O concentration was quantified by using the extinction coefficient given by Ludwig & Schatz, 1980, being $\varepsilon_{606-630\,\mathrm{nm}}^{\mathrm{reduced-oxidized}}$ = 23.4 mM^{-1} cm^{-1} [290]. 90.5 % of the applied C*c*O molecules (0.5 nmol) were attached to PLBs, what is in good agreement to the values determined on silica-PLBs, discussed in *Chapter 5B*. There, C*c*O binding and PLB occupancy are discussed more in detail. (The average number of C*c*O complexes per agarose-PLBs could not be determined, since the manufacturer did not provide the number of beads per mL suspension. Moreover, the agarose-PLBs are polydisperse in size.) 90.5 % corresponds to 4.52 x 10^{-10} mol per one preparation of 250 µL agarose PLBs (for the determination method see *Materials & Methods*). As mentioned before, only 12.3 of 250 µL agarose beads are contained in one sample (determined analogous). Taking this into account, one sample contained in average 1.34 x 10^{13} C*c*O complexes. Coming back to the pumped protons bound by the Tris buffer (since the other shares were negligible in comparison), it results in

$$\frac{8.80 \text{ x } 10^{14}\ \mathrm{H^+/s}}{1.34 \text{ x } 10^{13}\,\mathrm{CcOs}} = 66\,\frac{\mathrm{H^+}}{\mathrm{CcO \text{ x } s}}\ . \qquad (5A.6)$$

In the *Supplementary Information* of Geiss *et al.*, 2015a [295], the calculation is summarized in short lines. For the sample containing valinomycin, the initial turnover was 163 H^+/s per single C*c*O. Although the ratio of both values did not represent a conventional RCR measurement, since only valinomycin and no proton uncoupling agent was added, this ratio was 2.5 and hence contributes to the argumentation towards a dense membrane. Conventional RCR measurements, resulting in a similar value of 2.8, were carried out on nanometer-sized silica-PLBs, which is discussed in *Chapter 5B*.

Compared to literature [51, 57, 58], where maximum turnover values of more than 500, but at least of more than 300 per second and C*c*O were reported, the initial turnover numbers turned out to be significantly lower. However, these publications report the maximum catalytic activity in solubilized state (to compare with solubilized C*c*O, the value obtained in the presence of valinomycin is more representative), determined, for instance, by means of Michaelis-Menten kinetics measurements (see *Theory*). The comparison of cyt *c* reduction with proton release can be considered as valid because of the one-to-one stoichiometrie of accepted electrons and released protons. According to theory, there must be a released proton for every oxidized cyt *c* [25], so the observed process is the same, albeit the measurement principle differed (see the *Theory* part for extensive discussion of the C*c*O catalytic cycle). A major difference is that the maximum activity was obtained in the referenced publications. Although one could speculate

about hindrances due to the his-tag binding or a too little amount of valinomycin to compare with the solubilized enzyme, the explanation might be found easier by reconsidering the measurement process. As shown below by means of measurements with repetitive white light excitation (see Fig. 5A.21), a recovery of fluorescence intensity did not occur, indicating that the diffusion of protons within the whole sample could be considered as immediate, hence calculating with the whole buffer volume seemed to be justified. In contrast, having a laser-scanning microscope, an excitation of all enzymes at once did not occur (while due to the confocal way of imaging not only one plane of the PLB-bound enzymes was excited, instead only the light originating from one single plane is collected, see *Theory*). Also the laser was not illuminating the entire flow cell area. Taking this into account, the number of excited enzymes was probably overestimated. (The laser power was not increased as well to ensure saturating excitation light conditions, especially keeping in mind that the Ru excitation spectrally occurred at the very edge of its absorption peak (see Fig. 4.5); as an aside, any associations of the C*c*O turnover to the irradiated power was omitted, since the C*c*O is not a light-driven enzyme, but the light excitation is an entirely artificial situation that does not occur in nature). All in all, the C*c*O activity might not have been reduced at all. It is likely that the turnover was at least underestimated by calculating with the full number of enzymes within a sample. The vital information of the quantitative measurements was that the C*c*O can be integrated in PLBs retaining its activity without substantial losses and that the activity can indeed be quantified. In a next step, albeit with another protein (namely the cytochrome bc_1 complex) the complete sample was excited, and these constraints were finally overcome (see below).

A further interesting aspect deducible from the calibration plot (Fig. 5A.10) led to a reconsideration of the limit formation. In the observed range, the fluorescein response towards pH changes is linear, which means that for a linear intensity decrease, the acidification (the proton release) would need to be exponential. Even a linear proton release, not inhibited by an increasing gradient, would hence lead to a flattening of the intensity curves (and not only of the pH course). Obviously, there is no potential required to obtain intensity curves of a shape represented by the ones in Fig. 5A.10. Still, there were reasons found that might cause actual limit formations. Having another look at the calibration plot, the ability of the fluorescein to respond was exhausted at an intensity of 20 % of the emission at pH = 8. This value was never attained in measurement. But, by lowering the pH value, the activity of the C*c*O could be decreased in terms of the pH optimum. The pH optimum of the C*c*O depends on many factors [307, 308] and is difficult to specify for that reason, but it was observed that C*c*O aliquots lost their activity by time when stored unbuffered, which was traced back to the acidification due to

carbonic acid formation by water and air CO_2 (determined by Michaelis-Menten kinetics measurements as described in *Chapter 5B*). The activity was recovered directly after THK buffer addition (keeping in mind that the abbreviation THK buffer is always associated with a pH value adjusted to 8), so a reduced activity due to acidification was presumed (not shown). Retrospectively, it was of advantage to determine the activity in buffered solution on that score to avoid undesired activity losses caused by such side effects. Moreover, due to the results obtained in the presence of valinomycin, a notable membrane potential was evidenced as well, without which there would be no difference to the measurements in absence of the potassium carrier. In spite of finding other possible reasons, this initial assumption was not abandonned as being limiting. Although briefly discussed, there were no attempts to analyse the limit formation in detail, since it is – similar to the light-driven C*c*O – an artificial artefact anyway. Life is dependent on consuming this gradient via the ATPase. Therefore, a gradient that emerges in absence of the ATPase did not appear to be of reasonable interest.

As performed in the course of the qualitative measurements, unbuffered samples were initially planned to augment the quantifications (and performed). An example, compared to the results shown so far, is displayed in Fig. 5A.14.

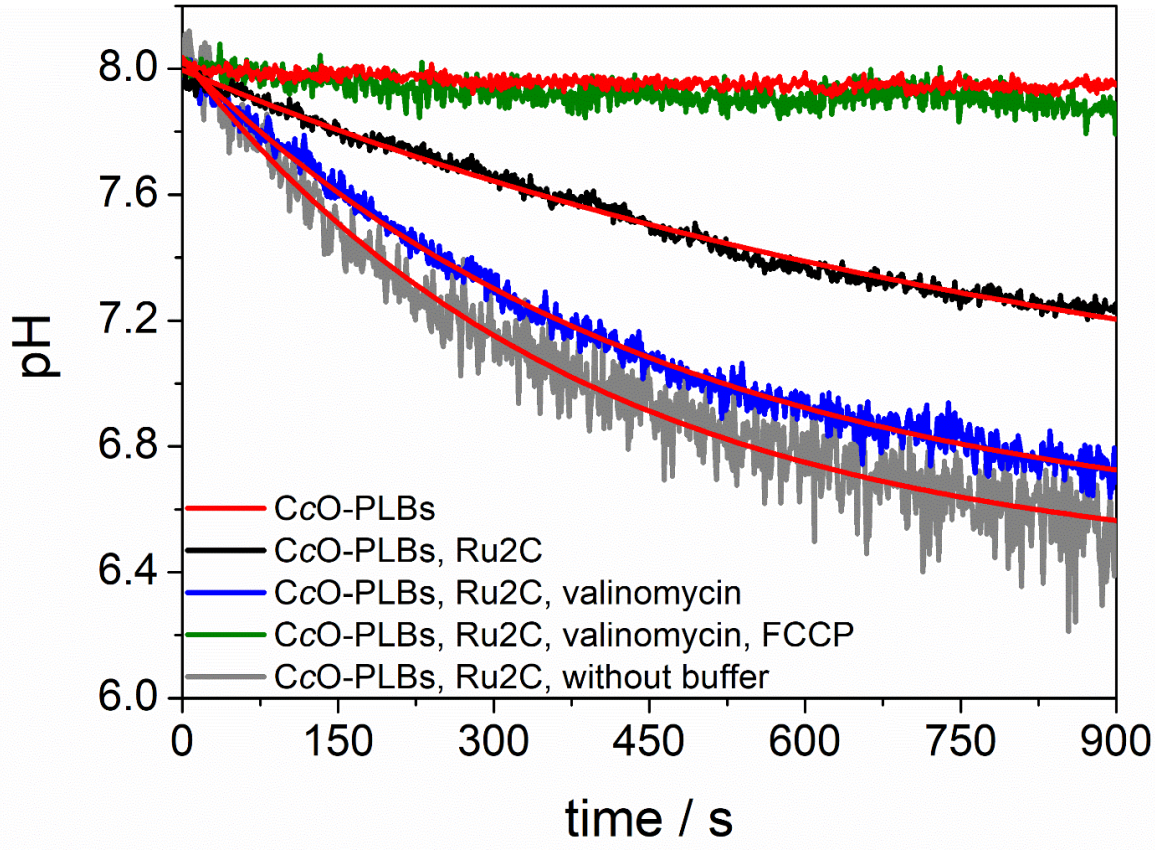

Figure 5A.14: Exemplary unbuffered measurement. The gray line represents a sample containing PLBs re-suspended in an unbuffered 40 mM KCl solution. For comparison, the results of Fig. 5A.12 are shown as well.

The intensity of the unbuffered sample ran similar to the one containing valinomycin, only a bit steeper, ending on a slightly lower pH value of approximately 6.6. At first glance, the unbuffered curve seemed to reflect the assumptions. The intensity dropped faster, but in contrast to the sample containing valinomycin, it did not indicate a faster C*c*O turnover. Instead, due to the lack of buffer, the pH value is decreasing faster, leading to an increased fluorescein protonation. This assumption could not be validated. It was not underpinned by calculations. Using the fit of the unbuffered sample in Fig. 5A.14, the evaluation resulted in a calculated turnover of less than one proton per single C*c*O and second. In other words: Presumed that the turnover is not influenced by the presence of Tris molecules directly and thus equaling the one of the buffered sample without valinomycin, a turnover of 66 protons per C*c*O and second would theoretically lead to a drastically faster decrease than it was measured, almost immediately escaping the displayed range towards lower pH values.

Yet the measurement could be explained by a process leading to miscalculation. Without buffer, drastic pH changes occur due to little effects. The excitation of the Ru complex by the residual room light is controversial due to the limited power and the limited quantum efficiency of the Ru complex (although enhanced towards the commercial Ru complexes); moreover, the sample was protected from light carefully. Nonetheless, the samples needed to be in focus, and even by the very short focusing process, especially using the coordinate saving option of the Leica software, there had been a few seconds of illumination before the measurement was started. Without buffer – although fluorescein is weakly buffering, but it was present in low concentrations – these seconds are of enormous effect in case of lacking buffer. Why is the slope not steeper then?

The fluorescein as a weak buffer is not a sufficient explanation, foremost because of its low concentration. Actually, the equations were not used properly at all because of the normalization. The pH value was normalized to 8, but must be assumed to be way lower already. Because of the non-linear pH scale, strongly influencing both equations, the results – looking suitable at first sight – are to discard completely. Assuming the turnover measured for the buffered sample (there is no reason to expect a different activity due to the lack of Tris molecules), the pH value would drop out of the displayed range during the first seconds of illumination, hence as a consequence of focussing already (a drop of pH to 6.5 in an unbuffered environment would correspond to 5.5 turnover cycles, which would happen within 83 ms, if the measured turnover of 66 H^+/s was assumed). So, the steep part could not be monitored. Then, having already a notable potential (due to the smaller volume, the pH increase inside the PLBs was presumed to proceed even faster) and maybe a reduced C*c*O activity due to low pH,

expectable minor changes were translated in notable ones by normalizing the small intensities to 1, erroneously assigned to a pH = 8. This also explained the weaker intensity observed at unbuffered PLB samples (not shown), which is indirectly shown in Fig. 5A.14 by the larger noise (having a weaker signal, the constant background noise is larger in relation). Moreover, it implies that the used equations non-linear equations were applied completely wrong.

Regarding the buffered measurements, these initial seconds were found to lead only to negligible inaccuracies due to normalization because of the distribution of pumped protons between Tris, fluorescein DHPE, and the aqueous phase. (Assuming a linear behavior of the ratio between the protons taken up by Tris and by water, respectively, and a linear pumping activity for the first ten seconds, further including the protons that are implied by pH = 8, 10 s of illumination to focus – which was not unrealistic because the coordinates could be saved by the program – would result in a calculated pH value of 7.99, thereby having neglected the protons that would be additionally removed from the aqueous phase by fluorescein DHPE protonation.) Hence, the evaluation was considered as valid if (and only if) the corresponding measurements were buffered.

The unbuffered measurements, on the other hand, which finally (also in regards to the ones shown in Fig. 5A.8) could not be evaluated quantitatively by assigning pH value changes and turnover numbers, retained only their qualitative significance in terms of evidencing the presence of any proton pump activity. Beyond, they were not meaningful at all. However, to refrain from unbuffered measurements (which initially were performed to be able to monitor any changes at all) was not considered to be accompanied with any loss of significance, since the C*c*O is naturally situated in an environment that contains buffering substances as well, and a direct influence of the additional Tris molecules on the C*c*O lacked any reasonable indication. Retrospectively, there was actually no need to measure in an unbuffered environment at all. Conversely, by buffering the samples and thereby confining the pH changes to rather narrow ranges, at least where affecting the evaluation (mostly between 7 and 8, including the following measurements), the natural situation was rather mimicked better and inaccuracies due to, for example, different initial pH conditions were avoided.

Finally, the reconstitution of the C*c*O in PLBs with preserved functionality could be supported with specified turnover numbers, being 66 and 163 pumped protons per C*c*O and second with and without a dense membrane, respectively. The rather low values compared to literature might be due to the not completely continuous illumination. Therefore, speculations about constraints that, e.g., might be due to the protein attachment were kind of idle. To continue with

a continuously excited enzyme that showed a functionally lossless PLB encapsulation, please proceed with subchapter 5A.7, within which the integration of more than one type of proteins is discussed, capable to interact with each other. Before, the residuary results obtained with C*c*O-PLB are discussed (dealing with the durability of PLBs, their applicability in commercial high-throughput assays, and the component exchangeability in terms of the lipid share), although this would be the reasonable continuation if prioritizing the achievable turnover.

As an aside: Within the *Theory* part it was outlined that, as soon as it comes to the investigation of the catalytic cycle of the C*c*O, an activation procedure is required to obtain a notably efficient catalysis (referred to as pulsed state) [25, 53, 59]. In contrast, others determined the turnover of the C*c*O with numbers that were by far exceeding the kinetic properties of the non-pulsed state C*c*O without performing any activation procedure [51, 57, 58]. Although lower than reported by the latter publications, with 163 protons per C*c*O and second in case of the uncoupled enzyme, the results presented here did not indicate a resting state (as the opposite of the pulsed state) C*c*O as well, although not having been activated. Seemingly, there is a conspicuous connection between the necessity to activate and the aim of monitoring partial steps within the catalytic cycle, while the determination of the overall turnover is apparently not associated with this requirement, as found in several cases (e.g., see the specified references). However, despite of all considerations, this remained completely enigmatic.

5A.4 Durability of PLBs

As mentioned before, the discussion of one measurement presented within the first publication, Frank *et al.*, 2015, was postponed. It dealt with the PLB durability in a qualitative way. The results are shown in Figure 5A.15.

The appearance of the freshly prepared PLBs displayed in Fig. 5A.15a and b did not differ from the ones shown so far. Indeed, all PLBs so far have been used freshly prepared, at least within the same week. The slight differences in color, appearing rather white instead of red is due to settings, more precisely to the imaging mode, which indicates saturation in blue and intensities close to saturation in white (depending on the set gain more than on the mere sensitivity of the sensor), thereby differing a bit in terms of depiction.

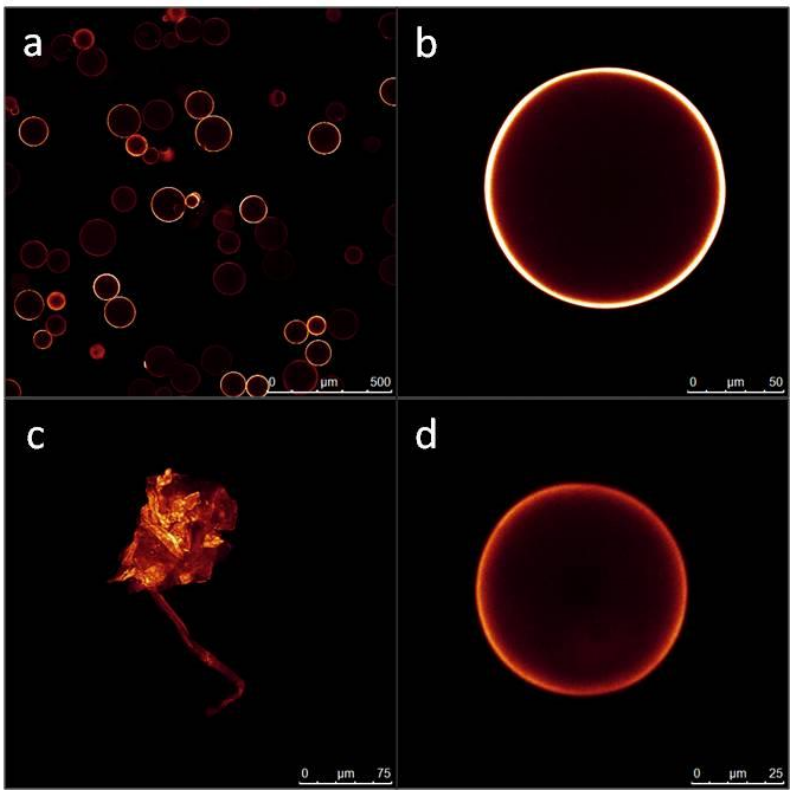

Figure 5A.15: Qualitative estimation of PLB durability. (A) Freshly prepared PLBs labeled with di-4-ANBDQBS in THK buffer. (B) Zoom at a single PLB of (A). (C) Zoom on single PLB after shock-freezing using liquid nitrogen and thawing without DMSO. (D) Thawed PLB after shock-freezing with DMSO. Figure published in Frank *et al.*, 2015 [299]. Lowercase letters were used according to the published illustration. Measurement and figure done by co-workers.

The PLB shown in Fig. 5A.15c did not exhibit a spherical shape, but a completely disordered one. Obviously, bead and membrane were destroyed during the freeze-thaw cycle. Conversely, apart from being less intense (but the overall intensity differed between different samples, which might be explained by the varying surface area accompanied by the different size distribution of the beads; the actual number of bound fluorescein molecules escaped our ability to measure), the shape of the PLB depicted in Fig. 5A.15d was normal in comparison to previously displayed ones. The destruction of the PLBs in Fig. 5A.15c is likely caused by ice crystal formation. The increasing volume might lead to PLB burst, and additionally, needle-shaped crystals might penetrate both membrane and agarose beads. Using liquid nitrogen prevents the structural changes upon water freezing, causing amorphous ice to emerge, since the freezing process is too fast for the molecules to rearrange. To ensure, the liquid nitrogen was poured onto the vessel to avoid Leydenfrost phenomena (evaporated nitrogen forms an insulating layer around the sample, which was avoided by flushing away the gaseous nitrogen with the liquid one. Nevertheless, this procedure is suitable, e.g., for electron microscopy, where the sample is discarded after imaging. Otherwise, it is problematic, since the thawing process is taking place slowly in any case, and the ice molecules rearrange upon this process, causing

the same damages as if freezing. DMSO is known to promote the formation of amorphous ice. So, the usage of DMSO resulted in a seemingly intact PLB (Fig. 5A.15d), whose actual functionality could not be assessed this way, as discussed above.

After introducing the quantification approach, this could be further investigated. The results are shown in Fig. 5A.16. The evaluation was done as described. As of now, the translated pH courses are shown representatively instead of each time displaying the intensity, the translated pH values, the subtracted negative control, and the final fitting.

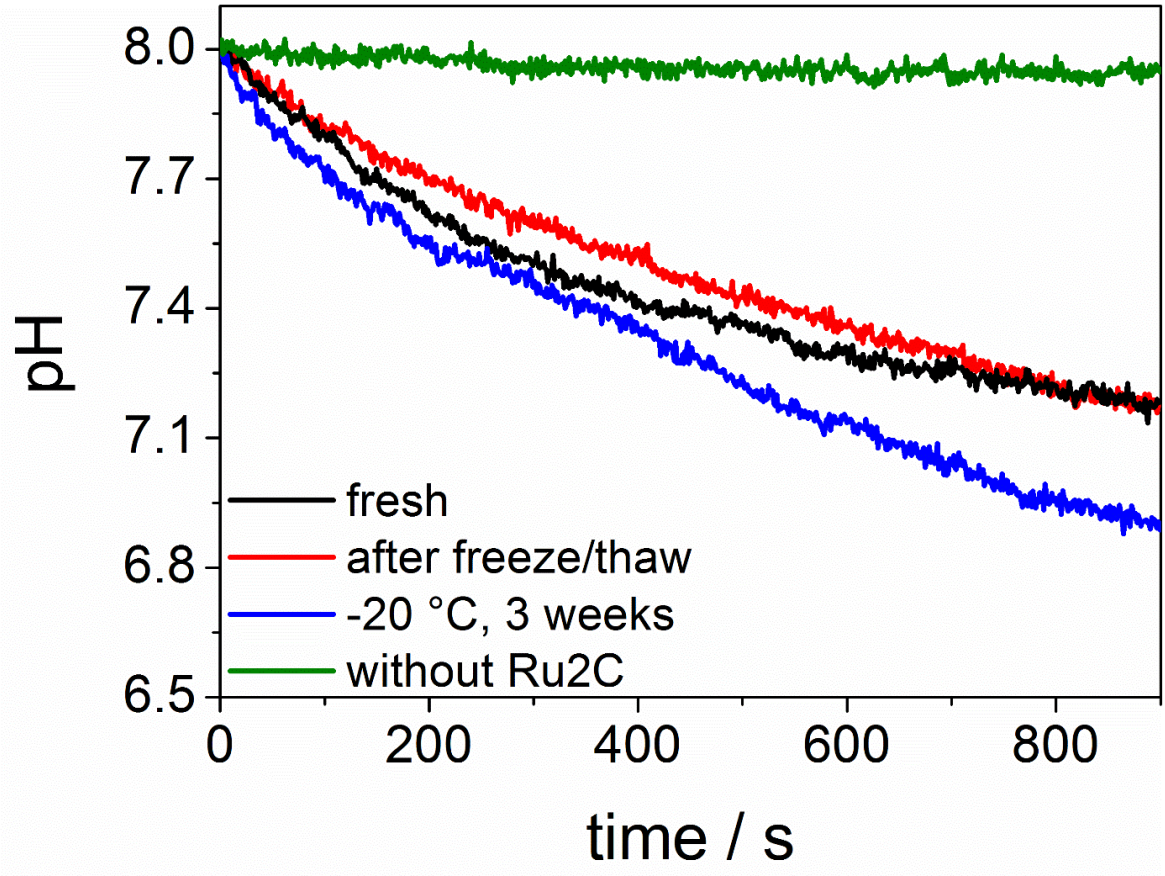

Figure 5A.16: Quantitative determination of the PLB durability. PLBs were prepared as described in the Materials & Methods section. Subsequently, a sample was taken to determine the activity of freshly prepared PLBs again (black), containing Ru_2C/aniline/3-CP. Another share was shock-frozen in the presence of 10 % (v/v) DMSO. One sample was thawed directly afterwards and measured in the presence of Ru_2C/aniline/3-CP (red). The residual preparation was stored for three weeks and afterwards probed accordingly (blue). A negative control, not comprising Ru_2C/aniline/3-CP, was measured, too (green). Figure published in Geiss *et al.*, 2017a [295].

The curves of Fig. 5A.16 were similar to the buffered one shown in Fig. 5A.12, and so are the final values, being about pH = 7.2 for the fresh sample and the one that underwent an immediate freeze-thaw cycle, andpH = 6.9 for the sample stored at -20 °C after shock-freezing in the presence of 10 % DMSO. However, although not identical, the curve progress is similar. The results of the calculations according to the ones presented previously yielded 61 H^+/s for the

directly thawed sample and 73 H^+/s for the one that was stored for three weeks. Of course, the turnover was not assumed to increase while storing, but keeping in mind that the calculation included simplification and was obviously not infinitively precise giving estimations rather (see, for example, the paragraph dealing with the pre-excitation while focusing, mentioned above), it was deduced that the C*c*O activity is preserved over time when PLBs are shock-frozen in the presence of 10 % DMSO. It was not tested for a longer period, but since the critical process is freezing and foremost the thawing, PLBs might retain their functionality even longer if treated with DMSO before freezing. Moreover, the DMSO obviously did not impair the protein function in a significant way. Long-term storage appeared to be an option, what is interesting especially in terms of commercial assays and and high-throughput applications.

5A.5 Applicability in commercial high-throughput FLIPR assay

Without pursuing a specific goal concerning any C*c*O functional parameter, it should be tested whether the PLB format could be applied to a commercial high-throughput assay. So, a fluorescence imaging plate reader (FLIPR) assay, which is commonly performed to test ion channels [263, 296, 297], was commissioned to SB Drug Delivery, Glasgow, UK. Having had investigated mainly the pH value progression before, the electric potential should be probed within this assay. For that purpose, the potential-sensitive FRET (Förster resonance energy transfer) pair CC2-DMPE/DiSBAC_2(3) was utilized after pre-testing the principal possibility to stain PLBs with the FRET pair (Fig. 5A.2H and I). Dependent on the electric potential across the membrane, the components, initially in close distance, locate more distant, so the energy transfer is weaker pronounced, and hence, the emission of both components will alter. If there is a strong FRET, the acceptor will receive a notable amount of energy absorbed by the donor and its fluorescence will be strong in comparison to the donor fluorescence. Conversely, if farther separated, the donor will keep its energy and release it by means of fluorescence [281]. The ratio of donor to acceptor fluorescence is therefore giving information about the electric potential development. For a detailed description see *Materials & Methods*.

After preparation the PLBs were sent to SB Drug Delivery, where the labeling according to the description given within the *Materials & Methods* section occurred. Subsequently, an assay was performed following their usual workflow. Different concentrations of cyt *c* were employed for activation, and the emission ratio was followed over time (cyt *c* had to be used also because the spectra of the FRET pair and the Ru complex were interfering). Afterwards the plots were linearly fitted (Fig. 4.17A).

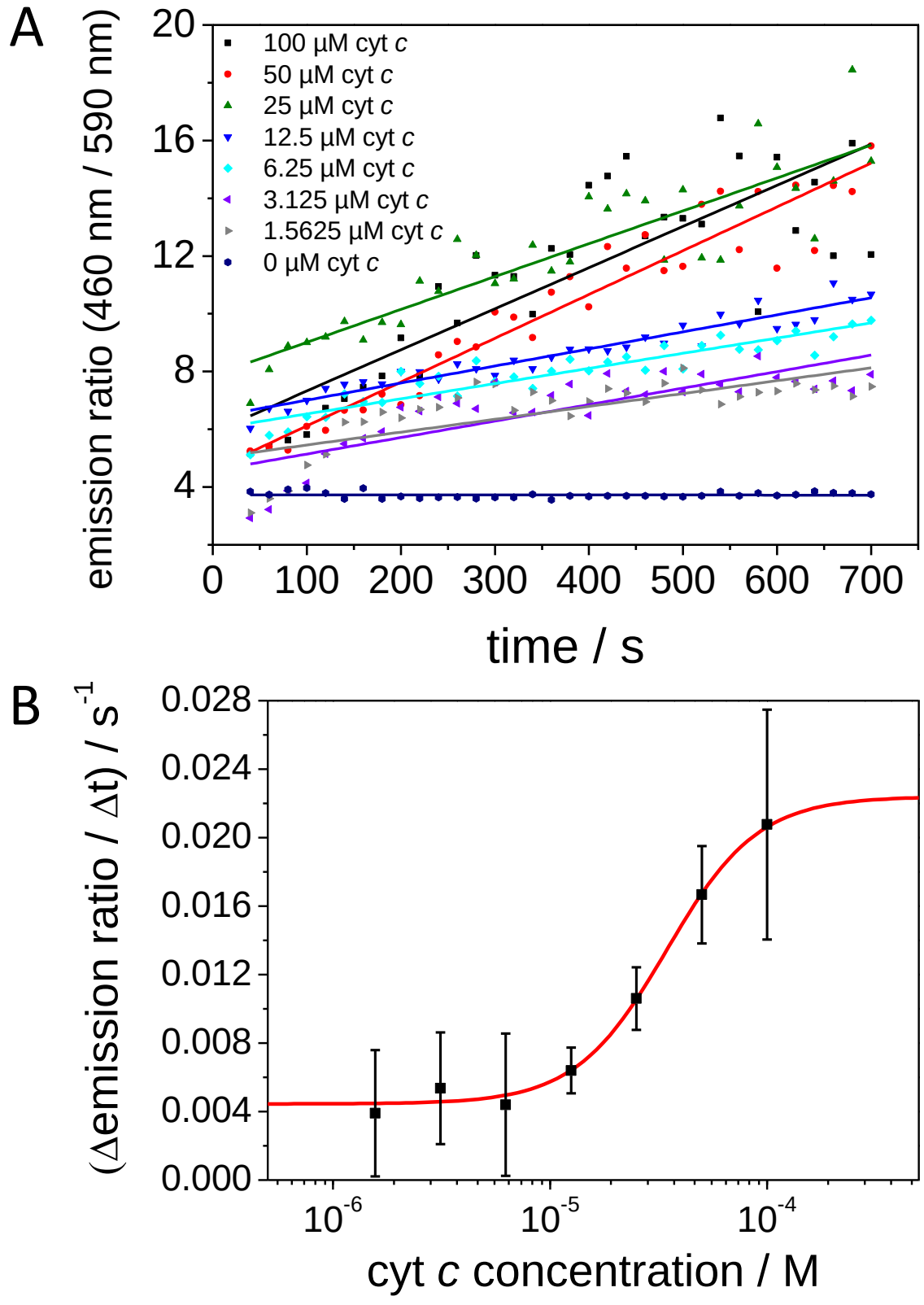

Figure 5A.17: FLIPR assay results. PLB samples were prepared following the standard procedure, resuspended in THK buffer and sent to SB Drug Delivery, where the samples were stained with the potential-sensitive FRET pair CC2-DMPE/DiSBAC$_2$(3). Afterwards, a high-throughput FLIPR assay was performed according to their standard protocol, eventually detecting donor and acceptor fluorescence after addition of different cyt *c* concentrations. The emission ratio was applied versus time and linearly fitted (A). The slopes of the linear fits were applied vs. the cyt *c* concentration. A sigmoid fit was used to determine the EC_{50} value (B). Figure published in Geiss *et al.*, 2017a [295].

The slopes of these fits were applied versus the cyt *c* concentration, yielding a dose-response curve, which can be fitted using a sigmoid function (Fig. 4.17B). This so-called dose-response (Fig. 4.17B) is of interest to compare agonists and antagonists on their respective target receptors (see aforementioned references for case examples), being a possible application for PLBs. The could be performed and evaluated straightforward, indicating PLBs as suitable for that kind of commercial high-throughput assays, although the EC_{50} value ("effective concentration", being the concentration that evokes 50 % of the maximum response, which was in this case the membrane potential formation) of 34.4 µM had no quantitative meaning in the case of the C*c*O.

Qualitatively, it can be stated that a potential arises upon substrate addition, which was moreover not collapsing by time, again indicating a dense membrane and a functionally embedded C*c*O, but as mentioned before, a such potential generation does not occur within the native environment of the C*c*O, since simultaneously the electrochemical potential is used by the ATP synthase for ATP formation, thereby compensating it, so the result was foremost the applicability of PLBs in such assays. The value itself carried no information. The EC_{50} value should not be confused with the later determined K_M value (*Chapter 5B*), which is a measure of substrate affinity.

5A.6 PLBs based on E. coli *lipid (Modular system I: the lipid share)*

As initially mentioned, the PLBs should finally serve as a modular system, providing a frame format that enables to choose beads, proteins, lipids, and labels can be chosen as desired. The labels, however, are no fundamental components of the PLBs. The usability of several was shown, but as of *Chapter 5B*, also applications that does not require a label are presented. Of the remaining three, the lipid was varied at first.

Therefore, the saturated and stable DiPhyPC, which was used as a model lipid, while natural cells or compartments thereof are surrounded by membranes composed of lipid mixtures comprising plenty of different components was a replaced by the commercially available polar lipid extract of *E. coli*. After the preparation of *E. coli* lipid-based PLBs, (the protocol was altered only in replacing the DiPhyPC with *E. coli* polar lipid using the same concentrations and quantities), the procedure of turnover quantification was performed again. The results are shown in Fig. 5A.17.

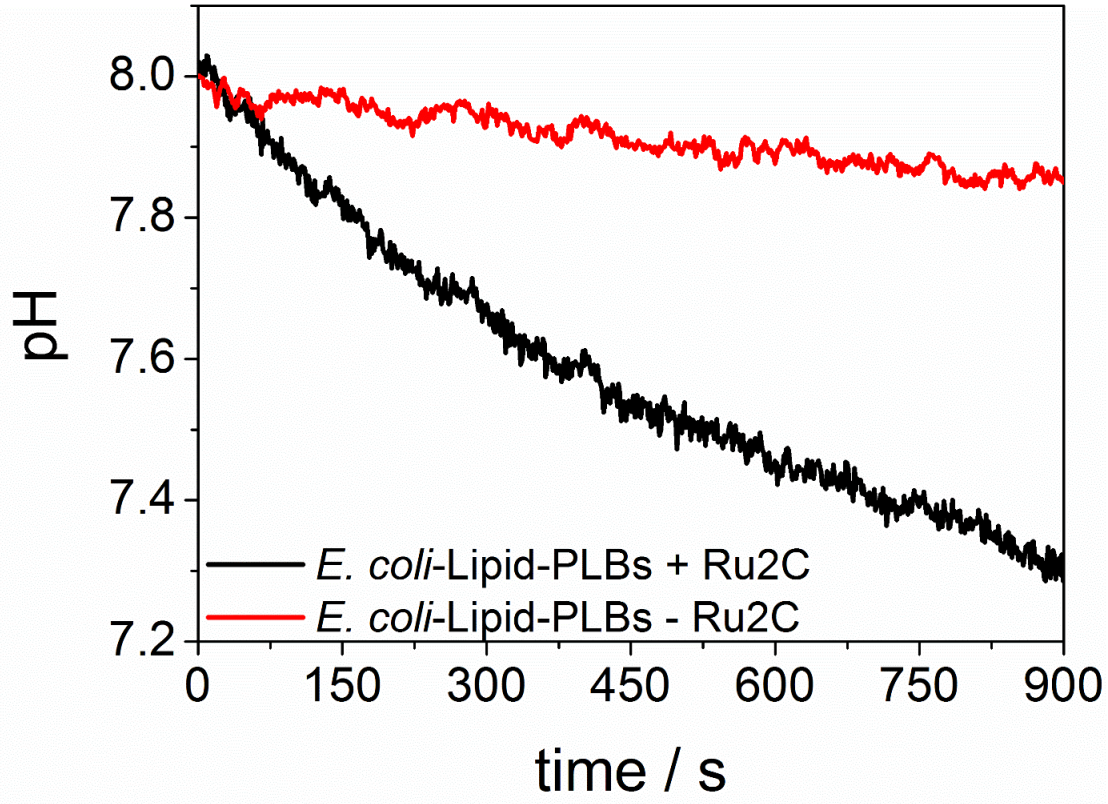

Figure 5A.18: Turnover quantification of PLBs prepared from *E. coli* lipid. Except from the usage of *E. coli* polar lipid extract, sample preparation, measurement procedure and evaluation were performed according to aforementioned experiments, described by the Figures 5A.12 and 5A.16. The black and red line represents the sample with and without Ru_2C/aniline/3-CP, respectively. Figure published in Geiss *et al.*, 2017a [295].

Regarding Fig. 5A.18, the measurement without Ru_2C/aniline/3-CP end attained a value of pH = 7.85, which was a bit lower than measured before, but in principle, it ran as usual (and the negative control was subtracted anyway). The initial turnover of the PLBs prepared using *E. coli* lipid was determined to be 72 H^+/s, thus having been in the range repeatedly observed using DiPhyPC. It was concluded that the lipid is exchangeable in principle. In contrast to the reported order, these experiments were performed at the very end of the laboratory time, so more tests, e.g., using Asolectin from the soybean, representing a lipid mixture originating from eukaryotic cells, could not be performed anymore. The initial turnover values are summarized in Table 5A.2.

Table 5A.2: Initial turnover values of C*c*O-PLBs measured under different conditions [295].

Initial rate [H^+/s]	**DiPhyPC**			***E. coli* polar lipid extract**
	fresh/4 °C	**freeze/thaw**	**-20 °C, 3 weeks**	
- valinomycin	66	61	73	72
+ valinomycin	163	---	---	---

Being in a range from 61 to 73 protons per seconds, differences were assigned to deviations rather than to differences due to the investigated process or composition. Before proceeding with the reconstitution of different proteins, the associated publication, published in the *Journal of Colloid and Interface Science*, is presented, herein referred to as Geiss *et al*., 2017a.

A. F. GEISS, C. BLIEM, P. FRANK, C. REINER-ROZMAN, J. KEWNEY, M. BOERSCH, AND R. L. C. NAUMANN: **Proteo-lipobeads to encapsulate cytochrome *c* oxidase from *Paracoccus denitrificans***. *Journal of Colloid and Interface Science* 500 (2017) pp. 119–125. doi: 10.1016/j.jcis.2017.04.009.

Publication II

<content not available in online version>

<content not available in online version>

<content not available in online version>

<content not available in online version>

<content not available in online version>

<content not available in online version>

<content not available in online version>

<content not available in online version>

<content not available in online version>

<content not available in online version>

<content not available in online version>

<content not available in online version>

<content not available in online version>

5A.7 PLBs based on RC and bc_1 *(Modular system II: the protein share)*

As a next step, PLBs were prepared from different proteins. Indeed, also the LHCII-PLBs were prepared as part of this stage (Fig. 5A.6), but those measurements were considered to match the discussion of the basic structure better. Moreover, the LHCII was embedded in PLBs, but its functional integration in terms of light forwarding was not investigated. Here, the functional integration of two different types of proteins, namely the photosynthetic reaction center P870 (RC) and the cytochrom bc_1 complex, requiring their interaction, was investigated.

The collaborating system that was aimed to be co-reconstituted within PLBs comprised four components, mimicking the light reaction of the anoxygenic photosynthesis type II, found, for instance, in purple bacteria like *Rhodobacter sphaeroides* (see *Theory*). Briefly, the RC utilizes light energy to reduce ubiquinone (UQ) via ubisemiquinone to ubiquinol (ubihydroquinone) (UQH_2). The latter is able to diffuse freely within the membrane. The bc_1 oxidizes UQH_2, thereby pumping protons as the C*c*O does (for a description of the *Q cycle*, please see the *Theory* part). At this point, the detection via fluorescein DHPE is possible as outlined above. As in the respiratory chain, cyt *c* is accepting the electrons from bc_1, here acting as a shuttle which transports the electrons back to the RC, where it comes full circle. A schematic, non-stoichiometric illustration, shown as desired to mimick in PLBs, is provided by Fig. 5A.19.

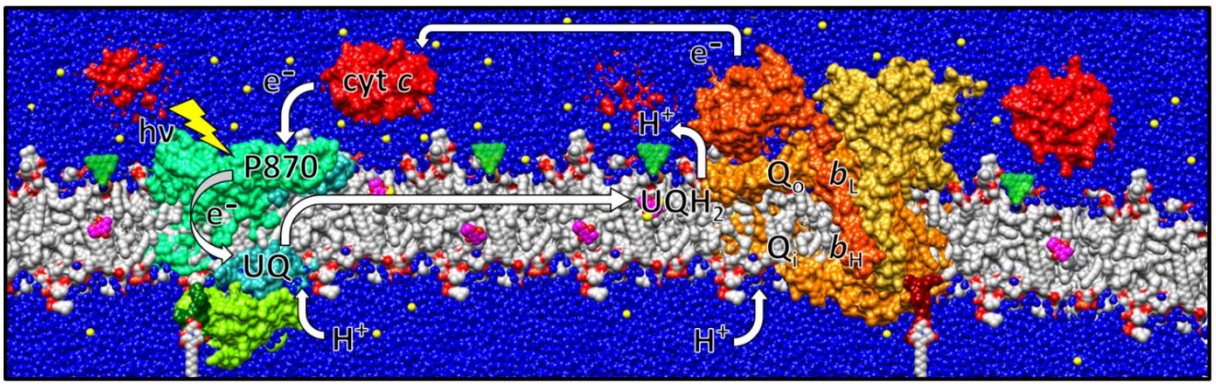

Figure 5A.19: Schematic (non-stoichiometric) reaction mechanism of the proteins co-reconstituted in PLBs. The photosynthetic reaction center P870 (RC, green; H subunit: yellow-green; L subunit: medium green; M subunit: blue-green; PDB file: 2UXJ [92]), immobilized via a genetically engineered 7-his-tag (dark green) at the C-terminus of the M subunit, is excited by light (symbolized by the flash symbol) and as a consequence reduces ubiquinone (UQ, magenta) to ubiquinol (UQH_2, intermediate step not shown). After diffusion to the cytochrome bc_1 complex (bc_1, orange; A and D subunit: medium orange; B and E subunit: yellow-orange; C and F subunit: red-orange; homodimer, so A is equivalent to D, B to E, and C to F; PDB file: 2QJK [284]), poly-his-tagged (dark orange) at the C-terminus of the cyt *b* (A, D) subunit, it is oxidized again there, while the bc_1 is forwarding the electrons to cytochrome (cyt) *c* (red, PDB file: 2B4Z [33]). This step is accompanied by proton (yellow, shown solely instead of bound to H_2O, forming H_3O^+) translocation across the membrane. Q_o and Q_i indicate UQ binding sites; the associated Q cycle is not shown here. The proton release can be sensed by the fluorophore (transparent green) of fluorescein DHPE, situated in the outer leaflet of the membrane. Cyt *c* shuttles the electrons back to the RC. The membrane (PDB file: dppc64 [285]) and the NTA-containing linker molecule (Ni^{2+} is hidden) are colored by element. Water molecules are depicted as blue spheres. Arrows indicate diffusion as well as electron and proton transitions only schematically. Figure published in Geiss *et al.*, 2017b [302].

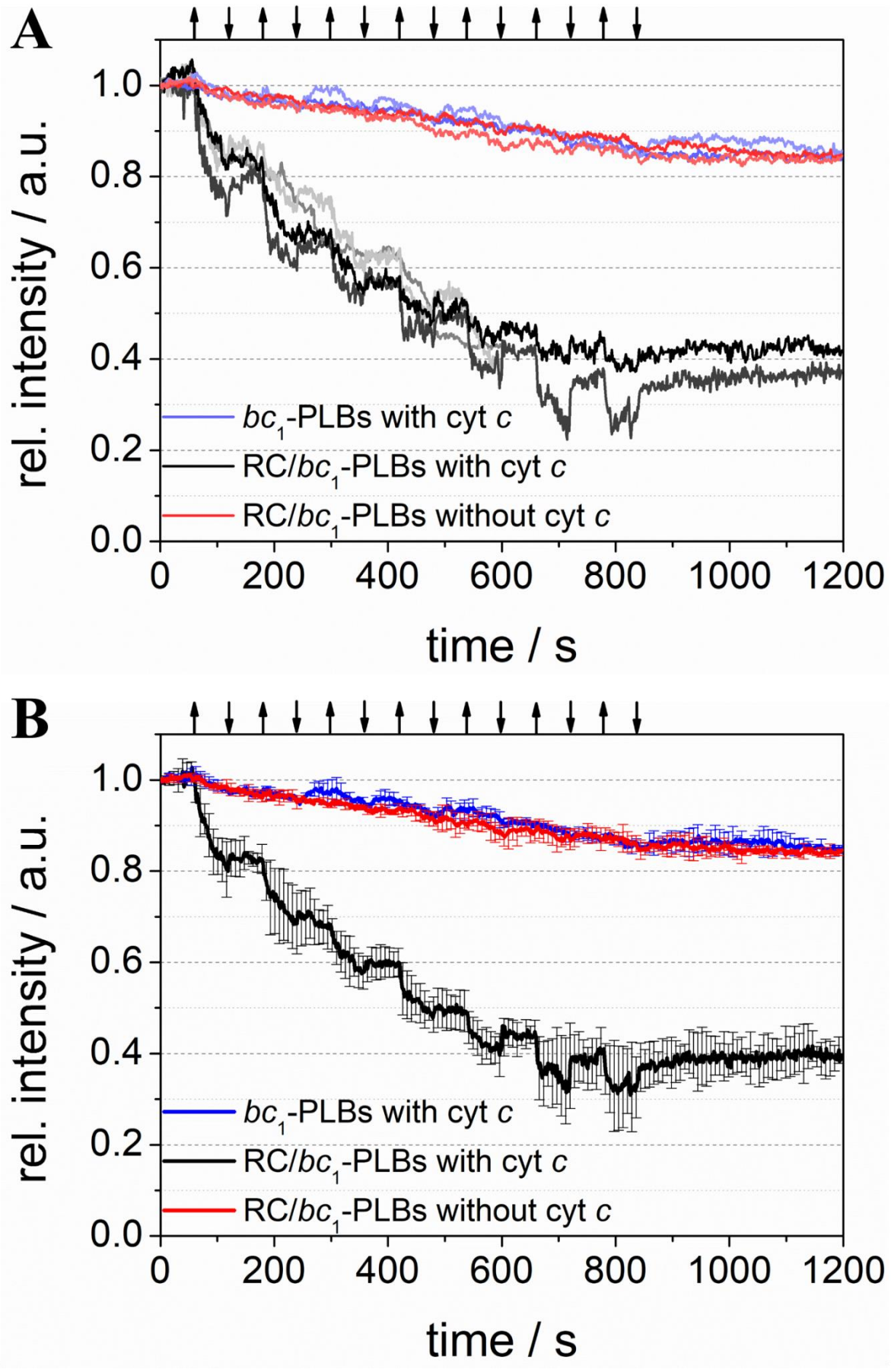

Figure 5A.20: (A) Repetitions of RC/*bc*$_1$-PLB experiments. (B) Mean value curves with standard deviations. For a detailed description, please see the following Figure 5A.21. Figure published in Geiss *et al.*, 2017b [302].

Instead of directly exciting the bc_1 by added UQH_2, the RC was excited by a halogen white light source. This led to light artefacts again, but there was no adequate possibility to excite the RC by one of the imaging lasers that were integrated in the measurement setup. The PLB illumination was carried out in seven intervals of 1 min, interrupted by equal periods without excitation. The results are shown in the Figs. 5A20 and 5A.21, the first showing several repetitions and the associated mean value curves with standard deviation, the second displaying the further processing.

The repetitions were considered to be similar enough to claim reproducibility, so the further evaluation of the results was done by means of the mean value curve (Figure 5A.21).

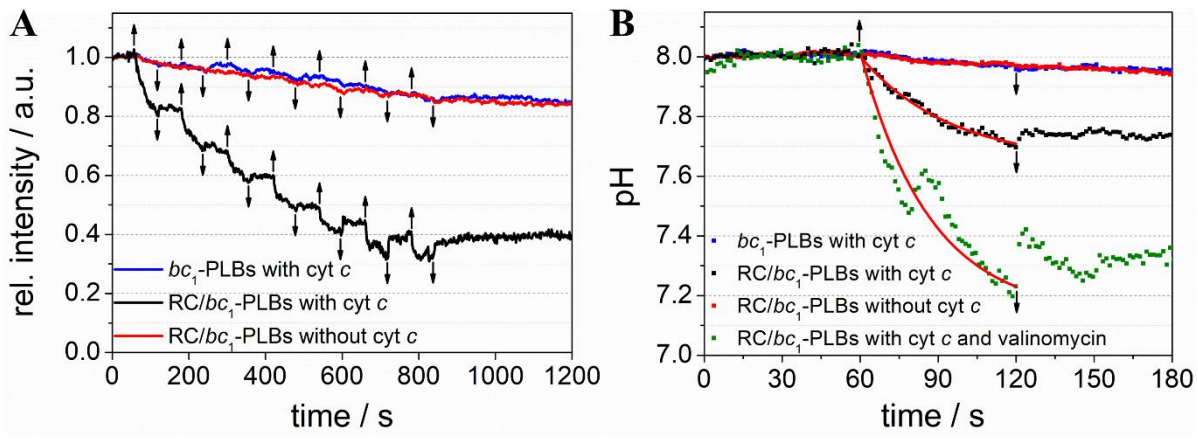

Figure 5A.21: Intensity and pH changes measured at illuminated RC/bc_1-PLBs. RC/bc_1-PLBs were prepared according to the standard procedure in THK buffer, given in *Material & Methods*. To provide an equal distribution, the proteins were premixed before the proteobead formation. The PLBs were labeled with fluorescein DHPE and imaged by LSM. (A) In seven steps of 1 min, the sample was illuminated by a halogen white light source, interrupted by 1 min intervals without illumination. (B) Magnification of the first illumination step, translated to pH values by means of the calibration plot shown in Fig. 5A.11 Data were exponentially fitted. The displayed curves are mean values of the repetitions shown in Fig. 5A.20. The sample containing all RC/bc_1-PLBs and a mixture of each 10 µM reduced and oxidized cyt *c*, respectively (black) was compared to two negative control measurements, one lacking the RC (blue) and the other lacking cyt *c* (red). One sample contained (beside RC and cyt *c*) 0.5 µM valinomycin in addition (green). The applied bc_1 amount was the same in any case (keeping in mind that the indication of concentrations is somewhat misleading having surface-attached proteins. Arrows indicate the beginning (↑) and the end (↓) of the illumination periods. Figure published in Geiss *et al.*, 2017b [302].

In the measurements displayed in Fig. 5A.21 the samples without RC and without cyt *c*, respectively, served as negative control. The first of them was to assure that excitation was indeed occurring via the RC. In contrast to the measurement including the RC, the fluorescence intensity dropped only little. The final level of 85 % of the initial intensity is a bit less than usually obtained with C*c*O-PLBs, but the white light excitation occurred in addition to the imaging laser, which was set as before, and hence, a stronger bleaching was arguable. The second negative control measurement without the cyt *c* mixture (10 µM reduced, 10 µM oxidized cyt *c*) followed a similar course, also attaining a final value of 85 % of the initial

intensity. Without cyt *c*, there is no subsequent electron acceptor and the bc_1 remains reduced. Thus, also one cycle of proton pumping, within which all RC molecules are oxidized, is unlikely. Therefore, it made sense that the measurement curves were so similar. Measurements lacking cyt *c* were performed to evidence that the presence of both the excitable and the proton pumping protein, coupled via UQH_2, was not sufficient for proton pumping, thus to confirm the proposed reaction cycle. Having already two negative controls, a further one containing FCCP was not performed. (The sample with additional valinomycin was nevertheless vital to be able to compare with the solubilized enzyme in a somewhat reasonable manner.) The sample containing all components was dropping in intensity whenever the white light source is switched on. It was concluded that the RC was indeed excited by the white light source and the proposed electron cycle, displayed in Fig. 5A.19, was taking place, leading to acidification by means of the protons translocated by the bc_1. The final level was 40 % of the initial intensity.

To quantify the results, the same approach as for the C*c*O-PLBs was applied. In addition to the bleaching subtraction (which was done by subtracting the intensities of the negative control measurement without RC), the switching process had to be taken into account. Thus, at first the bleaching curve was subtracted from the respective sample curve. In a second step, the switching process, being causal for the abrupt intensity changes due to scattered light (and thus leading to apparent, but erroneous pH changes), was identified to take place in the first and last three measurement points of the illumination period, so only the curve in between was fitted, extrapolating the fit to the excitation time point zero to obtain the initial slope.

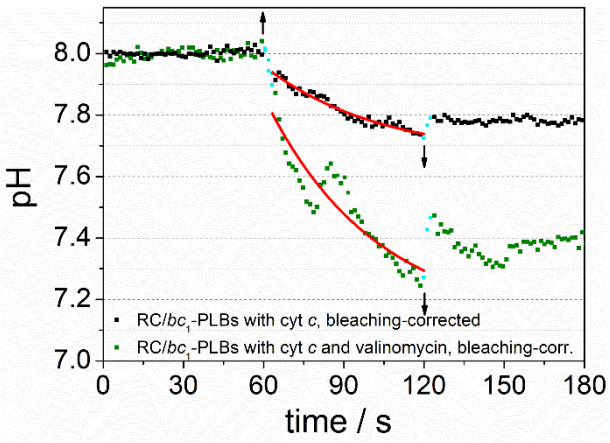

Fig. 5A.22: Bleaching and switching correction. The curves shown in Fig. 5A.21B were processed by subtracting the course of the negative control (without RC, blue line in Fig. 5A.21), assumed to represent the bleaching, from the sample with (green dots) and without (black dots) valinomycin, respectively, resulting in the bleaching-corrected curves. The cyan blue dots show the measurement points believed to display only apparent pH changes. The remaining intensity courses display the actual pH drop under continuous illumination conditions. Both were fitted exponentially (red lines). To quantify the initial turnover correctly, the fits were extrapolated to the start of the excitation period.

This process is depicted in Fig. 5A.22. For simplicity reasons, it was agreed to show the curves of Fig. 5A.21 in the respective publication, mentioning in the text that bleaching and switching artefacts were subtracted.

The quantification itself was done according to the above-mentioned calculations applied for C*c*O-PLBs, except from the number of proteins, which had to be determined individually. The procedure was nevertheless the same, being a UV/Vis determination of the mixture of RC and bc_1 after elution by imidazole treatment, using the extinction coefficients $\varepsilon_{802\ nm}$ = 288 mM^{-1} cm^{-1} for the RC [291] and $\varepsilon^{reduced-oxidized}_{562-575\ nm}$ = 25.6 mM^{-1} cm^{-1} for the bc_1 [292]. The spectra are displayed in Fig. 5A.23.

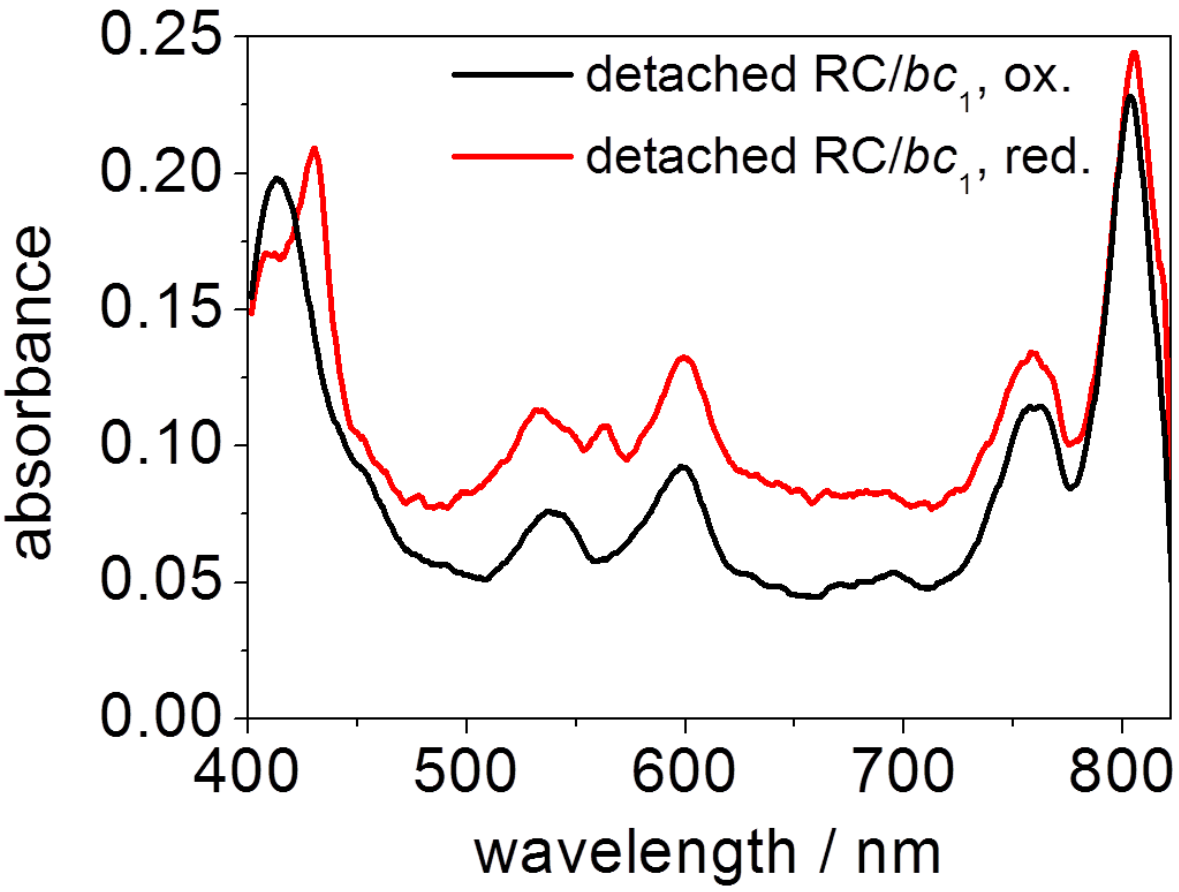

Figure 5A.23: Spectra of RC and bc_1, eluted from agarose-PLBs. A preparation of RC/bc_1 proteobeads was treated with THK buffer that additionally contained 300 mM imidazole. The agarose beads were separated by centrifugation, then the protein concentrations of the supernatant were determined by UV/Vis spectroscopy. After recording the spectra containing oxidized bc_1 (black), a few grains of sodium hydrosulfite were added to reduce it. Afterwards, the spectrum of reduced bc_1 (red) was measured.

The concentrations were determined by means of the Beer-Lambert law (eq. 4.1). It turned out that 85.7 and 91.7 % of the applied RCs and bc_1 complexes were immobilized to proteobeads, corresponding to 4.3 and 4.6 x 10^{-10} mol, respectively. Following the calculations described in the course of C*c*O turnover quantification, one sample contained 1.36 x 10^{13} bc_1 complexes. The complete calculations for the RC/bc_1 case is given within the *Supplementary Information* of the following publication (Geiss *et al.*, 2017b) [302], including the fit parameters. Briefly

summarized, the main part of protons was bound to the Tris buffer molecules again, while the shares bound to water and to fluorescein turned out to be negligible (being in the range of 10^{12}). The Tris molecules bound 3.89 x 10^{15} protons, yielding a turnover of each single bc_1 complex of 286 H^+/s. With valinomycin (applied only, since an additional proton uncoupler would have abolished the target effect), the turnover was 663 H^+/s. The ratio of the obtained turnover numbers with and without valinomycin was 2.3, indicating a dense membrane following the above-mentioned argumentation (although being not entirely comparable to a respiratory control ratio due to the lack of a proton uncoupler, an increased effect due to leakage formation would only emerge if the membrane was dense before). The RCR value was highly comparable with the one previously obtained at C*c*O-PLBs (2.5). Further, the final level remained stable for the last five minutes without signal recovery. If the membrane was leaky, the signal would have recovered due to redistribution of protons across the membrane. Both PLBs and evaluation technique were cross-checked by performing the experiment with another approach, being time-resolved attenuated total reflection surface-enhanced infrared absorption spectroscopy (tr-ATR-SEIRAS, see *Theory* for further explanation), carried out using a planar ptBLM on a gold surface, according Nowak *et al*., 2009 [298] and 2010 [60]. Afterwards, the results of both are discussed and compared with literature.

5A.8 Comparison with an established system

A protein-tethered bilayer lipid membrane (ptBLM) was prepared on a rough planar gold surface with co-reconstituted RC and bc_1 and investigated by time-resolved ATR-SEIRAS to be able to compare the new PLB system with an established one, and moreover to cross-check the evaluation technique that was introduced along with the PLBs. The membrane architectures are schematically depicted in Figure 5A.24. The schematic reaction depicted in Fig. 5A.19 applied in both cases. The infrared measurements were performed by the exchange internship student <content not available in online version>. Further evaluation, discussion, and publication was done by myself with the kind advice of <content not available in online version> of the University of Vienna, Austria.

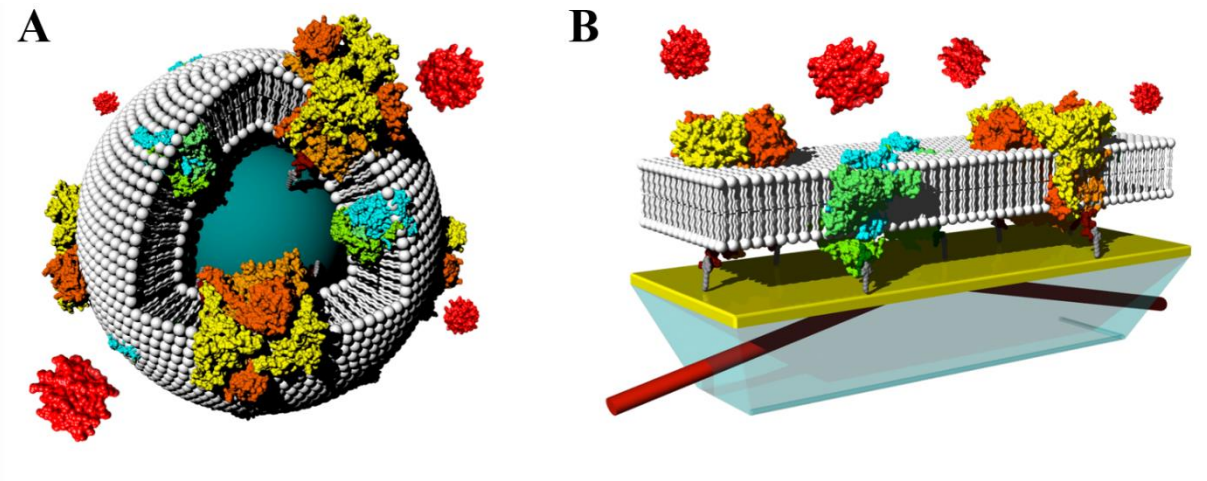

Figure 5A.24: Comparison of the spherical PLB and the planar ptBLM structure. (A) RC/bc_1-PLB based on an agarose core (turquoise) that is functionalized with a linker molecule carrying a Ni-NTA residue (gray). RCs are shown in blue to green colors, whereas the bc_1 complexes are shown in yellow to orange colors. The membrane is depicted in white, cyt *c* in red. Detailed information concerning the protein SU coloration is given in the caption of Fig. 5A.19, and so are the source PDB files including references. (B) RC and bc_1 co-reconstituted in a planar ptBLM. In order to perform ATR-SEIRAS measurements, the ptBLM is attached to a gold surface (gold) via thiol linkers, exhibiting a Ni-NTA residue at the opposite end (gray). The gold surface is – in contrast to the depiction – a rough one, evaporated and developed on top of an ATR crystal (transparent blue). The excitation laser is shown in red. The residual color code is the same as in (A). Figure published in Geiss *et al.*, 2017b [302].

The procedure that revealed information about the immobilization on top of the ATR crystal was done as described Nedelkovski et al., 2013 [119]. The increase of the vibrational components within the amide I region, exhibiting the maximum at 1652 cm^{-1}, was followed over the time of immobilization, thereby separating the share resulting from the O–H bending mode originating from water molecules ($k = 1642\ cm^{-1}$) by calculating the ratio of water stretching and bending modes within the same period. Changes of this ratio are therefore due to protein components. Further information about ATR-SEIRAS on ptBLMs can be attained in the aforementioned publications of Nowak *et al.*, 2009 [298] and 2010 [60], and in Schwaighofer *et al.*, 2013 [309], and Gebert *et al.*, 2015 [310].

For time-resolved measurements, a flash lamp was exciting the RC in a non-saturating manner with frequencies of 50 and 100 Hz, respectively. Non-saturating conditions mean that the flash was sufficient to excite each RC molecule only once or not, while double excitations did not occur or were at least statistically negligible. The first 25 spectra after excitation are displayed in Fig. 5A.25. Please note that the following spectra are averaged ones of hundred excitation cycles measured in a row.

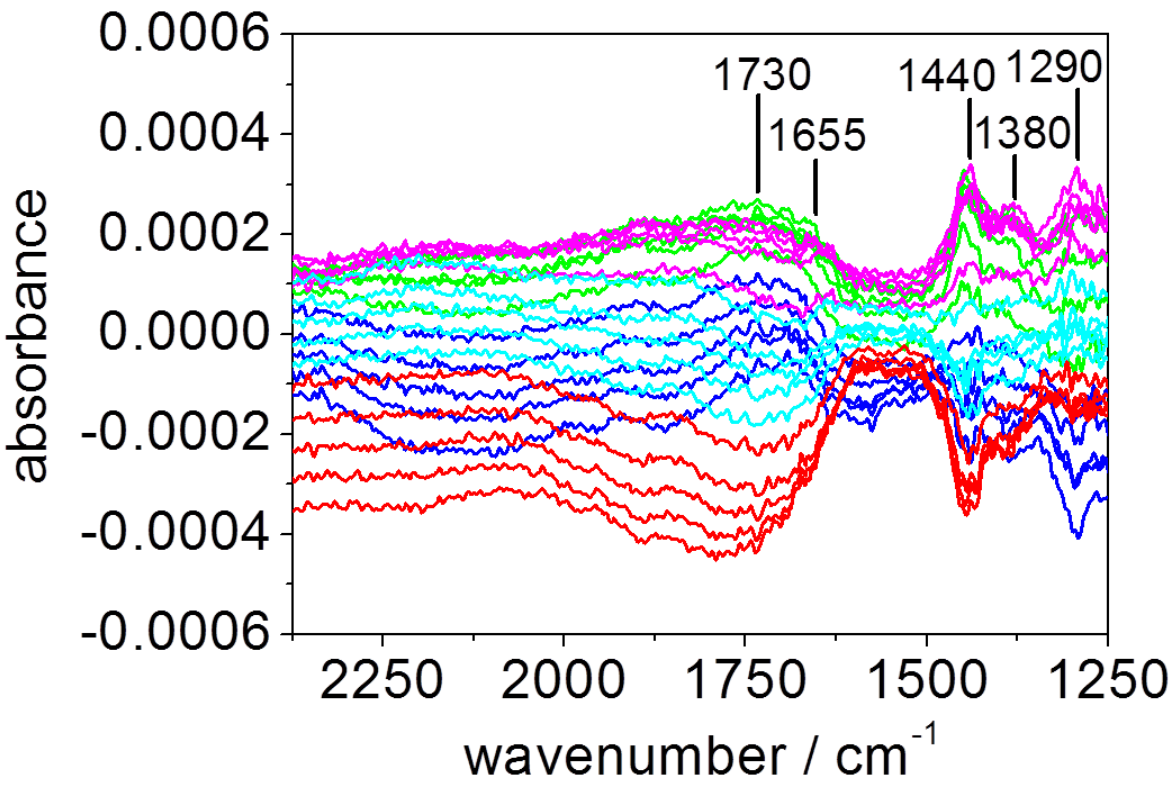

Figure 5A.25: Time-resolved ATR-SEIRAS spectra of RC and *bc*$_1$ complexes co-reconstituted within a ptBLM. Average spectra of the first 25 spectra of each cycle, encoded by colors: 1-5 in blue, 6-10 in green, 11-15 in magenta, 16-20 in cyan, and 21-25 in red. The excitation occurred with a frequency of 100 Hz. Figure published in Geiss *et al.*, 2017b [302].

The band positions were at approximately 1290, 1380, 1440, 1655, and 1730 cm^{-1} in both 50 and 100 Hz excitation experiments. The exact positions were determined by preparing orthogonal phase-resolved spectra, yielding peak wavenumbers of 1298, 1387, 1451, and 1654 cm^{-1}. The orthogonal phase-resolved spectra are shown in Fig. 5A.26, including the integrals that were used for further evaluation, see Fig. 5A.27.

The displayed bands between 1200 and 1700 cm^{-1} were obtained earlier performing similar measurements under continuous illumination with only the RC reconstituted within a planar ptBLM, which were at 1282, 1360, 1434, and 1642 cm^{-1} [311]. There were also indications for *bc*$_1$-caused changes, e.g., in the amide I region at approximately 1650 cm^{-1}, putatively due to conformational changes associated with the motion of the iron-sulfur protein between heme *b* and cytochrome c_1 [312]. In literature, large numbers of peaks are described for steady-state FTIR difference spectra, see, for example, Remy & Gerwert, 2003 [311].

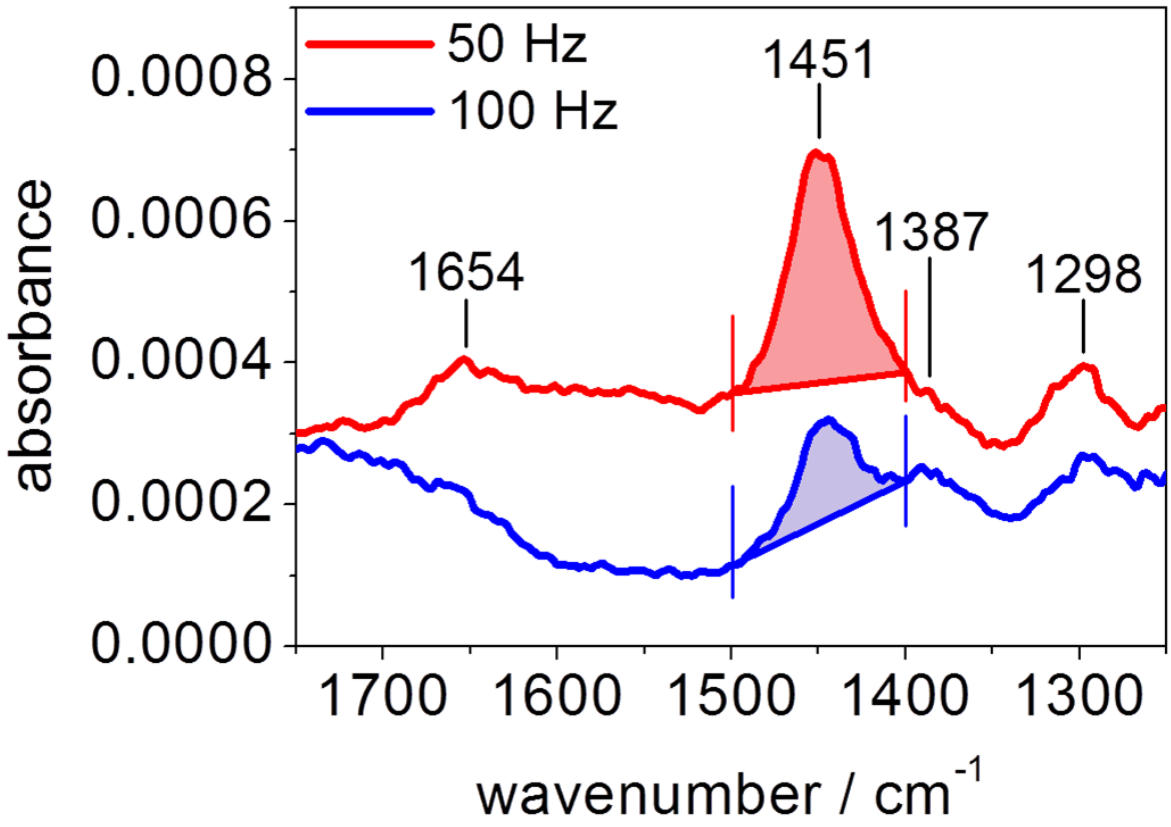

Figure 5A.26: Calculated overall absorbance changes, determined by orthogonal phase-resolved spectra (obtained from the spectra shown in Fig. 5A.25). The band positions are specified within the plot, the excitation frequency was 50 (red) and 100 Hz (blue), respectively. The shaded integrals were used to evaluate the time course, shown in Fig. 5A.27. Figure published in Geiss *et al.*, 2017b [302].

The surprisingly low spectral features can be explained by two different properties of the employed technique. On the one hand, due to the rough gold surface, only dipole moments (respectively components thereof) perpendicular to the surface could be detected, i.e., perpendicular to the membrane in this case. Different orientations of one component species could be represented in an enhanced way or not at all. The pre-orientation via his-tag binding could enhance the effect further. On the other hand, the combination of modulated excitation phase-resolved and difference spectra eliminated all components that were not part of the reaction and hence changed during a measurement cycle.

In literature, referring to FTIR spectra, the band at 1282 cm^{-1} was assigned to the reaction center after charge separation, $P870^{+}$, while another at 1434 cm^{-1} was associated to the vibrational stretching of the hydroxyl group of UQH_2 [119]. The latter was strongly pronounced – although slightly shifted – in the presented results. This band was evaluated further. The strong absorption implied – following the above-described argumentation – a relatively fixed orientation perpendicular to the gold surface, what was unlikely for the diffusing UQH_2 molecules in the lipid phase, which were rather thought to cancel each other out. Therefore, it

was assumed that the observed oriented ubiquinol molecules were the ones bound to Q_B site at the RC and at the UQH_2 binding site at the bc_1. Employing the phase-sensitive detection mentioned before, it was assured that absorption changes occurred approximately at 1440 cm^{-1} (Fig. 5A.25). Altogether, a periodic change of the respective peak was presumed, representing the UQH_2 production by the RC and its consumption by the bc_1. Therefore, further analyzation was done by integration of the region from 1500 to 1400 cm^{-1}, whereupon the integral area was plotted versus time (Fig. 5A.27).

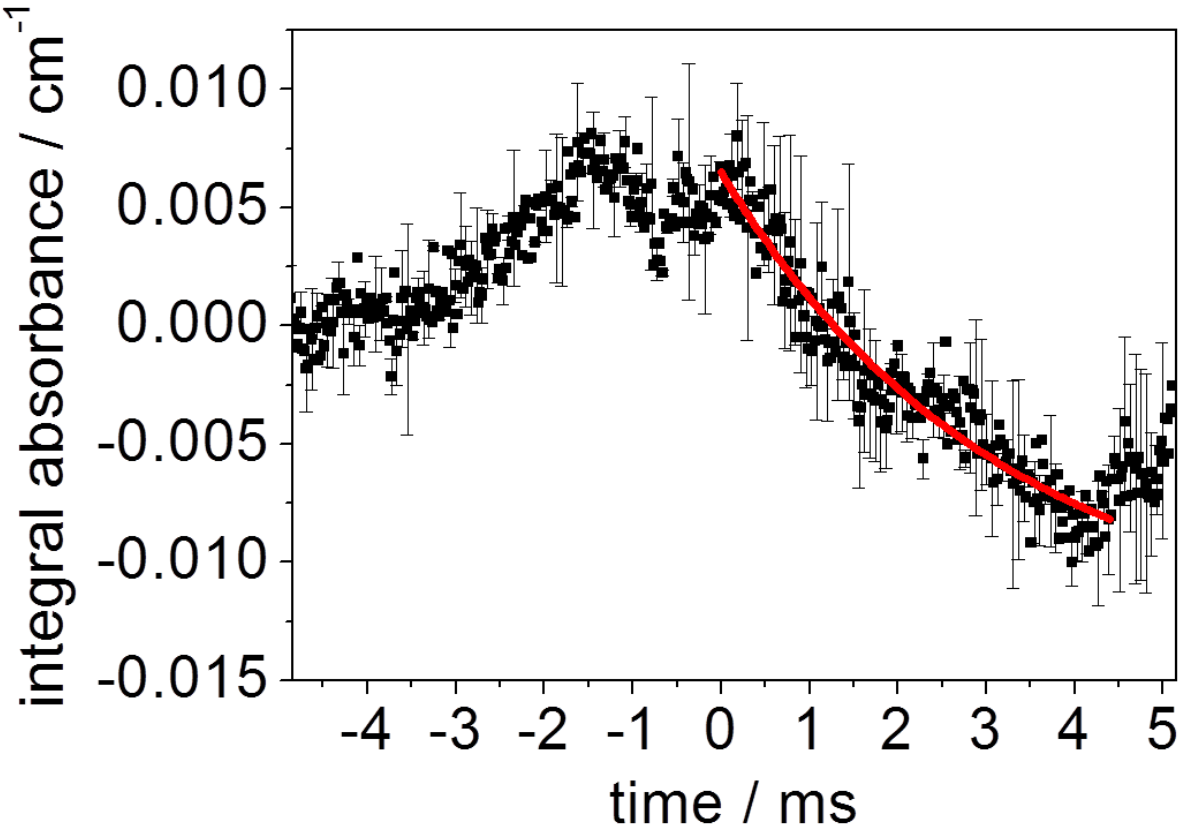

Figure 5A.27: Time course of the UQH_2-assigned spectral region. The integral area in the range 1500 to 1400 cm^{-1} of time-resolved SEIRA spectra, shown as shaded areas in Fig. 5A.26, was plotted versus time. The decreasing branch was fitted mono-exponentially. 2 series of each 100 cycles were averaged. Figure published in Geiss *et al.*, 2017b [302].

Fig. 5A.27 shows the periodical changes in the integral area deduced from Fig. 5A.26. Following the argumentation given above, this time course was attributed to the generation and consumption of UQH_2 by the RC and the bc_1, respectively. The expected periodic manner could be confirmed, even if the recovery of the initial value was not completely monitored. The graphs displayed in Fig. 5A.27 are averaged ones, whereby the cycle of generation and consumption was recorded one hundred times in a row with an excitation frequency of 50 Hz, followed by 10 ms of detection. Subsequently, those 100 cycles were averaged, whereupon the measurement

was repeated the same way. The sets of measurement were again averaged, yielding the displayed mean value curve and the associated standard deviation. Due to the usage of a single non-saturating flash, the RCs are presumed to having been excited simultaneously (or not at all). The loss and regain of integral absorbance between -2 and 0 s might be due to the (not strictly oriented) diffusion from RC to bc_1. By randomizing the UQ orientation upon leaving the RC binding site the absorbance might drop, then could recover upon reorienting at the bc_1 binding site, before being oxidized. However, this was not further investigated, thus it remained speculative. At least, this behavior was reproducible, so a mechanistic origin is likely.

Presuming that the decrease of absorbance that started at 0 s (set to 0 for reasons of evaluation with regard to the mono-exponential fit) was due to UQH_2 consumption by the bc_1, a time constant τ (1/e of the maximum value) could be determined, having been 3.17 ms. The latter was assigned – keeping in mind that the transfer of one electron was putatively observed – to a turnover number of 316 electrons per second and bc_1 complex.

To compare with the proton pumping activity of the bc_1 within PLBs, the ratio of pumped protons per electron was required to factor in. Due to the Q-cycle, this ratio is not 1. Instead, Crofts *et al.* [313] defined the overall reaction of the bc_1 to be

$$UQH_2 + 2\ \text{cyt}\ c^+ + 2\ H_N^+ \leftrightarrow UQ + 2\ \text{cyt}\ c + 4\ H_P^+ \qquad (5A.7)$$

implying that 4 protons are translocated per 2 electrons, at least for the uncoupled enzyme. Based on this 2:1 ratio, an electron turnover of 316 s^{-1} corresponds to a proton pumping activity of 632 s^{-1} per scond and bc_1 complex. The uncoupled enzymes embedded in PLBs, analyzed by LSM, exhibited a proton pump rate of 663 H^+/s. Further assuming that hundred single turnovers in succession was likely not enough to generate a notable electrochemical potential, the SEIRAS results of a planar ptBLM were comparable to the ones achieved with PLBs employing LSM. Regarding the 316 electrons per seconds, similar values can be found in literature, see, e.g., Czapla *et al.*, 2012 [201], who determined the electron turnover of solubilized bc_1 complexes with 333 e^-/s per bc_1 complex. Thus, the measured values were highly comparable to literature and to each other.

In contrast to the C*c*O-PLBs, the full activity could be measured after reconstituting the bc_1 in PLBs, even excited via interaction with the photosynthetic RC. This did not contradict the aforementioned argumentation at all, but rather supported it, because the RC was not excited with the imaging laser but by a halogen lamp that was adjusted to illuminate the complete sample in an indeed continuous way.

The third part regarding the modular system – the bead share – is still outstanding. By varying the core, PLBs can be varied in size tremendously, and since it was planned to be used for the design of a nano-PLBs, the analysis and in parts the preparation were necessarily completely different (to tailer the PLB size by means of the core was actually defined as the purpose of varying the beads), so this chapter is separated in two parts, whereby *Chapter 5B* is dealing with PLBs based on nanometer-sized silica particles. Before proceeding, the publication presenting the results obtained so far, namely having shown that small enzyme systems can be integrated in PLBs in a functionally fully active manner, published in the *Journal of Physical Chemistry B*, is attached, herein referred to as Geiss *et al.*, 2017b.

A. F. GEISS, R. KHANDELWAL, D. BAURECHT, C. BLIEM, C. REINER-ROZMAN, M. BOERSCH, G. M. ULLMANN, L. M. LOEW, AND R. L. C. NAUMANN: **pH and Potential Transients of the bc_1 Complex Co-Reconstituted in Proteo-Lipobeads with the Reaction Center from *Rb. sphaeroides***. *Journal of Physical Chemistry B* 121 (2017) pp. 143–152. doi: 10.1021/acs.jpcb.6b11116.

Publication III

<content not available in online version>

<content not available in online version>

<content not available in online version>

<content not available in online version>

<content not available in online version>

<content not available in online version>

<content not available in online version>

<content not available in online version>

<content not available in online version>

<content not available in online version>

<content not available in online version>

<content not available in online version>

<content not available in online version>

<content not available in online version>

<content not available in online version>

<content not available in online version>

<content not available in online version>

Chapter 5B *Silica-PLBs*

Agarose-based PLBs allow for any light microscopy techniques due to their size in the µm range. If the core particle is nanometer-sized, transmission spectroscopy techniques, such as UV/Vis spectroscopy, could be employed, as long as the resulting PLBs are still small enough that scattering effects are negligible. Not least in regards to address fundamental research questions (in the future), such as the severally mentioned bioenergetic questions dealing with catalytic cycles of enzymes like the C*c*O, a PLB nanoversion was aimed to establish, at the same time completing the concept of a modular system built of exchangeable components.

5B PLBs based on silica beads (Modular system III: the bead share)

Nanometer-sized Ni nitrile tri-acetic acid (NTA)-functionalized silica particles were commercially available in different sizes (see the *Materials* section for details), starting with 25 nm diameter and claimed to be of sufficient homogeneity. The agarose-PLB preparation protocol was adopted and slightly altered for silica-PLBs, as described in the methodological section, since the small bead versions cannot, for instance, be sedimented by centrifugation with the available table centrifuges. Conversely, the methodology was completely different, based on UV/Vis spectroscopy in the main.

5B.1 Structure

To assess the silica-based PLB structure, UV/Vis spectra of solubilized C*c*O and of the nanoparticles were recorded at first (Fig. 5B.1).

In the C*c*O spectrum (Fig. 5B.1A), two peaks were identified that change in response to the degree of oxidation. In the oxidized state, one was at 410 nm and shifts to 420 nm upon reduction. An increase in amplitude, as it can be observed in Fig. 5B.1A from 0.22 to 0.26, is typical. This peak is also referred to as Soret band. It is caused by the porphyrin ring that is contained by any heme (and chlorophyll), complexing the redox-active metal ion, i.e., Fe in the case of hemes (and Mg in the case of chlorophylls) [314].

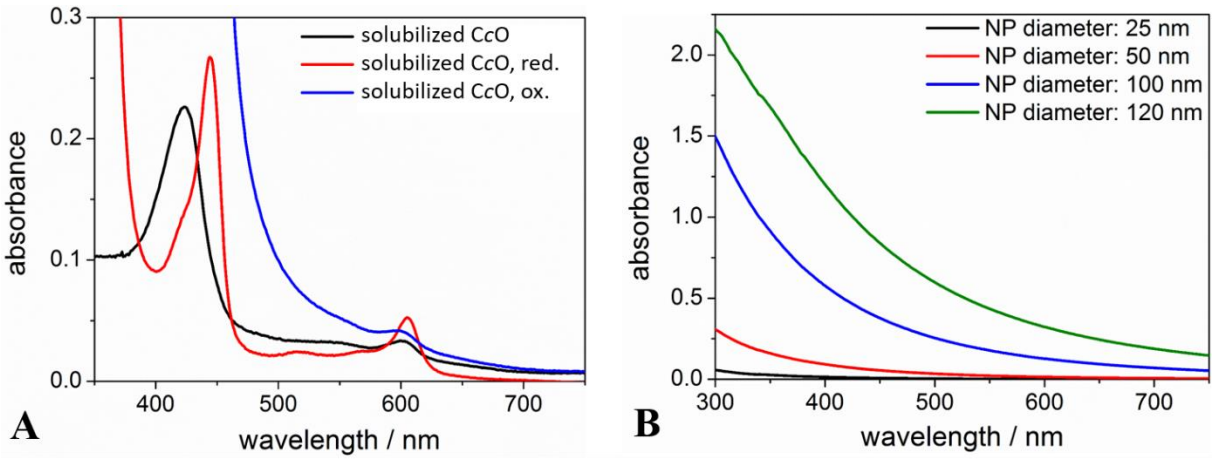

Fig. 5B.1: UV/Vis spectra of solubilized C*c*O (A) and silica nanoparticles (B). (A) C*c*O was solubilized in DDM/THK buffer (5 mM Tris-HCl, 35 mM KCl, pH = 8, 0.1 % DDM) (black). Afterwards, the enzyme was reduced by sodium dithionite (red) and oxidized by potassium ferricyanide (blue), respectively. The C*c*O concentration was 7.0 µM. (B) The nanoparticles (NPs) of different sizes (25, 50, 100, and 120 nm in diameter) were diluted to 4 mg/mL in the same buffer, corresponding to the concentration in PLB samples.

The other one was located at 606 nm and gives information about the C*c*O concentration according to the Beer-Lambert law (eq. 4.1). The used extinction coefficient $\varepsilon_{606-630\ \mathrm{nm}}^{\mathrm{reduced-oxidized}}$ = 23.4 was determined by Ludwig & Schatz, 1980 [290]. The peak at 606 nm is due to the heme *a* [59]. Due to reduction, the absorption at 606 nm increased. Due to dithionite treatment, a large peak below 400 nm emerged. If incubated for to long, the hydrolysis product superimposed the whole spectrum, which had to be discarded in this case (not shown). If oxidized by potassium ferricyanide, the peak at 410/420 nm is superimposed by the large ferricyanide peak and thus not visible. It turned out that the C*c*O aliquots are completely oxidized and ferricyanide was not necessary (not shown).

The spectra of the nanoparticles (NPs) are shown in Figure 5B.1B. According to theory, the scattering increased with decreasing wavelength and increasing size. While particles with 100 (blue) and 120 nm (green) diameter already displayed a relatively large absorption due to scattering – they appeared opaque by eye –, the 50 nm-sized NPs (red) might be suitable as PLB core, but especially the 25 nm-sized NPs (black) offered a negligible amount of scattering that was promising to not hinder UV/Vis spectroscopic applications.

C*c*O-proteobeads and C*c*O-PLBs were prepared as described in *Materials & Methods*, then UV/Vis spectra were recorded and compared to the one of solubilized C*c*O and NPs. The spectra are shown in Fig. 5B.2.

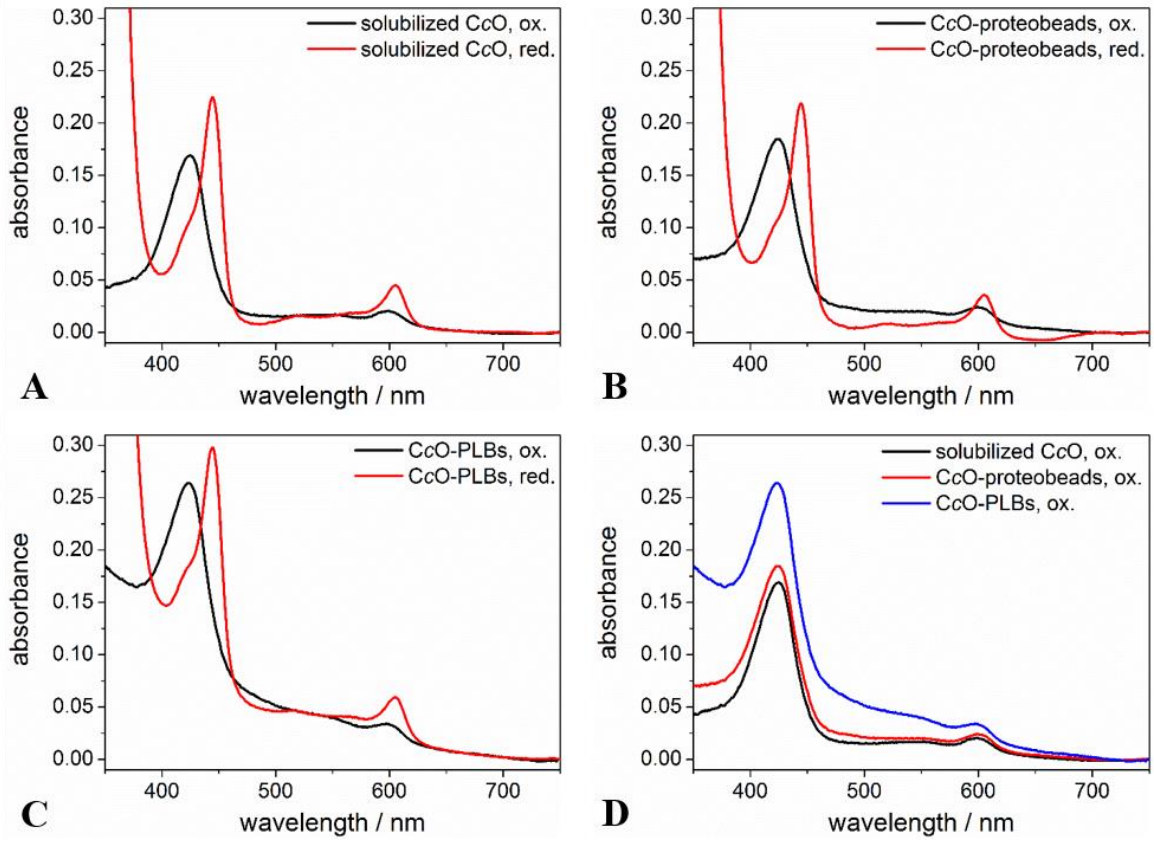

Figure 5B.2: UV/Vis spectra of different stages during the PLB preparation process. UV/Vis spectra were recorded of solubilized C*c*O (A), C*c*O-proteobeads (B) and C*c*O-PLBs (C) in oxidized (black) and reduced (red) state in THK buffer. A comparison of the oxidized spectra is shown in (D). Figure 5B.2A-C were published in slightly different presentation in Schadauer *et al.*, 2015 [315].

By comparing the spectra of solubilized C*c*O, C*c*O-proteobeads and C*c*O-PLBs, on the one hand it was found that the C*c*O spectrum was clearly apparent and not superimposed by the dispersion in a hindering way; on the other hand, due to the increasing size, the scattering part of the absorption increased (in a wavelength-dependent extent) as expected.

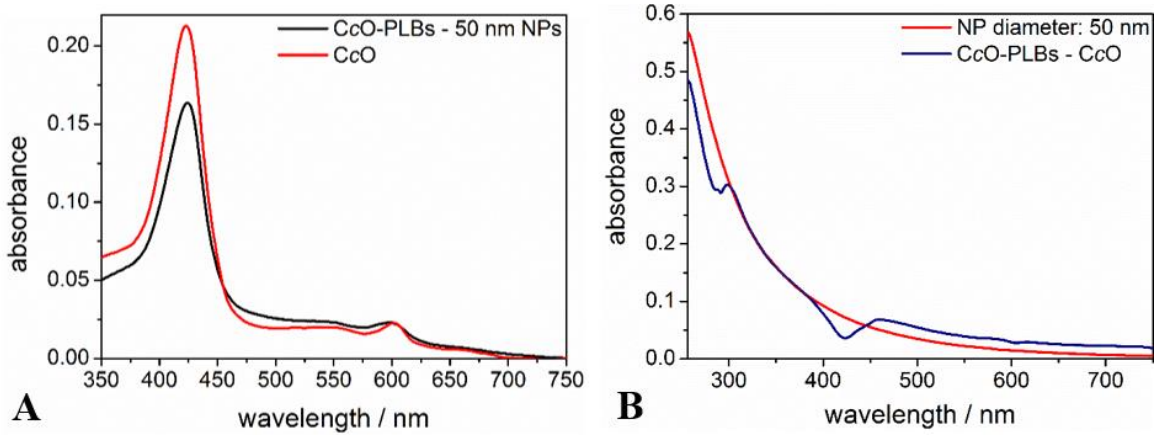

Figure 5B.3: Difference spectra of C*c*O-PLBs and 50 nm silica beads. (A) The spectra of the silica beads exhibiting a diameter of 50 nm was subtracted from the C*c*O-PLB spectrum and compared to the spectrum of solubilized C*c*O. (B) The spectrum of solubilized C*c*O was subtracted from the C*c*O-PLB spectrum and compared to the spectrum of 50 nm-sized (diameter) silica beads. Figure published in Schadauer *et al.*, 2015 [315].

By assuming an additional diameter of around 10 nm due to the protein-containing membrane (the maximum height of the C*c*O was reported with 9.5 nm [40]), the resulting diameter of the PLBs should be – including a short spacer – around 50 nm. The following difference spectra (Fig. 5B.3) confirmed this assumption.

By subtracting the spectrum of 50 nm-sized silica beads from the C*c*O-PLB spectrum, a difference spectrum is revealed that was very similar to the spectrum of solubilized C*c*O (Fig. 5B.3A). By comparing the difference spectra of C*c*O-PLBs minus solubilized C*c*O with the 50 nm-sized silica bead spectrum (Fig. 5B.3B), a large similarity was found as well except from minor deviations. Altogether, the difference spectra confirm the assumption, that the PLBs are around 50 nm in diameter. In Fig. 5B.4, a comparison of the above mentioned components is shown, additionally displaying the scattering share of the proteobeads.

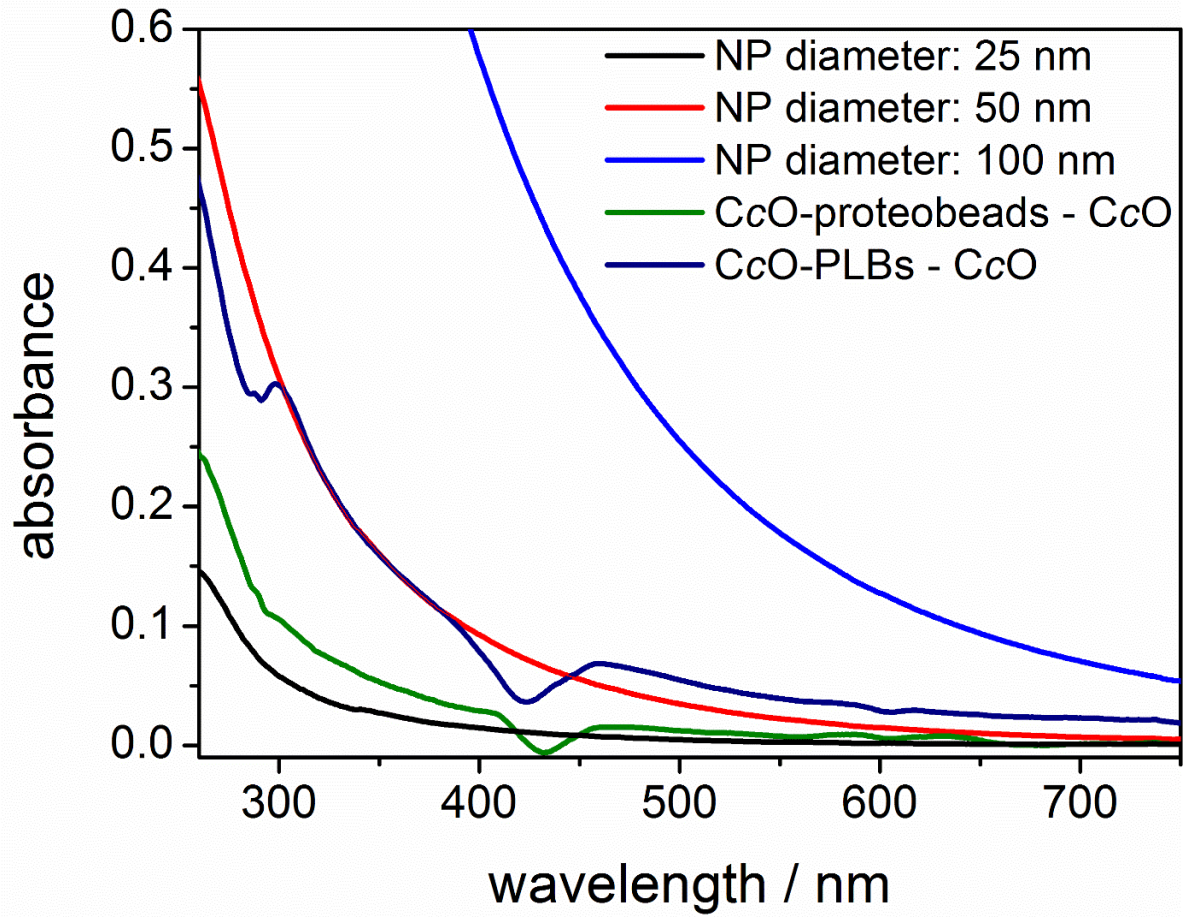

Figure 5B.4: Comparison of the NP spectra with the difference spectra shown in Fig. 5B.3. The spectrum of the silica NPs of a size of 25 (black), 50 (red) and 100 nm (blue), described in detail in Fig. 5B.1B, are compared to the difference spectra of C*c*O-proteobeads minus solubilized C*c*O (green) and C*c*O-PLBs minus solubilized C*c*O (navy blue). Figure published in Schadauer *et al.*, 2015 [315].

Fig. 5B.4 displays indirectly the growth in size expressed by the increased scattering effect, starting with the 25 nm-sized core particle ($A_{360\,nm}$ = 0.15) via C*c*O-proteobeads, which are

situated between the 25 nm and the 50 nm NP ($A_{360\,nm}$ = 0.25) to C*c*O-PLBs, which exhibited an absorbance value at 360 nm of $A_{360\,nm}$ = 0.47, but were considered as very similar to the 50 nm NPs ($A_{360\,nm}$ = 0.55) due to the overall course.

For further confirmation, dynamic light scattering (DLS) measurements were performed by <content not available in online version>, shown in Figure 5B.5.

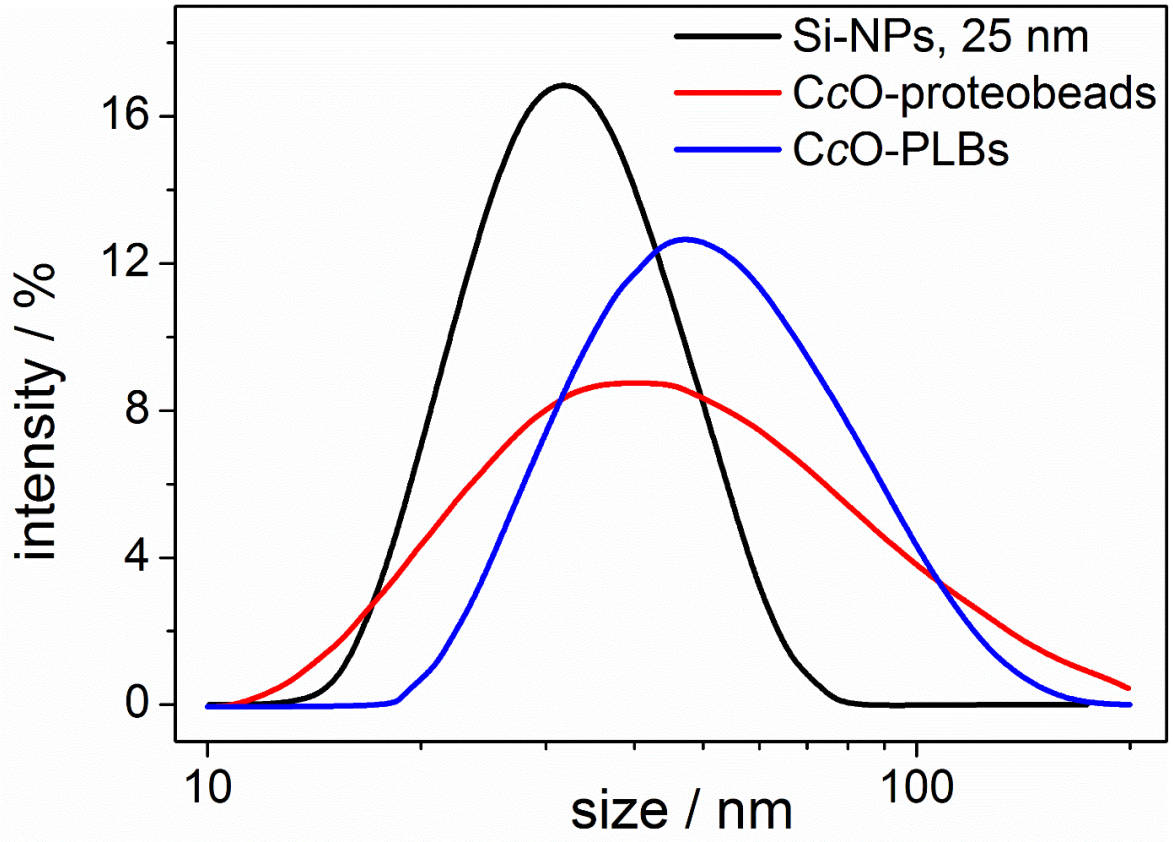

Figure 5B.5: Dynamic light scattering (DLS) measurement of the PLB preparation's intermediates. 25 nm silica beads (black), C*c*O-proteobeads (red) and C*c*O-PLBs (blue) were measured in THK buffer. All DLS measurements were performed at a scattering angle of 173 deg in DDM/DPK buffer (50 mM K_2HPO_4 and 100 mM KCl, pH = 8, 0.1 % DDM) in case of the NPs and the proteobeads and in DPK buffer (the same without DDM) in case of the PLBs. All samples were diluted to a NP concentration of 1 mg/mL. Figure published in Schadauer *et al.*, 2015 [315]. Measurements and plot performed by <content not available in online version>.

Fig. 5B.5 shows the size distributions of 25 nm-sized NPs, C*c*O-proteobeads and C*c*O-PLBs. The maximum of the pure NPs is around 30 nm. The size increases with the protein attachment and adhered detergent micelles to approximately 40 nm and reaches about 50 nm for the PLBs. The displayed size estimations were apparent sizes. For example, the protobeads with attached C*c*O likely did not differ much in their maximum diameter, but instead of a (alleged) continuous membrane, there are proteins with detergent micelles, potentially leaving gaps in between enabling to pass the light unaffected. As described in the *Theory* part, DLS measurements

assume a continuous spherical shape (at least using rather the basic function instead of more sophisticated further developments in DLS spectroscopy). This uniformity was not provided, foremost in case of the proteobeads as described. However, since a rough estimation was considered as sufficient, this was accepted. The spectrum of the purchased NPs shows a broader size distribution as expected, but nevertheless size and uniformity properties turned out to be sufficient as described later. Due to the size distribution of the NPs, the NP-based PLBs have a broader size distribution as well. The latter one was a bit broader, potentially because the outer PLB materials, i.e., lipids and proteins, are not that rigid as silica is, and exhibit a broader spectrum of local refractive indices. The distribution obtained with the proteobead sample was even broader. This could be explained by the flexibility of anchored proteins (and detergent micelles), which were presumed to have a certain motional freedom before becoming more fixed in the membrane, leading to a broader apparent size distribution. Again, the performed measurements were not of outstanding performance, regarding, e.g., the lack of multi-angle measurements. But in combination with the UV/Vis measurements presented above, the DLS spectra confirmed the assumption of a PLB size that was in average about 50 nm in diameter, which was considered as sufficiently accurate. Retrospectively, the even distribution over a logarithmic size scale was somewhat enigmatic, surprisingly indicating a small share of notably larger hydrodynamic diameter, but this was not further pursued.

The possibility to easily assess the C*c*O concentrations in PLB samples combined with the specification of the bead number per volume NP suspension, which was not provided in case of the agarose beads, the average number of C*c*O molecules per PLB could be determined. For that reason, UV/Vis spectra were taken with PLBs prepared with the standard C*c*O amount, described in the *Materials & Methods* section, and with the double and the triple amount to additionally investigate the maximum occupancy (Fig. 5B.6).

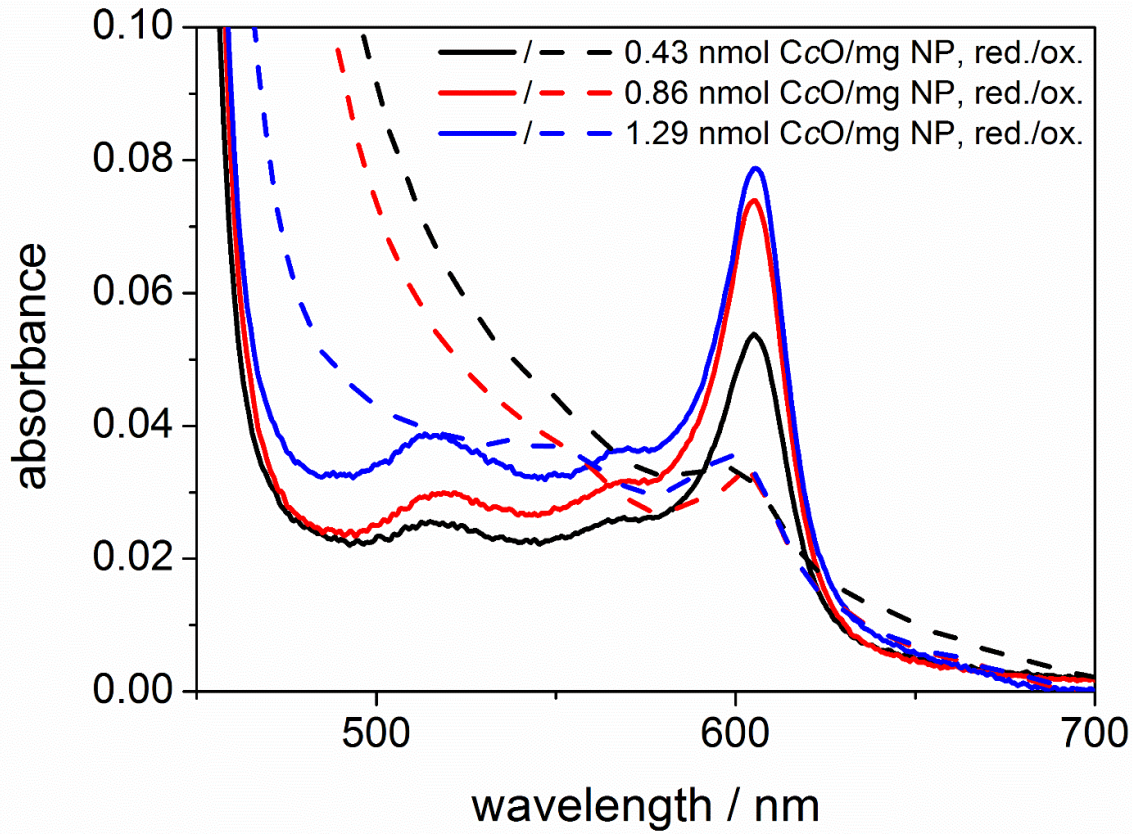

Fig. 5B.6: UV/Vis spectra of PLBs loaded with different C*c*O concentrations. PLB-bound C*c*O, re-suspended in THK buffer, was reduced with sodium dithionite and oxidized with potassium ferricyanide, respectively. Figure published in Schadauer *et al.*, 2015 [315].

In Figure 5B.6, the peak at 606 nm is displayed. The absorption was increased upon C*c*O reduction, which resulted in a value of 0.05 for the protocol amount of C*c*O (0.43 nmol per mg NPs), increased to 0.075 if the double C*c*O amount was used and further to 0.079 for the triple amount. Using the Beer-Lambert as described above and the Avogadro constant as described in the course of activity measurements on agarose-PLBs, this was translated into the numbers of C*c*O molecules. In a next step, since the number of NPs was specified by the manufacturer with 3.5 x 10^{13} beads per mg (and the concentration of the obtained solution with 25 mg/mL), the average number C*c*O molecules per PLB could be determined. To estimate the occupancy, the surface area of the silica NPs was calculated according to eq. 5B.1.

$$A_{sphere} = 4\pi r^2 \qquad (5B.1)$$

The silica bead radius (r) was used for calculations instead of the PLB radius, since the inner side of the PLB membrane was considered to be limiting, providing a smaller surface area. The linker's dimensions were presumed to be negligible, so the silica bead surface was considered to approximately represent the inner membrane area. The area occupied by the C*c*O was

estimated with an elliptical shape, defined by the major axis a = 9 nm and the minor axis b = 6 nm according to the crystal structure reported by Iwata *et al*., 1995 [40]. The area of an ellipse is given with

$$A_{ellipse} = ab\pi \ . \qquad (5B.2)$$

After dividing the surface area by the area occupied by a single C*c*O, the formula of dense sphere packing was applied as an approximation for the minimal losses due to the waste areas.

$$\frac{\pi}{3\sqrt{2}} = 0.74 \qquad (5B.3)$$

The obtained values are summarized in Table 5B.1.

Table 5B.1: C*c*O molecules bound to PLBs and PLB occupancy in absolute and relative quantities [315].

Added amount of C*c*O (nmol/mg NP)	C*c*O in PLBs (nmol/mg NP)	C*c*O bound (%)	C*c*O per PLB	PLB occupancy (%)
0.43	0.36	84	6.2	42
0.86	0.55	64	9.5	65
1.29	0.58	45	9.9	67

As summarized in Table 5B.1, it turned out that 6 to 10 C*c*O were immobilized to a single PLB in average, which corresponded to around 40 to 70 % of the maximum occupancy. Deduced from the non-linear occupancy increase, associated with smaller binding ratios, 70 % appeared to represent a value close to saturation (see also Fig. 5B.6). Due to the theoretical random binding of the C*c*O, an occupancy of 100 % (with respect to the dense sphere packing model), was considered as unlikely, resulting in larger waste areas as the theoretical mininum. The number of Ni-NTA residues on the bead surface was unknown, but assumed to be way higher.

Since the standard occupancy corresponded to only 6 enzymes per PLB, experiments with more than one kind of protein like the RC/*bc*$_1$-PLBs were not performed (and also due to limitations in time). The PLBs used in all of the following experiments were prepared with the lower C*c*O amount of 0.43 nmol/mg NP (hence with 6 C*c*Os per PLB in average).

5B.2 Enzyme activity and membrane denseness

To test the functionality of the entrapped C*c*O (since, as mentioned several times, a mere binding assay was not aimed, see *Introduction*), measurements according to the Michaelis-Menten concept were performed. The concept is outlined in the *Theory*. Briefly, by determining the initial turnover rates of an enzyme for different substrate concentrations, the maximum catalytic activity (k_{cat}) as well as a measure for the substrate affinity (K_M) can be obtained via fitting with the Michaelis-Menten equation (eq. 5B.4), then applying eq. 5B.5.

$$v_0 = \frac{v_{max}\,[S]}{K_M + [S]} \tag{5B.4}$$

$$k_{cat} = \frac{v_{max}}{[E_0]} \tag{5B.5}$$

In the eq. 5B.4 and 5B.5, v_0 is the initial rate, dependent on the substrate concentration, v_{max} is the maximum rate of a certain concentration of enzymes per second, [S] is the substrate concentration, K_M is the Michaelis-Menten constant – a measure of the substrate affinity; the smaller it is, the higher is the affinity –, $[E_0]$ is the enzyme concentration, which has to be constant in a set of measurements, and k_{cat} is the maximum catalytic activity of a single enzyme per second. Thus, K_M and k_{cat} are independent from individual measurement parameter like the substrate or enzyme concentration and is hence suitable to compare with literature.

The substrate of C*c*O is cytochrome (cyt) *c*, which is oxidized by the enzyme (see *Theory*). As well as the C*c*O spectrum, the cytochrome *c* spectrum showed significant differences between the oxidized and the reduced state. The spectrum of cyt *c* is shown in Figure 5B.7.

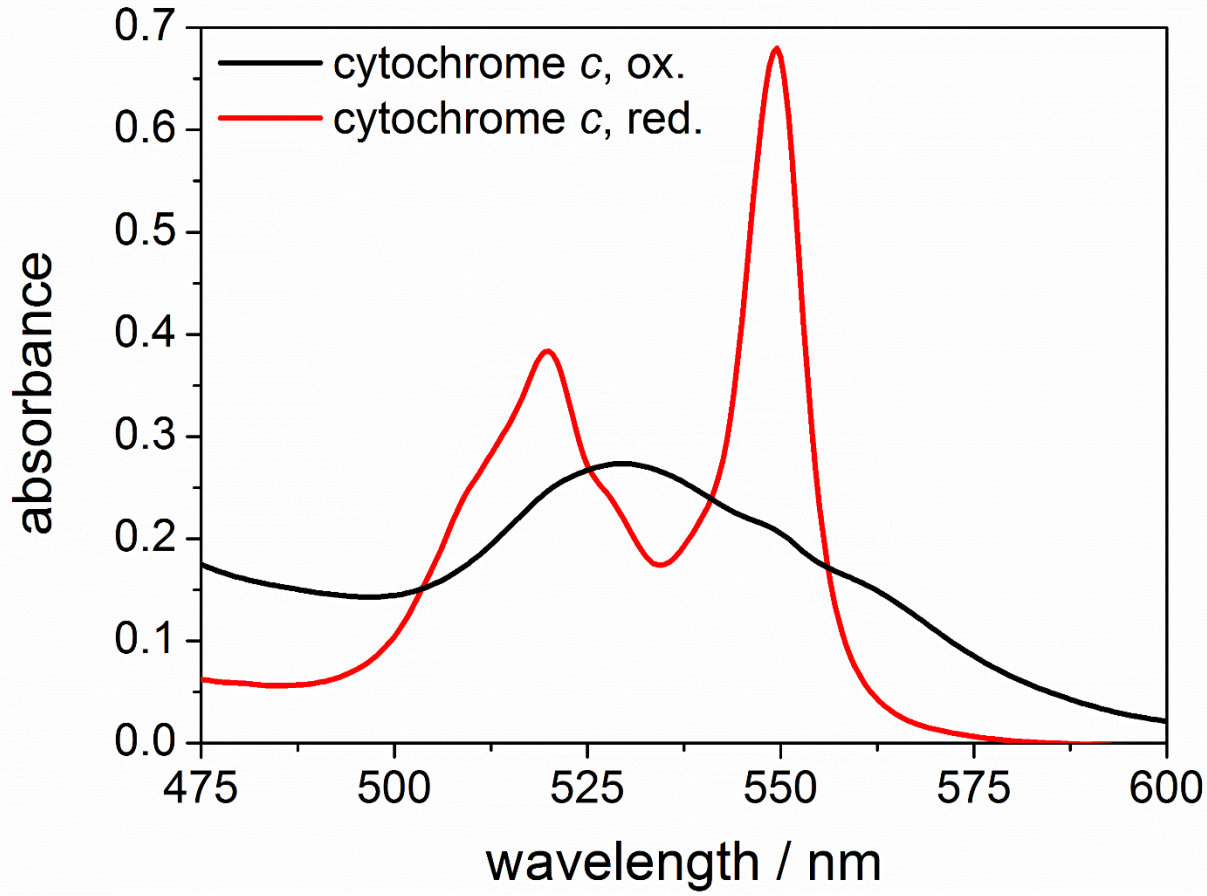

Figure 5B.7: UV/Vis spectra of cytochrome *c*. Oxidized cytochrome *c* was dissolved in THK buffer, then a spectrum was measured. Another sample was reduced using a few grains of sodium dithionite, which were afterwards removed by gel filtration before the spectrum was recorded.

The spectrum of oxidized cyt *c* exhibited a flat peak with a slight maximum at 530 nm, while the spectrum of reduced cyt *c* showed a sharp peak at 550 nm and a slightly broader one at 520 nm. With the help of the maximum at 550 nm, the concentration can be determined according to the Beer-Lambert law (eq. 4.1), using the extinction coefficient $\varepsilon = 27.7\ mM^{-1}\ cm^{-1}$ [289]. Moreover, the peak at 550 nm did not interfere with any peak in the C*c*O spectrum, so it was appropriate to use for the determination of the catalytic activity of the C*c*O.

Hence, the decrease of the maximum at 550 nm was observed over time. The concentration of PLB-bound C*c*O was adjusted that low that the decrease in the first 60 s was more or less linear, following the kind advice of <content not available in online version> of the University of Frankfurt a. M., Germany (although using of the Michaelis-Menten theory is critical because of the higher reaction order of the investigated reaction, it is done standardly, and literature was found to compare with [57]). To obtain data points to fit with the Michaelis-Menten equation (eq. 5B.4), different concentrations of cytochrome *c* were added to a certain concentration of

C*c*O, being either bound to PLBs, immobilized at proteobeads, or solubilized. An exemplary measurement of cyt *c* oxidation by solubilized C*c*O is shown in Figure 5B.8.

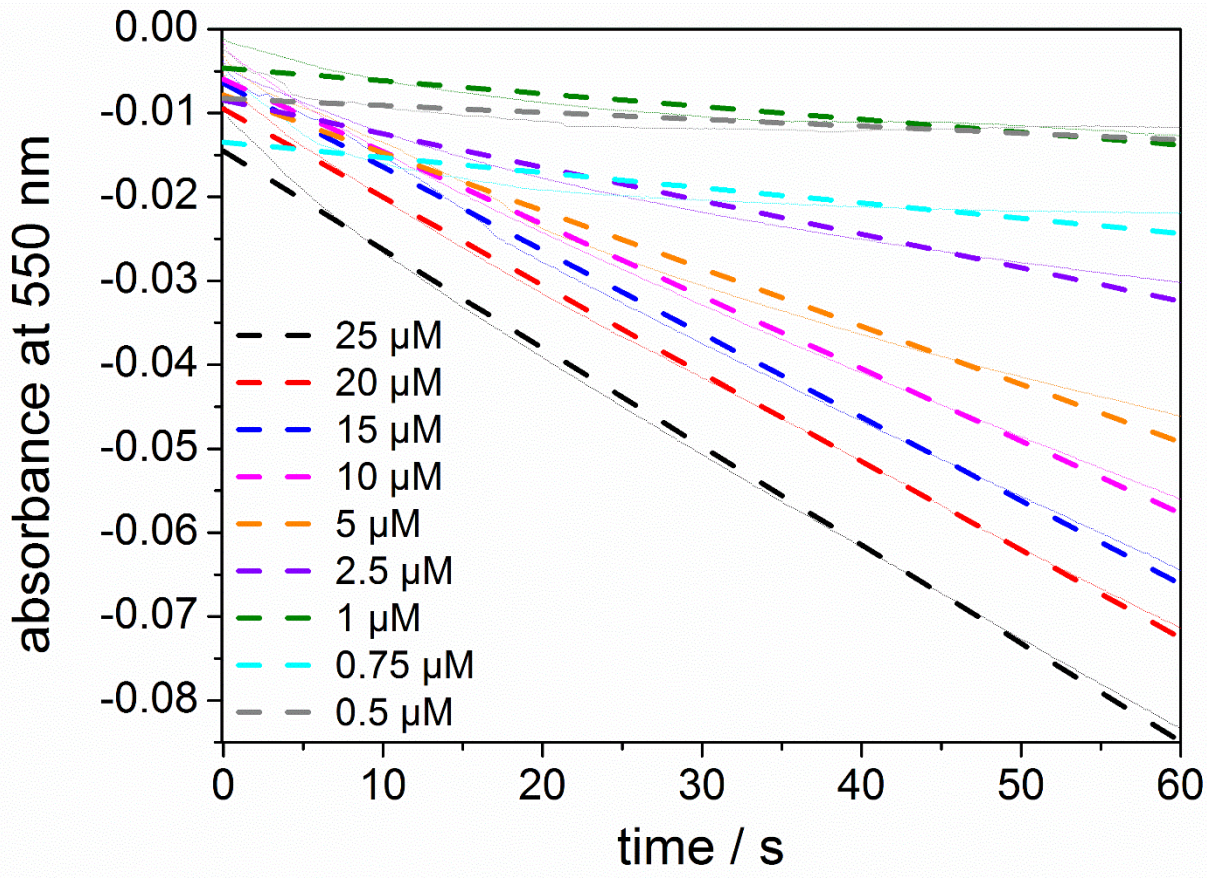

Figure 5B.8: Decrease of the peak at 550 nm, corresponding to reduced cytochrome *c*, versus time. The cytochrome *c* concentrations specified in the legend were applied to 0.2 nM of solubilized C*c*O in DDM/THK buffer. Immediately, the absorbance was set to 0 and the absorption decrease at 550 nm was recorded over time. The measured curves were fitted linearly.

Although the linearity of the curves displayed in Fig. 5B.8 was not perfect, the linear fitting was accepted to be fair enough. The slopes of the linear fits – corresponding to the initial rates of the C*c*O – were applied versus the cytochrome *c* concentration and fitted according to the Michaelis-Menten equation (eq. 5B.4). The Michaelis-Menten diagram is shown in Fig. 5B.9.

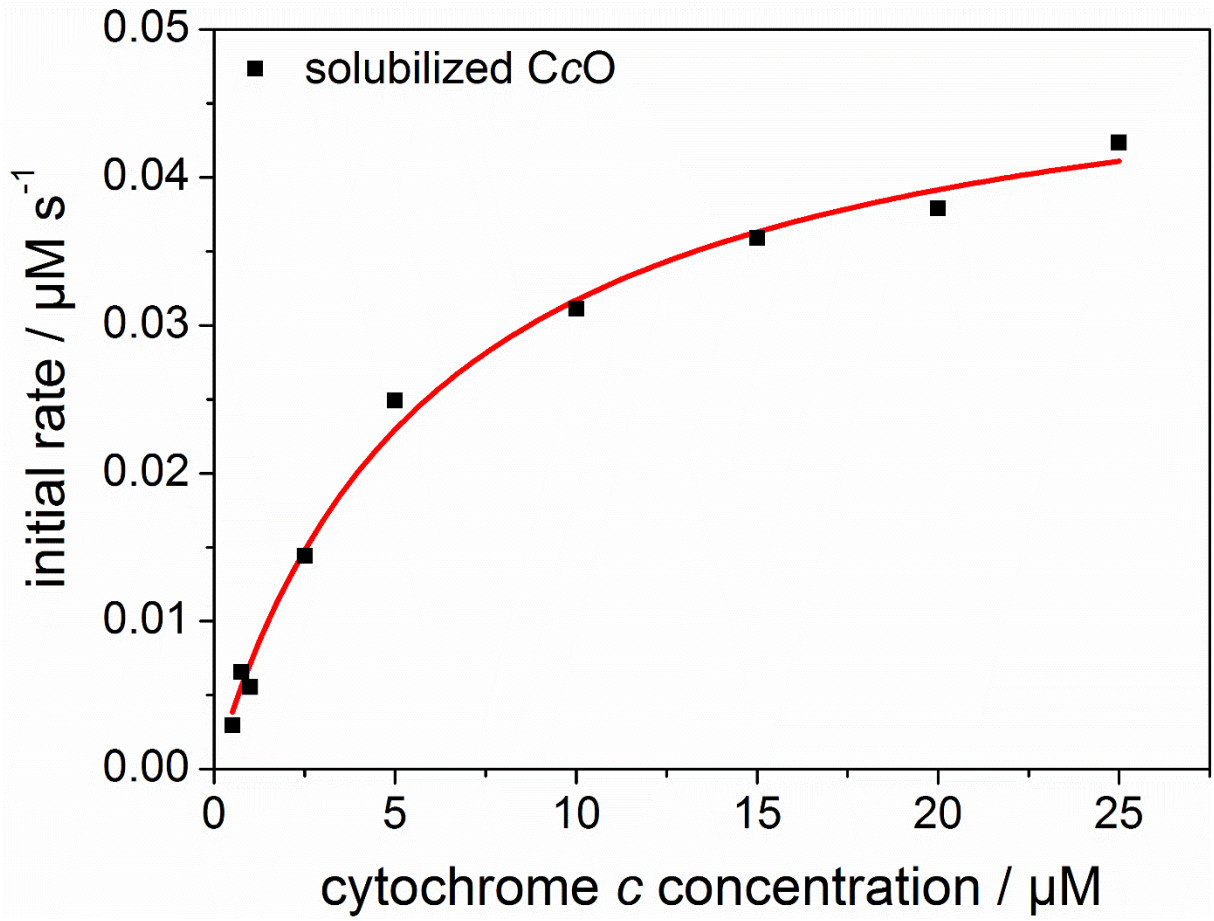

Figure 5B.9: Michaelis-Menten plot of solubilized C*c*O. The initial rates – determined by linear fitting of the measurements displayed in Fig. 5B.8 – of solubilized C*c*O in DDM/THK buffer were plotted versus the cytochrome *c* concentration and fitted according to the Michaelis-Menten equation (eq. 5B.4). The C*c*O concentration was adjusted to 0.2 nM.

The experiment was repeated three times. The repetitions including mean value curve and standard deviation is shown in Fig. 5B.10.

Via the hyperbolic fit in Figure 5.10B, the K_M value of solubilized C*c*O can be obtained directly, having been 5.8 ± 0.4 µM. By division of the maximum rate, corresponding to the limit value and also directly obtainable by the fit parameters, by the enzyme concentration, the catalytic activity can be deduced (eq. 5B.5). It was 264.1 ± 7.4 s^{-1} for the solubilized C*c*O. The discussion of these values – besides noticing a good fit with little standard deviation – follows after the determination of all needed constants, namely k_{cat} and K_M of the C*c*O immobilized at proteobeads, embedded in PLBs, and embedded in PLBs in the additional presence of valinomycin and FCCP to calculate the respiratory control ratio (RCR, see below).

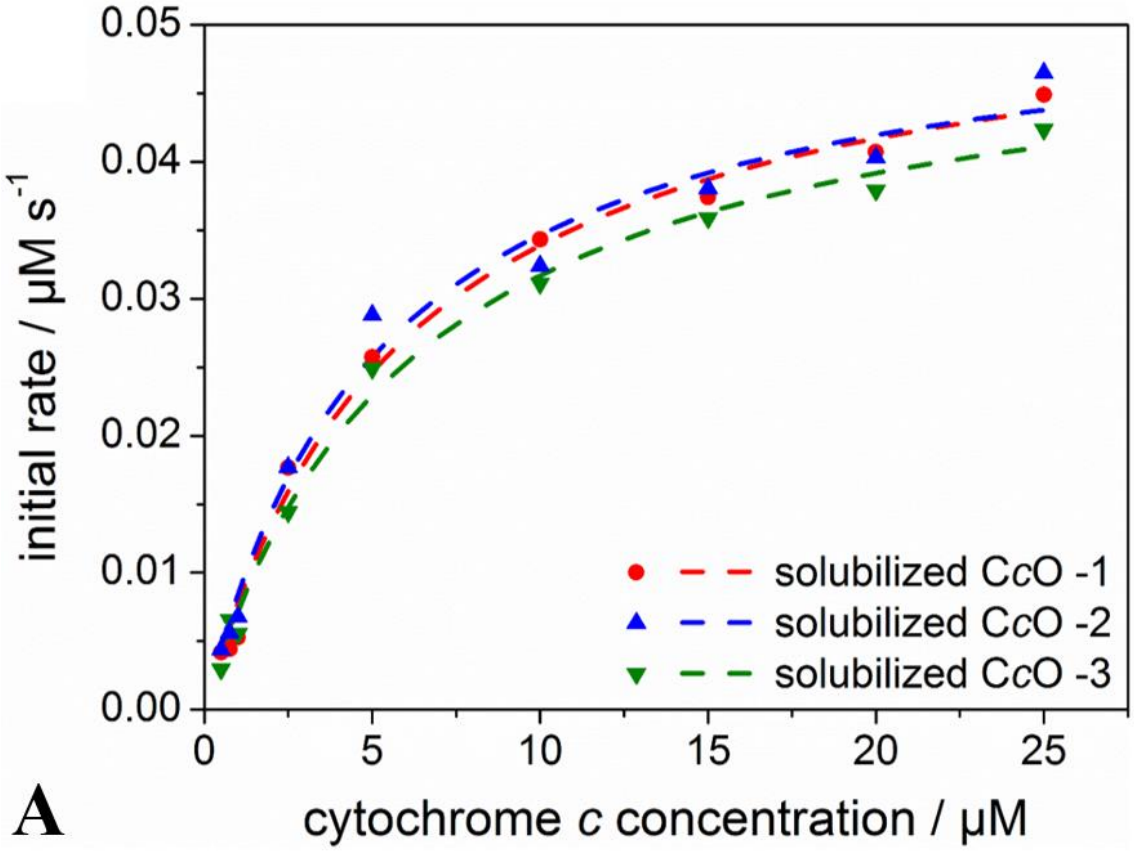

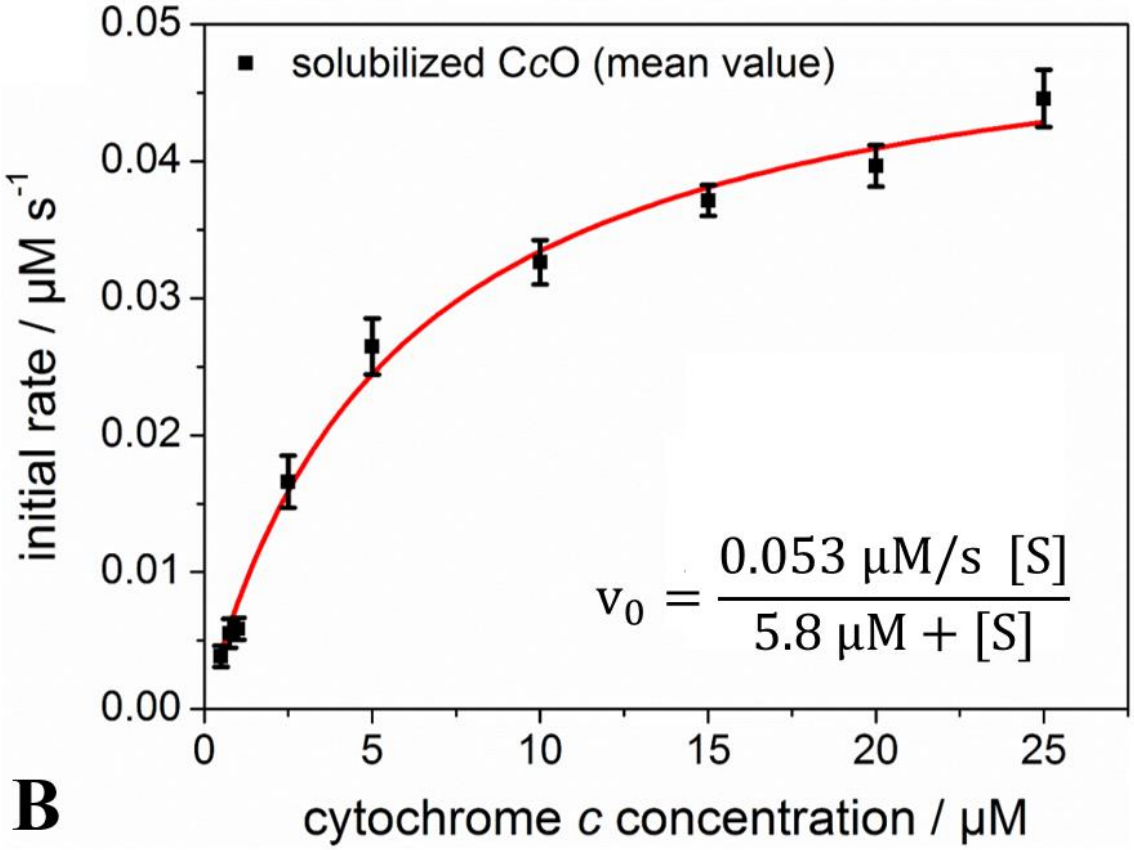

Figure 5B.10: Repetitions of the Michaelis-Menten measurements with solubilized C*c*O. Measurements and evaluation steps were performed as described in the captions of the Figures 5B.8. and 5B.9. (A) Single measurements. (B) Mean values with standard deviation. The fit parameters are specified as inset.

Following the same procedure, the values K_M and k_{cat} were determined for C*c*O immobilized in proteobeads as well as for C*c*O encapsulated in PLBs (Fig. 5B.11). The enzyme concentrations were adjusted to 0.6 and 2 nM, respectively. Please note that the different measurements resulted from different PLB/proteobead preparations, so that the similarity of the obtained curves indicated reproducibility of PLB/proteobead preparation, not only for the reliable measurement system.

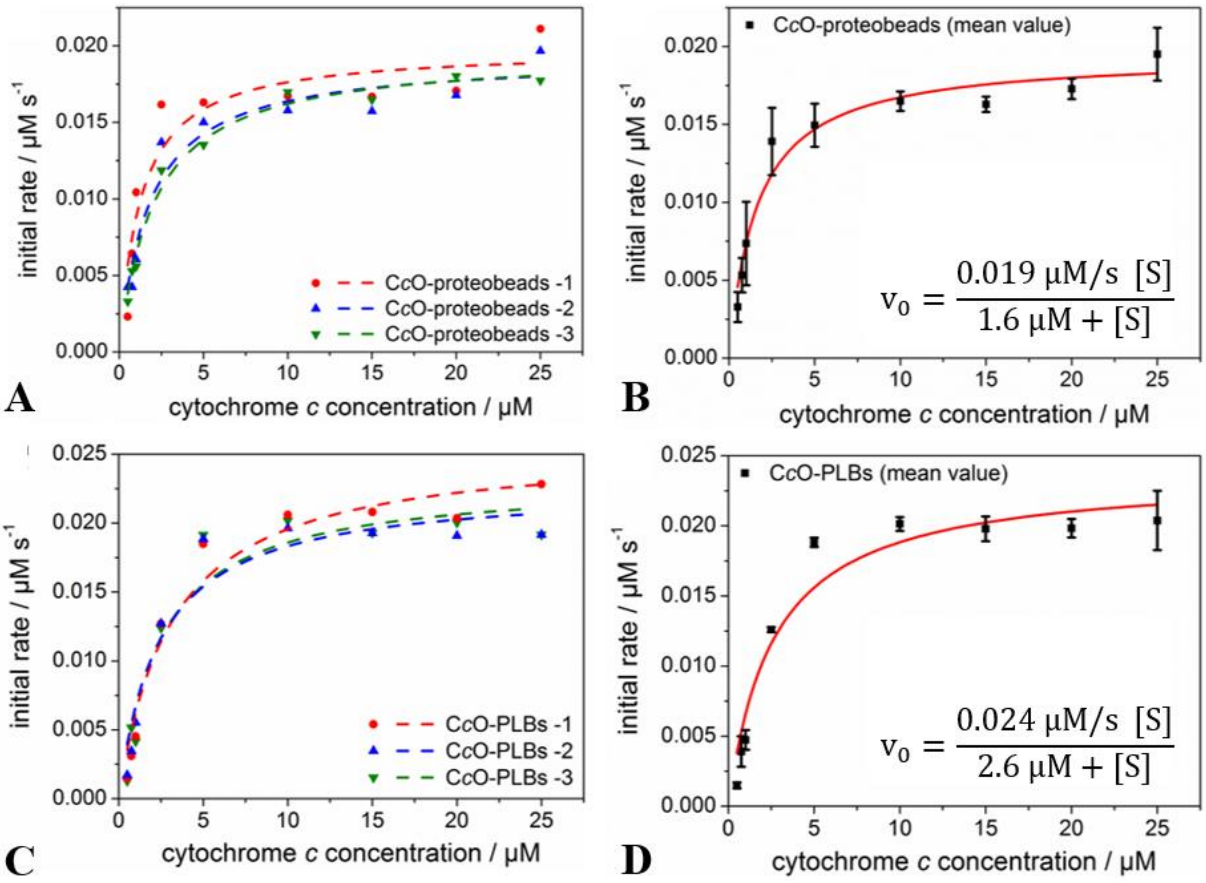

Figure 5B.11: Michaelis-Menten diagrams of C*c*O-proteobeads and C*c*O-PLBs. The procedure described in the captions of the Figures 5B.8 and 5B.9 was repeated for C*c*O-proteobeads (A: single measurements; B: mean values with standard deviation) and C*c*O-PLBs (C: single measurements; D: mean values with standard deviation), with only two changes: The concentrations of C*c*O encapsulated in proteobeads and PLBs were adjusted to 0.6 and 2 nM, respectively, to be able to measure with the same cytochrome *c* concentrations as used for the solubilized C*c*O. (The criterion was again the linearity of the absorption decrease within the first 60 s.) Second, the buffer was THK instead of DDM/THK in case of the PLBs.

To complete the set of measurements, C*c*O-PLBs were measured under so-called uncoupling conditions, i.e., in the presence of valinomycin and FCCP. Valinomycin acts as K^+ carrier, while FCCP enables protons to cross the membrane. The measurement is used to determine the membrane denseness by cancelling its sealing properties. Afterwards, the maximum turnover

numbers with and without valinomycin and FCCP are compared, which is quantified by the ratio (abbreviated RCR for respiratory control ratio). The results are shown in Fig. 5B.12.

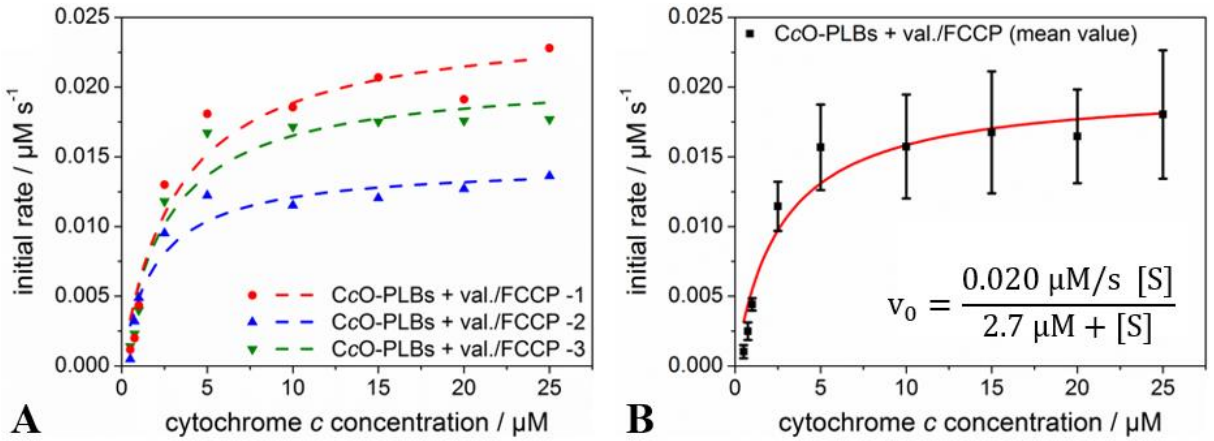

Fig. 5B.12: Michaelis-Menten plots of C*c*O-PLB under uncoupling conditions. The measurements shown in Fig. 5B.11C and D were performed again after incubation with 0.5 µM valinomycin and 1.2 µM FCCP, using the PLB amount corresponding to 0.6 nM C*c*O. (A) Single measurements. (B) Mean values with standard deviation.

As can be seen in Fig. 5B.12, the standard deviation in case of the measurements containing valinomycin and FCCP was notably larger. A possible reason could be different incorporation rates of the uncoupling agents, which would have been unwanted, since the concentrations of both were chosen to be significantly higher than required. On the other hand, in comparison with the other plots (see Fig. 5B.13, especially Fig. 5B.13B), the deviation turned out to be rather not critical. The four curves are depicted in comparison in Fig. 5B.13.

The obtained values are collected in Table 5B.2.

Table 5B.2: Catalytic activities and K_M values of the C*c*O in different conditions [315].

	C*c*O, solubilized	**C*c*O, in proteobeads**	**C*c*O, in PLBs**	
			- Val./FCCP	**+ Val./FCCP**
K_M / µM	5.8 ± 0.4	1.6 ± 0.4	2.6 ± 0.4	2.7 ± 0.6
k_{cat} / s^{-1}	264.1 ± 7.4	32.4 ± 0.5	11.9 ± 0.8	33.4 ± 8.8
Number of preparations	---	3	3	3
Number of measurements	3	3	3	3

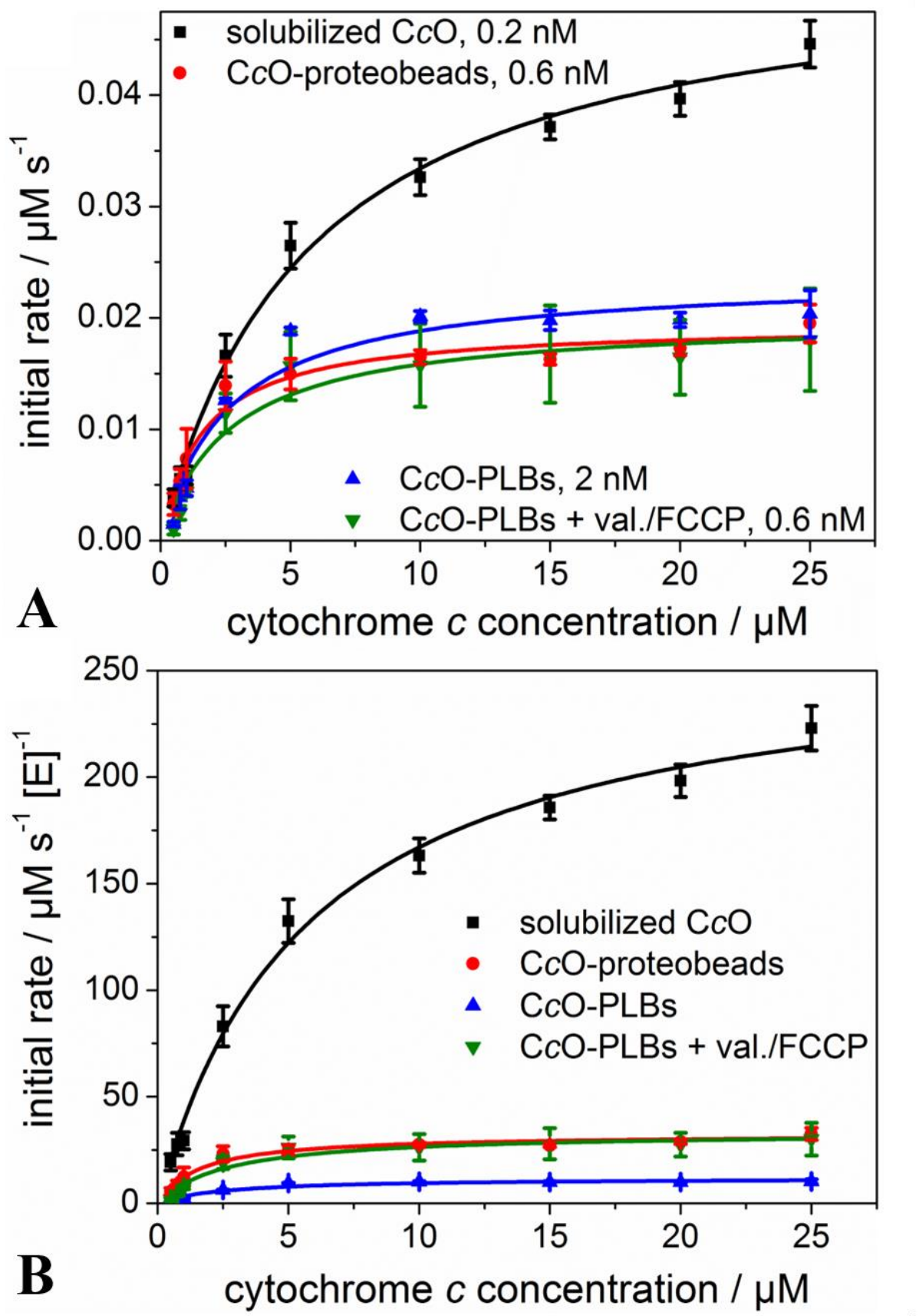

Figure 5B.13: Comparison of the Michaelis-Menten plots of the four different conditions of C*c*O. The Michaelis-Menten plots of the Figs. 5.11-5.13 are compared as shown in the corresponding figures (A), what gives a misleading bigger picture due to the different concentrations. Thus, the curves were normalized to each other by dividing by the respective enzyme concentrations (B).

The catalytic activity of the solubilized C*c*O is in the order of magnitude that is reported in literature, see, for example, Witt *et al.*, 1995 [57], who reported a catalytic activity of wild-type C*c*O 363 s^{-1}, which was considered to be not too different, as the determination of catalytic activities are not determined that reproducible and precise in literature as well, considering, for example, the aforementioned publication of Vanneste *et al.*, 1974 [58], where the catalytic activities are assigned to different preparation techniques, thereby ranging from 293 to 576 s^{-1}, and that is without considering the reported values obtained after further purification steps, associated with even lower turnover numbers (down to 74 s^{-1}; this value was not considered in terms of the agarose-PLB turnover when equipped with C*c*O, since it might correlate well with the measured turnover numbers of 61 to 73 H^+/s, but would nevertheless be misleading because of the different actual preparation method, which is outlined in the *Materials & Methods* chapter). The same accounts for the Michaelis-Menten constant, which was reported to be in the single-digit micromolar range. Finally, by finding catalytic activities that were comparable with the ones reported in literature, the method was considered as suitable to determine the catalytic activities of C*c*O embedded in PLBs. The standard deviation, being below 5 % (2.8 %) demonstrated the accuracy of the method as well as of the measurement setup, despite of improvisations (e.g., in terms of mixing), which were inevitable due to the available equipment. All measurements (including the following) were done with the same preparation of C*c*O, so possible differences within the protein preparation process would not affect the present set of measurements, but of different PLB preparations to evidence a reproducible quality between different preparations. The latter was indeed evidenced due to the rather small standard deviations, so the preparation procedure was regarded as reproducible. The deviations of the values obtained from the samples containing valinomycin and FCCP have been discussed already, see the respective results (Fig. 5B.12).

Regarding the proteobeads, a drastic drop of catalytic activity to 32 s^{-1} was observed. This was at first explained by possibly steric hindrances due to the attachment that might affect the necessary flexibility of catalytically active parts of the enzyme, but this was refuted by the agarose-PLB measurements (which are shown above, but were performed chronologically later).

Further hypotheses could thus address the differences of the bead properties. Those could be the larger curvature of the way smaller silica beads, the probably higher packing density (as mentioned before, this could not be determined for agarose-PLBs; still, the large membrane area corresponding to the bead size made this unlikely in case of the agarose-PLBs, also taking into account that the RC/bc_1-PLBs carried the double amount of protein without causing activity

decreases). A further potentially vital difference between the bead material was that the agarose provided an reservoir of water within the gel matrix, while in case of the solid silica, only the volume between bead surface and membrane serves as aqueous inner volume. On the other hand the same applied for the ptBLM that was established on top of a gold surface, which might include a somewhat larger inner volume due to the rough surface on top of the flat gold film, but this was hard to assess in terms of the actual difference (and the linker molecule was of comparable length). The latter also refuted the possibility that the associated proton transfer might be impeded by capillary forces that might have bound subjacent aqueous phase unusually strong to the surface.

The further activity drop in terms of the PLBs to 12 s^{-1} was considered as logical if the membrane is a sealing one. Indeed, under uncoupling conditions, the turnover number recovered to 33 s^{-1}. The RCR hence calculated to

$$\mathrm{RCR} = \frac{k_{cat}\ (+\ \mathrm{val./FCCP})}{k_{cat}\ (-\ \mathrm{val./FCCP})} = \frac{33.4\ s^{-1}}{11.9\ s^{-1}} = 2.8\ , \qquad (5B.6)$$

whereby an RCR significantly greater than 1 was, according to literature, considered to indicate a dense membrane [304], which was the case. Moreover, the activity under uncoupling conditions is almost accurately the same as in proteobeads, which underlined the argumentation that the membrane was causal for the further activity decrease of C*c*O embedded in PLBs, but, on the other hand, that there had to be something else than the membrane that caused the drastic activity drop towards the solubilized C*c*O. At least, the sealing membrane evidenced the presence of a bilayer, while having a multilayer, the cyt *c* would not be able to bind to the C*c*O.

Finally, the activity loss remained enigmatic. Since the curvature did not impede the membrane formation, it appeared to be unlikely that it hindered the C*c*O activity. Reasons concerning the C*c*O itself are refuted by the results obtained with C*c*O attached to agarose PLBs, the ones concerning the small volume between the bead and the membrane were not to bring in line with the ATR-SEIRAS measurements employing a planar ptBLM on a solid gold surface (with a linker molecule of comparable length), and neither membrane nor lipids could be considered as causal, since the drop occurred already at proteobeads.

What remained was the relatively dense packing, which likely was not the case having agarose-PLBs. So, it might be worthwhile to perform the measurements with differently occupied PLBs, also reducing the number of C*c*O per NP. This would also include further RCR measurements, since potentially increased activities due to a lower number of enzymes per PLB are possibly

associated with a decreased membrane stability, if the number of anchor molecules to establish the ptBLM, i.e., the C*c*O, undercuts a certain limit [316]. To find an optimum, PLBs based on NPs of 50 nm diameter, still exhibiting little scattering, and thus PLBs of a presumed size of around 75 nm, might be suitable as well. Besides, investigating a protein that can be monitored by UV/Vis spectroscopy due to its redox activity, but without being coupled to a transport process, could be interesting. In doing so, reasons associated with the net transport, which might have been refuted by other measurements, but also might still escape our notice, could be excluded or affirmed.

Concerning the further application of silica-NP, there might be a follow-up project focussing on ultrafast kinetic measurements to elucidate elusive questions on the catalytic cycle of the C*c*O. In this terms, there might be also capacities to find and maybe overcome the reason of decreased activity.

Finally, the publication presenting the results obtained at nanometer-sized silica-PLBs is attached, which was published in the journal *Langmuir*. Please note that <content not available in online version> and myself contributed equally to the following publication.

F. SCHADAUER, A. F. GEISS, J. SRAJER, B. SIEBENHOFER, P. FRANK, C. REINER-ROZMAN, B. LUDWIG, O.-M. H. RICHTER, C. NOWAK, AND R. L. C. NAUMANN: **Silica Nanoparticles for the Oriented Encapsulation of Membrane Proteins into Artificial Bilayer Lipid Membranes**. *Langmuir* 31 (2015) pp. 2511–2516. doi: 10.1021/la504417j.

Afterwards, a not further discussed review, summarizing the developments in the field of biomimetic membranes with focus on multi-redox center proteins, which was written during the time of this PhD thesis with contributions of myself, published in the *International Journal of Molecular Science*, is presented [317].

R. L. C. NAUMANN, A. F. GEISS, C. STEININGER, AND W. KNOLL: **Biomimetic Membranes for Multi-Redox Center Proteins**. *International Journal of Molecular Sciences* 17 (2016) 330. doi: 10.3390/ijms17030330.

Publication IV

<content not available in online version>

<content not available in online version>

<content not available in online version>

<content not available in online version>

<content not available in online version>

<content not available in online version>

Publication V

<content not available in online version>

<content not available in online version>

<content not available in online version>

<content not available in online version>

<content not available in online version>

<content not available in online version>

<content not available in online version>

<content not available in online version>

<content not available in online version>

<content not available in online version>

<content not available in online version>

<content not available in online version>

<content not available in online version>

<content not available in online version>

<content not available in online version>

Chapter 6 *Summary & Outlook*

To complement existing biomimetic membrane systems that facilititas the investigation of membrane proteins without requiring demanding cell culture-based assays, PLBs were designed, being supposed to overcome the issue of random protein insertion of spherically shaped liposomes and to enlarge the spectrum of applicable investigation techniques regarding planar protein-tethered membranes by being independent from solid surface. PLBs therefore use a spherical core to attach the proteins of interest and subsequently to establish a protein-tethered membrane. The primary aim was the integration of proteins in a functional manner to serve as potential pre-testing format for active substances, while the concept, however, might serve fundamental research as well.

Based on a core of agarose beads, confocal laser-scanning fluorescence microscopy could be employed to investigate the functionality of proton pumping enzymes by means of pH-sensitive fluorescence labels, which are known to intercalate into the outer leaflet of a bilayer lipid membrane. It was evidenced that the C*c*O, serving as model protein, could be integrated with retained functionality, however, with lowered activity. That was probably due to the investigation methods, which did not provide a twenty-twenty continuous illumination of the Ru complex that was used for excitation. Under continuous illumination, another proton pumping enzyme, the bc_1 complex, retained its full activity compared to values reported in literature. The bc_1 was activated by the products of the light-driven photosynthetic reaction center, thereby mimicking the light reaction of the type II photosynthesis, known from, for instance, purple bacteria. Hence, the integration of more than one protein could be achieved in a way that the enzyme complexes collaborated via electron shuttles (being cyt *c* and ubiquinone/ubihydroquinone in this case).

Further, PLBs were shown to be storable when deep-frozen with liquid nitrogen, if DMSO was added additionally to avoid recrystallization during the thawing process, and to be suitable to be used in commercially high-throughput FLIPR assays, by the means of which the potential development across the membrane upon C*c*O activity was monitored.

To use PLBs as a modular system, different labels (pH- and potential-sensitive), lipids (DiPhyPC and *E. coli* polar lipid extract), proteins (C*c*O, bc_1, RC, and LHCII), and core

particles (agarose beads, silica beads) were used. Regarding the latter, a nanometer-sized PLB version was prepared based on silica nanoparticles, having a diameter of about 50 nm, hence being small enough to use UV/Vis spectroscopy, which is a common technique to, e.g., investigate the catalytic cycles of multi-redox center proteins in basic research. In any case, the established membrane was shown to be sealing. Nevertheless, C*c*O embedded in the nano-version of PLBs showed significant decreases in activity, which remained enigmatic.

A reasonable outlook would thus be to further investigate the silica-based PLBs, e.g., in terms of packing density, which might have a hindering influence on that very small membrane systems. Due to the different experiments, several hypotheses to explain the activity decrease could be ruled out by comparing with each other. So, the more basic approach of integrating a protein that is not associated to transport processes could help to obtain a basic idea of the reason for the losses.

To continue the use of PLBs in terms of elucidating central questions in basic research, i.e., the catalytic cycle of the C*c*O in this case, a follow-up project might be performed using an equipment capable of monitoring ultrafast kinetics via UV/Vis spectroscopy.

Another reasonable further step would be to actually incorporate ion channels or other drug target proteins in PLBs to perform active substance pre-tests as initially planned as main purpose of PLB usage, or to enlarge the concept further by combining it with non-natural polymers known from the formation of polyerosomes, hence resulting in proteo-polymerobeads.

III Bio-UV-SPR

Exploring the ultraviolet spectral range for water-bound analytes in surface plasmon resonance spectroscopy

Chapter 7 *Introduction*

Surface plasmon resonance (SPR) spectroscopy has become a powerful tool not only to detect chemical and biological species, but further to study molecular interactions in real-time measurements, such as antibody-antigen binding analyses or, more recent, to analyze new DNA-based approaches like aptamers [318, 319]. Providing several advantages like the capability of label-free detection of proteins of sufficient size with a low limit of detection, the SPR sensor concept finds applications in medical diagnostics, food safety and more [320, 321].

Especially regarding biological purposes, the majority of SPR sensors utilizes gold or silver layers or nanoparticles in the visible and near-infrared spectral region. However, numerous biomolecules exhibit strong absorption, possibly coupled to auto-fluorescence, in the ultraviolet (UV) part of the spectrum. A few examples are DNA, proteins and aflatoxins [322–326]. The inherent absorption holds potential to increase the sensitivity, while the auto-fluorescence would further enable label-free surface-plasmon field-enhanced fluorescence spectroscopy (SPFS) with potentially even lower detection limits due to the more sensitive fluorescence-based method.

But the usage of the most common SPR metals, gold and silver, is confined to frequencies of above 550 and 400 nm, respectively, hence to the visible and infrared range [258]. Recently, there is a growing interest in aluminum as plasmonic material, which is capable of resonant surface plasmon polariton (SP) excitation as low as 200 nm [258, 327], being sufficient in terms of the aforementioned exemplary biological species DNA ($\lambda_{abs} \approx 260$ nm [322]), proteins ($\lambda_{abs} \approx 280$ nm & 190-230 nm [324]), and aflatoxins ($\lambda_{abs} \approx 265$ nm [326]). The naturally arising aluminum oxide (alumina) layer, which forms immediately when aluminum is subjected to air, provides an inertness similar to gold. Its thickness was reported to be 2-3 nm [256–258], which is by far below the penetration depth of SP-mediated electric fields. Thus, both the reactivity of aluminum and the insulating properties of the passivation layer does not restrict the utilization of aluminum for SPR-related purposes, but was even reported to be of advantage by avoiding fluorescence quenching in terms of applications like SPFS [255]. Although preferably used for other purposes so far, e.g., thin films solar cells [328] or chromatic nanostructures [329], some address UV-excited plasmonic fluorescence enhancement and point out the potential concerning biological samples [254, 255, 330, 331].

Nevertheless, although the last-mentioned publications report fluorescence detection of biological molecules like, e.g., tryptophan and tyrosine analogues, those took place *ex situ* in a non-natural environment, i.e., taken up in polyvinyl alcohol and spin-coated on the sensor surface. Measurements in natural environment, which is in any case an aqueous one, holds certain further restrictions. Utilizing the common attenuated total reflection technique to resonantly excite SP requires high-refractive index glasses to provide an enhanced momentum of the incident light, so the phase-matching conditions with the SP can be fulfilled. However, those glasses become increasingly absorptive in the UV spectral range, leaving only fused silica to serve as glass substrate. But the momentum enhancement mediated by fused silica might allow for probing at the interface to air, while having a metal/water interface, the refractive index of this glass type does not suffice for resonant SP excitation.

This work hence aims at overcoming the aforementioned restrictions to enable the detection of proteins in an aqueous environment at 280 nm, which was, to the author's knowledge, not done before. For that reason, an aluminum grating was used on top of a silica substrate. The naturally forming alumina layer on top of the corrugation was exploited in terms of a silane-based functionalization that allows to bind a polyhistidine(his)-tagged protein.

Due to limitations in time, further steps like fluorescence measurements or probing DNA were not implemented within this work, which focused on the proteo-lipobeads (Part II), while the UV-SPR-related research (Part III) was done only in addition. The choice of the protein, which served only as model protein herein, was, however, not completely without purpose. Recently, fluorescent analogs of odorant molecules were developed to study odorant-binding proteins linked to the sense of smell (of insects in this case) [332–334], whose absorption maxima go down to 315 nm. For that reason, the odorant-binding protein 14 (OBP14) of the honeybee (*Apis mellifera*) was used throughout the measurements, which was also used by the Biosensor Technology group (within the Austrian Institute of Technology) in terms of graphene-based field effect transistors [335–337]. So, the employed protein was indeed chosen to bridge to further research topics, albeit none of these were implemented within this work for the reasons mentioned above.

Chapter 8 *Materials & Methods*

The complete equipment, including devices, chemicals, proteins, software, etc., is listed in detail within this section. Further, the optical setup, all preparation steps, and the simulation procedure are outlined. In any case, water means purified water (18.2 MΩ/cm, see below).

8.1 Materials

8.1.1 Proteins

- The Odorant-binding protein 14 (OBP14) of the honey bee (*Apis mellifera*) with a genetically engineered hexahistidyltag (6-his-tag, his_6-tag, herein generally only his-tag) at the N-terminus was kindly provided by the group of <content not available in online version> (Department of Agriculture, Food & Environment, University of Pisa, Italy).

8.1.2 Software

- ACD/ChemSketch was used to draw chemical structures.
- Andor Solis for Imaging, being the software associated to the employed Andor spectrophotometer, was used for data acquisition.
- Citavi 6 was used for the reference management.
- Gwyddion was used to process AFM data.
- Microsoft Office 2013 was used for text writing (Word), math operations (Excel), and figure arrangement (Power Point).
- Origin Lab 8.5 was used for evaluation processes, math operations and graph plotting.
- PCGrate 6.6 (demo version) was used for grating-based simulations. Due to the limitations of the demo version, the simulated gratings had to be simplified as described in the respective section.

- Winspall was used for simulations of attenuated total reflection (ATR)-based surface plasmon resonance (SPR) spectroscopy measurements. Eventually, the respective simulations are displayed in the *Theory* part only.

8.1.3 Devices

- Atomic force microscope: Pico Plus (Molecular Imaging, Agilent Technologies, Santa Clara, CA, USA)
- Balance: ABT 120-5DM precision balance (Kern & Sohn, Balingen, Germany)
- Centrifuge: Heraeus Fresco 21 (Thermo Fisher Scientific, Waltham, MA, USA)
- Evaporator: Vacuum thermal evaporator HHV Edwards Auto 306 (HHV, Crawley, UK)
- Laser (lithography): HeCd laser IK 3031 R-C (Kimmon Koha Company, Tokyo, Japan)
- Magnetic stirrer with heatable plate: MR Hei-Tec (Heidolph Instruments, Schwabach, Germany)
- Optical table: PBI52523 (Thorlabs, Newton, NJ, USA)
- pH electrode: Seven Multi (Mettler Toledo, Columbus, OH, USA)
- Spectrometer: Andor Shamrock SR-303i-B spectrometer, equipped with the Andor CCD detector DU920P-OE (Andor Technology, Belfast, UK)
- Spincoater: G3P Spincoat (Specialty Coating Systems, Indianapolis, IN, USA)
- Ultrasonic bath: Elmasonic S10 (Elma Schmidbauer GmbH, Singen, Germany)
- UV lamp: Bio-Link 365 (Vilber Lourmat, Eberhardzell, Germany)
- Water purification: Arium Pro UV water purification system (Sartorius Stedim Biotech, Göttingen, Germany)
- Xe lamp: LSB510, with LSA122 adapter, LSH102 housing and LSN151 power supply (LOT-QuantumDesign, Darmstadt, Germany)

8.1.4 Utensils

- Glass substrates:
    - Fused silica, used as grating and flow cell substrate (Neubert-Glas, Geschwenda, Germany)
    - BK7, used as substrates for the photoresist master structures prepared by laser interference lithography (LIL) (Schott, Mainz, Germany)

- Lenses (UV-compatible): LA4052-ML (Thorlabs, Newton, NJ, USA)
- Optical fibers (UV-compatible): M92L01 (Thorlabs, Newton, NJ, USA)
- PDMS gaskets: The PDMS gaskets were kindly provided from the group of <content not available in online version> (Institute of Photonics and Electronics, Czech Academy of Science, Czech Republic).
- Polarizer (UV-compatible): WP12L-UB (Thorlabs, Newton, NJ, USA)
- Rotation stage: DT 40-D25 (Thorlabs, Newton, NJ, USA)

The flow cell was custom-made as described in the respective section part. The minor components like tubings, syringes, epoxy-based two component adhesive, drillers, screws etc. were taken from available stocks and are not listed in detail. The same applies for common minor setup components like holders, irises etc. and lab equipment like pipettes, pipette tips etc.

8.1.5 Chemicals

- 11-Pentafluorophenylundecanoatetriethoxysilane (Sikémia, Montpellier, France)
- Aluminum pellets for evaporation (Kurt J. Lesker Company, Hasting, United Kingdom)
- Amonil MMS 10 (AMO GmbH, Aachen, Germany)
- Bis(carboxymethyl)-L-lysine (Sigma-Aldrich, Steinheim, Germany)
- Developer AZ 303 (MicroChemicals, Ulm, Germany)
- Dimethyl sulfoxide (DMSO) (Sigma-Aldrich, Steinheim, Germany)
- Ethanol absolute for analysis (pro analysi, p.a.) (Sigma-Aldrich, Steinheim, Germany)
- Hellmanex III sollution (Sigma-Aldrich, Steinheim, Germany)
- Microposit S1805 (Shipley Chemicals, Coventry, UK)
- Natrium hydroxide (NaOH) (Sigma-Aldrich, Steinheim, Germany)
- Nickel(II) chloride ($NiCl_2$) (Sigma-Aldrich, Steinheim, Germany)
- Polydimethylsiloxane (PDMS) elastomer Sylgard 184 (Dow Corning, Midland, MI, USA)
- Tris(hydroxymethyl)aminomethane hydrochlorid (Tris-HCl) (Sigma-Aldrich, Steinheim, Germany)
- Water (18.2 MΩ/cm), purified by an Arium Pro UV purification system (Sartorius Stedim Biotech, Göttingen, Germany)

8.2 Methods

8.2.1 Buffer solutions

The buffer used in all experiments contained 5 mM of Tris-HCl, adjusted to a pH value of 8 with 5 M NaOH.

8.2.2 Protein aliquots

The OBP14 stock solution was aliquoted in 500 µL portions of 10 µM in 5 mM Tris-HCl buffer at pH = 8. The aliquots were stored at -20 °C.

8.2.3 Preparation of aluminum crossed gratings

All aluminum gratings were evaporated on photoresist replicas made from one master structure to provide reproducibility. The master structure was prepared by laser interference lithography (LIL) utilizing a HeCd laser with an operating wavelength of λ = 325 nm. The interference field was created using Lloyd's mirror configuration, schematically shown in Figure 8.1.

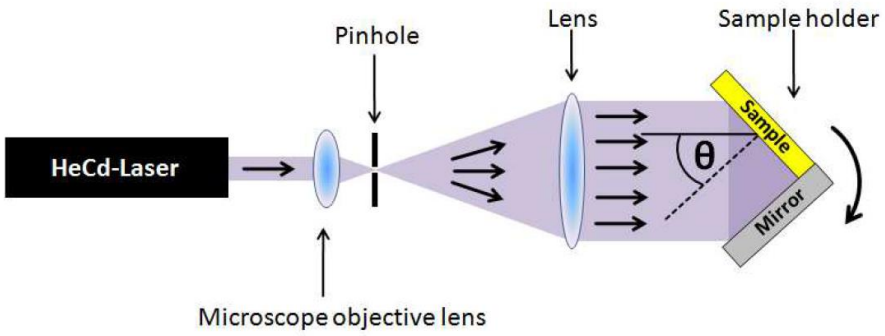

Figure 8.1: Lloyd's mirror configuration. The displayed geometry was applied to produce an interference field. The distance of intensity maxima can be adjusted via the angle θ. Figure adapted from Gogalic *et al*., 2015 [338].

By adjusting the angle θ, the desired grating period can be obtained. The required angle of incidence θ calculates by means of equation 8.1, with Λ as the grating period.

$$\Lambda = \frac{\sin \theta}{2\pi} \tag{8.1}$$

A photoresist layer (Microposit S1805) of 400 nm thickness was applied onto a BK7 glass substrate by 45 s of spin-coating at 4,500 rpm. The sample was soft-baked (98 °C, 120 s) and subsequently exposed to the interference field described above. The angle was adjusted to $\theta = 54.34$ deg to obtain a grating period of $\Lambda = 200$ nm. The calculated wavelength for resonant surface plasmon polariton (SP) excitation at normal incidence (see eq. 2.88) is 300 nm. Further tuning towards the desired wavelength was done by adjusting the angle of incidence in the respective measurements. The intensity was set to 32 µW/cm^2. Between two exposure periods of 60 s, the sample was rotated by 90 deg to obtain a crossed structure. After exposition, the sample was developed by submerging the sample into the developer AZ 303 for 25 s, which was previously diluted 1:14 with water.

Replicas of the master structure were prepared by UV nanoimprint lithography (NIL), which is schematically depicted by Fig. 8.2. First, the LIL corrugation was casted to PDMS, which was allowed to cure at room temperature for three days. Then, after the PDMS was detached from the LIL corrugation, they were used as stamps to prepare UV-transmitting Amonil MMS 10 (subsequently referred to as Amonil only) grating structures by NIL.

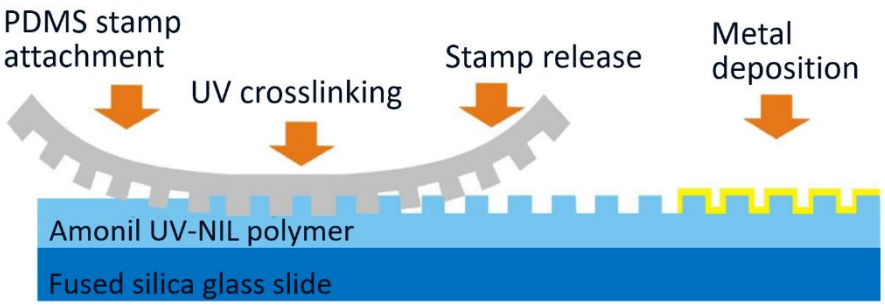

Figure 8.2: Nanoimprint lithography (NIL). The master structure (PDMS stamp) is reproduced by imprinting into an Amonil MMS 10 photoresist. The latter is developed by UV crosslinking. Afterwards, the desired metal, i.e., aluminum in this case, can be evaporated on top. A sinusoidal grating was used instead of a rectangular one. Figure adapted from Gogalic *et al.*, 2015 [338].

For that purpose, fused silica glass substrates of around 2 cm in square were thoroughly cleaned by ultrasonication for 10 min in 2 % Hellmanex III solution, followed by the same procedure with water and finally with ethanol. The substrates were spin-coated with 200 µL Amonil for 120 s at 2,000 rpm. The spin-coating settings were chosen to obtain a layer of 110 ± 5 nm thickness. The Amonil solution was stored and processed light protected. Any application took place under lamps covered with UV-absorbing foil, while the bottle was wrapped in alumina foil at any time. The PDMS stamps were placed (grating structure underneath) on top of the Amonil layer and then exposed to UV light of $\lambda = 365$ nm and an irradiation dose of 5 J/cm^2.

The Amonil corrugations thermally evaporated with an aluminum layer of around 20 nm thickness in a vacuum of at least 10^{-7} bar. The thickness was determined by a quartz crystal microbalance (QCM) chip that was located inside the evaporator. To obtain sensor chips with comparable aluminum layers on top and suitable reference chips, all samples used in a set of measurements were (beside originating from the same PDMS stamp) evaporated in one cycle. The reference chip was obtained by following the same procedure without imprinting the corrugation. Thus, a plane aluminum chip of the same layer thickness was obtained.

The alumina layer (Al_2O_3), utilized in terms of surface functionalization, forms immediately by getting in contact with air without any action, being of a thickness of 2-3 nm according to literature [256–258]. This film acts as passivation layer as well, preventing further corrosion of the aluminum beneath. After evaporation, the aluminum chips with and without crossed grating structure on top were analyzed utilizing atomic force microscopy (AFM) to check the topology. The chip is schematically depicted in Fig. 8.4A.

8.2.4. Atomic force microscopy

The atomic force microscopy measurements were done by <content not available in online version>, who had the necessary permission to work at the AFM instrument. The images were recorded with a PicoPlus AFM from Molecular Imaging, which operated in tapping mode.

8.2.5 Functionalization of the aluminum grating surface

The functionalization of the grating surface was not of high importance in this case, since a shift of the resonance wavelength can be observed due to nonspecific adhesion of proteins at the surface as well. For that reason, the linker reaction yield and putative shares of nonspecific binding events were not determined.

Each 10 µM the two common commercially available linker molecules 11-pentafluorophenylundecanoatetriethoxysilane and bis(carboxymethyl)-L-lysine were allowed to react overnight in 1 mL of water-free DMSO (stored over a molecular sieve and removed with a syringe pierced through a closing membrane) according to the reaction scheme displayed in Figure 8.3.

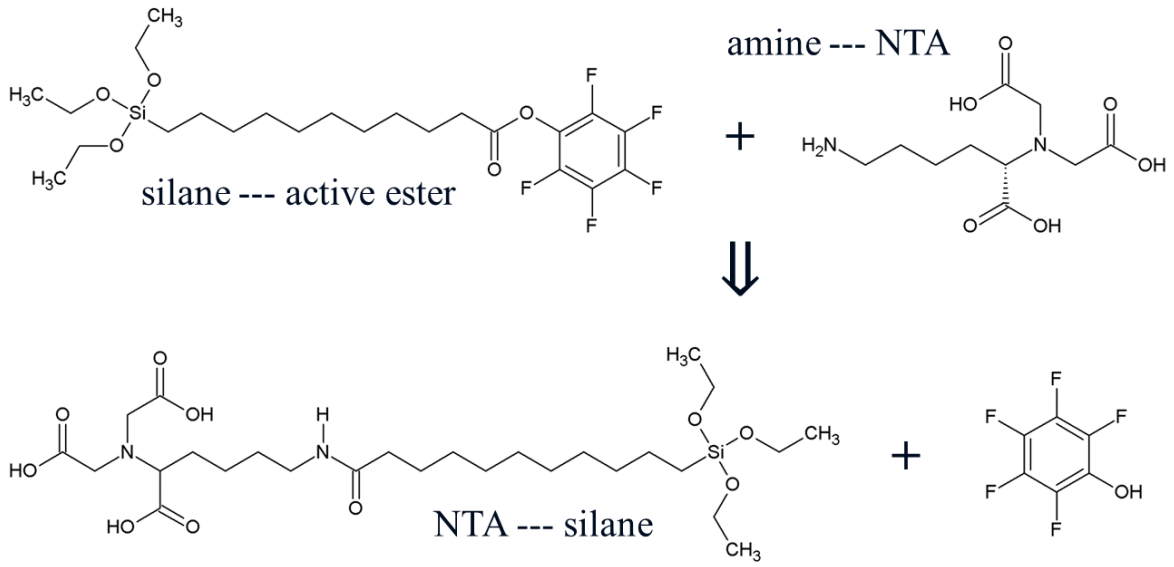

Figure 8.3: Linker reaction scheme. By the reaction of an amine-terminated bis(carboxymethyl)-L-lysine with a silane-based linker carrying an active ester at the opposite end, a linker emerges that is on the one hand able to bind to an oxide like alumina and on the other hand capable of capturing his-tagged proteins via the NTA (nitrile tri-acetic acid) residue after it was subjected to Ni^{2+} ions (not shown). Figure published in Geiss *et al.*, 2017c [339].

Due to the reaction of bis(carboxymethyl)-L-lysine with 11-pentafluorophenylundecanoate-triethoxysilane, an amide bond was formed as schematically depicted in Fig. 8.3, resulting in a silane-terminated linker molecule with an NTA (nitrile tri-acetic acid) residue at the opposite side.

200 µL of the reaction product was pipetted onto the chip surface with the native aluminum oxide on top. Afterwards, it was incubated until the DMSO was completely evaporated. The procedure was repeated two times, followed by another incubation step, this time for 2 hours at 80 °C. Subsequently, the chip was thoroughly rinsed with DMSO to remove the unbound linker molecules and with water to remove the DMSO. For 30 min, the chip was incubated with a 0.1 M $NiCl_2$ solution to obtain the desired Ni^{2+}-NTA-functionalization. Finally, the chip was rinsed with water again.

8.2.6 Protein attachment

Droplets of 10 µM OBP14 in 5 mM Tris-HCl buffer at a pH of 8 were spread on top of the functionalized sensor chip until the surface was completely covered (approximately 200 µL). The chip was placed in a Petri dish with a wet paper towel to maintain the air humid and therefore avoid any drying of the surface. It was incubated overnight at 4 °C. The next day, the solution was removed with a dry paper towel, which was carefully brought in contact at the

very edge to enable a tight mounting of gasket and flow cell, while at the same time the chip was supposed to remain wet at the area that was to be situated within the light path later on. After that, the flow cell was mounted and placed within the measurement setup.

8.2.7 Design and mounting of the flow cell

The flow cell is depicted schematically and in real life in Fig. 8.4. In Fig. 8.4A, the chip layer structure is shown, omitting the native alumina layer between aluminum and surface modification. Hereinafter, the plasmonic features attributed to SPs at the sample side, hence the aluminum/water interface (the influence of the alumina was discussed before and is, according to theory, slightly present but not of greater importance), are indicated with SP_s, while the ones at the opposite side of the alumina film, hence emerging at the aluminum/Amonil interface, are abbreviated with SP_a (Fig. 8.4A).

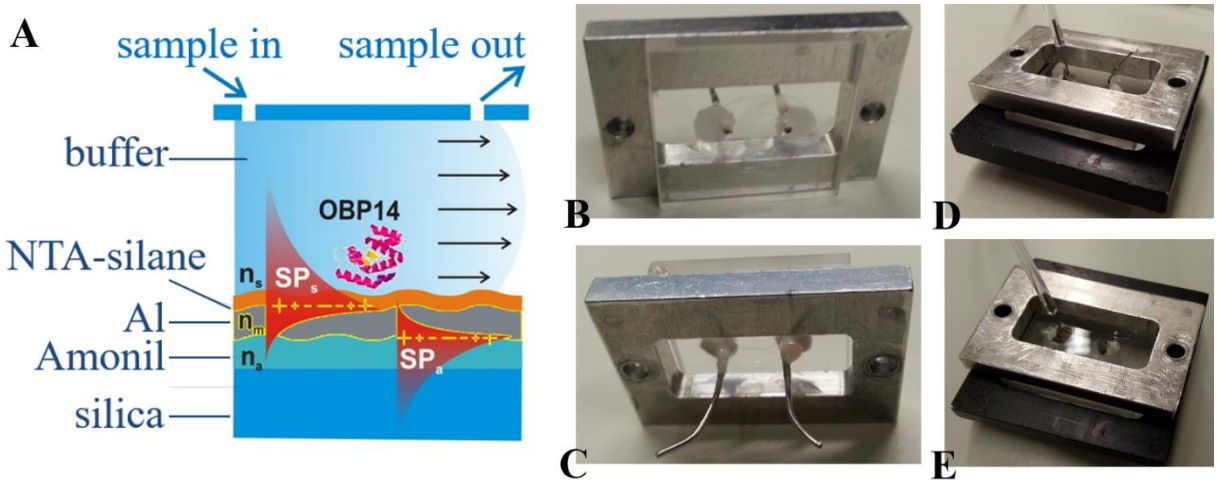

Figure 8.4: Flow cell. (A) Schematic depiction of flow cell and sensor chip. (B-E) Different views at the real flow cell. Description is given within the text. Fig. 8.4A published in Geiss *et al.*, 2017c [339].

The flow cell as implemented in real life comprised a sample chamber enclosed by a fused silica substrate (Fig. 8B and C) and the sensor chip (not shown), spaced by a PDMS gasket with an inner volume of 10 µL, only barely discernible in Fig. 8B. The gaskets were kindly provided by the group of <content not available in online version>. Adequately cut cannulas placed in drilled holes provided inflow and outflow, sealed with a customary two-component adhesive. After the gasket was placed appropriately to allow free flow through the cannulas, the sensor chip was placed carefully with the corrugation underneath, pointing towards the chamber, then tightened firmly by screwing the sample holder (black scaffold in Fig. 8D and E) upon the assembly. Customary hoses provided in- and outflow, which was finally not performed in terms

of *in situ* measurements, as the protein attachment was implemented *ex situ* as described above, measuring in before/after mode.

8.2.8 Optical setup and measurements

To characterize of the plasmonic properties of the crossed grating aluminum chips with and without proteins attached, a custom-made setup was employed. A schematic depiction and the actual setup are shown in Fig. 8.5.

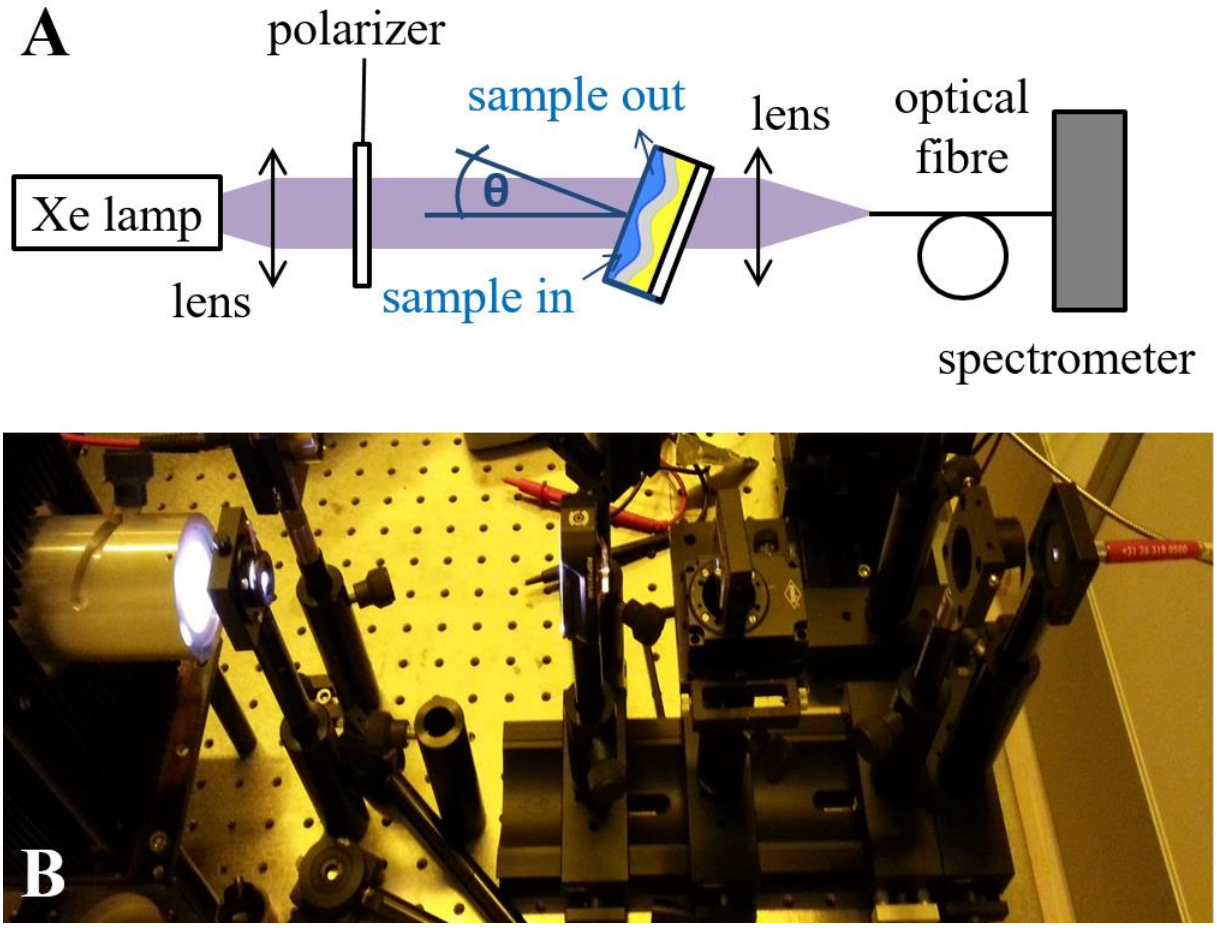

Figure 8.5: Optical setup. (A) The transmission setup is depicted schematically, comprising a Xe white lamp emitting in a spectral range down to 250 nm, an iris instead of the depicted lens, since finally the lamp intensity turned out to be high enough to measure without light collimation, a UV-compatible polarizer to provide TM-polarized light, a rotatable sample holder (not shown) and the sample flow cell described above, as well as a UV-compatible lens to focus at the as well UV-compatible optical fiber to guide the light into the spectrometer. (B) The real setup, mounted onto an optical table. Instead of the flow cell, an aluminum grating interfacing with air on top of a sample holder is shown, used for earlier adjustments of the beam path and the spectrometer settings. As mentioned before, all components were chosen with respect to UV transmittance. A possibility to adjust the azimuthal angle was not integrated, therefore the latter was set to $\varphi = 0$ all the time. Due to diffraction, only the light of the zeroth order diffraction mode was collimated and forwarded to an Andor Shamrock spectrometer with implemented CCD camera (not shown), while the higher order modes passed by laterally. Fig. 8.5A published in Geiss *et al.*, 2017c [339].

The beam of a Xe light source in a pre-mounted housing was narrowed by an iris only, since the intensity was high enough to omit beam collimation. The spectral range sufficed to record spectra as of 250 nm. With a UV-transmitting polarizer, TM-polarization was achieved, not further exploiting the crossed grating structure, which was done only standardly. Further, in favor of an easier construction, the possibility to adjust the azimuthal angle was not implemented, so it was set to $\varphi = 0$ deg at any time. Beyond the polarizer, light was shined onto the sample under a certain angle of incidence, which was freely selectable in the full range due to a rotatable stage.

Chip and flow cell were mounted as described above. All parts that were located within the light path (except from the grating structure) were built of UV-transmitting fused silica. A PDMS gasket between chip and flow cell provided a volume of 10 µL. Light was transmitted through the sample and focused at the opening of a UV-compatible optical fiber by a fused silica lens. The light was forwarded to a spectrometer, which was equipped with a CCD detector. Closer specifications of all parts of the setup are given within the *Materials* section.

Measurements were performed having an aluminum/air and an aluminum/buffer interface at the sample side to assign the spectral features to the interface the respective SPs emerged at, followed by measurements with attached protein (in buffer). The reference chips, prepared equally but without imprinting a corrugation, were measured in the same way. Every sample was measured under varying angles of incidence in a range of $\theta = 0\text{-}30$ deg in steps of 1 deg. At every angle of incidence, a whole spectrum was recorded in the wavelength range of $\lambda = 250\text{-}500$ nm. Below 250 nm, the emission intensity of the light source did not suffice any more. The output quantity were unprocessed counts. The data normalization was hence done afterwards with Origin Lab 8.5 and Microsoft Excel.

8.2.9 Data normalization

The data normalization in terms of background signal and reference spectra was done afterwards with Origin Lab 8.5 and Microsoft Excel using equation 8.2.

$$T = \frac{I_{sample} - I_{background}}{I_{reference} - I_{background}} \tag{8.2}$$

The resulting spectra were plotted as 3D surface plot and 2D cross sections thereof, the latter representing spectra at certain angles of incidence.

8.2.10 Simulations

Grating-coupled SPR spectra were simulated using the demo version of PCGrate. Due to the limitations of the demo versions, the simulated situation had to be simplified. So, only three layers (of which the upper and the lower had to be semi-infinite) could be taken into account, therefore the alumina film and the fused silica substrate underneath the Amonil had to be left out (leaving Amonil, aluminum, and air or water). Moreover, instead of a crossed grating, a linear one had to be simulated (which in fact makes no difference for TM-polarized light and an azimuthal angle of $\varphi = 0$ deg). Nevertheless, the simulation data were sufficient to be compared with the measurements and to assign the SP features to one of the interfaces.

The spectra (λ = 250-500 nm, increment: 1 nm) were simulated one by one for an angle of incidence range of θ = 0-30 deg, assuming a grating with a sinusoidal corrugation with a period of Λ = 200 nm and a modulation depth of 30 nm. (The same modulation depth was specified in the simulation shown in the *Theory* part (Fig. 2.26F), which was not indicated in the respective figure caption because this parameter was left out in this part for reasons of simplicity.) The light was chosen to come from the sample side. The required refractive index values were taken from Palik, 1985 [246], which was integrated in the software library, for Al, from the manufacturer's data sheet in case of the Amonil [340], and from Hale & Querry, 1973 [245], and Ciddor, 1996 [341] for water and air, respectively, the latter accessed via the refractive index database [237]. The output quantities were reflectance (finally shown in the *Theory* part only, see Fig. 2.26F), absorptance, transmittance and transmission efficiency of the zeroth diffraction order. In the case of transmittance as output quantity, the software simulates the event that all transmitted light is collected. That was not the case. Due to the setup geometry, only light of the zeroth diffraction order was collected. So, the zeroth order transmission efficiency corresponded to transmission measurements rather than the transmittance simulations. In any case, plasmonic features result in absorption peaks, thus absorptance simulations were used for their identification well, which were in some cases more lucid.

In terms of evaluating the necessity of employing grating-coupled SPR spectroscopy, attenuated total reflection (ATR) SPR measurements were simulated using WinSpall. Eventually, a few of those simulations are shown in the *Theory* part only (Fig. 2.26A and C), and the settings are described within the respective figure caption.

The data were exported to Origin Lab 8.5 and plotted therein.

Chapter 9 *Results & Discussion*

As described in detail in the *Theory* and *Introduction* part, analyzing water-bound samples in the UV range via surface plasmon resonance spectroscopy (SPR) is associated with certain limitations, which incapacitate the usage of the commonly applied sensor chip configuration, i.e., the Kretschmann/Raether geometry with a gold or silver layer on top of the substrate. Briefly repeated, the limitations and circumventions are the following:

I. Due to material properties, i.e., the real part of the material's permittivity, silver and gold cannot be used at wavelengths below 350 and 500 nm, respectively. An increasingly often used metal, which fulfils the necessary conditions, is aluminum.

II. Aluminum, as a base metal, is reactive, but undergoes a native passivation by forming a thin (2-3 nm) alumina (Al_2O_3) layer in contact with air. This passivation prevents corrosion comparable to precious metals, while it simultaneously allows the functionalization via silane-terminated linker molecules. The resonant excitation of surface plasmons (SPs) is not notably hindered, since the layer thickness is much smaller than the penetration depths of the SP-mediated evanescent fields.

III. Attenuated total reflection-based SPR spectroscopy is based on momentum enhancement (of the incoming light) by a glass prism with a sufficiently high refractive index. As turned out, the refractive index of fused silica does not suffice. On the other hand, all the higher-refractive index glasses like N-LASF9 or BK7 absorb the excitation light below 300 nm almost completely, and here, the only exemption is fused silica.

    Thus, grating-coupled resonant excitation of SPs was exploited to fulfill the matching conditions, utilizing an aluminum grating on top of a fused silica substrate. In this case, theoretically, no limitations occur until the absorption of air becomes crucial at the border to the vacuum-UV range. Practically, the lamp intensity sufficed only as of 250 nm.

At first, the sensor chips with an aluminum grating on top as well as the reference chips with a plane aluminum film of the same thickness (evaporated in the same evaporation cycle) were analyzed employing atomic force microscopy (AFM). An exemplary topology is shown in Figure 9.1.

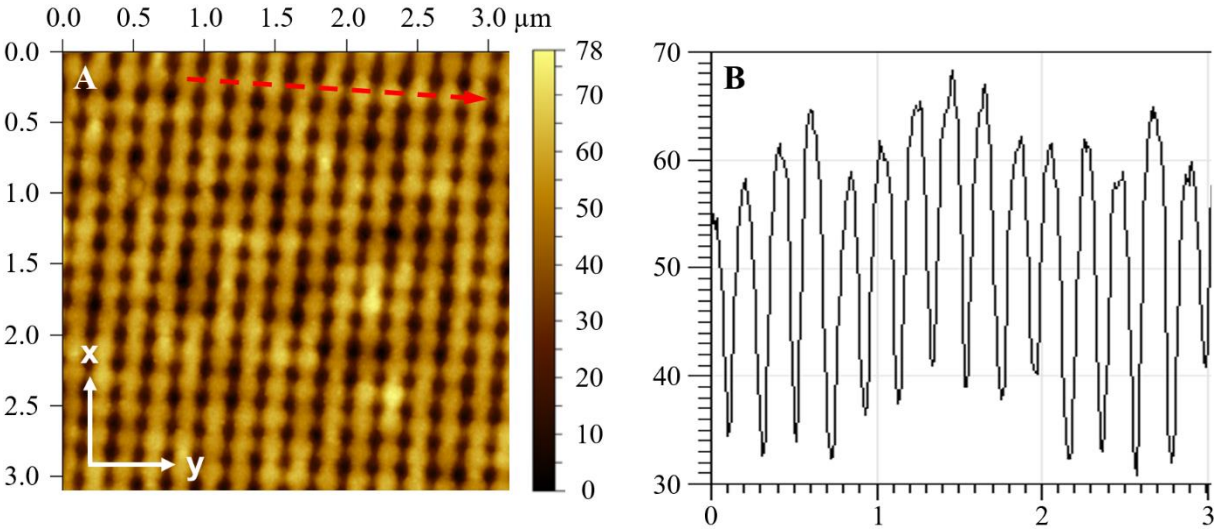

Figure 9.1: Atomic force microscopy (AFM) pictures of an exemplary aluminum grating. After the evaporation of about 20 nm aluminum (controlled by an integrated quartz crystal microbalance (QCM) chip), the grating was analyzed using AFM, with x and y as the scan directions. (A) Crossed grating structure with the calculated period of Λ = 200 nm in both directions. (B) Cross section of (A). The red arrow in (A) indicates the corresponding location. Figure published in Geiss *et al.*, 2017c [339].

As depicted in Figure 9.1A, the AFM records confirmed the proposed structure, having a period of approximately Λ = 200 nm and a depth of around 30 ± 5 nm, as shown in the profile (Fig. 9.1B, location indicated by the red arrow in Fig. 9.1A). The structure showed better properties in y-direction, so the chip was mounted correspondingly in the following experiments. Chips of lesser quality were discarded. The proposed flat aluminum film of the reference chip was validated by AFM as well (not shown). The displayed grating or equivalent ones were used for all measurements, further tuning the resonance wavelength by adjusting the angle of incidence.

The functionalized sensor chips were mounted within the flow cell and transmission spectra were recorded in a range of θ = 0-30 deg with an increment of 1 deg. The transmission matrices were normalized according to eq. 8.2. Below 250 nm, the lamp intensity was too low to obtain reasonable spectra. Spectra are shown as of Fig. 9.4. Before, simulations are discussed.

Utilizing grating-coupled SPR, SPs can be resonantly excited at both sides of the metal layer, while for ATR-SPR, phase-matching criteria can be fulfilled only at the backside metal-dielectric interface. The sensor chip was mounted with the sample side facing the excitation light (and simulations were done accordingly), since the light intensity to excite backside SPs

is much lower due to reflection and bulk metal absorption. Besides, resonant excitation of SPs at both sides evokes the necessity to correlate them to the interfaces. For that reason, measurements and simulations were performed for both water and air at the sample side. Due to the different refractive indices, the SP at the sample side was expected to change its spectral position, while the SP at the aluminum/Amonil interface would not be affected and hence the resonance wavelength would remain unaltered. Simulations of the absorption (displayed as absorptance, hence set in relation to the incoming light intensity) are displayed in Figure 9.2. Distinguished SPs are referred to as SP_s (assigned to the metal/sample interface) and SP_a (for the metal/Amonil interface) subsequently.

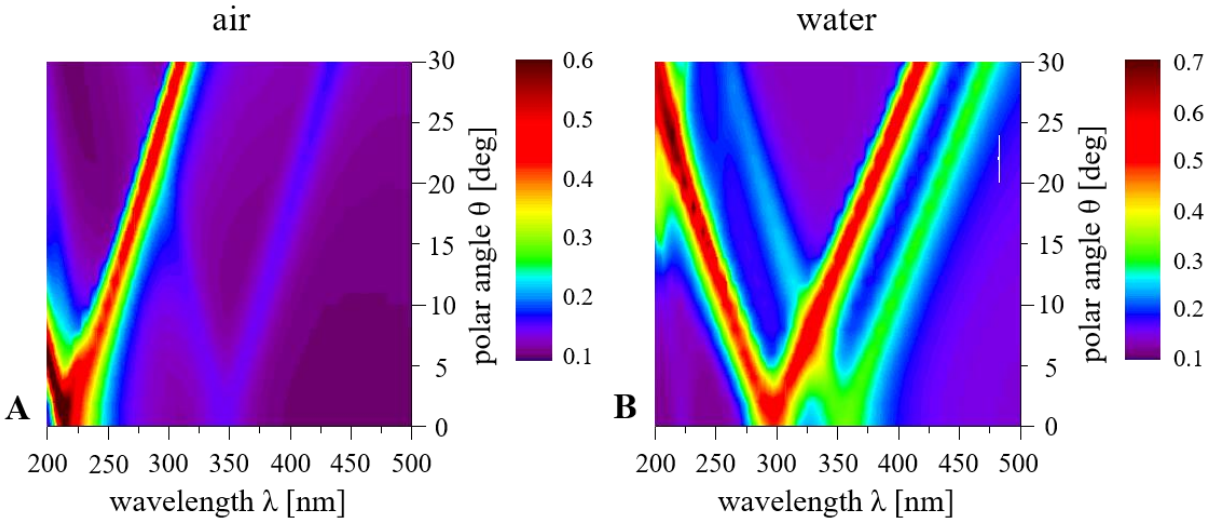

Figure 9.2: Absorptance simulations. Absorptances were simulated with respect to the used geometry. Closer description and deviations due to limitations of the demo version are described in the *Materials & Methods* section. The simulated absorptance is given for a flow cell filled with air (A) and water (B).

The absorptance simulation plot displayed in Figure 9.2 shows indeed two different features that were assigned to SP modes. By using eq. 2.88, the resonance wavelength at normal incidence was calculated to be $\lambda = 300$ nm for a grating period of $\Lambda = 200$ nm at the aluminum/water interface, mediated by the first diffraction order. Fig. 9.2B confirms this previous calculation ($\lambda_{resonance} = 297$ nm) and shows another absorption peak at 357 nm, which was hence assigned to the aluminum/Amonil interface. To further check this assignment, the geometry was simulated for an aluminum/air interface at the sample side, shown in Fig. 9.2A Indeed, the SP mode assigned to the sample side interface changed its resonance wavelength to approximately 214 nm, while the other one remained more or less unaltered in terms of the resonance wavelength (air: $\lambda_{resonance} = 345$ nm; water: $\lambda_{resonance} = 357$ nm). The appearance as V-shaped spectrum in the 3D plot can be explained in terms of mode splitting. At normal incidence, the $+1^{st}$ and -1^{st} diffraction order-mediated SPR modes couple (thus commonly

referred to as $\pm1^{st}$), appearing as a single absorption feature (for each interface) in the spectrum. With increasing angle of incidence, the coupled mode splits in individual $+1^{st}$ and -1^{st} diffraction order-mediated SPR features. This is illustrated theoretically by the SP dispersion relation for grating-coupled SPR in the *Theory* part, see Fig. 2.23. In Fig. 2.9B, at about λ = 222 nm and normal incidence, the $\pm2^{nd}$ order-mediated SPR mode of the SP_a can be seen in weak expression, which splits in the two branches of $+2^{nd}$ and -2^{nd} diffraction order-mediated SP_a, being superimposed by the way stronger absorption of the -1^{st} order-mediated SP_s mode as of about θ = 10 deg. Around 200 nm at higher angles (as of around θ = 15 deg), absorption features are recognizable that are putatively due to the $+2^{nd}$ order-mediated SP_s mode, which is partially coupling to the -1^{st} order-mediated mode. However, due to the weak lamp intensity, reasonable spectra could be measured as of 250 nm, so 2^{nd} order-mediated SPR features are not of importance.

The simulated absorption assigned to SPR at the sample side was much more pronounced than the one caused by the SP_a, which was expected because of the chip orientation. The complete incoming light intensity can potentially resonantly excite the SP_s, while not absorbed shares are reflected by the mirroring aluminum surface, so only a smaller share is transmitted to the backside that might resonantly excite the SP_a. For that reason the realized chip orientation was chosen. Since the spectral distance between $+1^{st}$ and -1^{st} diffraction order-mediated SPR modes increases along with the angle of incidence, amounting to 200 nm within the displayed range of θ = 0-30 deg, the spectral range of λ = 200-400 nm can be covered with this single corrugation of Λ = 200 nm. A restriction might only arise from the superimposition with backside SPR features, which would not change with refractive index changes at the sample side. To exploit this, a more demanding reflectivity setup (excitation source and detector cannot be mounted in-line, but the detector needs to move in response to the sample rotation) could be employed, at which a thicker aluminum film, showing no transmission at all and hence no second relevant interface, could be used.

After assigning SP_s and SP_a to the spectral features by means of absorptance simulations, the difference of transmittance and 0^{th} order transmission efficiency simulations was evaluated. The respective simulations are shown in Fig. 9.3

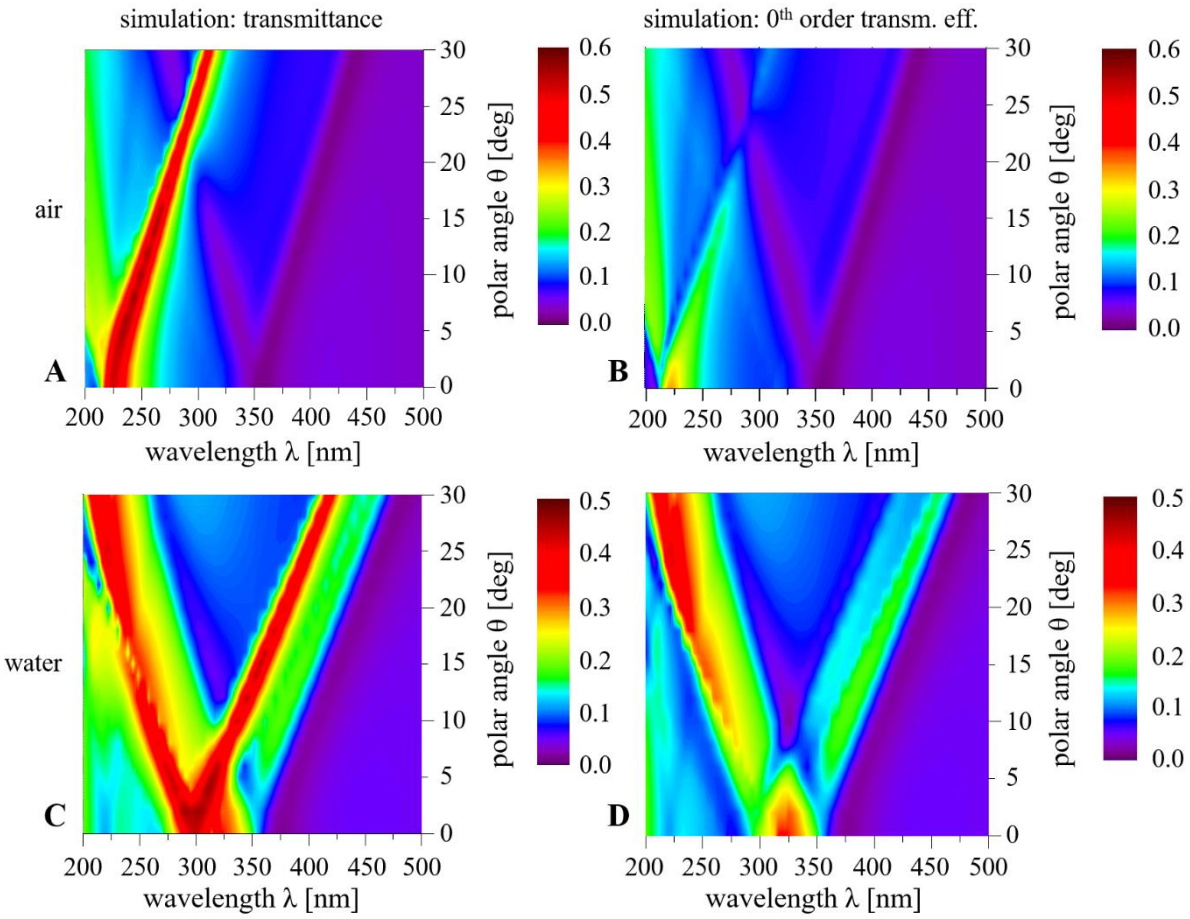

Figure 9.3: Transmittance (A, C) and 0th order transmission efficiency (B, D) simulations with air (A, B) and water (C, D) at the sample side, respectively. Except from the output value, the simulations were performed according to the absorptance simulations shown in Fig. 9.4. For further details, please see the *Materials & Methods* section.

In terms of the spectral position of the V-shaped SPR modes, the simulations shown in Fig. 9.3 corresponded quite well with the absorptance simulations displayed in Fig. 9.2. A fundamental difference was the presence of peaks instead of dips in case of the SP_s modes regarding the transmittance simulations, while the SP_a-related features were predicted as dips again. This was likely due to the possible out-coupling of light from SP modes. Due to the coupling of light to SP modes, the out-coupled waves that might emerge, and the interference of both with the transmitted light, SPR features might occur as dips or peaks in the transmittance spectra. Due to this several possibilities, there are spectral regions, within which the transmittance is difficult to explain, such as the whole part left from the -1st diffraction order-mediated SP_s peaks in the water-related simulation (Fig. 9.3C). For that reason, the evaluation of SPR modes and their assignments to the interfaces could be done in a more lucid manner by means of the absorptance simulations.

To compare with the measurement data, the 0th order transmission efficiency was simulated in addition to the transmittance, since in case of the transmittance, the simulation software

assumes that all the light transmitted into the semi-infinite half space beyond the sample is collected. As mentioned before, only the 0^{th} diffraction order light was collected. Out-coupling of waves usually occurs with respect to the diffraction order that mediated the coupling, being the 1^{st} diffraction order in the case of the SP_s-related peaks, which was not collected. If the 0^{th} order transmission efficiency is simulated, not all the light transmitted into the semi-infinite half space beyond the chip is considered, but only the light of the 0^{th} diffraction order. Therefore, this output quantity represents the measurement situation rather than mere transmittance simulations. Regarding the 0^{th} order transmission efficiency simulations (Fig. 9.3B and D), the peaks assigned to the SP_s of the transmittance simulation are indeed displayed as dips here (since the SP_s mode was assigned to the deep blue regions on the left of the green and red areas, the latter representing the interspace between the two SP modes), and so are the ones related to the SP_a (located on the right of the higher values displayed in green to red). Besides, except from minor shifts of the resonance wavelengths, such as the SP_s-related feature at normal incidence, which was slightly blue-shifted, the simulations are in accordance to the ones of the absorbance, supporting the associated argumentation. Regarding the protein absorption at $\lambda = 280$ nm, the simulation predicted resonant SP excitation at the sample side within the angle of incidence range of $\theta = 0\text{-}10$ deg. The measurement data are shown in Fig. 9.4.

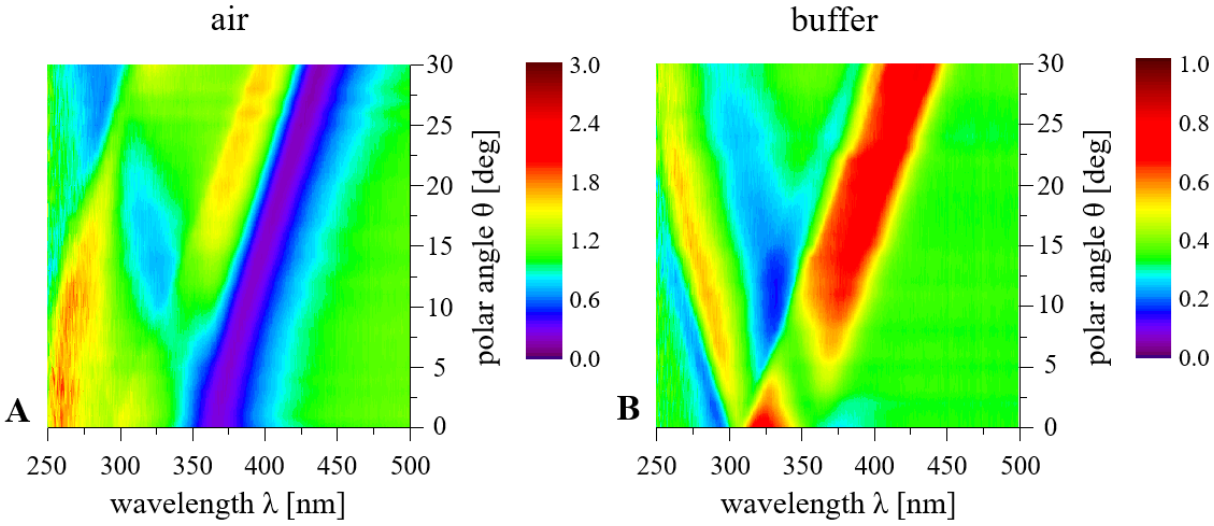

Figure 9.4: Measured transmission spectra. The geometry that was investigated by the simulations shown in the Figs. 9.2 and 9.3 was prepared and transmission spectra were recorded. The sample chamber, bordered by the flow cell, was filled with air (A) and buffer (B), respectively, without having been exposed to proteins before. A closer description is given in the *Materials & Methods* section.

To avoid extensive repetition, the measured transmission spectra (Fig. 9.4) are not outlined in detail but are discussed referring to the simulations and deduced assumptions. To provide a better comparability, the substantial simulation and measurement data are juxtaposed in

Fig. 9.5. So, by contrasting the measured transmission spectra with the simulation data, assumptions could be confirmed in principle. Minor differences, especially in terms of the magnitudes of intensities, might be due to differences between the simulated and the actual structure, which certainly exhibited imperfections in corrugation and layer thickness. Moreover, the simulated structure had to be simplified due to the limitations of the demo version. The air measurement was only done to confirm the assignment of the SP modes experimentally, while for probing biological samples, i.e., proteins in this case, those measurements are not of further worth. Regarding the buffer measurements (Fig. 9.4B), the presence of a high intensity ranges separating the two SP resonance features rather than being the plasmonic features themselves was even clearer visible in the measurement data than in the simulations. The SP_a feature mediated by the $+1^{st}$ diffraction order was missing, which could not be explained. However, this feature, attributed to the SP_a, was not of worth for SPR spectroscopy purposes anyway. The -1^{st} diffraction order-mediated SP_s mode, hence the crucial one to probe protein binding, was, by contrast, clearly pronounced and even better separated from the spectrally adjacent transmission intensities.

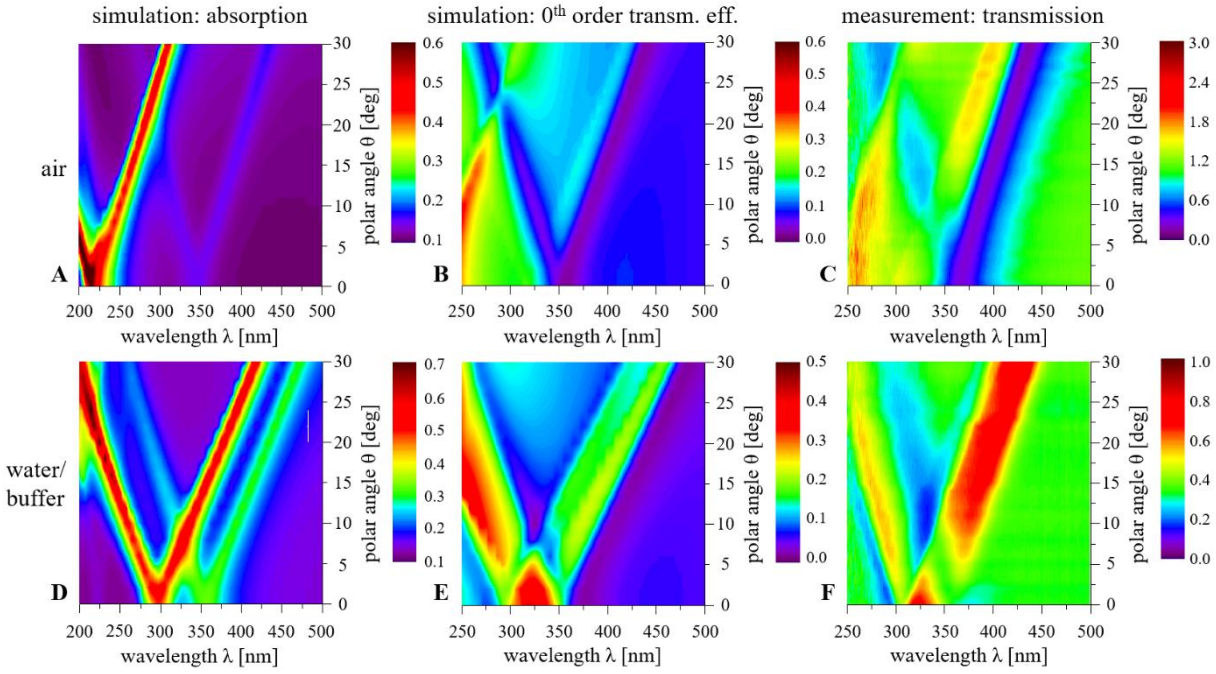

Figure 9.5: Comparison of simulation and measurement data. The essential simulations and measurements are arranged side by side for reasons of better comparability. For description, please see the respective figure caption above. Figure published in Geiss *et al.*, 2017c [339].

After probing the sensor chip with 5 mM Tris-HCl buffer (pH = 8) (the difference between water, as specified in terms of the simulations, and buffer, which was present in the actual measurements, was neglected), the chip surface was incubated with OBP14 in the same buffer,

as described in the *Materials & Methods* section, and subsequently measured again. The spectra before and after the incubation with OBP14 are shown in Fig. 9.6 as 2D cross sections of the respective 3D plots.

To tune the SP_s-related resonance feature to the wavelength of $\lambda = 280$ nm, the angle of incidence had to be adjusted to $\theta = 6$ deg. To demonstrate the tunability towards even lower wavelengths, the profiles at $\theta = 10$ deg is depicted as well. In the latter case, the resonance wavelength was situated at $\lambda = 270$ nm.

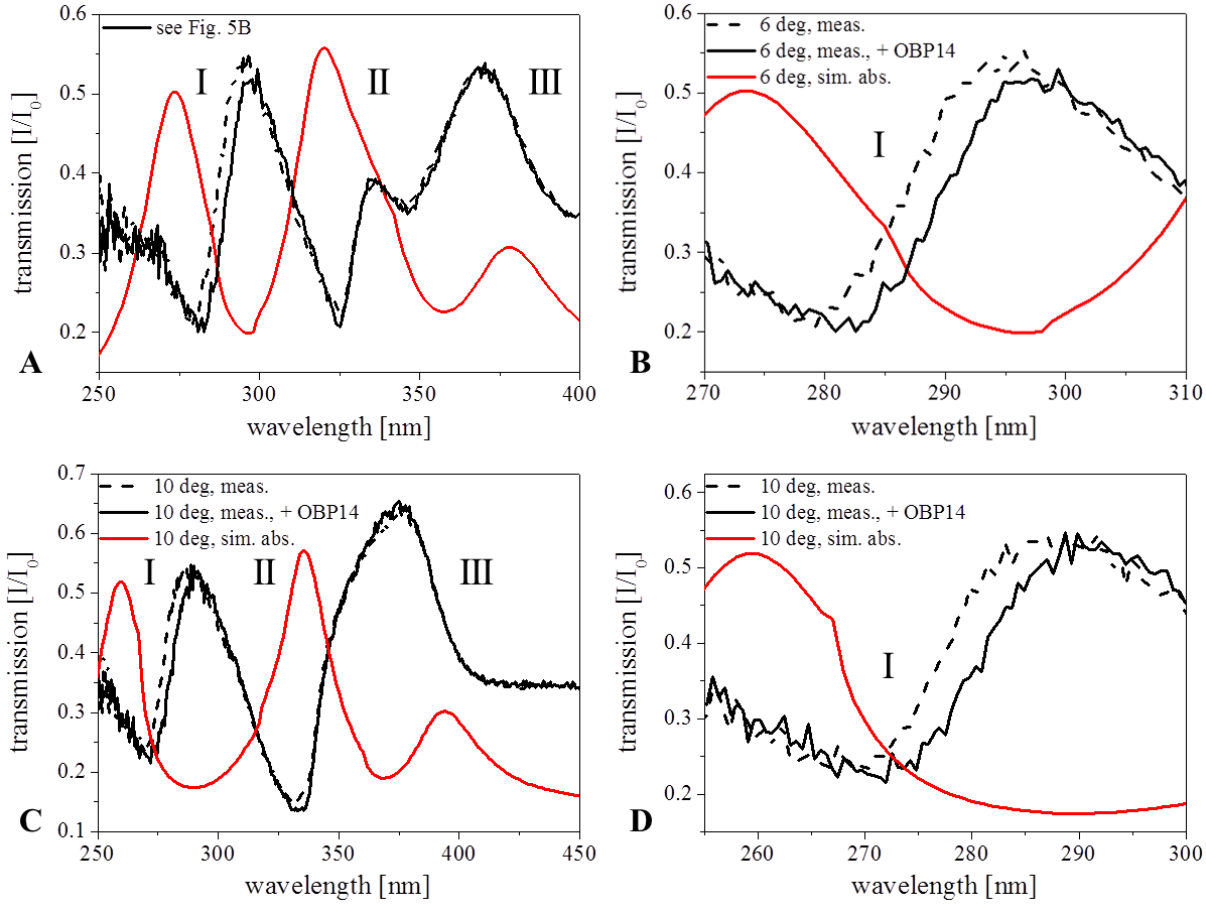

Figure 9.6: Transmission spectra at 280 and 270 nm, respectively, before and after protein attachment. The displayed spectra are cross-sections of the respective 3D matrix. Transmission spectra are shown for $\theta = 6$ (A, B) and 10 deg (C, D) before (dashed black line) and after (solid black line) protein attachment, respectively. Absorption simulations are depicted in addition (red lines). The roman digits are explained in the text. In B and D, magnifications of the spectral regions of interest are displayed. Figure published in Geiss *et al.*, 2017c [339].

In the spectra displayed in Fig. 9.6, three plasmonic features could be observed, consecutively numbered by means of roman digits. Absorption simulation spectra are shown in addition (red lines) to correlate the spectral features to the plasmonic ones described before. The positions did not exactly match, but are considered as close enough to confirm the plasmonic nature of the intensity dips. Possible reasons for deviations were indicated above. The dip assigned to the

absorption peak slightly below λ = 400 nm was, as aforementioned, not to observe due to unknown reasons. A shift could be observed only at position I, which is well in accordance with theory, because feature No. I was the only one exclusively resulting from the sample side SP, at the interface of which the attachment and thus the change in the refractive index took place. Feature No. III is assigned to the aluminum/amonil interface, where no change had occurred. Feature No. II was assigned to a mixture of both, being superimposed in the spectra. Since both interfaces contributed, a small change was not considered as unlikely, but it did not occur, nevertheless possibly due to the superimposition with the unaltered aluminum/amonil interface.

Coming back to the outlook of exploiting the DNA auto-fluorescence, the binding of OBP14 at a wavelength as low as λ = 260 nm was carried out (Fig. 9.7).

The spectral shift of about 3-4 nm is similar to measurements done by other groups that were utilizing diffraction-coupled SPR spectroscopy in the red part of the electromagnetic spectrum [250]. Using a protein of similar molecular mass, Adam and co-workers correlated this spectral shift with densely packed immobilized proteins, indicating that OBP14 was bound to the sensor chip surface to a greater extent. A differentiation between specifically bound and nonspecifically adsorbed OBP14 was not done within this work. The experiments prove that SPR measurements in the UV range below 350 nm with samples bound to an aqueous environment are possible by employing grating coupled SPR spectroscopy using aluminum for resonant excitation.

As mentioned before, limitations in direction of vacuum-UV were likely only due to the lamp intensity that became very weak at around 250 nm. Despite, resonance wavelength at 250 and 260 nm, although being affected by noise, were still possible to indicate as depicted in Figure 9.7.

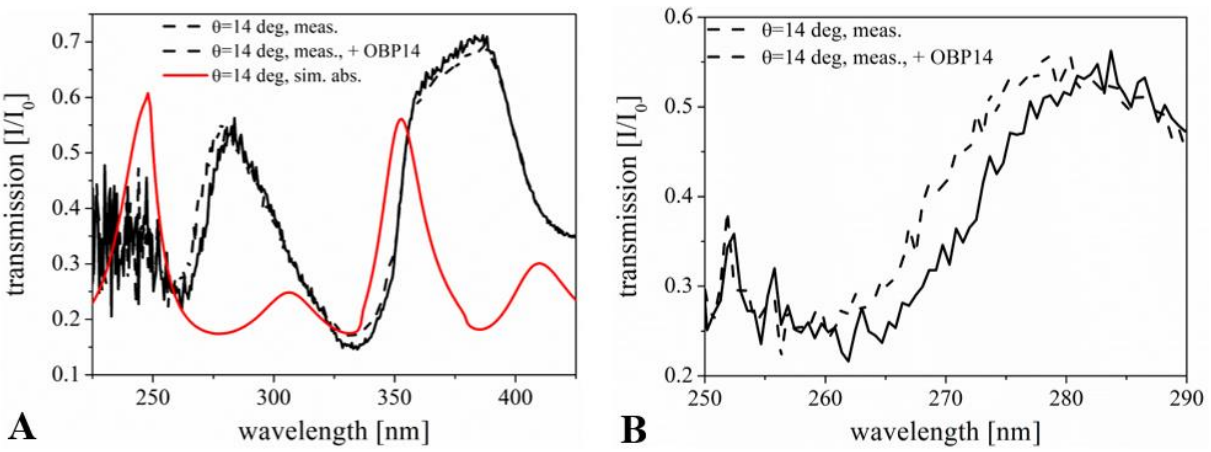

Figure 9.7: Protein shift at λ = 260 nm. The cross-section at an angle of incidence of θ = 14 deg is shown. For further description, please see Fig. 9.6.

The measurement at an angle of incidence of $\theta = 14$ deg (Fig. 9.7), corresponding to a resonance wavelength of $\lambda = 260$ nm for the -1st diffraction order-mediated SP_s, showed slightly larger deviations from the simulated absorption spectra, but was still considered to be in good accordance, attributing the differences to discrepancies between the idealized simulated and the actual grating structure. Nevertheless, a spectral shift due to protein binding comparable to the one described in terms of Fig. 9.6 could be observed, indicating a possible usability of the applied corrugation as low as $\lambda = 260$ nm. Below, at around $\lambda = 250$ nm, the noise becomes prevalent, which is likely due to the low lamp intensity at such low wavelength. Theoretically, the employed grating structure should be able to serve notably below that limit.

All in all, the possibility of detecting binding events in an aqueous environment by means of resonant SP excitation in the UV spectral range was shown to be possible. Further measurements towards the implementation of auto-fluorescence-based measurements regarding proteins and DNA (or aflatoxins, artificial odorants etc.) were not performed due to temporal limitations. These future perspectives require a more demanding setup, and might be challenging because of the low quantum yields of proteins [325] and DNA [323] (which contain, on the other hand, several to lots of fluorophores). Thus, a further enhancement via localized surface plasmons could turn out to be necessary, which is again rather common in the visible to infrared part of the spectrum [249], but was reported utilizing aluminum in the UV range as well [256, 328, 330]. Measurements of DNA and protein auto-fluorescence measurements in their native aqueous environment could also be considered as continuation of former works dealing with plasmonically amplified fluorescence of amino acid and nucleobase analogs taken up in polyvinyl alcohol (PVA) layers [254, 330, 331].

The results were published in the journal *Proceedings of SPIE* (herein referred to as Geiss *et al.*, 2017c). The publication is presented in the following.

F. A. GEISS, S. FOSSATI, I. KHAN, N. GISBERT QUILIS, W. KNOLL, AND J. DOSTALEK: **UV-SPR biosensor for biomolecular interaction studies**. *Proceedings of SPIE* 10231 (2017) 1023107. doi: 10.1117/12.2265683

Publication VI

<content not available in online version>

<content not available in online version>

<content not available in online version>

<content not available in online version>

<content not available in online version>

<content not available in online version>

<content not available in online version>

<content not available in online version>

Chapter 10 *Summary & Outlook*

UV-SPR excitation at an interface to water is of interest because of corresponding absorption bands of biological species like proteins ($\lambda \approx 280$ nm) and DNA ($\lambda \approx 260$ nm), whose auto-fluorescence could be exploited in terms of SPFS. Moreover, the absorbance of species like aflatoxins ($\lambda \approx 265$ nm) or fluorescent odorant analogues ($\lambda \geq 315$ nm), which recently attracted interest, are spectrally situated within the UV spectral region.

The implementation of SPR measurements in an aqueous environment in the UV spectral range is accompanied with certain difficulties: The mainly used SPR metals gold and silver cannot be employed below 550 and 400 nm, respectively. Moreover, the commonly applied ATR-coupling is not possible to realize for interfaces of metals with the native, therefore aqueous environment of biological species, since the required high-refractive index glasses are strongly absorbing at such low wavelengths and the suitable fused silica does not provide a sufficient refractive index.

Here, a crossed aluminum grating with a corrugation period of $\Lambda = 200$ nm is presented to overcome the aforementioned limitations by means of grating-coupled SPR spectroscopy. Using the water-soluble odorant-binding protein 14 of the *Apis mellifera* (honey bee), attached to the alumina layer on top via a silane-based Ni-NTA linker, a change of the resonance wavelengths could be shown for the wavelengths 260, 270, and 280 nm, evidencing the possibility of resonantly excite surface plasmons by UV light at a metal/buffer interface.

Subsequent to this basic proof of principle, plasmonic amplification of the native protein auto-fluorescence would be a reasonable next step. Exhibiting a low quantum yield, this further step would likely require even higher enhancement factors, which could be solved by replacing the continuous sinusoidal corrugation by nanostructures capable of localized surface plasmon excitation. Further, the aforementioned aim could be extended towards DNA and other species.

This future perspective would also continue former works of other groups that proved the possibility of auto-fluorescence detection of amino acid and nucleobase analogs, but within PVA layers instead of a native aqueous environment.

IV Directories

A References

[1] M. NIČ; J. JIRÁT; B. KOŠATA; A. JENKINS; A. MCNAUGHT: **IUPAC Compendium of Chemical Terminology: The Gold Book**. *International Union of Pure and Applied Chemistry (IUPAC)*, 2009. Accessed from: http://goldbook.iupac.org/html/L/L03571.html [last accessed: March 17, 2018].

[2] B. ALBERTS, A. JOHNSON, J. LEWIS, M. RAFF, K. ROBERTS, AND P. WALTER: **Molecular Biology of the Cell**, 4th edition. Garland Science, New York, NY, 2002. ISBN: 0815332181.

[3] D. SADAVA, D. M. HILLIS, H. C. HELLER, AND M. R. BERENBAUM: **Life**: **The Science of Biology**, 9th edition. W. H. Freeman & Company, Gordonsville, VA, 2011. ISBN: 1429246464.

[4] F. ULLMANN: **Ullmann's Encyclopedia of Industrial Chemistry**, 6th edition. Wiley-VCH, New York, NY, 2000. ISBN: 3527306730.

[5] T. E. ANDREOLI, J. F. HOFFMAN, D. D. FANESTIL, AND S. G. SCHULTZ: **Membrane Physiology**, 2nd edition. Springer, Boston, MA, 1987. ISBN: 9780306426971.

[6] J. RIGAUDY AND S. P. KLESNEY: **Nomenclature of Organic Chemistry**, 4th edition. *International Union of Pure and Applied Chemistry (IUPAC)*. Pergamon Press, Oxford, 1979. ISBN: 0080223699.

[7] H. CURTIS AND S. N. BARNES: **Biology**, 5th edition. W. H. Freeman & Company, New York, NY, 1989. ISBN: 9780879013943.

[8] R. HINE: **The Facts on File Dictionary of Biology**, 3rd edition. Checkmark Books, New York, NY, 1999. ISBN: 9780816039081.

[9] P. W. KUCHEL AND G. B. RALSTON: **Theory and Problems of Biochemistry**. McGraw-Hill, New York, NY, 1988. ISBN: 9780070355798.

[10] J. E. JOHNSON AND R. B. CORNELL: **Amphitropic proteins: regulation by reversible membrane interactions (Review)**. *Molecular Membrane Biology* 16 (1999) pp. 217–235. doi: 10.1080/096876899294544.

[11] ENCYCLOPÆDIA BRITANNICA, 15th edition. Chicago, IL, 2007. ISBN: 1593392923.

[12] S. J. SINGER AND G. L. NICOLSON: **The Fluid Mosaic Model of the Structure of Cell Membranes**. *Science* 175 (1972) pp. 720–731. doi: 10.1126/science.175.4023.720.

[13] K. BRAECKMANS, L. PEETERS, N. N. SANDERS, S. C. de SMEDT, AND J. DEMEESTER: **Three-Dimensional Fluorescence Recovery after Photobleaching with the Confocal Scanning Laser Microscope**. *Biophysical Journal* 85 (2003) pp. 2240–2252. doi: 10.1016/S0006-3495(03)74649-9.

[14] M. PHILPOTT, C. M. ROGERS, C. YAPP, C. WELLS, J.-P. LAMBERT, C. STRAIN-DAMERELL, N. A. BURGESS-BROWN, A.-C. GINGRAS, S. KNAPP, AND S. MÜLLER: **Assessing cellular efficacy of bromodomain inhibitors using fluorescence recovery after photobleaching**. *Epigenetics & Chromatin* 7:14 (2014). doi: 10.1186/1756-8935-7-14.

[15] H. OHVO-REKILÄ, B. RAMSTEDT, P. LEPPIMÄKI, AND J. P. SLOTTE: **Cholesterol interactions with phospholipids in membranes**. *Progress in Lipid Research* 41 (2002) pp. 66–97. doi: 10.1016/S0163-7827(01)00020-0.

[16] J. M. BERG, J. L. TYMOCZKO, AND L. STRYER: **Biochemistry**, 7th edition. W. H. Freeman & Company, New York, NY, 2011. ISBN: 9781429276351.

[17] M. THOMPSON AND U. J. KRULL: **The electroanalytical response of the bilayer lipid membrane to valinomycin: membrane cholesterol content**. *Analytica Chimica Acta* 141 (1982) pp. 33–47. doi: 10.1016/S0003-2670(01)95308-5.

[18] J. KRAICER AND S. J. DIXON: **Measurement and Manipulation of Intracellular Ions**. Academic Press, San Diego, CA, 1995. ISBN: 9781281056856.

[19] P. JOHN AND F. R. WHATLEY: ***Paracoccus denitrificans* and the evolutionary origin of the mitochondrion**. *Nature* 254 (1975) pp. 495. doi: 10.1038/254495a0.

[20] T. GABALDÓN AND M. A. HUYNEN: **Reconstruction of the Proto-Mitochondrial Metabolism**. *Science* 301 (2003) pp. 609. doi: 10.1126/science.1085463.

[21] M. SARASTE: **Oxidative Phosphorylation at the *fin de siècle***. *Science* 283 (1999) pp. 1488–1493. doi: 10.1126/science.283.5407.1488.

[22] I. BELEVICH: **Proton Translocation Coupled to Electron Transfer Reactions in Terminal Oxidases**. PhD thesis, University of Helsinki, 2007.

[23] M. WIKSTRÖM: **Two protons are pumped from the mitochondrial matrix per electron transferred between NADH and ubiquinone**. *FEBS Letters* 169 (1984) pp. 300–304. doi: 10.1016/0014-5793(84)80338-5.

[24] A. V. BOGACHEV, R. A. MURTAZINA, AND V. P. SKULACHEV: **H^+/e^- Stoichiometry for NADH Dehydrogenase I and Dimethyl Sulfoxide Reductase in Anaerobically Grown *Escherichia coli C*ells**. *Journal of Bacteriology* 178 (1996) pp. 6233–6237. doi: 10.1128/jb.178.21.6233-6237.1996.

[25] M. WIKSTRÖM, K. KRAB, AND V. SHARMA: **Oxygen Activation and Energy Conservation by Cytochrome *c* Oxidase**. *Chemical Reviews* 118 (2018) pp. 2469–2490. doi: 10.1021/acs.chemrev.7b00664.

[26] Y. HATEFI: **The Mitochondrial Electron Transport and Oxidative Phosphorylation System**. *Annual Review of Biochemistry* 54 (1985) pp. 1015–1069. doi: 10.1146/annurev.bi.54.070185.005055.

[27] M. I. VERKHOVSKY AND A. V. BOGACHEV: **Sodium-translocating NADH:quinone oxidoreductase as a redox-driven ion pump**. *Biochimica et Biophysica Acta* 1797 (2010) pp. 738–746. doi: 10.1016/j.bbabio.2009.12.020.

[28] N. P. BELEVICH, Y. V. BERTSOVA, M. L. VERKHOVSKAYA, A. A. BAYKOV, AND A. V. BOGACHEV: **Identification of the coupling step in Na^+-translocating NADH:quinone oxidoreductase from real-time kinetics of electron transfer**. *Biochimica et Biophysica Acta* 1857 (2016) pp. 141–149. doi: 10.1016/j.bbabio.2015.12.001.

[29] P. MITCHELL: **Protonmotive redox mechanism of the cytochrome *b*-c_1 complex in the respiratory chain: Protonmotive ubiquinone cycle**. *FEBS Letters* 56 (1975) pp. 1–6. doi: 10.1016/0014-5793(75)80098-6.

[30] H.-W. HELDT AND B. PIECHULLA: **Pflanzenbiochemie**, 4th edition. Spektrum Akademischer Verlag, Heidelberg, 2008. ISBN: 3827413303.

[31] I. BERTINI, G. CAVALLARO, AND A. ROSATO: **Cytochrome *c*: Occurrence and Functions**. *Chemical Reviews* 106 (2006) pp. 90–115. doi: 10.1021/cr050241v.

[32] W. M. FITCH: **The molecular evolution of cytochrome *c* in eukaryotes**. *Journal of Molecular Evolution* 8 (1976) pp. 13–40. doi: 10.1007/BF01738880.

[33] N. MIRKIN, J. JACONCIC, V. STOJANOFF, AND A. MORENO: **High resolution X-ray crystallographic structure of bovine heart cytochrome *c* and its application to the design of an electron transfer biosensor**. *Proteins: Structure, Function, and Bioinformatics* 70 (2008) pp. 83–92. doi: 10.1002/prot.21452.

[34] Y. ANRAKU AND R. B. GENNIS: **The aerobic respiratory chain of *Escherichia coli***. *Trends in Biochemical Sciences* 12 (1987) pp. 262–266. doi: 10.1016/0968-0004(87)90131-9.

[35] J. A. GARCÍA-HORSMAN, B. BARQUERA, J. RUMBLEY, J. MA, AND R. B. GENNIS: **The Superfamily of Heme-Copper Respiratory Oxidases**. *Journal of Bacteriology* 176 (1994) pp. 5587–5600.

[36] A. HARRENGA AND H. MICHEL: **The Cytochrome *c* Oxidase from *Paracoccus denitrificans* Does Not Change the Metal Center Ligation upon Reduction**. *Journal of Biological Chemistry* 274 (1999) pp. 33296–33299. doi: 10.1074/jbc.274.47.33296.

[37] I. BELEVICH: **Homepage of Molecular Physics Group, University of Helsinki**: http://www.biocenter.helsinki.fi/bi/biophys/research_CcO.html [last accessed: November 25, 2017].

[38] I. BELEVICH, D. A. BLOCH, N. BELEVICH, M. WIKSTRÖM, AND M. I. VERKHOVSKY: **Exploring the proton pump mechanism of cytochrome *c* oxidase in real time**. *Proceedings of the National Academy of Sciences of the United States of America* 104 (2007) pp. 2685–2690. doi: 10.1073/pnas.0608794104.

[39] O. FARVER, E. GRELL, B. LUDWIG, H. MICHEL, AND I. PECHT: **Rates and Equilibrium of Cu_A to heme *a* electron transfer in *Paracoccus denitrificans* cytochrome *c* oxidase**. *Biophysical Journal* 90 (2006) pp. 2131–2137. doi: 10.1529/biophysj.105.075440.

[40] S. IWATA, C. OSTERMEIER, B. LUDWIG, AND H. MICHEL: **Structure at 2.8 Å resolution of cytochrome *c* oxidase from *Paracoccus denitrificans***. *Nature* 376 (1995) pp. 660-669. doi: 10.1038/376660a0.

[41] T. TSUKIHARA, H. AOYAMA, E. YAMASHITA, T. TOMIZAKI, H. YAMAGUCHI, K. SHINZAWA-ITOH, R. NAKASHIMA, R. YAONO, AND S. YOSHIKAWA: **The Whole Structure of the 13-Subunit Oxidized Cytochrome *c* Oxidase at 2.8 Å**. *Science* 272 (1996) pp. 1136–1144. doi: 10.1126/science.272.5265.1136.

[42] M. SVENSSON-EK, J. ABRAMSON, G. LARSSON, S. TÖRNROTH, P. BRZEZINSKI, AND S. IWATA: **The X-ray Crystal Structures of Wild-type and EQ(I-286) Mutant Cytochrome *c* Oxidases from *Rhodobacter sphaeroides***. *Journal of Molecular Biology* 321 (2002) pp. 329–339. doi: 10.1016/S0022-2836(02)00619-8.

[43] MESH MEDICAL SUBJECT HEADINGS DESCRIPTOR DATA: **Cytochromes**. *U. S. National Library of Medicine*, 2018. Accessed from: https://meshb.nlm.nih.gov/record/ui?name=Cytochromes [last accessed: March 03, 2018].

[44] M. R. BRATTON, M. A. PRESSLER, AND J. P. HOSLER: **Suicide Inactivation of Cytochrome *c* Oxidase: Catalytic Turnover in the Absence of Subunit III Alters the Active Site**. *Biochemistry* 38 (1999) pp. 16236–16245. doi: 10.1021/bi9914107.

[45] G. GILDERSON, L. SALOMONSSON, A. AAGAARD, J. GRAY, P. BRZEZINSKI, AND J. HOSLER: **Subunit III of Cytochrome *c* Oxidase of *Rhodobacter sphaeroides* Is Required to Maintain Rapid Proton Uptake through the D Pathway at Physiologic pH**. *Biochemistry* 42 (2003) pp. 7400–7409. doi: 10.1021/bi0341298.

[46] J. P. HOSLER: **The influence of subunit III of cytochrome *c* oxidase on the D pathway, the proton exit pathway and mechanism-based inactivation in subunit I**. *Biochimica et Biophysica Acta* 1655 (2004) pp. 332–339. doi: 10.1016/j.bbabio.2003.06.009.

[47] J. P. SHAPLEIGH AND R. B. GENNIS: **Cloning, sequencing and deletion from the chromosome of the gene encoding subunit I of the *aa*$_3$-type cytochrome *c* oxidase of *Rhodobacter sphaeroides***. *Molecular Microbiology* 6 (1992) pp. 635–642. doi: 10.1111/j.1365-2958.1992.tb01511.x.

[48] J. CAO, J. SHAPLEIGH, R. GENNIS, A. REVZIN, AND S. FERGUSON-MILLER: **The gene encoding cytochrome *c* oxidase subunit II from *Rhodobacter sphaeroides*; comparison of the deduced amino acid sequence with sequences of corresponding peptides from other species**. *Gene* 101 (1991) pp. 133–137. doi: 10.1016/0378-1119(91)90235-4.

[49] J. CAO, J. HOSLER, J. SHAPLEIGH, A. REVZIN, AND S. FERGUSON-MILLER: **Cytochrome *aa*$_3$ of *Rhodobacter sphaeroides* as a Model for Mitochondrial Cytochrome *c* Oxidase**. *Journal of Biological Chemistry* 267 (1992) pp. 24273-24278.

[50] B. KADENBACH AND M. HÜTTEMANN: **The subunit composition and function of mammalian cytochrome *c* oxidase**. *Mitochondrion* 24 (2015) pp. 64–76. doi: 10.1016/j.mito.2015.07.002.

[51] E. SEDLÁK AND N. C. ROBINSON: **Destabilization of the Quaternary Structure of Bovine Heart Cytochrome *c* Oxidase upon Removal of Tightly Bound Cardiolipin**. *Biochemistry* 54 (2015) pp. 5569–5577. doi: 10.1021/acs.biochem.5b00540.

[52] B. CHANCE, C. SARONIO, AND J. S. LEIGH: **Functional Intermediates in the Reaction of Membrane-bound Cytochrome Oxidase with Oxygen**. *Journal of Biological Chemistry* 250 (1975) pp. 9226–9237.

[53] I. BELEVICH AND M. I. VERKHOVSKY: **Molecular mechanism of proton translocation by cytochrome *c* oxidase**. *Antioxidants & Redox Signaling* 10 (2008) pp. 1–29. doi: 10.1089/ars.2007.1705.

[54] M. WIKSTRÖM: **Active site intermediates in the reduction of O_2 by cytochrome oxidase, and their derivatives**. *Biochimica et Biophysica Acta* 1817 (2012) pp. 468–475. doi: 10.1016/j.bbabio.2011.10.010.

[55] D. BLOCH, I. BELEVICH, A. JASAITIS, C. RIBACKA, A. PUUSTINEN, M. I. VERKHOVSKY, AND M. WIKSTRÖM: **The catalytic cycle of cytochrome *c* oxidase is not the sum of its two halves**. *Proceedings of the National Academy of Sciences of the United States of America* 101 (2004) pp. 529–533. doi: 10.1073/pnas.0306036101.

[56] V. R. I. KAILA, M. I. VERKHOVSKY, AND M. WIKSTRÖM: **Proton-Coupled Electron Transfer in Cytochrome Oxidase**. *Chemical Reviews* 110 (2010) pp. 7062–7081. doi: 10.1021/cr1002003.

[57] H. WITT, V. ZICKERMANN, AND B. LUDWIG: **Site-directed mutagenesis of cytochrome *c* oxidase reveals two acidic residues involved in the binding of cytochrome *c***. *Biochimica et Biophysica Acta* 1230 (1995) pp. 74–76.

[58] W. H. VANNESTE, M. YSEBAERT-VANNESTE, AND H. S. MASON: **The Decline of Molecular Activity of Cytochrome Oxidase during Purification**. *Journal of Biological Chemistry* 249 (1974) pp. 7390–7401.

[59] S. E. BRAND, S. RAJAGUKGUK, K. GANESAN, L. GEREN, M. FABIAN, D. HAN, R. B. GENNIS, B. DURHAM, AND F. MILLETT: **A New Ruthenium Complex to Study Single-Electron Reduction of the Pulsed O_H State of Detergent-Solubilized Cytochrome Oxidase**. *Biochemistry* 46 (2007) pp. 14610–14618. doi: 10.1021/bi701424d.

[60] C. NOWAK, M. G. SANTONICOLA, D. SCHACH, J. ZHU, R. B. GENNIS, S. FERGUSON-MILLER, D. BAURECHT, D. WALZ, W. KNOLL, AND R. L. C. NAUMANN: **Conformational transitions and molecular hysteresis of cytochrome c oxidase: Varying the redox state by electronic wiring**. *Soft Matter* 6 (2010) pp. 5523. doi: 10.1039/c0sm00160k.

[61] T. VYGODINA AND A. KONSTANTINOV: **Effect of pH on the spectrum of cytochrome *c* oxidase hydrogen peroxide complex**. *Biochimica et Biophysica Acta* 973 (1989) pp. 390–398. doi: 10.1016/S0005-2728(89)80380-9.

[62] D. ZASLAVSKY, R. C. SADOSKI, S. RAJAGUKGUK, L. GEREN, F. MILLETT, B. DURHAM, AND R. B. GENNIS: **Direct measurement of proton release by cytochrome *c* oxidase in solution during the F→O transition**. *Proceedings of the National Academy of Sciences of the United States of America* 101 (2004) pp. 10544–10547. doi: 10.1073/pnas.0401521101.

[63] S. YOSHIKAWA AND A. SHIMADA: **Reaction Mechanism of Cytochrome *c* Oxidase**. *Chemical Reviews* 115 (2015) pp. 1936–1989. doi: 10.1021/cr500266a.

[64] S. RIISTAMA, A. PUUSTINEN, A. GARCÍA-HORSMAN, S. IWATA, H. MICHEL, AND M. WIKSTRÖM: **Channelling of dioxygen into the respiratory enzyme**. *Biochimica et Biophysica Acta* 1275 (1996) pp. 1–4. doi: 10.1016/0005-2728(96)00040-0.

[65] S. RIISTAMA, A. PUUSTINEN, M. I. VERKHOVSKY, J. E. MORGAN, AND M. WIKSTRÖM: **Binding of O_2 and Its Reduction Are Both Retarded by Replacement of Valine 279 by Isoleucine in Cytochrome *c* Oxidase from *Paracoccus denitrificans***. *Biochemistry* 39 (2000) pp. 6365–6372. doi: 10.1021/bi000123w.

[66] I. HOFACKER AND K. SCHULTEN: **Oxygen and Proton Pathways in Cytochrome c Oxidase**. *Proteins: Structure, Function, and Genetics* 30 (1998) pp. 100–107.

[67] T. H. HAINES AND N. A. DENCHER: **Cardiolipin: a proton trap for oxidative phosphorylation**. *FEBS Letters* 528 (2002) pp. 35–39. doi: 10.1016/S0014-5793(02)03292-1.

[68] G. PLUSCHKE, Y. HIROTA, AND P. OVERATH: **Function of phospholipids in *Escherichia coli***. *Journal of Biological Chemistry* 253 (1978) pp. 5048–5055.

[69] F. JIANG, H. S. RIZAVI, AND M. L. GREENBERG: **Cardiolipin is not essential for the growth of *Saccharomyces cerevisiae* on fermentable or non-fermentable carbon sources**. *Molecular Microbiology* 26 (1997) pp. 481–491. doi: 10.1046/j.1365-2958.1997.5841950.x.

[70] E. M. LOHMEIER-VOGEL, K. T. LEUNG, H. LEE, J. T. TREVORS, AND H. J. VOGEL: **Phosphorus-31 Nuclear Magnetic Resonance Study of the Effect of Pentachlorophenol (PCP) on the Physiologies of PCP-Degrading Microorganisms**. *Applied and Environmental Microbiology* 67 (2001) pp. 3549–3556. doi: 10.1128/AEM.67.8.3549-3556.2001.

[71] C. ARNAREZ, S. J. MARRINK, AND X. PERIOLE: **Molecular mechanism of cardiolipin-mediated assembly of respiratory chain supercomplexes**. *Chemical Science* 7 (2016) pp. 4435–4443. doi: 10.1039/C5SC04664E.

[72] J. KOOLMAN AND K.-H. RÖHM: **Color Atlas of Biochemistry**, 2nd edition. Thieme, Stuttgart, 2005. ISBN: 3131003723.

[73] R. K. PORTER: **Uncoupling protein 1: a short-circuit in the chemiosmotic process**. *Journal of Bioenergetics and Biomembranes* 40 (2008) pp. 457. doi: 10.1007/s10863-008-9172-8.

[74] C. C. O'NEAL AND P. D. BOYER: **Assessment of the Rate of Bound Substrate Interconversion and of Assessment of the Rate of Bound Substrate Interconversion and of ATP Acceleration of Product Release during Catalysis by Mitochondrial Adenosine Triphosphatase**. *Journal of Biological Chemistry* 259 (1984) pp. 5761–5767.

[75] S. D. STROOP AND P. D. BOYER: **Characteristics of the chloroplast ATP synthase as revealed by reaction at low ADP concentrations**. *Biochemistry* 24 (1985) pp. 2304–2310. doi: 10.1021/bi00330a027.

[76] P. D. BOYER: **The Unusual Enzymology of ATP Synthase**. *Biochemistry* 26 (1987) pp. 8503–8507.

[77] J. E. WALKER, M. SARASTE, M. J. RUNSWICK, AND N. J. GAY: **Distantly related sequences in the alpha- and beta-subunits of ATP synthase, myosin, kinases and other ATP-requiring enzymes and a common nucleotide binding fold**. *EMBO Journal* 1 (1982) pp. 945–951. doi: 10.1002/j.1460-2075.1982.tb01276.x.

[78] J. E. WALKER, I. M. FEARNLEY, N. J. GAY, B. W. GIBSON, F. D. NORTHROP, S. J. POWELL, M. J. RUNSWICK, M. SARASTE, AND V.L.J. TYBULEWICZ: **Primary structure and subunit stoichiometry of F_1-ATPase from bovine mitochondria**. *Journal of Molecular Biology* 184 (1985) pp. 677–701. doi: 10.1016/0022-2836(85)90313-4.

[79] J. C. SKOU: **The influence of some cations on an adenosine triphosphatase from peripheral nerves**. *Biochimica et Biophysica Acta* 23 (1957) pp. 394–401. doi: 10.1016/0006-3002(57)90343-8.

[80] A. G. STEWART, L. K. LEE, M. DONOHOE, J. J. CHASTON, AND D. STOCK: **The dynamic stator stalk of rotary ATPases**. *Nature Communications* 3 (2012) pp. 1–8. doi: 10.1038/ncomms1693.

[81] D. OKUNO, R. IINO, AND H. NOJI: **Rotation and structure of F_oF_1-ATP synthase**. *Journal of Biochemistry* 149 (2011) pp. 655–664. doi: 10.1093/jb/mvr049.

[82] R. H. GARRETT AND C. M. GRISHAM: **Biochemistry**, 3rd edition. Thomson Brooks/Cole, Belmont, CA, 2005. ISBN: 0534410200.

[83] R. K. PORTER AND M. D. BRAND: **Mitochondrial proton conductance and $H^+/0$ ratio are independent of electron transport rate in isolated hepatocytes**. *Biochemical Journal* 310 (1995) pp. 379–382. doi: 10.1042/bj3100379.

[84] P. MITCHELL: **Chemiosmotic coupling in energy transduction: A logical development of biochemical knowledge**. *Journal of Bioenergetics and Biomembranes* 3 (1972) pp. 5–24. doi: 10.1007/BF01515993.

[85] G. FUCHS AND H. G. SCHLEGEL: **Allgemeine Mikrobiologie**, 8th edition. Thieme, Stuttgart, 2006. ISBN: 9783134446081.

[86] B. BOLGIANO, L. SMITH, AND H. C. DAVIES: **Kinetics of the interaction of the cytochrome c oxidase of *Paracoccus denitrificans* with its own and bovine cytochrome *c***. *Biochimica et Biophysica Acta* 933 (1988) pp. 341–350. doi: 10.1016/0005-2728(88)90041-2.

[87] C. SUN, A.-M. CAREY, B.-R. GAO, C. A. WRAIGHT, N. W. WOODBURY, AND S. LIN: **Ultrafast Electron Transfer Kinetics in the LM Dimer of Bacterial Photosynthetic Reaction Center from *Rhodobacter sphaeroides***. *Journal of Physical Chemistry B* 120 (2016) pp. 5395–5404. doi: 10.1021/acs.jpcb.6b05082.

[88] S. LIN, P. R. JASCHKE, H. WANG, M. PADDOCK, A. TUFTS, J. P. ALLEN, F. I. ROSELL, A. G. MAUK, N. W. WOODBURY, AND J. T. BEATTY: **Electron transfer in the *Rhodobacter sphaeroides* reaction center assembled with zinc bacteriochlorophyll**. *Proceedings of the National Academy of Sciences of the United States of America* 106 (2009) pp. 8537–8542. doi: 10.1073/pnas.0812719106.

[89] A. R. CROFTS, J. T. HOLLAND, D. VICTORIA, D. R. J. KOLLING, S. A. DIKANOV, R. GILBRETH, S. LHEE, R. KURAS, AND M. G. KURAS: **The Q-cycle reviewed: How well does a monomeric mechanism of the *bc*$_1$ complex account for the function of a dimeric complex?** *Biochimica et Biophysica Acta* 1777 (2008) pp. 1001–1019. doi: 10.1016/j.bbabio.2008.04.037.

[90] A. R. CROFTS, S. HONG, C. WILSON, R. BURTON, D. VICTORIA, C. HARRISON, AND K. SCHULTEN: **The mechanism of ubihydroquinone oxidation at the Q$_o$-site of the cytochrome *bc*$_1$ complex**. *Biochimica et Biophysica Acta* 1827 (2013) pp. 1362–1377. doi: 10.1016/j.bbabio.2013.01.009.

[91] G. RICHTER: **Stoffwechselphysiologie der Pflanzen**, 6th edition. Thieme, Stuttgart, 1998. ISBN: 9783134420067.

[92] J. KOEPKE, E.-M. KRAMMER, A. R. KLINGEN, P. SEBBAN, G. M. ULLMANN, AND G. FRITZSCH: **pH Modulates the Quinone Position in the Photosynthetic Reaction Center from *Rhodobacter sphaeroides* in the Neutral and Charge Separated States**. *Journal of Molecular Biology* 371 (2007) pp. 396–409. doi: 10.1016/j.jmb.2007.04.082.

[93] F. L. MULLER, Y. LIU, AND H. VAN REMMEN: **Complex III Releases Superoxide to Both Sides of the Inner Mitochondrial Membrane**. *Journal of Biological Chemistry* 279 (2004) pp. 49064–49073. doi: 10.1074/jbc.M407715200.

[94] A. R. CROFTS, S. W. ROSE, R. L. BURTON, A. V. DESAI, P. J. A. KENIS, AND S. A. DIKANOV: **The Q-Cycle Mechanism of the *bc*$_1$ Complex: A Biologist's Perspective on Atomistic Studies**. *Journal of Physical Chemistry B* 121 (2017) pp. 3701–3717. doi: 10.1021/acs.jpcb.6b10524.

[95] E. A. BERRY, L.-S. HUANG, L. K. SAECHAO, N. G. PON, M. VALKOVA-VALCHANOVA, AND F. DALDAL: **X-Ray Structure of *Rhodobacter Capsulatus* Cytochrome *bc*$_1$: Comparison with its Mitochondrial and Chloroplast Counterparts**. *Photosynthesis Research* 81 (2004) pp. 251–275.

[96] R. E. BLANKENSHIP, M. T. MADIGAN, AND C. E. BAUER: **Anoxygenic Photosynthetic Bacteria**. Springer, New York, NY, 2006. ISBN: 9780306479540.

[97] K. MUNK: **Mikrobiologie**. Thieme, Stuttgart, 2008. ISBN: 9783131448613.

[98] W. R. LEIFERT, A. L. ALOIA, O. BUCCO, R. V. GLATZ, AND E. J. MCMURCHIE: **G-Protein-Coupled Receptors in Drug Discovery: Nanosizing Using Cell-Free Technologies and Molecular Biology Approaches**. *Journal of Biomolecular Screening* 10 (2005) pp. 765–779. doi: 10.1177/1087057105280517.

[99] R. ROBELEK, E. S. LEMKER, B. WILTSCHI, V. KIRSTE, R. NAUMANN, D. OESTERHELT, AND E.-K. SINNER: **Incorporation of In Vitro Synthesized GPCR into a Tethered Artificial Lipid Membrane System**. *Angewandte Chemie* 46 (2007) pp. 605–608. doi: 10.1002/anie.200602231.

[100] M. ANTONIETTI AND S. FÖRSTER: **Vesicles and Liposomes: A Self-Assembly Principle Beyond Lipids**. *Advanced Materials* 15 (2003) pp. 1323–1333. doi: 10.1002/adma.200300010.

[101] J. S. DUA, A. C. RANA, AND A. K. BHANDARI: **Liposome: Methods of Preparation and Applications**. *International Journal of Pharmaceutical Studies and Research* 3 (2012) pp. 14–20.

[102] P. MUELLER, D. O. RUDIN, H. T. TIEN, AND W. C. WESCOTT: **Reconstitution of Cell Membrane Structure *in vitro* and its Transformation into an Excitable System**. *Nature* 194 (1962) pp. 979–980. doi: 10.1038/194979a0.

[103] H. T. TIEN, S. CARBONE, AND E. A. DAWIDOWICZ: **Formation of "Black" Lipid Membranes by Oxidation Products of Cholesterol**. *Nature* 212 (1966) pp. 718–719. doi: 10.1038/212718a0.

[104] W. HANKE AND W.-R. SCHLUE: **Planar Lipid Bilayers**: **Methods and Applications**. Academic Press, London, 1993. ISBN: 9780123229946.

[105] E. T. CASTELLANA AND P. S. CREMER: **Solid supported lipid bilayers: From biophysical studies to sensor design**. *Surface Science Reports* 61 (2006) pp. 429–444. doi: 10.1016/j.surfrep.2006.06.001.

[106] H. SCHINDLER: **Formation of planar bilayers from artificial or native membrane vesicles**. *FEBS Letters* 122 (1980) pp. 77–79. doi: 10.1016/0014-5793(80)80405-4.

[107] R. CORONADO AND R. LATORRE: **Phospholipid bilayers made from monolayers on patch-clamp pipettes**. *Biophysical Journal* 43 (1983) pp. 231–236. doi: 10.1016/S0006-3495(83)84343-4.

[108] M. ERAY, N. S. DOGAN, L. LIU, A. R. KOCH, D. F. MOFFETT, M. SILBER, AND B. J. VAN WIE: **Highly stable bilayer lipid membranes (BLMs) formed on microfabricated polyimide apertures**. *Biosensors and Bioelectronics* 9 (1994) pp. 343–351. doi: 10.1016/0956-5663(94)80034-0.

[109] M. MAYER, J. K. KRIEBEL, M. T. TOSTESON, AND G. M. WHITESIDES: **Microfabricated Teflon Membranes for Low-Noise Recordings of Ion Channels in Planar Lipid Bilayers**. *Biophysical Journal* 85 (2003) pp. 2684–2695. doi: 10.1016/S0006-3495(03)74691-8.

[110] N. MALMSTADT, M. A. NASH, R. F. PURNELL, AND J. J. SCHMIDT: **Automated Formation of Lipid-Bilayer Membranes in a Microfluidic Device**. *Nano Letters* 6 (2006) pp. 1961–1965. doi: 10.1021/nl0611034.

[111] H. SUZUKI, K. TABATA, Y. KATO-YAMADA, H. NOJI, AND S. TAKEUCHI: **Planar lipid bilayer reconstitution with a micro-fluidic system**. *Lab on a Chip* 4 (2004) pp. 502–505. doi: 10.1039/B405967K.

[112] W. RÖMER AND C. STEINEM: **Impedance Analysis and Single-Channel Recordings on Nano-Black Lipid Membranes Based on Porous Alumina**. *Biophysical Journal* 86 (2004) pp. 955–965. doi: 10.1016/S0006-3495(04)74171-5.

[113] A. LEITMANNOVA LIU: **Advances in Planar Lipid Bilayers and Liposomes**: **Volume 7**, 1st edition. Academic Press, San Diego, CA, 2008. ISBN: 9780123743084.

[114] O. GASSMANN, M. KREIR, C. AMBROSI, J. PRANSKEVICH, A. OSHIMA, C. RÖLING, G. SOSINSKY, N. FERTIG, AND C. STEINEM: **The M34A mutant of Connexin26 reveals active conductance states in pore-suspending membranes**. *Journal of Structural Biology* 168 (2009) pp. 168–176. doi: 10.1016/j.jsb.2009.02.004.

[115] P. BARTSCH, C. WALTER, P. SELENSCHIK, A. HONIGMANN, AND R. WAGNER: **Horizontal Bilayer for Electrical and Optical Recordings**. *Materials* 5 (2012) pp. 2705–2730. doi: 10.3390/ma5122705.

[116] M. G. FRIEDRICH: **Vibrational Spectroscopic and Electrochemical Investigations of Multi-centered Heme Proteins in Biomimetic Membrane Architectures**. PhD thesis, Johannes Gutenberg University, Mainz, 2007.

[117] F. GIESS, M. G. FRIEDRICH, J. HEBERLE, R. L. NAUMANN, AND W. KNOLL: **The Protein-Tethered Lipid Bilayer: A Novel Mimic of the Biological Membrane**. *Biophysical Journal* 87 (2004) pp. 3213–3220. doi: 10.1529/biophysj.104.046169.

[118] R. P. RICHTER AND A. R. BRISSON: **Following the Formation of Supported Lipid Bilayers on Mica: A Study Combining AFM, QCM-D, and Ellipsometry**. *Biophysical Journal* 88 (2005) pp. 3422–3433. doi: 10.1529/biophysj.104.053728.

[119] V. NEDELKOVSKI, A. SCHWAIGHOFER, C. A. WRAIGHT, C. NOWAK, AND R. L. C. NAUMANN: **Surface-Enhanced Infrared Absorption Spectroscopy (SEIRAS) of Light-Activated Photosynthetic Reaction Centers from *Rhodobacter sphaeroides* Reconstituted in a Biomimetic Membrane System**. *Journal of Physical Chemistry C* 117 (2013) pp. 16357–16363. doi: 10.1021/jp4056347.

[120] C. ROSSI, J. HOMAND, C. BAUCHE, H. HAMDI, D. LADANT, AND J. CHOPINEAU: **Differential Mechanisms for Calcium-Dependent Protein/Membrane Association as Evidenced from SPR-Binding Studies on Supported Biomimetic Membranes**. *Biochemistry* 42 (2003) pp. 15273–15283. doi: 10.1021/bi035336a.

[121] S. HEYSE, T. STORA, E. SCHMID, J. H. LAKEY, AND H. VOGEL: **Emerging techniques for investigating molecular interactions at lipid membranes**. *Biochimica et Biophysica Acta* 1376 (1998) pp. 319–338.

[122] M. TANAKA AND E. SACKMANN: **Polymer-supported membranes as models of the cell surface**. *Nature* 437 (2005) pp. 656–663. doi: 10.1038/nature04164.

[123] W. KNOLL, I. KÖPER, R. NAUMANN, AND E.-K. SINNER: **Tethered bimolecular lipid membranes—A novel model membrane platform**. *Electrochimica Acta* 53 (2008) pp. 6680–6689. doi: 10.1016/j.electacta.2008.02.121.

[124] K. ATAKA, F. GIESS, W. KNOLL, R. NAUMANN, S. HABER-POHLMEIER, B. RICHTER, AND J. HEBERLE: **Oriented Attachment and Membrane Reconstitution of His-Tagged Cytochrome *c* Oxidase to a Gold Electrode: In Situ Monitoring by Surface-Enhanced Infrared Absorption Spectroscopy**. *Journal of the American Chemical Society* 126 (2004) pp. 16199–16206. doi: 10.1021/ja045951h.

[125] B. MAHERANI, E. ARAB-TEHRANY, M. R. MOZAFARI, C. GAIANI, AND M. LINDER: **Liposomes: A Review of Manufacturing Techniques and Targeting Strategies**. *Current Nanoscience* 7 (2011) pp. 436–452. doi: 10.2174/157341311795542453.

[126] P. WALDE, K. COSENTINO, H. ENGEL, AND P. STANO: **Giant Vesicles: Preparations and Applications**. *European Journal of Chemical Biology* 11 (2010) pp. 848–865. doi: 10.1002/cbic.201000010.

[127] A. D. SEZER: **Recent Advances in Novel Drug Carrier Systems**. IntechOpen, London, 2012. ISBN: 978-953-51-0810-8.

[128] E. FLEIGE, M. A. QUADIR, AND R. HAAG: **Stimuli-responsive polymeric nanocarriers for the controlled transport of active compounds: Concepts and applications**. *Advanced Drug Delivery Reviews* 64 (2012) pp. 866–884. doi: 10.1016/j.addr.2012.01.020.

[129] S. MAY, M. ANDREASSON-OCHSNER, Z. FU, Y. X. LOW, D. TAN, H.-P. M. de HOOG, S. RITZ, M. NALLANI, AND E.-K. SINNER: **In Vitro Expressed GPCR Inserted in Polymersome Membranes for Ligand-Binding Studies**. *Angewandte Chemie* 52 (2013) pp. 749–753. doi: 10.1002/anie.201204645.

[130] M. SCALISE, L. POCHINI, N. GIANGREGORIO, A. TONAZZI, AND C. INDIVERI: **Proteoliposomes as Tool for Assaying Membrane Transporter Functions and Interactions with Xenobiotics**. *Pharmaceutics* 5 (2013) pp. 472–497. doi: 10.3390/pharmaceutics5030472.

[131] M. DIEZ, B. ZIMMERMANN, M. BÖRSCH, M. KÖNIG, E. SCHWEINBERGER, S. STEIGMILLER, R. REUTER, S. FELEKYAN, V. KUDRYAVTSEV, C. A. M. SEIDEL, AND P. GRÄBER: **Proton-powered subunit rotation in single membrane-bound F_0F_1-ATP synthase**. *Nature Structural & Molecular Biology* 11 (2004) pp. 135–141. doi: 10.1038/nsmb718.

[132] THE NIST REFERENCE ON CONSTANTS, UNITS, AND UNCERTAINTY: **Fundamental Physical Constants**. *National Institute of Standards and Technology (NIST)*, 2018. Accessed from: https://physics.nist.gov/cuu/index.html [last accessed: March 10, 2018].

[133] J. D. BARROW: **The Constants of Nature**: **From Alpha to Omega – The Numbers That Encode the Deepest Secrets of the Universe**. Pantheon Books, New York, NY, 2002. ISBN: 9780375422218.

[134] G. GAUGLITZ AND T. VO-DINH: **Handbook of Spectroscopy**, 1st edition. Wiley-VCH, Weinheim, 2005. ISBN: 9783527602308.

[135] L. DE BROGLIE: **The Reinterpretation of Wave Mechanics**. *Foundations of Physics* 1 (1970) pp. 5–15. doi: 10.1007/BF00708650.

[136] C. DAVISSON AND L. H. GERMER: **Diffraction of Electrons by a Crystal of Nickel**. *Physical Review* 30 (1927) pp. 705–740. doi: 10.1103/PhysRev.30.705.

[137] R. EISBERG AND R. RESNICK: **Quantum Physics of Atoms, Molecules, Solids, Nuclei, and Particles**, 2nd edition. Wiley, New York, NY, 1985. ISBN: 9780471873730.

[138] A. SCHWAIGHOFER: **Vibrational Spectroscopy of Proteins**. PhD thesis, University of Natural Resources and Life Sciences, Vienna, 2013.

[139] S. J. WILLIAMSON AND H. Z. CUMMINS: **Light and Color in Nature and Art**. Wiley, New York, NY, 1983. ISBN: 9780471083740.

[140] P. GILBERT AND W. HAEBERLI: **Physics in the Arts**. Elsevier Academic Press, Amsterdam, 2008. ISBN: 9780123741509.

[141] J. D. JACKSON: **Classical Electrodynamics**, 3rd edition. Wiley, New York, NY, 1999. ISBN: 9780471309321.

[142] W. OCKENGA: **Homepage of Leica Microsystems**: **Phase Contrast**: https://www.leica-microsystems.com/science-lab/phase-contrast [last accessed: January 25, 2018].

[143] W. DEMTRÖDER: **Experimentalphysik 3**: **Atome, Moleküle und Festkörper**, 4th edition. Springer, Berlin, 2009. ISBN: 9783642039102.

[144] M. SRINIVASARAO: **Nano-Optics in the Biological World: Beetles, Butterflies, Birds, and Moths**. *Chemical Reviews* 99 (1999) pp. 1935–1962. doi: 10.1021/cr970080y.

[145] C. W. MASON: **Blue Eyes**. *Journal of Physical Chemistry* 28 (1923) pp. 498–501. doi: 10.1021/j150239a007.

[146] H. WANG, S. LIN, X. LIU, AND S. B. KANG: **Separating reflections in human iris images for illumination estimation**. *IEEE International Conference on Computer Vision* (2005) pp. 1691-1698. doi: 10.1109/ICCV.2005.215.

[147] W. BENENSON, J. W. HARRIS, H. STOCKER, AND H. LUTZ: **Handbook of Physics**. Springer, New York, NY, 2002. ISBN: 9780387952697.

[148] M. BORN AND E. WOLF: **Principles of Optics**: **Electromagnetic Theory of Propagation, Interference and Diffraction of Light**, 7th edition. Cambridge University Press, Cambridge, 1999. ISBN: 9780521642224.

[149] D. J. GRIFFITHS: **Introduction to Electrodynamics**, 3rd edition. Prentice Hall, Upper Saddle River, NJ, 1999. ISBN: 013805326X.

[150] J. A. BITTENCOURT: **Fundamentals of Plasma Physics**, 3rd edition. Springer, New York, NY, 2004. ISBN: 9780387209753.

[151] F. RICHTER: **Die Photodegradation von Poly(2,6-dimethyl-1,4-phenylenether) - Untersuchungen am Polymer und an Modellverbindungen**. PhD thesis, Friedrich-Alexander-Universität Erlangen-Nürnberg, 1998.

[152] P. W. ATKINS AND J. DE PAULA: **Atkins' Physical Chemistry**, 7th edition. Oxford University Press, Oxford, 2002. ISBN: 9780198792857.

[153] K. K. GAN AND A. T. LAW: **Measuring slit width and separation in a diffraction experiment**. *European Journal of Physics* 30 (2009) pp. 1271–1276. doi: 10.1088/0143-0807/30/6/006.

[154] R. BACH, D. POPE, S.-H. LIOU, AND H. BATELAAN: **Controlled double-slit electron diffraction**. *New Journal of Physics* 15 (2013) 033018. doi: 10.1088/1367-2630/15/3/033018.

[155] J. LEKNER: **Theory of Reflection of Electromagnetic and Particle Waves**. Springer, Dordrecht, 1987. ISBN: 9789048182992.

[156] J. W. STRUTT: **XV. On the light from the sky, its polarization and colour**. *London, Edinburgh, and Dublin Philosophical Magazine and Journal of Science* 41 (1871) pp. 107–120. doi: 10.1080/14786447108640452.

[157] J. W. STRUTT: **LVIII. On the scattering of light by small particles**. *London, Edinburgh, and Dublin Philosophical Magazine and Journal of Science* 41 (1871) pp. 447–454. doi: 10.1080/14786447108640507.

[158] LORD RAYLEIGH F. R. S.: **X. On the electromagnetic theory of light**. *London, Edinburgh, and Dublin Philosophical Magazine and Journal of Science* 12 (1881) pp. 81–101. doi: 10.1080/14786448108627074.

[159] LORD RAYLEIGH F. R. S.: **XXXIV. On the transmission of light through an atmosphere containing small particles in suspension, and on the origin of the blue of the sky**. *London, Edinburgh, and Dublin Philosophical Magazine and Journal of Science* 47 (1899) pp. 375–384. doi: 10.1080/14786449908621276.

[160] A. T. YOUNG: **Rayleigh scattering**. *Applied Optics* 20 (1981) pp. 533–535. doi: 10.1364/AO.20.000533.

[161] C. F. BOHREN AND D. R. HUFFMAN: **Absorption and Scattering of Light by Small Particles**. Wiley-VCH, Weinheim, 2008. ISBN: 9780471293408.

[162] J. BRION, A. CHAKIR, J. CHARBONNIER, D. DAUMONT, C. PARISSE, AND J. MALICET: **Absorption Spectra Measurements for the Ozone Molecule in the 350–830 nm Region**. *Journal of Atmospheric Chemistry* 30 (1998) pp. 291–299. doi: 10.1023/A:1006036924364.

[163] C. V. RAMAN AND A. JAYARAMAN: **The structure and optical behaviour of iridescent opal**. *Proceedings of the Indian Academy of Sciences - Section A* 38 (1953) pp. 343–354. doi: 10.1007/BF03045242.

[164] R. AROCA: **Surface-Enhanced Vibrational Spectroscopy**. Wiley, Chichester, 2006. ISBN: 9780471607311.

[165] P. G. ETCHEGOIN, E. C. LE RU, AND M. MEYER: **An analytic model for the optical properties of gold**. *Journal of Chemical Physics* 125 (2006) 164705. doi: 10.1063/1.2360270.

[166] C. W. MOON, S. Y. LEE, W. SOHN, D. M. ANDOSHE, D. H. KIM, K. HONG, AND H. W. JANG: **Plasmonic Octahedral Gold Nanoparticles of Maximized Near Electromagnetic Fields for Enhancing Catalytic Hole Transfer in Solar Water Splitting**. *Particle & Particle Systems Characterization* 34 (2017) 1600340. doi: 10.1002/ppsc.201600340.

[167] M. A. ORDAL, R. J. BELL, R. W. ALEXANDER, L. L. LONG, AND M. R. QUERRY: **Optical properties of fourteen metals in the infrared and far infrared: Al, Co, Cu, Au, Fe, Pb, Mo, Ni, Pd, Pt, Ag, Ti, V, and W**. *Applied Optics* 24 (1985) pp. 4493–4499. doi: 10.1364/AO.24.004493.

[168] WORLD GOLD COUNCIL: **Gold Jewellery Alloys**. *World Gold Council*, 2018. Accessed from: https://web.archive.org/web/20080619061619/http://www.utilisegold.com/jewellery_technology/colours/colour_alloys/ [last accessed: March 10, 2018].

[169] R. A. MEYERS: **Encyclopedia of Analytical Chemistry**. John Wiley & Sons, Hoboken, NJ, 2006. ISBN: 9780470027318.

[170] R. B. M. SCHASFOORT AND A. J. TUDOS: **Handbook of Surface Plasmon Resonance**. RSC Publishing, Cambridge, 2008. ISBN: 9780854042678.

[171] F. GOOS AND H. HÄNCHEN: **Ein neuer und fundamentaler Versuch zur Totalreflexion**. *Annalen der Physik* 436 (1947) pp. 333–346. doi: 10.1002/andp.19474360704.

[172] E. GOORMAGHTIGH, V. RAUSSENS, AND J. M. RUYSSCHAERT: **Attenuated total reflection infrared spectroscopy of proteins and lipids in biological membranes**. *Biochimica et Biophysica Acta* 1422 (1999).

[173] N. J. HARRICK: **Surface Chemistry from Spectral Analysis of Totally Internally Reflected Radiation**. *Journal of Physical Chemistry* 64 (1960) pp. 1110–1114. doi: 10.1021/j100838a005.

[174] S. ZHU, A. W. YU, D. HAWLEY, AND R. ROY: **Frustrated total internal reflection: A demonstration and review**. *American Journal of Physics* 54 (1986) pp. 601–607. doi: 10.1119/1.14514.

[175] M. WILSON: **Homepage of Leica Microsystems**: **Microscope Resolution: Concepts, Factors and Calculation**: https://www.leica-microsystems.com/science-lab/microscope-resolution-concepts-factors-and-calculation [last accessed: January 28, 2018].

[176] E. VERDET: **Leçons d'Optique Physique (Paris)**. Victor Masson et fils, Paris, 1869.

[177] E. ABBE: **Beiträge zur Theorie des Mikroskops und der mikroskopischen Wahrnehmung**. *Archiv für mikroskopische Anatomie* 9 (1873) pp. 413–418. doi: 10.1007/BF02956173.

[178] E. ABBE: **Ueber einen neuen Beleuchtungsapparat am Mikroskop**. *Archiv für mikroskopische Anatomie* 9 (1873) pp. 469–480. doi: 10.1007/BF02956177.

[179] G. B. AIRY: **On the diffraction of an object-glass with circular aperture**. *Transactions of the Cambridge Philosophical Society* 5 (1835) pp. 283–291.

[180] H. RÜHL: **Homepage of Leica Microsystems**: **Optical Microscopes - Some Basics**: https://www.leica-microsystems.com/science-lab/optical-microscopes-some-basics [last accessed: January 27, 2018].

[181] G. C. COX: **Optical Imaging Techniques in Cell Biology**, 2nd edition. CRC Press, Boca Raton, FL, 2012. ISBN: 9781439848258.

[182] G. GÖKE: **Moderne Methoden der Lichtmikroskopie**: **Vom Durchlicht-Hellfeld- bis zum Lasermikroskop**. Franckh, Stuttgart, 1988. ISBN: 3440057658.

[183] H. VON HELMHOLTZ: **Die theoretische Grenze für die Leistungsfähigkeit der Mikroskope**. *Poggendorfer Annalen* 136 (1874).

[184] H. VON HELMHOLTZ AND H. FRIPP: **On the Limits of the Optical Capacity of the Microscope**. *Monthly Microscopical Journal* 16 (1876) pp. 15–39. doi: 10.1111/j.1365-2818.1876.tb05606.x.

[185] LORD RAYLEIGH F. R. S.: **XII. On the Manufacture and Theory of Diffraction-gratings**. *London, Edinburgh, and Dublin Philosophical Magazine and Journal of Science* 47 (1874) pp. 81–93. doi: 10.1080/14786447408640996.

[186] LORD RAYLEIGH F. R. S.: **XXXI. Investigations in optics, with special reference to the spectroscope**. *London, Edinburgh, and Dublin Philosophical Magazine and Journal of Science* 8 (1879) pp. 261–274. doi: 10.1080/14786447908639684.

[187] LORD RAYLEIGH, SEC. R. S.: **XV. On the Theory of Optical Images, with Special Reference to the Microscope**. *London, Edinburgh, and Dublin Philosophical Magazine and Journal of Science* 42 (1896) pp. 167–195. doi: 10.1080/14786449608620902.

[188] S. W. HELL AND J. WICHMANN: **Breaking the diffraction resolution limit by stimulated emission: stimulated-emission-depletion fluorescence microscopy**. *Optics Letters* 19 (1994) pp. 780. doi: 10.1364/OL.19.000780.

[189] E. RITTWEGER, K. Y. HAN, S. E. IRVINE, C. EGGELING, AND S. W. HELL: **STED microscopy reveals crystal colour centres with nanometric resolution**. *Nature Photonics* 3 (2009) pp. 144–147. doi: 10.1038/nphoton.2009.2.

[190] M. J. RUST, M. BATES, AND X. ZHUANG: **Sub-diffraction-limit imaging by stochastic optical reconstruction microscopy (STORM)**. *Nature Methods* 3 (2006) pp. 793–795. doi: 10.1038/nmeth929.

[191] E. BETZIG, G. H. PATTERSON, R. SOUGRAT, O. W. LINDWASSER, S. OLENYCH, J. S. BONIFACINO, M. W. DAVIDSON, J. LIPPINCOTT-SCHWARTZ, AND H. F. HESS: **Imaging Intracellular Fluorescent Proteins at Nanometer Resolution**. *Science* 313 (2006) pp. 1642–1645. doi: 10.1126/science.1127344.

[192] S. T. HESS, T. P. K. GIRIRAJAN, AND M. D. MASON: **Ultra-High Resolution Imaging by Fluorescence Photoactivation Localization Microscopy**. *Biophysical Journal* 91 (2006) pp. 4258–4272. doi: 10.1529/biophysj.106.091116.

[193] J. I. GOLDSTEIN, D. E. NEWBURY, J. R. MICHAEL, N. W.M. RITCHIE, J. H. J. SCOTT, AND D. C. JOY: **Scanning Electron Microscopy and X-Ray Microanalysis**, 4th edition. Springer, New York, NY, 2018. ISBN: 9781493966745.

[194] E. HECHT: **Optik**, 4th edition. Oldenbourg, München, 2005. ISBN: 3486273590.

[195] J. R. LAKOWICZ: **Principles of Fluorescence Spectroscopy**, 3rd edition. Springer, New York, NY, 2008. ISBN: 9780387312781.

[196] B. J. BERNE AND R. PECORA: **Dynamic Light Scattering**, Dover edition. Dover Publications, Mineola, NY, 2000. ISBN: 0486411559.

[197] WYATT TECHNOLOGY CORPORATION: **Homepage of Wyatt Technology Corporation**: **Understanding Dynamic Light Scattering**: https://www.wyatt.com/library/theory/dynamic-light-scattering-theory.html [last accessed: February 10, 2018].

[198] R. H. PETRUCCI, F. G. HERRING, J. D. MADURA, AND C. BISSONNETTE: **General Chemistry**: **Principles and Modern Applications**, 11th edition. Pearson, Toronto, 2016. ISBN: 9780132931281.

[199] G. E. BRIGGS AND J. B. S. HALDANE: **A Note on the Kinetics of Enzyme Action**. *Biochemical Journal* 19 (1925) pp. 338–339.

[200] M. E. STROPPOLO, M. FALCONI, A. M. CACCURI, AND A. DESIDERI: **Superefficient enzymes**. *Cellular and Molecular Life Sciences* 58 (2001) pp. 1451–1460. doi: 10.1007/PL00000788.

[201] M. CZAPLA, A. BOREK, M. SAREWICZ, AND A. OSYCZKA: **Enzymatic Activities of Isolated Cytochrome bc_1-like Complexes Containing Fused Cytochrome *b* Subunits with Asymmetrically Inactivated Segments of Electron Transfer Chains**. *Biochemistry* 51 (2012) pp. 829–835. doi: 10.1021/bi2016316.

[202] J. M. CHALMERS AND P. R. GRIFFITHS: **Handbook of Vibrational Spectroscopy**. John Wiley & Sons, Chichester, UK, 2006. ISBN: 9780471988472.

[203] B. SCHRADER: **Infrared and Raman Spectroscopy**: **Methods and Applications**. Wiley-VCH, Weinheim, 1995. ISBN: 9783527264469.

[204] A. BARTH: **Infrared spectroscopy of proteins**. *Biochimica et Biophysica Acta* 1767 (2007) pp. 1073–1101. doi: 10.1016/j.bbabio.2007.06.004.

[205] A. A. MICHELSON: **XXVIII. Visibility of Interference-Fringes in the Focus of a Telescope**. *London, Edinburgh, and Dublin Philosophical Magazine and Journal of Science* 31 (1891) pp. 256–259. doi: 10.1080/14786449108620101.

[206] W. D. PERKINS: **Fourier transform-Infrared Spectroscopy: Part l. Instrumentation**. *Journal of Chemical Education* 63 (1986) pp. A5-A10.

[207] J. W. COOLEY AND J. W. TUKEY: **An Algorithm for the Machine Calculation of Complex Fourier Series**. *Mathematics of Computation* 19 (1965) pp. 297–301.

[208] J. L. R. ARRONDO, A. MUGA, J. CASTRESANA, AND F. M. GOÑI: **Quantitative studies of the structure of proteins in solution by fourier-transform infrared spectroscopy**. *Progress in Biophysics and Molecular Biology* 59 (1993) pp. 23–56. doi: 10.1016/0079-6107(93)90006-6.

[209] J. C. LINDON, G. E. TRANTER, AND D. W. KOPPENAAL: **Encyclopedia of Spectroscopy and Spectrometry**, 3rd edition. Academic Press, Amsterdam, 2017. ISBN: 9780128032244.

[210] J. FAHRENFORT: **Attenuated Total Reflection: A New Principle for the Production of Useful Infra-Red Reflection Spectra of Organic Compounds**. *Spectrochimica Acta* 17 (1961) pp. 698–709. doi: 10.1016/0371-1951(61)80136-7.

[211] F. M. MIRABELLA: **Internal Reflection Spectroscopy**: **Theory and Applications**. CRC Press, Boca Raton, FL, 1992. ISBN: 0824787307.

[212] M. OSAWA: **Dynamic Processes in Electrochemical Reactions Studied by Surface-Enhanced Infrared Absorption Spectroscopy (SEIRAS)**. *Bulletin of the Chemical Society of Japan* 70 (1997) pp. 2861–2880. doi: 10.1246/bcsj.70.2861.

[213] S. KAWATA: **Near-Field Optics and Surface Plasmon Polaritons**. Springer, Berlin & Heidelberg, 2001. ISBN: 9783540445524.

[214] M. OSAWA AND M. IKEDA: **Surface-Enhanced Infrared Absorption of p-Nitrobenzoic Acid Deposited on Silver Island Films: Contributions of Electromagnetic and Chemical Mechanisms**. *Journal of Physical Chemistry* 95 (1991) pp. 9914–9919.

[215] M. OSAWA AND K.-I. ATAKA: **Electromagnetic Mechanism of Enhanced Infrared Absorption of Molecules Adsorbed on Metal Island Films**. *Surface Science* 262 (1992) pp. L118-L122. doi: 10.1016/0039-6028(92)90119-Q.

[216] P. R. GRIFFITHS, B. L. HIRSCHE, AND C. J. MANNING: **Ultra-rapid-scanning Fourier transform infrared spectrometry**. *Vibrational Spectroscopy* 19 (1999) pp. 165–176. doi: 10.1016/S0924-2031(99)00006-5.

[217] R. A. PALMER, J. L. CHAO, R. M. DITTMAR, V. G. GREGORIOU, AND S. E. PLUNKETT: **Investigation of Time-Dependent Phenomena by Use of Step-Scan FT-IR**. *Applied Spectroscopy* 47 (1993) pp. 1297–1310.

[218] A. BARTH AND C. ZSCHERP: **What vibrations tell about proteins**. *Quarterly Reviews of Biophysics* 35 (2002) pp. 369–430. doi: 10.1017/S0033583502003815.

[219] B. STUART: **Biological Applications of Infrared Spectroscopy**. Wiley, Chichester, 1997. ISBN: 0471974137.

[220] D. BAURECHT AND U. P. FRINGELI: **Quantitative modulated excitation Fourier transform infrared spectroscopy**. *Review of Scientific Instruments* 72 (2001) pp. 3782–3792. doi: 10.1063/1.1400152.

[221] D. K. DAS, T. MONDAL, U. MANDAL, AND K. BHATTACHARYYA: **Probing Deuterium Isotope Effect on Structure and Solvation Dynamics of Human Serum Albumin**. *ChemPhysChem: A European Journal of Chemical Physics and Physical Chemistry* 12 (2011) pp. 814–822. doi: 10.1002/cphc.201000912.

[222] A. KOHEN AND H. H. LIMBACH: **Isotope Effects In Chemistry and Biology**. CRC Press, Boca Raton, FL, 2005. ISBN: 9780824724498.

[223] J. L. R. ARRONDO AND F. M. GOÑI: **Structure and dynamics of membrane proteins as studied by infrared spectroscopy**. *Progress in Biophysics and Molecular Biology* 72 (1999) pp. 367–405. doi: 10.1016/S0079-6107(99)00007-3.

[224] E. RIAL, A. MUGA, J. M. VALPUESTA, J.-L. R. ARRONDO, AND F. M. GOÑI: **Infrared spectroscopic studies of detergent-solubilized uncoupling protein from brown-adipose-tissue mitochondria**. *European Journal of Biochemistry* 188 (1990) pp. 83–89. doi: 10.1111/j.1432-1033.1990.tb15374.x.

[225] R. P. SHERIDAN, E. T. KNIGHT, AND L. C. ALLEN: **The effect of deuterium substitution on hydrogen bonds in redox proteins**. *Biopolymers* 23 (1984) pp. 195–200. doi: 10.1002/bip.360230203.

[226] O. FARVER, J. ZHANG, Q. CHI, I. PECHT, AND J. ULSTRUP: **Deuterium isotope effect on the intramolecular electron transfer in *Pseudomonas aeruginosa* azurin**. *Proceedings of the National Academy of Sciences of the United States of America* 98 (2001) pp. 4426–4430. doi: 10.1073/pnas.071043798.

[227] H. GAO, J. M. MCMAHON, M. H. LEE, J. HENZIE, S. K. GRAY, G. C. SCHATZ, AND T. W. ODOM: **Rayleigh anomaly-surface plasmon polariton resonances in palladium and gold subwavelength hole arrays**. *Optics Express* 17 (2009) pp. 2334. doi: 10.1364/OE.17.002334.

[228] N. W. ASHCROFT AND N. D. MERMIN: **Solid State Physics**, 1st edition. Cengage Learning, Boston, MA, 1976. ISBN: 9780030839931.

[229] E. KAXIRAS: **Atomic and Electronic Structure of Solids**. Cambridge University Press, Cambridge, 2003. ISBN: 9780521523394.

[230] M. BAUCH: **New enhancement strategies for plasmon-enhanced fluorescence biosensors**. PhD thesis, Johannes Gutenberg University, Mainz, 2014.

[231] K. V. SREEKANTH, A. DE LUCA, AND G. STRANGI: **Experimental demonstration of surface and bulk plasmon polaritons in hypergratings**. *Scientific Reports* 3 (2013) 3291. doi: 10.1038/srep03291.

[232] N. VASILANTONAKIS, M. E. NASIR, W. DICKSON, G. A. WURTZ, AND A. V. ZAYATS: **Bulk plasmon-polaritons in hyperbolic nanorod metamaterial waveguides**. *Laser & Photonics Reviews* 9 (2015) pp. 345–353. doi: 10.1002/lpor.201400457.

[233] P. R. WEST, S. ISHII, G. V. NAIK, N. K. EMANI, V. M. SHALAEV, AND A. BOLTASSEVA: **Searching for better plasmonic materials**. *Laser & Photonics Reviews* 4 (2010) pp. 795–808. doi: 10.1002/lpor.200900055.

[234] K. M. MCPEAK, S. V. JAYANTI, S. J. P. KRESS, S. MEYER, S. IOTTI, A. ROSSINELLI, AND D. J. NORRIS: **Plasmonic Films Can Easily Be Better: Rules and Recipes**. *ACS Photonics* 2 (2015) pp. 326–333. doi: 10.1021/ph5004237.

[235] S. BABAR AND J. H. WEAVER: **Optical constants of Cu, Ag, and Au revisited**. *Applied Optics* 54 (2015) pp. 477–481. doi: 10.1364/AO.54.000477.

[236] I. H. MALITSON: **Interspecimen Comparison of the Refractive Index of Fused Silica**. *Journal of the Optical Society of America* 55 (1965) pp. 1205–1209. doi: 10.1364/JOSA.55.001205.

[237] M. N. POLYANSKIY: **Refractive Index Database**: https://refractiveindex.info [last accessed: March 15, 2018].

[238] A. OTTO: **Excitation of Nonradiative Surface Plasma Waves in Silver by the Method of Frustrated Total Reflection**. *Zeitschrift für Physik A Hadrons and Nuclei* 216 (1968) pp. 398–410. doi: 10.1007/BF01391532.

[239] E. KRETSCHMANN AND H. RAETHER: **Radiative Decay of Non Radiative Surface Plasmons Excited by Light**. *Zeitschrift für Naturforschung A* 23 (1968) pp. 2135–2136. doi: 10.1515/zna-1968-1247.

[240] P. A. HIBBINS: **Grating coupling of surface plasmon polaritons at visible and microwave frequencies**. PhD thesis, University of Exeter, 1999.

[241] D. CAI, Y. LU, K. LIN, P. WANG, AND H. MING: **Improving the sensitivity of SPR sensors based on gratings by double-dips method (DDM)**. *Optics Express* 16 (2008) pp. 14597–14602. doi: 10.1364/OE.16.014597.

[242] P. BERINI: **Long-range surface plasmon polaritons**. *Advances in Optics and Photonics* 1 (2009) pp. 484–588. doi: 10.1364/AOP.1.000484.

[243] R. W. WOOD: **XLII. On a remarkable case of uneven distribution of light in a diffraction grating spectrum**. *London, Edinburgh, and Dublin Philosophical Magazine and Journal of Science* 4 (1902) pp. 396–402. doi: 10.1080/14786440209462857.

[244] R. W. WOOD: **XXVII. Diffraction gratings with controlled groove form and abnormal distribution of intensity**. *London, Edinburgh, and Dublin Philosophical Magazine and Journal of Science* 23 (1912) pp. 310–317. doi: 10.1080/14786440208637224.

[245] G. M. HALE AND M. R. QUERRY: **Optical Constants of Water in the 200-nm to 200-µm Wavelength Region**. *Applied Optics* 12 (1973) pp. 555–563. doi: 10.1364/AO.12.000555.

[246] E. D. PALIK: **Handbook of Optical Constants of Solids (Academic, Orlando, 1985)**. Academic Press, Orlando, FL, 1985. ISBN: 9780125444156.

[247] SCHOTT AG: **Schott Zemax catalog 2017-01-20b**: https://refractiveindex.info/?shelf=glass&book=LASF9&page=SCHOTT [last accessed: April 10, 2018].

[248] T. LIEBERMANN AND W. KNOLL: **Surface-plasmon field-enhanced fluorescence spectroscopy**. *Colloids and Surfaces A: Physicochemical and Engineering Aspects* 171 (2000) pp. 115–130. doi: 10.1016/S0927-7757(99)00550-6.

[249] M. BAUCH AND J. DOSTALEK: **Collective localized surface plasmons for high performance fluorescence biosensing**. *Optics Express* 21 (2013) pp. 20470–20483. doi: 10.1364/OE.21.020470.

[250] P. ADAM, J. DOSTÁLEK, AND J. HOMOLA: **Multiple surface plasmon spectroscopy for study of biomolecular systems**. *Sensors and Actuators B: Chemical* 113 (2006) pp. 774–781. doi: 10.1016/j.snb.2005.07.029.

[251] S. ZENG, X. YU, W.-C. LAW, Y. ZHANG, R. HU, X.-Q. DINH, H.-P. HO, AND K.-T. YONG: **Size dependence of Au NP-enhanced surface plasmon resonance based on differential phase measurement**. *Sensors and Actuators B: Chemical* 176 (2013) pp. 1128–1133. doi: 10.1016/j.snb.2012.09.073.

[252] G. V. NAIK, V. M. SHALAEV, AND A. BOLTASSEVA: **Alternative Plasmonic Materials: Beyond Gold and Silver**. *Advanced Materials* 25 (2013) pp. 3264–3294. doi: 10.1002/adma.201205076.

[253] E. WIJAYA, C. LENAERTS, S. MARICOT, J. HASTANIN, S. HABRAKEN, J.-P. VILCOT, R. BOUKHERROUB, AND S. SZUNERITS: **Surface plasmon resonance-based biosensors: From the development of different SPR structures to novel surface functionalization strategies**. *Current Opinion in Solid State and Materials Science* 15 (2011) pp. 208–224. doi: 10.1016/j.cossms.2011.05.001.

[254] H. MISHRA, A. DRAGAN, AND C. D. GEDDES: **UV to NIR Surface Plasmon Coupled and Metal-Enhanced Fluorescence Using Indium Thin Films: Application to Intrinsic (Label-less) Protein Fluorescence Detection**. *Journal of Physical Chemistry C* 115 (2011) pp. 17227–17236. doi: 10.1021/jp106671t.

[255] A. ONO, M. KIKAWADA, R. AKIMOTO, W. INAMI, AND Y. KAWATA: **Fluorescence enhancement with deep-ultraviolet surface plasmon excitation**. *Optics Express* 21 (2013) pp. 17447–17453. doi: 10.1364/OE.21.017447.

[256] Y. EKINCI, H. H. SOLAK, AND J. F. LÖFFLER: **Plasmon resonances of aluminum nanoparticles and nanorods**. *Journal of Applied Physics* 104 (2008) 083107. doi: 10.1063/1.2999370.

[257] C. LANGHAMMER, M. SCHWIND, B. KASEMO, AND I. ZORIĆ: **Localized Surface Plasmon Resonances in Aluminum Nanodisks**. *Nano Letters* 8 (2008) pp. 1461–1471. doi: 10.1021/nl080453i.

[258] M. W. KNIGHT, N. S. KING, L. LIU, H. O. EVERITT, P. NORDLANDER, AND N. J. HALAS: **Aluminum for Plasmonics**. *ACS Nano* 8 (2014) pp. 834–840. doi: 10.1021/nn405495q.

[259] S. EKGASIT, C. THAMMACHAROEN, F. YU, AND W. KNOLL: **Influence of the Metal Film Thickness on the Sensitivity of Surface Plasmon Resonance Biosensors**. *Applied Spectroscopy* 59 (2005) pp. 661–667. doi: 10.1366/0003702053945994.

[260] M. G. BLABER, M. D. ARNOLD, AND M. J. FORD: **A review of the optical properties of alloys and intermetallics for plasmonics**. *Journal of Physics: Condensed Matter* 22 (2010) 143201. doi: 10.1088/0953-8984/22/14/143201.

[261] L. TIEFENAUER AND S. DEMARCHE: **Challenges in the Development of Functional Assays of Membrane Proteins**. *Materials* 5 (2012) pp. 2205–2242. doi: 10.3390/ma5112205.

[262] C. H. NIELSEN: **Biomimetic membranes for sensor and separation applications**. *Analytical and Bioanalytical Chemistry* 395 (2009) pp. 697–718. doi: 10.1007/s00216-009-2960-0.

[263] J. E. GONZÁLEZ, K. OADES, Y. LEYCHKIS, A. HAROOTUNIAN, AND P. A. NEGULESCU: **Cell-based assays and instrumentation for screening ion-channel targets**. *Drug Discovery Today* 4 (1999) pp. 431–439. doi: 10.1016/S1359-6446(99)01383-5.

[264] C. VON BALLMOOS, O. BINER, T. NILSSON, AND P. BRZEZINSKI: **Mimicking respiratory phosphorylation using purified enzymes**. *Biochimica et Biophysica Acta* 1857 (2016) pp. 321–331. doi: 10.1016/j.bbabio.2015.12.007.

[265] L. N. ÖJEMYR, C. VON BALLMOOS, K. FAXÉN, E. SVAHN, AND P. BRZEZINSKI: **The Membrane Modulates Internal Proton Transfer in Cytochrome *c* Oxidase**. *Biochemistry* 51 (2012) pp. 1092–1100. doi: 10.1021/bi201795c.

[266] A. MECKE, C. DITTRICH, AND W. MEIER: **Biomimetic membranes designed from amphiphilic block copolymers**. *Soft Matter* 2 (2006) pp. 751–759. doi: 10.1039/b605165k.

[267] M. SEZER, A.-L. WOELKE, E. W. KNAPP, R. SCHLESINGER, M. A. MROGINSKI, AND I. M. WEIDINGER: **Redox induced protonation of heme propionates in cytochrome *c* oxidase: Insights from surface enhanced resonance Raman spectroscopy and QM/MM calculations**. *Biochimica et Biophysica Acta* 1858 (2017) pp. 103–108. doi: 10.1016/j.bbabio.2016.10.009.

[268] S. E. CHOBOT, H. ZHANG, C. C. MOSER, AND P. L. DUTTON: **Breaking the Q-cycle: finding new ways to study Qo through thermodynamic manipulations**. *Journal of Bioenergetics and Biomembranes* 40 (2008) pp. 501–507. doi: 10.1007/s10863-008-9175-5.

[269] K. L. DÜRR, J. KOEPKE, P. HELLWIG, H. MÜLLER, H. ANGERER, G. PENG, E. OLKHOVA, O.-M. H. RICHTER, B. LUDWIG, AND H. MICHEL: **A D-Pathway Mutation Decouples the *Paracoccus denitrificans* Cytochrome *c* Oxidase by Altering the Side-Chain Orientation of a Distant Conserved Glutamate**. *Journal of Molecular Biology* 384 (2008) pp. 865–877. doi: 10.1016/j.jmb.2008.09.074.

[270] J. O. GOLDSMITH AND S. G. BOXER: **Rapid isolation of bacterial photosynthetic reaction centers with an engineered poly-histidine tag**. *Biochimica et Biophysica Acta* 1276 (1996) pp. 171–175. doi: 10.1016/0005-2728(96)00091-6.

[271] C. KIRMAIER, P. D. LAIBLE, K. CZARNECKI, A. N. HATA, D. K. HANSON, D. F. BOCIAN, AND D. HOLTEN: **Comparison of M-Side Electron Transfer in *Rb. sphaeroides* and *Rb. capsulatus* Reaction Centers**. *Journal of Physical Chemistry B* 106 (2002) pp. 1799–1808. doi: 10.1021/jp013264w.

[272] M. GUERGOVA-KURAS, R. SALCEDO-HERNANDEZ, G. BECHMANN, R. KURAS, R. B. GENNIS, AND A. R. CROFTS: **Expression and One-Step Purification of a Fully Active Polyhistidine-Tagged Cytochrome bc_1 Complex from *Rhodobacter sphaeroides***. *Protein Expression and Purification* 15 (1999) pp. 370–380. doi: 10.1006/prep.1998.1018.

[273] H. PAULSEN, B. FINKENZELLER, AND N. KUHLEIN: **Pigments induce folding of light-harvesting chlorophyll *a*/*b*-binding protein**. *European Journal of Biochemistry* 215 (1993) pp. 809–816. doi: 10.1111/j.1432-1033.1993.tb18096.x.

[274] H. PAULSEN, U. RÜMLER, AND W. RÜDIGER: **Reconstitution of pigment-containing complexes from light-harvesting chlorophyll *a*/*b*-binding protein overexpressed in *Escherichia coli***. *Planta* 181 (1990) pp. 204–211. doi: 10.1007/BF02411539.

[275] H. ROGL: **Struktur und Funktion des Lichtsammelkomplexes LHC-II der höheren Pflanzen**. PhD thesis, Goethe University, Frankfurt am Main, 2000.

[276] F. A. GEISS: **Herstellung einer 4xCys-Mutante des Light Harvesting Complex II und dessen Stabilisierung durch kovalente Verknüpfung der Untereinheiten mittels Bismaleimido-Crosslinkern**. Diploma thesis, Johannes Gutenberg University, Mainz, 2012.

[277] THERMO FISHER SCIENTIFIC CORPORATION: **Homepage of Thermo Fisher Scientific**: **Product information of NBD-PE**: https://www.thermofisher.com/order/catalog/product/N360 [last accessed: January 20, 2018].

[278] THERMO FISHER SCIENTIFIC CORPORATION: **Homepage of Thermo Fisher Scientific**: **Product information of Fluorescein DHPE**: https://www.thermofisher.com/order/catalog/product/F362 [last accessed: January 20, 2018].

[279] THERMO FISHER SCIENTIFIC CORPORATION: **Homepage of Thermo Fisher Scientific**: **Product information of 5-(and-6)-carboxy-SNARF-1**: https://www.thermofisher.com/order/catalog/product/C1270 [last accessed: January 20, 2018].

[280] THERMO FISHER SCIENTIFIC CORPORATION: **Homepage of Thermo Fisher Scientific**: **Product information of di-8-ANEPPS**: https://www.thermofisher.com/order/catalog/product/D3167 [last accessed: January 20, 2018].

[281] THERMO FISHER SCIENTIFIC CORPORATION: **Homepage of Thermo Fisher Scientific**: **Product information of the FRET pair CC2-DMPE/DiSBAC$_2$(3)**: https://www.thermofisher.com/order/catalog/product/K1016 [last accessed: January 20, 2018].

[282] A. MATIUKAS, B. G. MITREA, A. M. PERTSOV, J. P. WUSKELL, M.-D. WEI, J. WATRAS, A. C. MILLARD, AND L. M. LOEW: **New near-infrared optical probes of cardiac electrical activity**. *American Journal of Physiology: Heart and Circulatory Physiology* 290 (2006) pp. H2633-H2643. doi: 10.1152/ajpheart.00884.2005.

[283] K. O. JOHANSSON, J. A. LOTOSKI, C. C. TONG, AND G. S. HANAN: **Toward high nuclearity ruthenium complexes: creating new binding sites in metal complexes**. *Chemical Communications* (2000) pp. 819–820. doi: 10.1039/a910257o.

[284] L. ESSER, M. ELBERRY, F. ZHOU, C.-A. YU, L. YU, AND DI XIA: **Inhibitor-complexed Structures of the Cytochrome *bc*$_1$ from the Photosynthetic Bacterium *Rhodobacter sphaeroides***. *Journal of Biological Chemistry* 283 (2008) pp. 2846–2857. doi: 10.1074/jbc.M708608200.

[285] S.-J. MARRINK, O. BERGER, P. TIELEMAN, AND F. JÄHNIG: **Adhesion Forces of Lipids in a Phospholipid Membrane Studied by Molecular Dynamics Simulations**. *Biophysical Journal* 74 (1998) pp. 931–943. doi: 10.1016/S0006-3495(98)74016-0.

[286] H. M. BERMAN, J. WESTBROOK, Z. FENG, G. GILLILAND, T. N. BHAT, H. WEISSIG, I. N. SHINDYALOV, AND P. E. BOURNE: **The Protein Data Bank**. *Nucleic Acids Research* 28 (2000) pp. 235–242. doi: 10.1093/nar/28.1.235.

[287] H. M. BERMAN, J. WESTBROOK, Z. FENG, G. GILLILAND, T. N. BHAT, H. WEISSIG, I. N. SHINDYALOV, AND P. E. BOURNE: **The Protein Data Bank**: http://www.rcsb.org/ [last accessed: May 02, 2018].

[288] P. TIELEMAN: **Bilayer simulations**: http://people.ucalgary.ca/~tieleman/download.html [last accessed: November 11, 2017].

[289] E. MARGOLIASH AND N. FROHWIRT: **Spectrum of Horse-Heart Cytochrome *c***. *Biochemical Journal* 71 (1959) pp. 570–572. doi: 10.1042/bj0710570.

[290] B. LUDWIG AND G. SCHATZ: **A two-subunit cytochrome *c* oxidase (cytochrome aa_3) from *Paracoccus dentrificans***. *Proceedings of the National Academy of Sciences of the United States of America* 77 (1980) pp. 196–200. doi: 10.1073/pnas.77.1.196.

[291] S. C. STRALEY, W. W. PARSON, D. C. MAUZERALL, AND R. K. CLAYTON: **Pigment content and molar extinction coefficients of photochemical reaction centers from *Rhodopseudomonas spheroides***. *Biochimica et Biophysica Acta* 305 (1973) pp. 597–609. doi: 10.1016/0005-2728(73)90079-0.

[292] R. HIELSCHER, T. WENZ, C. HUNTE, AND P. HELLWIG: **Monitoring the redox and protonation dependent contributions of cardiolipin in electrochemically induced FTIR difference spectra of the cytochrome bc_1 complex from yeast**. *Biochimica et Biophysica Acta* 1787 (2009) pp. 617–625. doi: 10.1016/j.bbabio.2009.01.006.

[293] P. J. G. BUTLER AND W. KÜHLBRANDT: **Determination of the aggregate size in detergent solution of the light-harvesting chlorophyll a/b-protein complex from chloroplast membranes**. *Proceedings of the National Academy of Sciences of the United States of America* 85 (1988) pp. 3797–3801. doi: 10.1073/pnas.85.11.3797.

[294] E. FLUHLER, V. G. BURNHAM, AND L. M. LOEW: **Spectra, membrane binding, and potentiometric responses of new charge shift probes**. *Biochemistry* 24 (1985) pp. 5749–5755.

[295] A. F. GEISS, C. BLIEM, P. FRANK, C. REINER-ROZMAN, J. KEWNEY, M. BOERSCH, AND R. L. C. NAUMANN: **Proteo-lipobeads to encapsulate cytochrome *c* oxidase from *Paracoccus denitrificans***. *Journal of Colloid and Interface Science* 500 (2017) pp. 119–125. doi: 10.1016/j.jcis.2017.04.009.

[296] K. SOLLY, J. CASSADAY, J. P. FELIX, M. L. GARCIA, M. FERRER, B. STRULOVICI, AND L. KISS: **Miniaturization and HTS of a FRET-Based Membrane Potential Assay for K_{ir} Channel Inhibitors**. *ASSAY and Drug Development Technologies* 6 (2008) pp. 225–234. doi: 10.1089/adt.2008.123.

[297] C. WOLFF, B. FUKS, AND P. CHATELAIN: **Comparative Study of Membrane Potential-Sensitive Fluorescent Probes and Their Use in Ion Channel Screening Assays**. *Journal of Biomolecular Screening* 8 (2003) pp. 533–543. doi: 10.1177/1087057103257806.

[298] C. NOWAK, C. LUENING, W. KNOLL, AND R. L. C. NAUMANN: **A Two-Layer Gold Surface with Improved Surface Enhancement for Spectro-Electrochemistry Using Surface-Enhanced Infrared Absorption Spectroscopy**. *Applied Spectroscopy* 63 (2009) pp. 1068–1074.

[299] P. FRANK, B. SIEBENHOFER, T. HANZER, A. F. GEISS, F. SCHADAUER, C. REINER-ROZMAN, B. DURHAM, L. M. LOEW, B. LUDWIG, O.-M. H. RICHTER, C. NOWAK, AND R. L. C. NAUMANN: **Proteo-lipobeads for the oriented encapsulation of membrane proteins**. *Soft Matter* 11 (2015) pp. 2906–2908. doi: 10.1039/c4sm02646b.

[300] M. G. FRIEDRICH, J. W. F. ROBERTSON, D. WALZ, W. KNOLL, AND R. L. C. NAUMANN: **Electronic Wiring of a Multi-Redox Site Membrane Protein in a Biomimetic Surface Architecture**. *Biophysical Journal* 94 (2008) pp. 3698–3705. doi: 10.1529/biophysj.107.117846.

[301] THERMO FISHER SCIENTIFIC CORPORATION: **Fluorescence SpectraViewer**: **Fluorescein**: https://www.thermofisher.com/at/en/home/life-science/cell-analysis/labeling-chemistry/fluorescence-spectraviewer.html [last accessed: January 30, 2018].

[302] A. F. GEISS, R. KHANDELWAL, D. BAURECHT, C. BLIEM, C. REINER-ROZMAN, M. BOERSCH, G. M. ULLMANN, L. M. LOEW, AND R. L. C. NAUMANN: **pH and Potential Transients of the *bc*$_1$ Complex Co-Reconstituted in Proteo-Lipobeads with the Reaction Center from *Rb. sphaeroides***. *Journal of Physical Chemistry B* 121 (2017) pp. 143–152. doi: 10.1021/acs.jpcb.6b11116.

[303] M. KOTULSKA AND K. KUBICA: **Modeling the effect of ionic strength on durability of lipid membrane in the gel phase**. *Acta Physica Polonica B* 36 (2005) pp. 1641–1651.

[304] G. NORDLUND, J. B. SING NG, L. BERGSTRÖM, AND P. BRZEZINSKI: **A Membrane-Reconstituted Multisubunit Functional Proton Pump on Mesoporous Silica Particles**. *ACS Nano* 3 (2009) pp. 2639–2646. doi: 10.1021/nn9005413.

[305] M. M. MARTIN AND L. LINDQVIST: **The pH dependence of fluorescein fluorescence**. *Journal of Luminescence* 10 (1975) pp. 381–390. doi: 10.1016/0022-2313(75)90003-4.

[306] D. MARSH: **CRC Handbook of Lipid Bilayers**, 1st edition. CRC Press, Boca Raton, FL, 1990. ISBN: 9780849332555.

[307] W. W. WAINIO, B. EICHEL, AND A. GOULD: **Ion and pH Optimum for the Oxidation of Ferrocytochrome *c* by Cytochrome *c* Oxidase in Air**. *Journal of Biological Chemistry* 235 (1960) pp. 1521–1525.

[308] T. YONETANI: **Studies on Cytochrome Oxidase**. *Journal of Biological Chemistry* 240 (1965) pp. 3392–3399.

[309] A. SCHWAIGHOFER, C. STEININGER, D. M. HILDENBRANDT, J. SRAJER, C. NOWAK, W. KNOLL, AND R. L. C. NAUMANN: **Time-Resolved Surface-Enhanced IR-Absorption Spectroscopy of Direct Electron Transfer to Cytochrome *c* Oxidase from *R. sphaeroides***. *Biophysical Journal* 105 (2013) pp. 2706–2713. doi: 10.1016/j.bpj.2013.10.037.

[310] J. GEBERT, C. REINER-ROZMAN, C. STEININGER, V. NEDELKOVSKI, C. NOWAK, C. A. WRAIGHT, AND R. L. C. NAUMANN: **Electron Transfer to Light-Activated Photosynthetic Reaction Centers from *Rhodobacter sphaeroides* Reconstituted in a Biomimetic Membrane System**. *Journal of Physical Chemistry C* 119 (2015) pp. 890–895. doi: 10.1021/jp510006n.

[311] A. REMY AND K. GERWERT: **Coupling of light-induced electron transfer to proton uptake in photosynthesis**. *Nature Structural Biology* 10 (2003) pp. 637–644. doi: 10.1038/nsb954.

[312] J. HAVENS, M. CASTELLANI, T. KLEINSCHROTH, B. LUDWIG, B. DURHAM, AND F. MILLETT: **Photoinitiated Electron Transfer within the *Paracoccus denitrificans* Cytochrome *bc* Complex: Mobility of the Iron-Sulfur Protein is Modulated by the Occupant of the Q(o) Site**. *Biochemistry* 50 (2011) pp. 10462–10472. doi: 10.1021/bi200453r.

[313] A. R. CROFTS, V. P. SHINKAREV, D. R. J. KOLLING, AND S. HONG: **The Modified Q-cycle Explains the Apparent Mismatch Between the Kinetics of Reduction of Cytochromes c_1 and b_H in the bc_1 Complex**. *Journal of Biological Chemistry* 278 (2003) pp. 36191–36201. doi: 10.1074/jbc.M305461200.

[314] E. HEFTMANN: **Chromatography**: **Part B: Applications**, 5th edition. Elsevier, Amsterdam, 1991. ISBN: 9780080858593.

[315] F. SCHADAUER, A. F. GEISS, J. SRAJER, B. SIEBENHOFER, P. FRANK, C. REINER-ROZMAN, B. LUDWIG, O.-M. H. RICHTER, C. NOWAK, AND R. L. C. NAUMANN: **Silica Nanoparticles for the Oriented Encapsulation of Membrane Proteins into Artificial Bilayer Lipid Membranes**. *Langmuir* 31 (2015) pp. 2511–2516. doi: 10.1021/la504417j.

[316] M. G. FRIEDRICH, V. U. KIRSTE, J. ZHU, R. B. GENNIS, W. KNOLL, AND R. L. C. NAUMANN: **Activity of Membrane Proteins Immobilized on Surfaces as a Function of Packing Density**. *Journal of Physical Chemistry B* 112 (2008) pp. 3193–3201. doi: 10.1021/jp709717k.

[317] R. L. C. NAUMANN, A. F. GEISS, C. STEININGER, AND W. KNOLL: **Biomimetic Membranes for Multi-Redox Center Proteins**. *International Journal of Molecular Sciences* 17 (2016) 330. doi: 10.3390/ijms17030330.

[318] B. LIEDBERG, C. NYLANDER, AND I. LUNDSTRÖM: **Biosensing with surface plasmon resonance — how it all started**. *Biosensors and Bioelectronics* 10 (1995) pp. i–ix. doi: 10.1016/0956-5663(95)96965-2.

[319] K. SERGELEN, B. LIEDBERG, W. KNOLL, AND J. DOSTÁLEK: **A surface plasmon field-enhanced fluorescence reversible split aptamer biosensor**. *Analyst* 142 (2017) pp. 2995–3001. doi: 10.1039/C7AN00970D.

[320] J. W. CHUNG, S. D. KIM, R. BERNHARDT, AND J. C. PYUN: **Application of SPR biosensor for medical diagnostics of human hepatitis B virus (hHBV)**. *Sensors and Actuators B: Chemical* 111-112 (2005) pp. 416–422. doi: 10.1016/j.snb.2005.03.055.

[321] M. PILIARIK, L. PÁROVÁ, AND J. HOMOLA: **High-throughput SPR sensor for food safety**. *Biosensors and Bioelectronics* 24 (2009) pp. 1399–1404. doi: 10.1016/j.bios.2008.08.012.

[322] M. J. CAVALUZZI AND P. N. BORER: **Revised UV extinction coefficients for nucleoside-5'-monophosphates and unpaired DNA and RNA**. *Nucleic Acids Research* 32 (2004) e13. doi: 10.1093/nar/gnh015.

[323] A. N. PISAREVSKII, S. N. CHERENKEVICH, AND V. T. ANDRIANOV: **Fluorescence spectrum and quantum yield of DNA in solution**. *Journal of Applied Spectroscopy* 5 (1966) pp. 452–454. doi: 10.1007/BF00608872.

[324] A. R. GOLDFARB, L. J. SAIDEL, AND E. MOSOVICH: **The ultraviolet absorption spectra of proteins**. *Journal of Biological Chemistry* 193 (1951) pp. 397–404.

[325] A. G. SZABO AND D. M. RAYNER: **Fluorescence Decay of Tryptophan Conformers in Aqueous Solution**. *Journal of the American Chemical Society* 102 (1980) pp. 554–563.

[326] G. N. WOGAN: **Chemical Nature and Biological Effects of the Aflatoxins**. *Bacteriological Reviews* 30 (1966) pp. 460–470.

[327] D. GÉRARD AND S. K. GRAY: **Aluminium plasmonics**. *Journal of Physics D: Applied Physics* 48 (2015) 184001. doi: 10.1088/0022-3727/48/18/184001.

[328] M. LEE, J. U. KIM, K. J. LEE, S. AHN, Y.-B. SHIN, J. SHIN, AND C. B. PARK: **Aluminum Nanoarrays for Plasmon-Enhanced Light Harvesting**. *ACS Nano* 9 (2015) pp. 6206–6213. doi: 10.1021/acsnano.5b01541.

[329] J. OLSON, A. MANJAVACAS, L. LIU, W.-S. CHANG, B. FOERSTER, N. S. KING, M. W. KNIGHT, P. NORDLANDER, N. J. HALAS, AND S. LINK: **Vivid, full-color aluminum plasmonic pixels**. *Proceedings of the National Academy of Sciences of the United States of America* 111 (2014) pp. 14348–14353. doi: 10.1073/pnas.1415970111.

[330] M. H. CHOWDHURY, K. RAY, S. K. GRAY, J. POND, AND J. R. LAKOWICZ: **Aluminum Nanoparticles as Substrates for Metal-Enhanced Fluorescence in the Ultraviolet for the Label-Free Detection of Biomolecules**. *Analytical Chemistry* 81 (2009) pp. 1397–1403. doi: 10.1021/ac802118s.

[331] K. RAY, M. H. CHOWDHURY, AND J. R. LAKOWICZ: **Aluminum Nanostructured Films as Substrates for Enhanced Fluorescence in the Ultraviolet-Blue Spectral Region**. *Analytical Chemistry* 79 (2007) pp. 6480–6487. doi: 10.1021/ac071363l.

[332] R. MASTROGIACOMO, I. IOVINELLA, AND E. NAPOLITANO: **New fluorescent probes for ligand-binding assays of odorant-binding proteins**. *Biochemical and Biophysical Research Communications* 446 (2014) pp. 137–142. doi: 10.1016/j.bbrc.2014.02.067.

[333] S. KATTI, N. LOKHANDE, D. GONZÁLEZ, A. CASSILL, AND R. RENTHAL: **Quantitative analysis of pheromone-binding protein specificity**. *Insect Molecular Biology* 22 (2013) pp. 31–40. doi: 10.1111/j.1365-2583.2012.01167.x.

[334] S. SPINELLI, A. LAGARDE, I. IOVINELLA, P. LEGRAND, M. TEGONI, P. PELOSI, AND C. CAMBILLAU: **Crystal structure of *Apis mellifera* OBP14, a C-minus odorant-binding protein, and its complexes with odorant molecules**. *Insect Biochemistry and Molecular Biology* 42 (2012) pp. 41–50. doi: 10.1016/j.ibmb.2011.10.005.

[335] M. LARISIKA, C. KOTLOWSKI, C. STEININGER, R. MASTROGIACOMO, P. PELOSI, S. SCHÜTZ, S. F. PETEU, C. KLEBER, C. REINER-ROZMAN, C. NOWAK, AND W. KNOLL: **Electronic Olfactory Sensor Based on *A. mellifera* Odorant-Binding Protein 14 on a Reduced Graphene Oxide Field-Effect Transistor**. *Angewandte Chemie* 127 (2015) pp. 13443–13446. doi: 10.1002/ange.201505712.

[336] C. REINER-ROZMAN, C. KOTLOWSKI, AND W. KNOLL: **Electronic Biosensing with Functionalized rGO FETs**. *Biosensors* 6 (2016) 17. doi: 10.3390/bios6020017.

[337] C. KOTLOWSKI, M. LARISIKA, P. M. GUERIN, C. KLEBER, T. KRÖBER, R. MASTROGIACOMO, C. NOWAK, P. PELOSI, S. SCHÜTZ, A. SCHWAIGHOFER, AND W. KNOLL: **Fine discrimination of volatile compounds by graphene-immobilized odorant-binding proteins**. *Sensors and Actuators B: Chemical* 256 (2018) pp. 564–572. doi: 10.1016/j.snb.2017.10.093.

[338] S. GOGALIC, S. HAGENEDER, C. CTORTECKA, M. BAUCH, I. KHAN, C. PREININGER, U. SAUER, AND J. DOSTALEK: **Plasmonically amplified fluorescence bioassay with microarray format**. *Proceedings of SPIE* 9506 (2015) 95060N. doi: 10.1117/12.2179470.

[339] F. A. GEISS, S. FOSSATI, I. KHAN, N. GISBERT QUILIS, W. KNOLL, AND J. DOSTALEK: **UV-SPR biosensor for biomolecular interaction studies**. *Proceedings of SPIE* 10231 (2017) 1023107. doi: 10.1117/12.2265683.

[340] AMO GMBH: **Fact Sheet AMONIL®**: **AMONIL® & AMOPRIME - low viscosity imprint resist and adhesion promoter**: https://www.amo.de/products-services/amonil/ [last accessed: March 15, 2018].

[341] P. E. CIDDOR: **Refractive index of air: new equations for the visible and near infrared**. *Applied Optics* 35 (1996) pp. 1566–1573. doi: 10.1364/AO.35.001566.

B Abbreviations

AFM	Depending on context either atomic force microscopy or atomic force microscope
3-CP	3-(carboxy)-2,2,5,5-tetramethyl-1-pyrrolidinyloxy, 3-carboxy-2,2,5,5-tetramethyl-1-pyrrolidinyloxy, free radical, also referred to as 3-carboxy-PROXYL
abs.	Absorption (in figure legends)
ANBDQBS	4-(1-[2-(di-n-butylamino)-6-naphthyl]-4-butadienyl)-1-(4-butylsulfonate) quinolinium betaine
ANEPPS	Di-8-butyl-amino-naphtyl-ethylene-pyridinium-propyl-sulfonate
ADP	Adenosine diphosphate
ATP	Adenosine triphosphate
ATR	Attenuated total reflection
ATR-SEIRAS	Attenuated total reflection surface-enhanced infrared absorption spectroscopy
bc_1, bc_1 complex	Coenzyme Q : cytochrome *c* – oxidoreductase, also referred to as ubiquinol : cytochrome *c* oxidoreductase or cytochrome bc_1 complex
BLM	Originally black lipid membrane; later also used for bilayer lipid membrane
CcO	Cytochrome *c* oxidase
CMC	Critical micellar concentration
cyt	Cytochrome
DDM	N-dodecyl-β-D-maltoside
DDM/DPK	Same as DPK buffer solution, containing 0.1 % DDM in addition
DDM/THK	Same as THK buffer solution, containing 0.1 % DDM in addition
DiPhyPC	1,2-diphytanoyl-sn-glycero-3-phosphocholine
DLS	Dynamic light scattering
DMSO	Dimethyl sulfoxide
DNA	Deoxyribonucleic acid
DPK	50 mM K_2HPO_4/100 mM KCl buffer solution, pH=8, adjusted with HCl; inherited abbreviation, exact meaning unknown
DTNTA	Dithiobis(nitrile acetic acid butylamidyl propionate)

DTP	3,3'-dithiodipropionic acid
eff.	Efficiency (in figure legends)
ESI-MS	Electrospray ionization mass spectroscopy
$FADH_2$, FAD	Flavin adenine dinucleotide, reduced and oxidized, respectively
FCCP	Carbonyl cyanide 4-(trifluoromethoxy)phenylhydrazone
Fig.	Figure
Fluorescein DHPE	1-(8-((3',6'-dihydroxy-3-oxo-spiro(isobenzofuran-1(3H),9'-(9H)xanthen)-5-yl)amino)-3-hydroxy-8-thioxo-2,4-dioxa-7-aza-3-phosphaoct-1-yl)-1,2-ethanediyl ester, P-oxide
FRAP	Fluorescence recovery after photobleaching
FRET	Foerster resonance energy transfer
FTIR (spectrometer)	Fourier transform infrared (spectrometer)
his-tag	Polyhistidyltag
IgG	Immunoglobulin G
IR	Infrared absorption spectroscopy
ISP	Iron-sulfur protein
LH1, LH2	Light-harvesting complex 1 & 2 in anorganic photosynthesis, not to be confused with the LHCII of green plants
LHCII	Light harvesting complex II, folded and associated with pigments
LHCP	Light harvesting complex II apoprotein
LSM	Laser-scanning microscopy; in the present thesis at any time confocal laser-scanning fluorescence microscopy
MP	Membrane protein
MPTES	3-mercaptopropyltrimethoxysilane
NADH, NAD^+	Nicotinamide adenine dinucleotide, reduced and oxidized, respectively
NADPH, $NADP^+$	Nicotinamide adenine dinucleotide phosphate, reduced and oxidized, respectively
NBD-PE	1,2-dihexadecanoyl-sn-glycero-3-phospho-(N-[4-nitrobenz-2-oxa-1,3-diazolyl)ethanolamine
NP	Nanoparticle; in the present thesis: Ni-NTA-functionalized silica nanoparticles
N-side	Negatively charged side of a membrane (membrane potential)

NTA	Nitrile tri-acetic acid
OBP14	Odorant-binding protein 14 (of *Apis mellifera*, honeybee)
p. a.	Pro analysi (highest degree of purity, meaning analytically pure)
P870	Reaction center P870 (of *Rhodobacter sphaeroides*); number derived from absorption maximum
P_i	Inorganic phosphate
PLB	Proteo-lipobead
PMMA	Poly(methyl methacrylate)
PSD	Phase-sensitive detection
P-side	Positively charged side of a membrane (membrane potential)
ptBLM	Protein-tethered bilayer lipid membrane
puriss.	Purissimum (second highest degree of purity, means purest, situated between purum (pure) and pro analysi (analytically pure, p. A.)
RC	Reaction center P870 (of *Rhodobacter sphaeroides*)
rpm	Revelations per minute
Ru_2C, Ru complex	$(2,2'\text{-bipyridine})_2Ru(\text{diphenanthroline})Ru(2,2'\text{-bipyridine})_2](PF_6)_4$
sim.	Simulation (in figure legends)
SNARF	Benzenedicarboxylic acid, 2(or 4)-[10-(dimethylamino)-3-oxo-3H-benzo[c]xanthene-7-yl])
SP	Surface plasmon
SPFS	Surface-plasmon field-enhanced fluorescence spectroscopy
SPR	Surface plasmon resonance
SU	Subunit
TE	Transversal electric (polarisation; synonymous for s- or σ-polarized)
THK	5 mM Tris-HCl/35 mM KCl buffer solution, pH=8, adjusted with NaOH
TM	Transversal magnetic (polarisation; synonymous for p- or π-polarized)
transm.	Transmission (in figure legends)
Tris	Tris(hydroxymethyl)aminomethane
tr-SEIRAS	Time-resolved surface-enhanced infrared absorption spectroscopy

UQ	Ubiquinone, also referred to as coenzyme Q_{10}
UQH_2	Ubiquinol, also referred to as ubihydroquinone
UV	Ultraviolet
UV/Vis	Ultraviolet/Visible
val. (tables)	Valinomycin

C Figures

D Tables

E Equations

F Publications

V Acknowledgements

At first, I would like to thank my former supervisors, <content not available in online version>, for the education that prepared me for this work.

I would like to thank my supervisor <content not available in online version> for accepting me as his Ph. D. student, for his infinite wealth of ideas, and for always finding quick solutions in cases that would have taken a long time without him.

I would like to thank <content not available in online version>, who actually did supervise me in the laboratory, for sharing her experience and her inexhaustible knowledge about respiratory enzyme complexes.

I would like to thank <content not available in online version>, who guided me – a non-phycisist – through the challenges of surface plasmon resonance spectroscopy.

I would like to thank all the other professors and doctors that provided help and guidance, or, not of lesser importance, proteins, labels, and other molecules that made this work possible. Especially, I would like to thank <content not available in online version> for their advice.

I would like to thank <content not available in online version>, again, and <content not available in online version>, who accepted to act as reviewers of this thesis. Moreover, I would like to thank <content not available in online version>, who guided me during the writing process.

I would like to thank my colleagues, not only for the shared work, but also for the great atmosphere at workplace.

I would like to thank the colleagues that became good friends over time, for becoming good friends.

And <content not available in online version>, for a lot of things…

Finally, I would like to thank this thesis for ending at last.

Declaration

I hereby confirm that I have conducted this work by myself and without any aids or references other than the specified ones. Services in return for payment were not utilized.

Mainz, November 05, 2018 _____

Frank Andreas Geiss

Erklärung

Hiermit versichere ich, dass ich die vorliegende Arbeit eigenständig angefertigt und keine anderen als die angegebenen Hilfsmittel und Quellen verwendet habe. Es wurde keine entgeltliche Hilfe Dritter in Anspruch genommen.

Mainz, 05. November 2018 _____

Frank Andreas Geiss